University of Alberta

Library Release Form

Name of Author: Ayça Sivrikoz

Title of Thesis: Enhanced Oil Recovery Modeling Using a Pressure Pulse-Geomechanical Black Oil Simulator

Degree: Doctor of Philosophy

Year this Degree Granted: 2009

_____

UNIVERSITY OF ALBERTA

ENHANCED OIL RECOVERY MODELING USING A PRESSURE PULSE-GEOMECHANICAL BLACK OIL SIMULATOR

by

AYÇA SIVRIKOZ

A THESIS
SUBMITTED TO THE FACULTY OF GRADUATE STUDIES AND RESEARCH IN
PARTIAL FULFILLMENT OF THE REQUIREMENTS FOR THE DEGREE OF
DOCTOR OF PHILOSOPHY
IN GEOTECHNICAL ENGINEERING

Department of Civil and Environmental Engineering

Edmonton, Alberta

Spring 2009

University of Alberta

Faculty of Graduate Studies and Research

The undersigned certify that they have read, and recommend to the Faculty of Graduate Studies and Research for acceptance, a thesis entitled ENHANCED OIL RECOVERY MODELING USING A PRESSURE PULSE-GEOMECHANICAL BLACK OIL SIMULATOR submitted by AYÇA SIVRIKOZ in partial fulfillment of the requirements for the degree of DOCTOR OF PHILOSOPHY.

Dr. Rick Chalaturnyk
Supervisor

Dr. Dave Chan

Dr. Timothy Joseph

Dr. Apostolos Kantzas
External Examiner

Dr. Derek Martin

Dr. Mauricio Sacchi

ABSTRACT

Pressure pulse is a high amplitude dynamic excitation of a porous medium which can be generated by injecting a low-frequency pulse of fluid into the medium. The process of pressure pulsing is a potential method for improving productivity and increasing recovery from oil reservoirs.

In this work enhanced oil recovery via the application of pressure pulsing is simulated by coupling geomechanics and pressure pulse equations. While the inclusion of geotechnical relationships leads to static changes in the rock properties, the pressure pulse equations capture the dynamic variations in porosity which allow improvement in oil recovery. The isothermal pressure pulse equations are derived based in part on the De la Cruz-Spanos theory. An iterative, fully coupled reservoir simulator was developed to analyze the effects of pressure pulses in reservoir fluid flow and oil recovery. Moreover, a system of equations derived by Osorio was solved to develop a 3D finite difference, fully implicit geotechnical model which simulated elastic deformations during production from a reservoir.

A series of sensitivity analyses were run to investigate the effects of rock and fluid properties on the pressure pulse propagation. Also, the impact of boundary conditions and geotechnical properties on permeability variation was studied. The results confirmed that the frequency of pressure pulses should be well tailored to the rock and fluid properties (e.g. permeability, rock compressibility, porosity, viscosity) so that an optimum pressure gradient can be generated within the reservoir in order to improve oil flow. The developed pressure pulse coupled reservoir simulator was used to investigate the reasons for unsuccessful pressure pulse laboratory experiments performed by BP at their Sunbury facilities. The conclusion that can be drawn from these results is that highly compressible materials in contact with the porous medium (such as Neoprene, rubber, or like materials used as membranes to protect the specimen during testing) can dampen the impulse that is applied to the porous medium, adversely affecting the propagation of a porosity-pressure wave and thereby resulting in no significant increase in fluid flow. It was

concluded that boundary conditions are crucial for a successful pressure pulse experiment in the lab. As for the static changes, boundary conditions are the most important factors determining permeability variations with pore pressure changes in the reservoir. Two domain models yield a greater change in permeability than single domain models.

ACKNOWLEDGMENTS

I would like to thank all people who have helped and provided inspiration to me during my doctoral study.

To my supervisor Dr. Rick Chalaturnyk I express my sincere gratitude for the assistance and constructive discussions regarding the research contained in this thesis. His guidance and support extended far beyond the bounds of an academic supervisor and for that I am very appreciative.

I would also like to thank Wavefront Energy and Environmental Services, CEO Brett Davidson. I was very fortunate to have the opportunity to work with and have many discussions with Dr. Tim Spanos and Dr. Norman Udey, both being very helpful in the completion of this work.

I sincerely appreciate the constructive criticism and effort put forth by my review committee, especially Dr. Carl Mendoza and Dr. Dave Chan, in helping to make this work more complete and accurate. I would also like to thank Dr. Luciane Cunha for her discussions and ideas pertaining to this thesis. A special thanks is reserved for Dr. Marcel Polikar for his never-ending encouragement and sense of humor. I would also like to express my appreciation to my colleague Raul Valdez and supervisor Jan Sherman at Shell for their support.

I would like to thank my mother, Elmira Sivrikoz, and father, Halit Sivrikoz, for being supportive and understanding during my time away from home and for providing me with the means to pursue this advanced degree.

Lastly, I am very grateful to my husband John Meyers for his love and patience during this period of our lives. One of the best experiences that we lived through during this time was the birth of our son, Evren, who provided an added motivational and joyful dimension to our life mission.

TABLE OF CONTENTS

1 INTRODUCTION 1

1.1 Statement of the Problem 1

1.2 Objectives and Scope 2

1.3 Organization of Thesis 3

2 LITERATURE REVIEW 5

3 BOAST ALGORITHM 11

4 GEOMECHANICS 19

4.1 Background 19

4.2 Fluid Flow Theory: 22

4.3 Linear Poroelastic Theory: 29

4.4 Numerical Analysis Approach 33

4.4.1 Notation Convention 33

4.5 Discretization of the Pore pressure Equation 35

4.6 Numerical Solution Procedure 36

5 PRESSURE PULSE EQUATIONS 37

5.1 Background 37

5.2 Mechanisms 37

5.2.1 Non-Conventional EOR Methods 37

5.2.2 Darcy Theory and Biot Theory 38

5.2.3 The Porosity Dilation Wave 41

5.2.4 Benefits to Flow Process 42

5.3 Theory Development 46

5.3.1 Fluid Phase Equations 46

5.3.2 Solid Phase Equations 54

5.3.3 Porosity 61

5.3.4 Coupled Wave Equations 64

5.3.5 Summary of Fluid and Solid Equations 65

5.3.6 Wave Equation 66

5.3.7 The Porosity Wave 80
5.4 Discretization of the Fluid and Solid Wave Equations 82
5.4.1 Discretization of the Fluid Wave Equations 82
5.4.2 Discretization of the Solid Wave Equations 84
5.5 Summary 86
6 COUPLING GEOMECHANICS AND PRESSURE PULSES IN BOAST 87
6.1 Methodology 87
6.2 A 1D Validation of the Pressure Pulse Model 92
6.3 Validation of the 3D Geomechanics Model 97
6.4 Sensitivity Analysis of the Geomechanics Model 103
6.4.1 Outer Boundary Conditions 103
6.4.2 Layer Locations with Respect to the Layer Boundary 105
6.4.3 Elastic Moduli of the Outer Domain 106
6.4.4 Using a Single Domain Instead of a Two-Domain Model 107
6.5 Sensitivity Analysis of the Pressure Pulse Model 110
6.5.1 Permeability Sensitivity 111
6.5.2 Viscosity Sensitivity 123
6.5.3 Porosity Sensitivity 138
6.5.4 Compressibility Sensitivity 154
6.5.5 Frequency Sensitivity 157
7 CONCLUSIONS 161
8 RECOMMENDATIONS 165
APPENDIX A – IMPES PROCEDURE 168
APPENDIX B – VERIFICATION OF PPT CODE WITH BP EXPERIMENT 176
REFERENCES 181

LIST OF TABLES

Table 6.1: Additional parameters used in simulations validating the geomechanics model 98

Table 6.2: Input data for sensitivity analysis 111

Table 6.3: Incremental cumulative production versus pulse frequency for fluid viscosities of 4000 and 50 cP 158

LIST OF FIGURES

Figure 1-1: Field example of the benefit of pressure pulsing on the oil production..... 1

Figure 3-1: BOAST algorithm..... 12

Figure 4-1: Physical system representing the 2-domain approach..... 20

Figure 5-1: Range of frequencies for dynamic excitation[21]..... 39

Figure 5-2: Pulsing at the pore scale..... 43

Figure 5-3: Pulsing overcomes capillarity..... 44

Figure 5-4: Viscous Instabilities..... 45

Figure 6-1: BOAST with Geomechanics and PPT Algorithm..... 87

Figure 6-2: Diagram of the Relation of Increasing Porosity and Fluid Saturation..... 89

Figure 6-3: PPT and BOAST..... 91

Figure 6-4: Experimental setup used in the pressure pulse test of Davidson, et al. [3]..... 92

Figure 6-5: Experimentally measured pressure drops at three locations in the porous medium (reproduced from the work of Davison, et al.[3])..... 94

Figure 6-6: Predicted pressure drops at three locations in the porous medium..... 95

Figure 6-7: Experimentally measured cumulative production for cases with and without pressure pulsing (reproduced from the work of Davison, et al.3)..... 96

Figure 6-8: Predicted cumulative production for cases with and without pressure pulsing..... 96

Figure 6-9: Bulk compressibility versus mean effective stress (Osorio[68])..... 99

Figure 6-10: Shear modulus versus mean effective stress (Osorio[68])..... 99

Figure 6-11: Permeability versus mean effective stress (Osorio[68])..... 100

Figure 6-12: Predicted permeability profile at various times for Case 1 (permeability is a function of only pore pressure)..... 101

Figure 6-13: Predicted permeability profile at various times for Case 2 (permeability is a function of both pore pressure and total stress) 101

Figure 6-14: Predicted permeability profile at various times and where permeability is a function of only pore pressure (reproduced from Osorio) 102

Figure 6-15: Predicted permeability profile at various times and where permeability is a function of both pore pressure and total stress (Osorio[68]) 102

Figure 6-16: Predicted permeability profile at the intersection of mid layer with the vertical plane containing the well after 500 and 4000 days of production for Cases 1, 2, and 3 104

Figure 6-17: Predicted permeability profile at the intersection of the upper and lower layers with the vertical plane containing the well after 500 and 4000 days of production for Cases 1, 2, and 3 105

Figure 6-18: Predicted volumetric strain profile at the intersection of the mid layer and the upper and lower layers with the vertical plane containing the well 106

Figure 6-19: Predicted permeability profile at the intersection of the mid layer with the vertical plane containing the well after 500 and 4000 days of production for Young's moduli of 72,000 and 720,000 psi 107

Figure 6-20: Predicted permeability profile at the intersection of the mid layer with the vertical plane containing the well for various times for a one domain model..... 108

Figure 6-21: Predicted permeability profile at the intersection of the mid layer with the vertical plane containing the well for various times for a two domain model 109

Figure 6-22: Predicted cumulative production for cases with and without pressure pulsing for a model with a permeability of 7000 mD (Run1) 112

Figure 6-23: Predicted cumulative production for cases with and without pressure pulsing for a model with a permeability of 5000 mD (Run2) 113

Figure 6-24: Predicted cumulative production for cases with and without pressure pulsing for a model with a permeability of 3000 mD (Run3) 113

Figure 6-25: Predicted cumulative production for cases with and without pressure pulsing for a model with a permeability of 1000 mD (Run4) 114

Figure 6-26: Predicted cumulative production for cases with and without pressure pulsing for a model with a permeability of 500 mD (Run5) 114

Figure 6-27: Predicted cumulative production for cases with and without pressure pulsing for a model with a permeability of 300 mD (Run6) 115

Figure 6-28: Predicted cumulative production for cases with and without pressure pulsing for a model with a permeability of 200 mD (Run7) 115

Figure 6-29: Predicted cumulative production for cases with and without pressure pulsing for a model with a permeability of 100 mD (Run8) 116

Figure 6-30: Predicted cumulative production for cases with and without pressure pulsing for a model with a permeability of 50 mD (Run9) 116

Figure 6-31: Predicted cumulative production at 30 minutes versus permeability for cases with and without pressure pulsing..... 117

Figure 6-32: Predicted ratio of cumulative production with pressure pulsing to cumulative production without pressure pulsing versus permeability 118

Figure 6-33: Predicted pressure profile at four locations for a model with a permeability of 7000 mD (Run1) 119

Figure 6-34: Predicted pressure profile at four locations for a model with a permeability of 5000 mD (Run2) 119

Figure 6-35: Predicted pressure profile at four locations for a model with a permeability of 3000 mD (Run3) 120

Figure 6-36: Predicted pressure profile at four locations for a model with a permeability of 1000 mD (Run4) 120

Figure 6-37: Predicted pressure profile at four locations for a model with a permeability of 500 mD (Run5)..... 121

Figure 6-38: Predicted pressure profile at four locations for a model with a permeability of 300 mD (Run6)..... 121

Figure 6-39: Predicted pressure profile at four locations for a model with a permeability of 200 mD (Run7)..... 122

Figure 6-40: Predicted pressure profile at four locations for a model with a permeability of 100 mD (Run8)..... 122

Figure 6-41: Predicted pressure profile at four locations for a model with a permeability of 50 mD (Run9) 123

Figure 6-42: Predicted cumulative production for cases with and without pressure pulsing for a model with a fluid viscosity of 4000 cP (Run10)..... 124

Figure 6-43: Predicted cumulative production for cases with and without pressure pulsing for a model with a fluid viscosity of 2000 cP (Run11)..... 125

Figure 6-44: Predicted cumulative production for cases with and without pressure pulsing for a model with a fluid viscosity of 1000 cP (Run12)..... 125

Figure 6-45: Predicted cumulative production for cases with and without pressure pulsing for a model with a fluid viscosity of 700 cP (Run13)..... 126

Figure 6-46: Predicted cumulative production for cases with and without pressure pulsing for a model with a fluid viscosity of 300 cP (Run14)..... 126

Figure 6-47: Predicted cumulative production for cases with and without pressure pulsing for a model with a fluid viscosity of 50 cP (Run15)..... 127

Figure 6-48: Predicted cumulative production for cases with and without pressure pulsing for a model with a fluid viscosity of 5 cP (Run16)..... 127

Figure 6-49: Predicted cumulative production at 30 minutes versus fluid viscosity for cases with and without pressure pulsing..... 128

Figure 6-50: Predicted ratio of cumulative production with pressure pulsing to cumulative production without pressure pulsing versus fluid viscosity..... 128

Figure 6-51: Predicted pressure profile at four locations for a model with a fluid viscosity of 4000 cP (Run10) 129

Figure 6-52: Predicted pressure profile at four locations for a model with a fluid viscosity of 2000 cP (Run11) 130

Figure 6-53: Predicted pressure profile at four locations for a model with a fluid viscosity of 1000 cP (Run11) 130

Figure 6-54: Predicted pressure profile at four locations for a model with a fluid viscosity of 700 cP (Run13) 131

Figure 6-55: Predicted pressure profile at four locations for a model with a fluid viscosity of 300 cP (Run14) 131

Figure 6-56: Predicted pressure profile at four locations for a model with a fluid viscosity of 50 cP (Run15) 132

Figure 6-57: Predicted pressure profile at four locations for a model with a fluid viscosity of 5 cP (Run16) 132

Figure 6-58: Predicted ratio of cumulative production with pressure pulsing to cumulative production without pressure pulsing versus permeability for a model with a fluid viscosity of 4000 cP 134

Figure 6-59: Predicted ratio of cumulative production with pressure pulsing to cumulative production without pressure pulsing versus permeability for a model with a fluid viscosity of 2000 cP 134

Figure 6-60: Predicted ratio of cumulative production with pressure pulsing to cumulative production without pressure pulsing versus permeability for a model with a fluid viscosity of 1000 cP 135

Figure 6-61: Predicted ratio of cumulative production with pressure pulsing to cumulative production without pressure pulsing versus permeability for a model with a fluid viscosity of 700 cP 135

Figure 6-62: Predicted ratio of cumulative production with pressure pulsing to cumulative production without pressure pulsing versus permeability for a model with a fluid viscosity of 300 cP 136

Figure 6-63: Predicted ratio of cumulative production with pressure pulsing to cumulative production without pressure pulsing versus permeability for a model with a fluid viscosity of 50 cP 136

Figure 6-64: Predicted ratio of cumulative production with pressure pulsing to cumulative production without pressure pulsing versus permeability for a model with a fluid viscosity of 5 cP 137

Figure 6-65: Summary of the effect of fluid viscosity on the predicted ratio of cumulative production with pressure pulsing to cumulative production without pressure pulsing versus permeability..... 138

Figure 6-66: Predicted cumulative production for cases with and without pressure pulsing for a model with a fluid viscosity of 4000 cP, a porosity of 0.45 and a permeability of 2000 mD..... 139

Figure 6-67: Predicted cumulative production for cases with and without pressure pulsing for a model with a fluid viscosity of 4000 cP, a porosity of 0.45 and a permeability of 1150 mD..... 139

Figure 6-68: Predicted cumulative production for cases with and without pressure pulsing for a model with a fluid viscosity of 4000 cP, a porosity of 0.45 and a permeability of 1000 mD..... 140

Figure 6-69: Predicted cumulative production for cases with and without pressure pulsing for a model with a fluid viscosity of 4000 cP, a porosity of 0.45 and a permeability of 700 mD..... 140

Figure 6-70: Predicted cumulative production for cases with and without pressure pulsing for a model with a fluid viscosity of 2000 cP, a porosity of 0.45 and a permeability of 700 mD..... 141

Figure 6-71: Predicted cumulative production for cases with and without pressure pulsing for a model with a fluid viscosity of 2000 cP, a porosity of 0.45 and a permeability of 500 mD..... 141

Figure 6-72: Predicted cumulative production for cases with and without pressure pulsing for a model with a fluid viscosity of 2000 cP, a porosity of 0.45 and a permeability of 400 mD..... 142

Figure 6-73: Predicted cumulative production for cases with and without pressure pulsing for a model with a fluid viscosity of 1000 cP, a porosity of 0.45 and a permeability of 500 mD..... 142

Figure 6-74: Predicted cumulative production for cases with and without pressure pulsing for a model with a fluid viscosity of 1000 cP, a porosity of 0.45 and a permeability of 250 mD..... 143

Figure 6-75: Predicted cumulative production for cases with and without pressure pulsing for a model with a fluid viscosity of 1000 cP, a porosity of 0.45 and a permeability of 100 mD..... 143

Figure 6-76: Predicted cumulative production for cases with and without pressure pulsing for a model with a fluid viscosity of 700 cP, a porosity of 0.45 and a permeability of 300 mD..... 144

Figure 6-77: Predicted cumulative production for cases with and without pressure pulsing for a model with a fluid viscosity of 700 cP, a porosity of 0.45 and a permeability of 175 mD..... 144

Figure 6-78: Predicted cumulative production for cases with and without pressure pulsing for a model with a fluid viscosity of 700 cP, a porosity of 0.45 and a permeability of 75 mD..... 145

Figure 6-79: Predicted cumulative production for cases with and without pressure pulsing for a model with a fluid viscosity of 300 cP, a porosity of 0.45 and a permeability of 130 mD..... 145

Figure 6-80: Predicted cumulative production for cases with and without pressure pulsing for a model with a fluid viscosity of 300 cP, a porosity of 0.45 and a permeability of 75 mD..... 146

Figure 6-81: Predicted cumulative production for cases with and without pressure pulsing for a model with a fluid viscosity of 50 cP, a porosity of 0.45 and a permeability of 25 mD..... 146

Figure 6-82: Predicted cumulative production for cases with and without pressure pulsing for a model with a fluid viscosity of 50 cP, a porosity of 0.45 and a permeability of 12 mD..... 147

Figure 6-83: Predicted cumulative production for cases with and without pressure pulsing for a model with a fluid viscosity of 50 cP, a porosity of 0.45 and a permeability of 7 mD..... 147

Figure 6-84: Predicted cumulative production for cases with and without pressure pulsing for a model with a fluid viscosity of 2000 cP, a porosity of 0.2 and a permeability of 90 mD..... 148

Figure 6-85: Predicted cumulative production for cases with and without pressure pulsing for a model with a fluid viscosity of 2000 cP, a porosity of 0.2 and a permeability of 80 mD..... 148

Figure 6-86: Predicted cumulative production for cases with and without pressure pulsing for a model with a fluid viscosity of 2000 cP, a porosity of 0.2 and a permeability of 60 mD..... 149

Figure 6-87: Predicted cumulative production for cases with and without pressure pulsing for a model with a fluid viscosity of 1000 cP, a porosity of 0.2 and a permeability of 60 mD..... 149

Figure 6-88: Predicted cumulative production for cases with and without pressure pulsing for a model with a fluid viscosity of 1000 cP, a porosity of 0.2 and a permeability of 40 mD..... 150

Figure 6-89: Predicted cumulative production for cases with and without pressure pulsing for a model with a fluid viscosity of 1000 cP, a porosity of 0.2 and a permeability of 30 mD..... 150

Figure 6-90: Predicted cumulative production for cases with and without pressure pulsing for a model with a fluid viscosity of 700 cP, a porosity of 0.2 and a permeability of 28 mD..... 151

Figure 6-91: Predicted cumulative production for cases with and without pressure pulsing for a model with a fluid viscosity of 700 cP, a porosity of 0.2 and a permeability of 15 mD..... 151

Figure 6-92: Predicted cumulative production for cases with and without pressure pulsing for a model with a fluid viscosity of 300 cP, a porosity of 0.2 and a permeability of 20 mD..... 152

Figure 6-93: Predicted cumulative production for cases with and without pressure pulsing for a model with a fluid viscosity of 300 cP, a porosity of 0.2 and a permeability of 12 mD..... 152

Figure 6-94: Predicted cumulative production for cases with and without pressure pulsing for a model with a fluid viscosity of 300 cP, a porosity of 0.2 and a permeability of 8 mD..... 153

Figure 6-95: Summary of the optimum permeabilities at which pressure pulsing is beneficial versus porosity for various values of fluid viscosity 154

Figure 6-96: Summary of the optimum permeabilities at which pressure pulsing is beneficial versus fluid viscosity for various values of porosity 154

Figure 6-97: Predicted cumulative production for cases with and without pressure pulsing for a model with a rock compressibility of $3x10^{-7}$ psi^{-1} 155

Figure 6-98: Predicted cumulative production for cases with and without pressure pulsing for a model with a rock compressibility of $3x10^{-5}$ psi^{-1} 156

Figure 6-99: Predicted cumulative production for cases with and without pressure pulsing for a model with a rock compressibility of $3x10^{-4}$ psi^{-1} 156

Figure 6-100: Schematic showing the undesired behavior of low frequency pressure pulses 159

Figure 6-101: Schematic showing the desired behavior of optimal frequency pressure pulses 159

Figure A-1: Conservation of mass 168

Figure B-2: Schematic of the pressure pulse experiment performed by BP 176

Figure B-3: Flowrate versus pressure resulting from the BP pressure pulse test 177

Figure B-4: Cross-section of the simulation model of the BP pressure pulse test..... 178

Figure B-5: Predicted pressure response at three locations within the porous medium 179

Figure B-6: Predicted pressure response at three locations within the membrane 179

LIST OF SYMBOLS

A	Gridblock area perpendicular to the flow-direction [cm^2]
a	Attenuation [Q^{-1}]
B_f	Formation factor of the pore fluid [RB/STB]
b	Bulk attenuation [Q^{-1}]
c_b	Bulk compressibility of the sample [psi^{-1}]
c_f	Compressibility of the pore fluid [psi^{-1}]
c_p	Fluid/pore compressibility [psi^{-1}]
c_s	Unjacketed bulk compressibility [psi^{-1}]
c_t	Total compressibility [psi^{-1}]
$D_{\phi s}$	Diffusion coefficient
E	Young's Modulus [psi]
e	Volumetric strain
f_s	External force density [N/m^3]
f	Source terms [N]
G	Shear modulus [GPa]
K	Absolute permeability [md, m^2]
K_f	Bulk modulus of the fluid [Pa]
K_b	Rock bulk modulus [Pa]
K_ϕ	Porosity's bulk modulus [Pa]
$K_{\alpha\alpha}$	Relative permebility, fluid α
$K_{\alpha\beta}$	Change in relative permeability of fluid α due to acceleration from fluid β at pressure pulse
$R_{\alpha\alpha}$	Darcy resistance function
$R_{\alpha\beta}$	Darcy resistance function
k	Relative permeability
$\dot{m}_f$	Rate of mass of fluid injected [lb/sec]
$\delta\dot{m}$	Deviation from the unperturbed mass rate [lb/sec]
P	Fluid pressure [psi]

P_c	Confining pressure, capillary pressure [psi]
P_{COW}	Capillary pressure for oil-water system [psi]
P_d	Differentail pressure: P_c-P [psi]
q	Flow rate [lb/sec]
R_{Sf}	Solution gas fluid ratio [scf/STB]
S_f	Fluid saturation
S_1	Fluid saturation, fluid one
S_2	Fluid saturation, fluid two
T	Transmissibility
u	Displacement [cm, m]
V_b	Bulk volume [cc]
V_p	Pore volume [cc]
υ_o	Undamped wave speed [m/s]
α	Biot's coefficient
δ	Derivation from the unperturbed value, dilation factor
ε_{ij}	Strain tensor
ε_{ii}	Bulk strain
ϕ	Porosity
η	Percentage of the rock space, 1-ϕ
λ_f	Mobility
μ	Viscosity [cp]
ν	Poisson's Ratio
ρ	Density [kg/m^3, lb/cft]
σ'	Effective stress [psi, kPa, MPa]
σ_{ij}	Stress tensor [psi, kPa, MPa]
σ_m	Mean stress [psi, kPa, MPa]
υ_f	Fluid velocity [m/s]
υ_s	Solid velocity [m/s]
ξ_f	Bulk viscosity [cp]

1 INTRODUCTION

1.1 Statement of the Problem

In practical terms, pressure pulsing is simply the high-amplitude dynamic excitation of a porous medium which, under a pressure gradient, increases the flow rate of liquid along the direction of the pressure gradient. Mechanical means of excitation involve injecting a low-frequency pulse of fluid into the medium creating many different waves, such as seismic waves.

Low-frequency pulses of fluid in a porous medium also create a slow strain wave called the porosity dilation wave which results from the interactions and deformations between the fluid and matrix in the porous media. The porosity dilation wave travels at velocities on the order of 5–150 m/s and is characterized by a spreading front of elastic porosity changes which are responsible for the flow rate enhancement effect. A field example of the impact of pressure pulsing on the oil rate is shown in Figure 1-1. Pressure pulsing is applied to a heavy oil field which was approaching to the end of its life. As soon as the pressure pulsing started the drop in the oil rate slowed significantly.

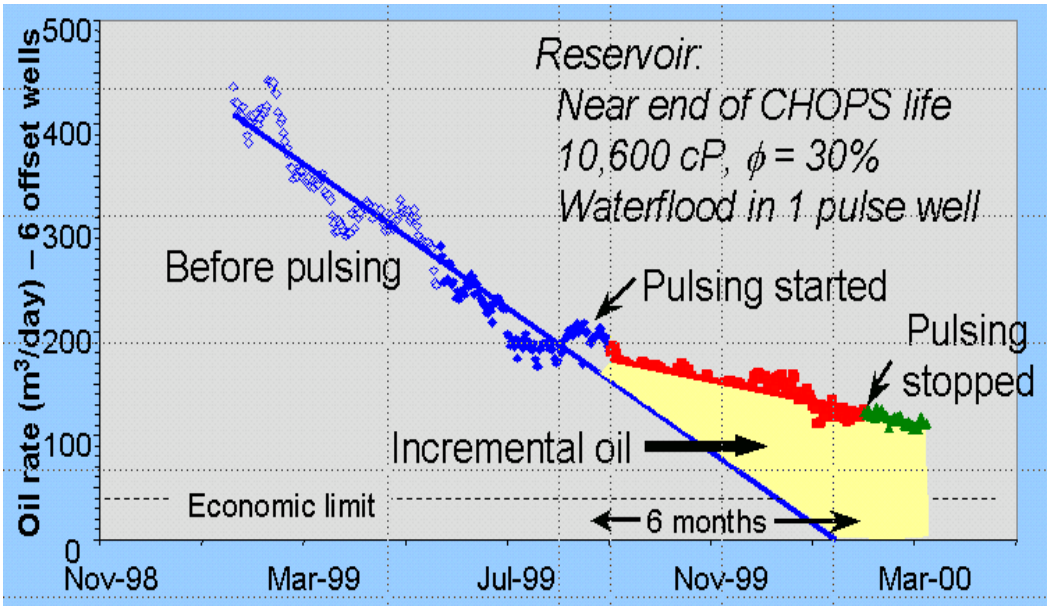

Figure 1-1: Field example of the benefit of pressure pulsing on the oil production

As waves of increased and decreased porosity pass through a medium they induce the pore fluid to flow. In addition to significantly increasing the flow of the pore fluid, pressure pulsing also has an associated reservoir pressurization effect that is seen in both the field and laboratory[1,2,7]. The flow enhancement effect is integrally linked with the reservoir pressurization effect. As the porosity diffusion wave moves through the porous medium, it is accompanied by an increase in pressure. The cause of this pressurization is that as the porosity wave dies off, it leaves the fluid with no place to go. The fluid, in turn, causes the matrix to elastically compress, which leaves that portion of the reservoir pressurized. It is important to note here that the distance the porosity diffusion wave travels is dependent on variables such as fluid viscosity, confining stress, porosity, permeability, and pore geometry. Therefore, because the confining pressure has been increased in this portion of the reservoir, the next diffusion wave and accompanying fluid can permeate even further. The end result is that the entire reservoir becomes pressurized.

1.2 Objectives and Scope

While a theoretical framework exists for pressure-pulsing theory and field evidence has been obtained to confirm the concept, no capability currently exists for modeling the influence of pressure pulsing on multi phase flow within a reservoir.

The main research objectives are:

i. develop an iterative, fully coupled procedure that permits the analysis of pressure pulsing by modeling the propagation of porosity waves in a reservoir.
ii. In addition to a model of pressure pulsing, a 3D finite difference, fully implicit geomechanical model will be developed to simulate the physical phenomena occuring during production from reservoirs with stress-sensitive mechanical and fluid-flow properties. The combined effect of stress changes (elastic deformations), fluid flow and reservoir property changes on oil recovery will be evaluated by a fully coupled procedure that integrates pressure pulsing, geomechanics and reservoir simulation (BOAST, Black Oil Applied Simulation Tool).

In this study a simplified black oil simulator, rather than a compositional simulator, is used. For low-volatility oil systems, consisting mainly of methane and heavy components, this model can be used to describe the hydrocarbon equilibrium. In this model it is assumed that gas can dissolve both in water and in oil.

In the geomechanical model only elastic deformations are assumed. This is realistic as long as the injection pressure does not exceed the formation fracture presssure. For most oil reservoir simulators, porosity is a simple function of pore pressure, however in this study, the governing equations describing the deformation of the solid part of the rock are fully coupled with governing equations describing the changes in pore pressure.

Our goal is to build a two-phase numerical reservoir simulator capable of modeling the process of pressure pulsing. No experimental work will be conducted in this research. After completing the numerical analyses, field/lab data, obtained from various industrial sources, will be used for history match and sensitivity studies.

1.3 Organization of Thesis

The literature search is presented in Chapter 2. It provides an overview of the existing laboratory and theoretical works studying the effects of elastic wave excitation in porous media. In Chapter 3 an introduction and overview of BOAST (Black Oil Applied Simulator Tool) is given. The workflow and main parts of the algorithm are reviewed in this chapter. The main oil simulation equations are presented which will be combined with pressure pulsing and geomechanical theory in subsequent chapters. Chapter 4 focuses on the concept of geomechanics in reservoir production. A coupled solution of the fluid flow and stress deformation model is presented by developing a fluid flow model and a linear poroelastic model. A numerical analysis is also presented which reviews the approaches taken to discretize nonlinear partial differential equations of fluid flow and stress deformation.

Chapter 5 is devoted to the concept of pressure pulsing. It provides an overview of the background, field and laboratory studies performed in the literature. It introduces the new pressure pulsing theory and compares it with well-known theories, i.e. Darcy and Biot theories. Chapter 5 also presents the mechanisms of pressure pulsing and addresses why pressure pulsing can be used as an enhanced oil recovery method. Finally, theory development and derivation of wave equations are presented.

Chapter 6 details a method to decoupling geomechanics and pressure pulsing in BOAST. Such a methodology encompasses all the knowledge and understanding gathered from the theoretical work and can be applied elsewhere, i.e. other commercial reservoir simulators. Following the methodology, both the pressure pulse model and 3D geomechanics model are validated against lab results and literature. For the pressure pulse model, the results of two laboratory core flood tests are used in validation; the first one conducted by Davidson, et al.[3] and the other by Dusseault, M.B[71]. As for the 3D geomechanical model, the results of our study are compared to the work of J.G. Osario, et al.[63]. Finally a sensitivity study is conducted both for the pressure pulsing and for the 3D geomechanical model.

Chapters 7 and 8 present the conclusions and recommendations based on a study of the assumptions taken and results of our research.

2 LITERATURE REVIEW

The existence of coupled diffusion dynamic processes in porous media is well documented in the literature.

Empirical evidence is found in many papers from Russia describing enhanced production from oil reservoirs due to earthquakes. These papers report increased production rates and the release of fines into production wells following seismic events[20]. Also, a comprehensive review of field, laboratory and theoretical work studying the effects of elastic wave excitation was performed by Beresnev and Johnson[30]. The authors found that, due its effect on permeability, elastic wave excitation could increase production of hydrocarbons from porous media.

Fundamental work on the application of elastic wave theory to fluid-saturated porous media was performed by Biot[12]. In this work, Biot described the propagation of elastic wave a saturated porous medium and derived the Biot equation. Biot[12] developed a theory for the propagation of stress waves in a porous elastic solid containing a compressible viscous fluid. He studied both the low frequency range, where the assumption of Poiseuille flow is valid, and the higher frequencies. In his papers he established relations between stress and strain for static deformation then analyzed the wave propagation when the fluid is viscous and non-viscous. The breakdown of Poiseuille flow beyond the critical frequency is discussed for pores of flat and circular shapes. The emphasis of the treatment is on cases where fluid and solids are of comparable densities.

Biot's work was used by numerous authors studying porous media. Deresiewicz and Rice[13] used the equation to study wave scattering in a saturated medium. Birch[14] noted a strong nonlinear dependence of modulus on pressure, and a nonlinear stress-strain relation due to structural discontinuities in the form of cracks, grain boundaries, etc. Stoll and Bryan[15] and Norris[38] characterized the wave attenuation mechanism in a poroelastic medium and demonstrated how these effects might be incorporated into Biot's equation.

Hamilton[16] proposed to describe the static and dynamic nonlinear behavior by expanding the modulus in Hook's law as a power series in strain. Bonnet[32] reviewed some extensions of Biot's equations and derived the complete basic singular solution in the frequency domain for dynamic poroelasticity problems by analogy with thermoelasticity.

Zobnin, Kudryavtsev and Parton[33] explored the flow in inhomogeneous porous systems through the analysis of model periodic structures and obtained an integral differential equation that describes the motion of a viscous fluid in a rigid porous medium of periodic structure. Depollier, Allard and Lauriks[34] pointed out that the homogenization process of Biot's equation only applied for a significantly small viscosity fluid. Zinov'yeva et al.[35] demonstrated that rock showed a large nonlinear response under relatively small strain. Hassanzadeh[36] developed the Biot acoustic formula by adopting a finite difference algorithm based on a homogeneous approach. Zhu and McMechan[37] studied the poroelastic wave equation based on a homogeneous approach. Norris[38] discussed the analog between the equation of static poroelasticity and the equation of thermoelasticity including entropy, and derived a method of determining the effective parameters in an inhomogeneous poroelastic medium using known results from the literature on the effective thermal expansion coefficient and the effective heat capacity of a disordered thermoelastic continuum. Johnson and McCall[39] proposed that as the wave propagates, there is a local increase in the density and modulus during compression and a local decrease in density and modulus during rarefaction. Zimmerman and Stern[40] obtained a series of solutions for the plane compression wave scattering by a spherical poroelastic inhomogeneity medium, which started from Biot's poroelastic model. Dai, Vafidis and Kanasewich[41] simulated the seismic wave propagation in a porous medium by using a particle velocity-stress, finite-difference method. The modeling enabled them to obtain the particle velocity fields of the volume-averaged solid and fluid motion, and the volume-averaged solid stress and fluid pressure wavefields. Furthermore, this method enabled them to model the seismic response of a heterogeneous medium without introducing numerical approximations of the space derivatives of the physical parameters. Abousleiman et al.[42] addressed the phenomena of mechanical creep and deformation in rock formations coupled with the hydraulic effects of fluid flow. Johnson

et al.[43] developed a relationship between the nonlinear elastic parameters of rocks and the stress-induced effects on waves propagating in rocks. Li, Cederbaum and Schulgasser[44] noted that axial fluid diffusion in vibrating beams could easily provide a very strong damping mechanism.

Ochs, Chen and Teufel[66] investigated the rock stress response to the transient fluid pressure in a well with a stationary vertical fracture within the framework of Biot's poroelasticity. Laboratory observation of elastic wave propagation provided evidence to verify the theoretical and modeling approaches. Brown[45] pointed out that in the absence of viscosity, a flow pattern minimizes the inertial effects of the fluid; while in the absence of the inertial forces, a flow pattern minimizes the viscous resistivity to flow. At intermediate frequencies, both inertial and viscous forces are significant and any developed flow pattern must be a compromise that minimizes neither viscous nor inertial effects. Winkler and Nur[46] illustrated that shear wave attenuation is more sensitive in fully saturated rock than that of compression waves, and the attenuation of both shear waves and compression waves are significantly different in fully saturated rock and partially saturated rock. Williams et al.[67] showed that both velocity and attenuation of elastic waves could be correlated with porous medium permeability. Chang, Liu and Johnson[47] predicted the in-situ rock permeability through low-frequency tube wave stimulation. Winkler, Liu and Johnson[51] indicated experimentally that in oil-field boreholes, Stoneley-wave observations will generally be made in the low-frequency range of theory and suggested that Stoneley wave velocity and attenuation may be indicative of the formation permeability. Auriault[48,49] investigated the macroscopic quasistatic description of a deformable porous medium with a double porosity constituted by pores and structures, based on a homogeneous technique. The work exhibited a coupling between the flow and the pores and structures. Auriault[48,49] demonstrated that macroscopic behavior of the double porosity medium shows two characteristic pulsations, one corresponds to the quasistatic viscous fluid flow through the microporous medium, and one is the characteristic pulsation of the dynamic fluid flow in the fractures. Bernabe[50] evaluated the standard frequency dependence of dynamic permeability during the transition from macroscopic viscous flow at low frequency to inertial flow at high

frequency, and observed that in networks with large amount of storage pore space, the fluid compressibility could affect the result drastically.

Pan[52] investigated single-phase intermediate frequency stimulation by modeling the coupling of the solid and liquid motions at the pore scale. Starting from the basic Navier-Stokes equation which is suitable for describing fluid flow in pores and combining with the homogenization process, Pan derived five separate characteristic macroscopic models to describe the macroscopic behaviour of deformable porous media. Pan showed that the response of a porous medium to harmonic perturbations depended on the parameters of the pore structure, the properties of the fluid and the frequencies of the excitation signal. The elastic wave vibration had a positive impact on fluid flow under harmonic perturbation.

Odeh and McMillen[28] derived a nonlinear differential equation which can approximately describe the space-behavior of a small propagating pressure pulse in an air-saturated porous medium. Haskett, Narahara and Holditch[29] studied pressure transients analytically utilizing gas flow in small volumes and stated that the result is very sensitive to both porosity and permeability.

De la Cruz and Spanos[79] attempted to formulate macroscopic relations for equilibrium thermodynamics from the well-understood pore scale description. They used volume-averaged equations to provide the linkage to pore scale thermodynamics. In this study, porosity is treated as a new purely macroscopic variable and its natural thermodynamic role was investigated. In Biot's theory porosity is not explicitly taken as a variable. The de la Cruz - Spanos porous media model was formulated from basic physical properties to describe wave propagation in porous media. Most importantly, this model includes porosity as a dynamic variable that plays a fundamental role in both the thermomechanics and thermodynamics of the porous medium.

Spanos and coworkers[4,21] introduced pressure pulse flow enhancement as a non-conventional EOR method, describing it with both lab experiment results and field

evidence. The porosity diffusion wave, which is responsible for flow enhancement, and its foundations were explained. A brief synopsis of the two major applicable theories of wave propagation in fluid filled porous media, conventional (Biot) wave propagation theory and the most recent multi-component (de la Cruz-Spanos) theory, was given. A five spot pattern field trial, conducted by Wascana Energy Inc., was investigated with the results showing that pressure pulsing increases the fluid gradient across the sand destabilization zone and decreases the water content of the produced fluid.

Geilikman, Spanos and Nyland[5] showed that a porosity diffusion wave propagates from a seismic source in fluid-saturated porous media. It was observed that this process would cause a travelling pulse of pressure associated with the spreading front of porosity and would result in variations in fluid levels in the earth's crust following a seismic event. Analytical solutions were given to describe porosity and pressure changes as a function of spatial coordinates and time.

Hickey and coworkers[6] introduced a one-parameter family of compressibilities which included the drained and undrained compressibilities as members. The family of compressibilities were also used to obtain an expression for the pore pressure build-up coefficient.

De la Cruz and his coworkers[7,9] discussed the concept of macroscopic pressure difference between two immiscible incompressible fluid phases flowing through homogeneous porous media. In their study the analysis is restricted to the case of incompressible, slow, quasi-static flow.

Dusseault, Shand and Davidson[8] investigated performing pressure pulse workovers on heavy oil wells. According to their study, pressure-pulsing had a combination of various effects, including perforation unblocking, far field excitation and good placement chemical dispersion. Pressure-pulsing remolded and liquefied compacted sand around the wellbore, prevented sand blockage and helped the Cold Heavy Oil Production Stimulation (CHOPS) well start producing sand during primary completion attempts.

Moreover, the authors showed pressure-pulsing could be used when the well became disconnected from the far-field pressure and gravity driving forces and in cases when it is desired to place a workover chemical in a well-dispersed fashion around a well. Because the sharp pulses tended to suppress fingering and partially overcome capillary blockage at pore throats, treatment chemicals were well-dispersed around the wellbore.

De la Cruz and Spanos[7,9] presented a complete set of equations to describe low-frequency seismic wave phenomena in a fluid-filled porous medium. A straightforward analysis of equations yielded predictions of wave velocities and attenuations as functions of frequency. The attendant thermal aspects are explicitly taken into account.

In summary, a study of the literature has shown that the effects of elastic wave excitation on production of hydrocarbons have been observed and reported. The fundamental theory of propagation of elastic waves in saturated porous media has been developed by Biot. Numerous authors have studied different methods to simulate seismic wave propagation in porous media. The macroscopic models to describe the macroscopic behaviour of elastic wave propagation have also been developed and studied in the literature. Our literature search shows that a theoretical framework exists for pressure-pulsing theory and field evidence has been obtained to confirm the concept. However, no capability currently exists for modeling the influence of pressure pulsing on two-phase flow within a reservoir.

3 BOAST ALGORITHM

BOAST was selected to serve as the structural framework for implementing the coupled pressure pulse and geomechanical models proposed in this thesis. It is a three-dimensional, three-phase black oil applied simulation tool and was released by the US Department of Energy in 1982. As it is a public domain program, it has been extensively used by various research, academic and industry organizations[53,54].

The BOAST II program simulates isothermal, Darcy flow in three dimensions. It assumes reservoir fluids can be described by three fluid phases (oil, gas and water) of constant composition with physical properties that depend on pressure only. Technically, BOAST II is a finite-difference, implicit pressure-explicit saturation (IMPES) numerical simulator. It contains both direct and iterative solution techniques for solving systems of algebraic equations.

Figure 3-1 shows the basic structure of the BOAST algorithm. While further information can be obtained from the BOAST User's Manual[53], the main parts in the algorithm are explained below:

Initialization Data (1-8): Initialization data files, i.e. restart and post plot options, reservoir model grid dimensions and geometry, porosity and permeability distributions, relative permeability and capillary pressure data, fluid PVT data, initial pressure and saturation distribution, matrix solution method, run control and diagnostic parameters and aquifer parameters are specified. These files are read only once at the beginning of the simulation. They must be read in the order shown in flow chart. Detailed explanations for each step are given in the next section.

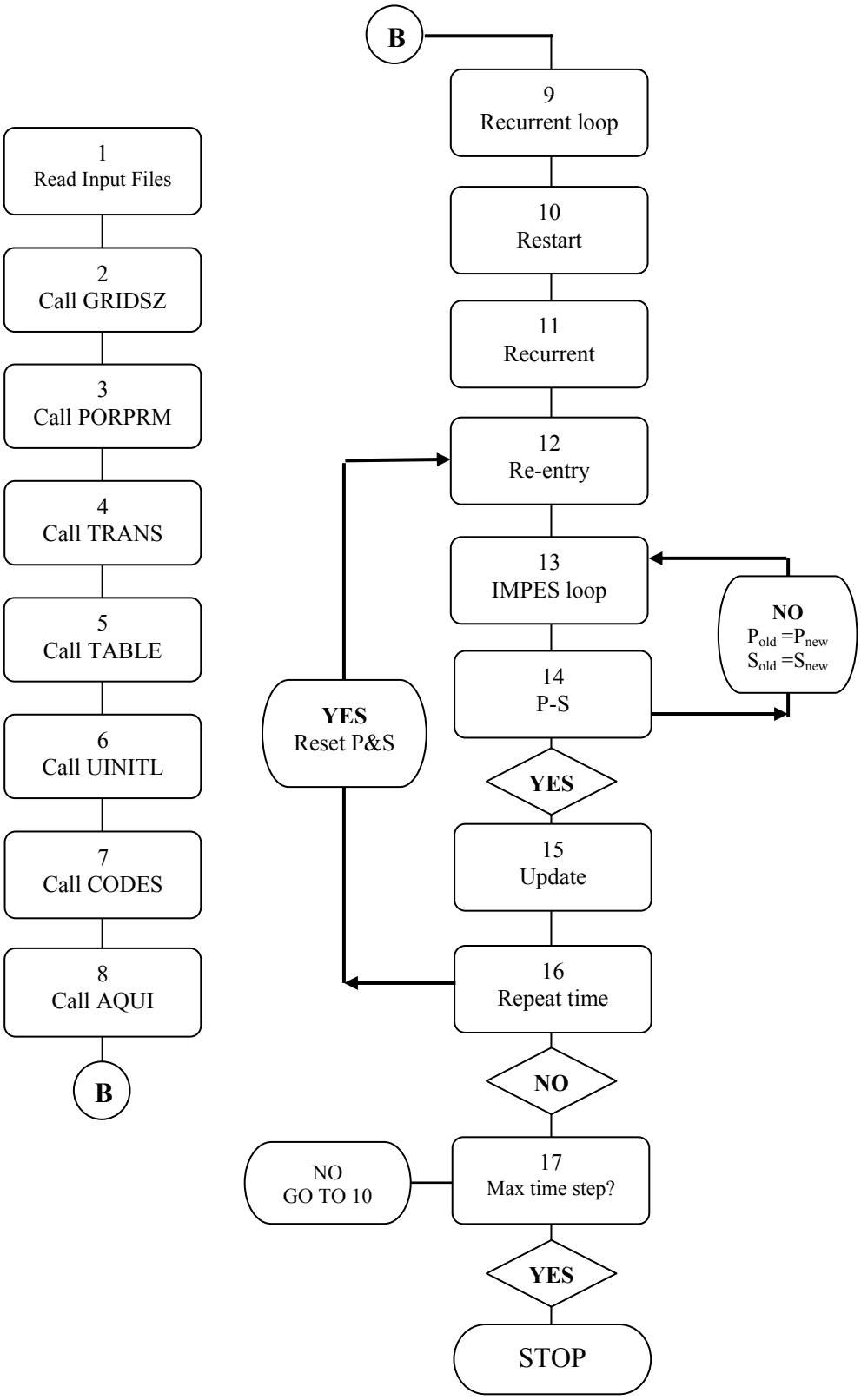

Figure 3-1: BOAST algorithm

Recurrent Data: Recurrent data files are read repeatedly during the course of the simulation run. These data include the location and specification of wells in the model, changes in well completions and field operations over time, a schedule of well rate and/or pressure performance over time, time step control information for advancing the simulation through time, and controls on the type and frequency of printout information provided by the simulator.

1- Read Input Files: Input files with grid coordinates; rock and fluid are read into the program.

2- Call GRIDSZ: From the data given in an input file, grid block length (DX(I,J,K)), gridblock width (DY(I,J,K)), gridblock gross thickness (DZ(I,J,K)), gridblock net thickness DZNET(I,J,K) and node mid-point elevations (EL(I,J,K)) are established.

3- Call PORPRM: From the data given in an input file, the three dimensional porosity and permeability distributions, VP(I,J,K), KX(I,J,K), KY(I,J,K), KZ(I,J,K), are read either as constant values over the entire grid or on a block-by-block basis.

4- Call TRANS: Using the input given above in subroutines 2 and 3, the transmissibility arrays, TX(I,J,K), TY(I,J,K) and TZ(I,J,K), are calculated. The transmissibility in the x-direction is:

$$TX(I,J,K) = 0.012656 \frac{A1(I-1,J,K) * A1(I,J,K)}{DX(I-1,J,K) * A1(I,J,K) + DX(I,J,K) * A1(I-1,J,K)} \quad (3.1)$$

where 'A1' is a function of both the permeability in the x-direction and the gridblock area perpendicular to the x-direction.

$$FACX = \frac{4 * DX(I,J,K)}{2 * DX(I,J,K) + DX(I-1,J,K) + DX(I+1,J,K)} \quad (3.2)$$

$$A1(I,J,K) = FACX * KX(I,J,K) * DY(I,J,K) * DZNET(I,J,K) \tag{3.3}$$

The transmissibility in the y-direction is:

$$TY(I,J,K) = 0.012656 \frac{A2(I,J-1,K) * A2(I,J,K)}{DY(I,J-1,K) * A2(I,J,K) + DY(I,J,K) * A2(I,J-1,K)} \tag{3.4}$$

where 'A2' is a function of both the permeability in the y-direction and the gridblock area perpendicular to the y-direction.

$$FACY = \frac{4 * DY(I,J,K)}{2 * DY(I,J,K) + DY(I,J-1,K) + DY(I,J+1,K)} \tag{3.5}$$

$$A2(I,J,K) = FACY * KY(I,J,K) * DX(I,J,K) * DZNET(I,J,K) \tag{3.6}$$

The transmissibility in the z-direction is:

$$TZ(I,J,K) = 0.012656 \frac{A3(I,J,K-1) * A3(I,J,K)}{DZ(I,J,K-1) * A3(I,J,K) + DZ(I,J,K) * A3(I,J,K-1)} \tag{3.7}$$

where 'A3' is a function of both the permeability in the z-direction and the gridblock area perpendicular to the z-direction.

$$FACZ = \frac{4 * DZ(I,J,K)}{2 * DZ(I,J,K) + DZ(I,J,K-1) + DZ(I,J,K+1)} \tag{3.8}$$

$$A3(I,J,K) = FACZ * KZ(I,J,K) * DX(I,J,K) * DY(I,J,K) \tag{3.9}$$

5- Call TABLE: The following data/tables are read:

- Relative permeability and capillary pressure tables
- Irreducible water saturation, initial saturations, bubble point pressure
- PVT properties (viscosity, formation volume factor, solution gas ratio)
- Rock compressibility

6- Call UINITL: The initial conditions are established within this subroutine. The initial pressure distribution, P(I,J,K), is either calculated by the program for equilibrium conditions given the location of the gas/oil contact and oil/water contact and pressure at both contacts, or it can be read on a block-by-block basis as in the case of a non-equilibrium initialization. Phase saturations, SO(I,J,K), SW(I,J,K), SG(I,J,K), can be read as constant values over the entire grid, or the entire SO and SW distributions can be read on a block-by-block basis. In the latter case, the program calculates the SG distribution for each block as SG=1.0-SO-SW.

7- Call CODES: Several codes for controlling diagnostic output for use in program debugging are provided. These codes are normally set to zero. Since activating any of these codes will generate an extremely large volume of output, it is advised not to activate them. Run control parameters, e.g. maximum number of time steps, factor for increasing/decreasing time step size, limiting maximum water/oil or gas/oil ratio for a producing oil well, limiting minimum/maximum field average pressure, are specified in this section. Additionally, solution methods, such as direct solution, successive overrelaxation method, are determined.

8- Call AQUI: Aquifer model option (no aquifer, steady state, Carter-Tracy etc.) is selected. Also, the aquifer parameters, e.g. location, thickness, porosity, permeability, compressibility, and external radius are determined and written in an output file.

9- Recurrent Calculation loop: This is where a new time step is started.

10- Restart Algorithm Loop: This part controls the print of restart records and is skipped if the restart records are specified to not be written.

11- Recurrent Data: This section includes the location and initial specifications of wells in the model, time step control information for advancing the simulation through time, a schedule of individual well rate and/or pressure performance, changes in well completions and operations over time, and controls on the type and frequency of printout information provided by the simulator.

12- Re-Entry Point For Repeated Time Step: The time step size is updated in this section and pressure and saturations will be solved for the repeated time step. For the initial time step, oil, water, gas, total compressibilities and original fluids in place are calculated. Otherwise, a material balance is run and the pressure-saturation distribution is written.

13- Outer Iteration Loop for IMPES: Seven diagonal matrices for the solution of the flow equation are established. With the solution method chosen earlier, pressures are solved iteratively after which new fluid saturations are calculated. Also, with a simplified geomechanical model, porosities are updated.

The method by which the pressure and saturation equations are built and solved by the IMPES procedure is explained in Appendix A. Pressure equation derived in Appendix A is:

$$\begin{aligned}&\left(B_o - R_{so}B_g\right)\left[\nabla\frac{\vec{K}\lambda_o}{B_o}\nabla P_o + CG_o - \frac{q_o}{\rho_{osc}}\right] + \left(B_w - R_{sw}B_g\right)\left[\nabla\frac{\vec{K}\lambda_w}{B_w}\nabla P_o + CG_w - \frac{q_w}{\rho_{wsc}}\right] + \\ &B_g\nabla\left[\vec{K}\left(\frac{\lambda_g}{B_g} + \frac{R_{so}\lambda_o}{B_o} + \frac{R_{sw}\lambda_w}{B_w}\right)\right]\nabla P_o + CG_g - \frac{q_g}{\rho_{gsc}} = \phi c_t\frac{\partial P_o}{\partial t}\end{aligned}; \quad (3.10)$$

where:

$$CG_o = -\nabla \frac{\vec{K}\lambda_o}{B_o} \nabla\left(\frac{\rho_o z}{144}\right) \ ; \tag{3.11}$$

$$CG_w = -\nabla \frac{\vec{K}\lambda_w}{B_w} \nabla\left(\frac{\rho_w z}{144} + P_{COW}\right) \ ; \tag{3.12}$$

$$CG_g = -\nabla\left\{\vec{K}\left[\frac{\lambda_g}{B_g}\nabla\left(P_{CGO} - \frac{\rho_g z}{144}\right) - \frac{R_{so}\lambda_o}{B_o}\nabla\frac{\rho_o z}{144} - \frac{R_{sw}\lambda_w}{B_w}\nabla\left(P_{COW} - \frac{\rho_w z}{144}\right)\right]\right\} . \tag{3.13}$$

Equation (3.10) is called the pressure equation because no explicit time derivatives of saturations are present. BOAST numerically solves the flow equations for P_o then, it finds S_o, S_w and S_g from flow equations given in Appendix A ((A.13), (A.14), (A.15)) and from $S_o+S_w+S_g=1$.

The finite difference form of the pressure equation leads to a system of linear equations for each grid block, N=I×J×K unknowns $P_{i,j,k}^{n+1}$, where 1<i<I, 1<j<J, 1<k<K. Here, $P_{i,j,k}^{n+1}$ denotes the pressure at grid block (i,j,k) at the new (n+1) time level. This system of equations can be written as:

$$\underline{\underline{A}} = \begin{bmatrix} a_{1,1} & a_{1,2} & \dots & a_{1,N} \\ a_{2,1} & a_{2,2} & \dots & a_{2,N} \\ . & & & \\ . & & & \\ . & & & \\ a_{N,1} & a_{N,2} & \dots & a_{N,N} \end{bmatrix} \quad \underline{P} = \begin{bmatrix} P_1 \\ P_2 \\ . \\ . \\ . \\ P_N \end{bmatrix} \quad \underline{q} = \begin{bmatrix} q_1 \\ q_2 \\ . \\ . \\ . \\ q_N \end{bmatrix} . \tag{3.14}$$

Various methods exist for solving such a system of linear equations, but generally these methods fall into one of the two groups – direct methods or iterative methods. BOAST has the option of selecting one of two direct methods (BAND or D4), or selecting an iterative technique (LSOR) to solve its system of equations.

14- Pressure and Saturation Convergence: If the difference between the new calculated pressure and saturations and the previous iteration's pressure and saturations are greater than the convergence criteria then the iteration is repeated until the convergence is reached.

15- Update: When the convergence criterion is reached, the fluid properties and compressibilities are updated.

16- Repeat Time Step?: If the present time step pressure and saturation values are not much greater than the previous time step, then the time step size is made larger, the pressure and saturations are reset to the previous value and all calculations are repeated for the same time step. Otherwise, the new pressures and saturations, a well report, time step summary, material balance errors and average reservoir pressure are printed and arrays are updated and the next time step is initiated.

17- If Maximum Time Step Reached: If the maximum time step is reached then the post plot package is called, results are printed and the simulation is terminated, otherwise, it goes to back to #10 to start a new time step.

4 GEOMECHANICS

4.1 Background

The ability of a reservoir to produce fluid is influenced by several factors, such as reservoir pressure, the type of drive mechanism and reservoir permeability. In general, the effect of factors such as reservoir pressure and the type of drive mechanism on reservoir productivity changes with the degree of reservoir depletion. The effect of reservoir absolute permeability, however, is usually considered to remain the same during the producing life of the reservoir regardless of degree of reservoir depletion.

For stress-sensitive rocks however published laboratory studies indicate that the absolute permeability may change significantly with variation of the pore pressure and the stress state[57,58,59]. On the other hand field observations show that the pore pressure and stress state changes throughout the reservoir as well as with time[60,61,62]. The combined effect of these suggest that the reduction of permeability due to changes in the pore pressure and stress state as production from the reservoir takes place, may have significant effects on the productivity of stress-sensitive reservoirs. To study the impact of permeability reduction on reservoir productivity, it is necessary to fully couple the governing equations describing the deformation of the solid part of the rock with governing equations describing the changes in pore pressure.

A 3-D finite difference, fully implicit model, which was developed by Osorio et al.[63,64] is employed in this research to represent the physical phenomena occurring during the production from reservoirs with stress-sensitive mechanical and fluid-flow properties. The model considers two different physical domains: 1) an inner domain representing the reservoir, where fluid flow and rock deformation occur; and 2) an outer (surrounding) domain representing the extended stress-disturbed region caused by reservoir depletion. The physical system is illustrated in Figure 4-1. The inclusion of the surrounding domain leads to realistic modeling of the actual geomechanical boundary conditions taking place in the subsurface. The size of the surrounding or outer domain is assumed to be large

enough to assure that its boundaries are not "perturbed" by the production/injection of reservoir fluids during the time period of interest.

Figure 4-1: Physical system representing the 2-domain approach

In both the inner and outer domains, the solid deformation is determined by changes in the effective stress acting on the solid skeleton of the porous rock. Any change in the pore pressure of the inner domain results from the combined effect of two different physical processes: 1) expansion/compression of reservoir fluids due to fluid production/injection; and 2) expansion/compression of the solid part of the rock due to changes in the local stress state. However, since there is no fluid production/injection from/into the outer domain, any change in the pore pressure of the outer domain is caused only by expansion/compression of the solid part of the rock due to changes in the local stress state.

The model is based on the simultaneous solution of three sets of non-linear differential equations: 1) a fluid-flow model, describing the pore pressure distribution in the porous system; 2) a stress-deformation model, describing the deformation of the solid part of the rock, and 3) a well performance model, describing the inner boundary conditions.

The development of the governing equations is based on the following general assumptions:

- Isothermal, multi-phase fluid flow in the inner domain,
- The pore space of the outer domain is filled with fluids, but no fluid flow is allowed in the outer domain,
- The rock is assumed to be isotropic with respect to the rock mechanical properties,
- The mechanical properties and the permeability are assumed to be functions of the mean effective stress,
- The deformation of the solid part of the rock behaves as a non-linear elastic medium with small strains, and
- All fluid-flow/geomechanical coupling effects in the well model are assumed to take place through the permeability terms.

The primary variables in the resulting system of governing equations are the displacements and the pore pressure. Therefore, its solution requires the definition of initial values for the pore pressure and the displacements. The initial pore pressure distribution is calculated in BOAST initialization data section. However, in practice, the initial displacements are unknown.

To deal with this difficulty, the approach taken in this study treats the displacements and the pore pressure in incremental form from initial conditions, i.e. the change in the primary variables, rather than their absolute values, are computed as production from the reservoir evolves.

The physical system is represented in Cartesian coordinates and discretized by means of a block centered grid. The nonlinear equations are approximated by using second-order approximations in space. A fully-implicit procedure is adopted for maximum numerical stability. A Picard-like iteration is used to solve the nonlinear equations where the nonlinear terms are updated as soon as new values for one of the dependent variables is computed. The linear equations are arranged as a 4×4 block matrix system corresponding

to each of the four primary unknowns (i.e., the incremental displacements in the x, y, and z directions or the pore pressure). The numerical procedure used to solve this system of equations involves a block Gauss-Seidel iteration. The iterative sequence includes evaluation of nonlinear properties as function of pore pressure and stress state.

It is assumed that the orientation of the x-y-z coordinate system is aligned with the initial orientation of the principal stresses. This implies that the initial shear stresses in the x. y. and z directions are zero. Also, it is assumed that the stress state at the boundaries of the outer domain are equal to the initial stress state and do not change.

4.2 Fluid Flow Theory:

Combining the fluid flow equations for isothermal, single-phase flow[64] and multiphase flow[65], three basic principles of fluid flow, mass conservation, Darcy's law and equation of state, are obtained for multiphase, isothermal fluid flow.

Mass Conservation:

$$\text{Oil:} \quad \nabla \cdot (\rho_o \phi S_o v_o) + q_o + \frac{\partial(\rho_o \phi S_o)}{\partial t} = 0 \tag{4.1}$$

$$\text{Water:} \quad \nabla \cdot (\rho_w \phi S_w v_w) + q_w + \frac{\partial(\rho_w \phi S_w)}{\partial t} = 0 \tag{4.2}$$

$$\text{Solid:} \quad \nabla \cdot (\rho_s (1-\phi) v_s) + \frac{\partial(\rho_s (1-\phi))}{\partial t} = 0 \tag{4.3}$$

Darcy's Law:

$$\text{Oil:} \quad \phi S_o (v_o - v_s) = -\frac{K k_{ro}}{\mu_o} \nabla \left(P_o - \frac{\rho_o g z}{144 g_c} \right) \tag{4.4}$$

$$\text{Water:} \quad \phi S_w (v_w - v_s) = -\frac{K k_{rw}}{\mu_w} \nabla \left(P_w - \frac{\rho_w g z}{144 g_c} \right) \tag{4.5}$$

Equation of State (isothermal fluid compressibility):

$$\text{Oil:} \quad c_o = \frac{1}{\rho_o} \frac{\partial \rho_o}{\partial P_o} \tag{4.6}$$

$$\text{Water:} \quad c_w = \frac{1}{\rho_w} \frac{\partial \rho_w}{\partial P_w} \tag{4.7}$$

An additional relation required to complete the formulation of governing equations is:

$$S_o + S_w = 1 \quad . \tag{4.8}$$

In Equations (4.1) through (4.7), 'ρ' is the fluid mass density (mass per unit fluid volume), 'v' is the fluid velocity vector, 'c' is the fluid compressibility, and the subscripts 'o', 'w', and 's' refer to the oil, water and solid phase, respectively. Also, '∇' and '∇·' denote the gradient and divergence, respectively, 'μ' is the fluid viscosity, 'K' is the absolute permeability, 'k_r' is the relative permeability, 'ϕ' is the effective porosity, 'P' is the fluid pressure, 'S' is the saturation, 'g' is the acceleration due to gravity, 'g_c' is the gravitational constant, 'q' is the produced fluid volume per unit time and 't' is time.

The following section describes the development of the governing equations for fluid flow :

Introducing Darcy's law into Equations (4.1) to (4.2) gives

$$\text{Oil:} \quad \nabla \cdot \left\{ \rho_o \phi S_o \left[-\frac{K k_{ro}}{\phi S_o \mu_o} \nabla \left(P_o - \frac{\rho_o g z}{144 g_c} \right) + v_s \right] \right\} + q_o + \frac{\partial (\rho_o \phi S_o)}{\partial t} = 0 \ ; \tag{4.9}$$

$$\text{Water:}\quad \nabla\cdot\left\{\rho_w\phi S_w\left[-\frac{Kk_{rw}}{\phi S_w\mu_w}\nabla\left(P_w-\frac{\rho_w gz}{144g_c}\right)+v_s\right]\right\}+q_w+\frac{\partial(\rho_w\phi S_w)}{\partial t}=0\,. \quad (4.10)$$

Assuming that g = g_c and expanding the left hand side of Equations (4.9) and (4.10) gives:

$$\text{Oil:}\quad \nabla\cdot\left(\rho_o\left[-\frac{Kk_{ro}}{\mu_o}\nabla\left(P_o-\frac{\rho_o z}{144}\right)\right]\right)+\nabla\cdot(\rho_o\phi S_o v_s)+q_o+\frac{\partial(\rho_o\phi S_o)}{\partial t}=0\;; \quad (4.11)$$

$$\text{Water:}\quad \nabla\cdot\left(\rho_w\left[-\frac{Kk_{rw}}{\mu_w}\nabla\left(P_w-\frac{\rho_w z}{144}\right)\right]\right)+\nabla\cdot(\rho_w\phi S_w v_s)+q_w+\frac{\partial(\rho_w\phi S_w)}{\partial t}=0\cdot \quad (4.12)$$

Equations (4.10) and (4.11) can be rearranged to provide:

$$\text{Oil:}\quad \nabla\cdot\left(\rho_o\frac{Kk_{ro}}{\mu_o}\nabla\left(P_o-\frac{\rho_o z}{144}\right)\right)=v_s\nabla\cdot(\rho_o\phi S_o)+\rho_o\phi S_o\nabla\cdot v_s+q_o+\frac{\partial(\rho_o\phi S_o)}{\partial t}\,; \quad (4.13)$$

$$\text{Water:}\quad \nabla\cdot\left(\rho_w\frac{Kk_{rw}}{\mu_w}\nabla\left(P_w-\frac{\rho_w z}{144}\right)\right)=v_s\nabla\cdot(\rho_w\phi S_w)+\rho_w\phi S_w\nabla\cdot v_s+q_w+\frac{\partial(\rho_w\phi S_w)}{\partial t}\cdot \quad (4.14)$$

Defining the material derivative d(·)/dt with respect to a moving solid:

$$\frac{d(\cdot)}{dt}=\frac{\partial(\cdot)}{\partial t}+v_s\cdot\nabla(\cdot)\quad . \quad (4.15)$$

Equation (4.15) links a Lagrangian concept to a spatial or Eulerian description. Note that for nondeformable media the material derivative is equivalent to a partial derivative since v_s=0. Applying Equation (4.15) to Equation (4.13) and (4.14) gives:

$$\text{Oil:}\quad \nabla\cdot\left(\rho_o\frac{Kk_{ro}}{\mu_o}\nabla\left(P_o-\frac{\rho_o z}{144}\right)\right)=\frac{d(\rho_o\phi S_o)}{dt}+\rho_o\phi S_o\nabla\cdot v_s+q_o\quad ; \quad (4.16)$$

$$\text{Water:} \quad \nabla \cdot \left(\rho_w \frac{Kk_{rw}}{\mu_w} \nabla \left(P_w - \frac{\rho_w z}{144} \right) \right) = \frac{d\left(\rho_w \phi S_w\right)}{dt} + \rho_w \phi S_w \nabla \cdot v_s + q_w \quad . \tag{4.17}$$

Expanding the left hand side of Equations (4.16) and (4.17) results in:

$$\text{Oil:} \quad \nabla \cdot \left(\rho_o \frac{Kk_{ro}}{\mu_o} \nabla \left(P_o - \frac{\rho_o z}{144} \right) \right) = \rho_o \phi S_o \left[\frac{1}{\rho_o} \frac{d\rho_o}{dt} + \frac{1}{\phi} \frac{d\phi}{dt} + \frac{1}{S_o} \frac{dS_o}{dt} + \nabla \cdot v_s \right] + q_o \; ; \tag{4.18}$$

$$\text{Water:} \quad \nabla \cdot \left(\rho_w \frac{Kk_{rw}}{\mu_w} \nabla \left(P_w - \frac{\rho_w z}{144} \right) \right) = \rho_w \phi S_w \left[\frac{1}{\rho_w} \frac{d\rho_w}{dt} + \frac{1}{\phi} \frac{d\phi}{dt} + \frac{1}{S_w} \frac{dS_w}{dt} + \nabla \cdot v_s \right] + q_w \; . \tag{4.19}$$

Expanding the first term of the solid mass balance equation, Equation (4.3), and applying Equation (4.14) gives:

$$\nabla \cdot v_s = \frac{1}{(1-\phi)\rho_o} \frac{d\left[(1-\phi)\rho_o\right]}{dt} \quad . \tag{4.20}$$

For constant solid mass and noting that $\phi = V_p / V_b$ and $V_b = V_p + V_s$ where V_b, V_p and V_s are bulk, pore and solid volume, respectively, Equation (4.20) is equivalent to

$$\nabla \cdot v_s = \frac{1}{V_b} \frac{dV_b}{dt} \quad . \tag{4.21}$$

Thus, the divergence of the solid velocity simply reflects the rate of change of bulk volume. Note that Equation (4.21) is nothing more than a statement of the solid mass balance, since it is derived exclusively from Equation (4.3). From Equation (4.21), $v_s = 0$ (nondeformable) implies $dV_b = 0$.

Applying the relation $d\phi/\phi = dV_p/V_p - dV_b/V_b$ and Equation (4.21) to Equations (4.18) and (4.19) results in

$$\text{Oil:} \qquad \nabla \cdot \left(\rho_o \frac{Kk_{ro}}{\mu_o} \nabla \left(P_o - \frac{\rho_o z}{144} \right) \right) = \rho_o \phi S_o \left[\frac{1}{\rho_o} \frac{d\rho_o}{dt} + \frac{1}{V_p} \frac{dV_p}{dt} + \frac{1}{S_o} \frac{dS_o}{dt} \right] + q_o \quad ; \tag{4.22}$$

$$\text{Water:} \quad \nabla \cdot \left(\rho_w \frac{Kk_{rw}}{\mu_w} \nabla \left(P_w - \frac{\rho_w z}{144} \right) \right) = \rho_w \phi S_w \left[\frac{1}{\rho_w} \frac{d\rho_w}{dt} + \frac{1}{V_p} \frac{dV_p}{dt} + \frac{1}{S_w} \frac{dS_w}{dt} \right] + q_w \; . \tag{4.23}$$

The form of Darcy velocities can be simplified by defining the potential Φ_p of phase p as

$$\Phi_p = P_p - \frac{\rho_p z}{144} \quad . \tag{4.24}$$

Equation (4.22) and (4.23) can be written as:

$$\text{Oil:} \qquad \nabla \cdot \left(\rho_o \frac{Kk_{ro}}{\mu_o} \nabla \Phi_o \right) = \rho_o \phi S_o \left[\frac{1}{\rho_o} \frac{d\rho_o}{dt} + \frac{1}{V_p} \frac{dV_p}{dt} + \frac{1}{S_o} \frac{dS_o}{dt} \right] + q_o \quad ; \tag{4.25}$$

$$\text{Water:} \quad \nabla \cdot \left(\rho_w \frac{Kk_{rw}}{\mu_w} \nabla \Phi_w \right) = \rho_w \phi S_w \left[\frac{1}{\rho_w} \frac{d\rho_w}{dt} + \frac{1}{V_p} \frac{dV_p}{dt} + \frac{1}{S_w} \frac{dS_w}{dt} \right] + q_w \, . \tag{4.26}$$

Equations (4.25) and (4.26) are key fundamental equations in this study. The right-hand-side of Equations (4.25) and (4.26) basically represents the rate of change of fluid density, pore volume and fluid saturation.

The presence of oil and water phase pressures in these equations complicates the problem. We simplify the handling of the phase pressures and potentials in the flow

equations by using the capillary pressure concept. Let us define the difference in phase pressures as

$$P_{cow} = P_o - P_w \quad . \tag{4.27}$$

The difference P_{cow} is the capillary pressure for oil-water system. Experimentally, P_{cow} has been observed to be principally a function of water saturation. Using capillary pressure the water phase potential can be written as:

$$\Phi_w = P_o - P_{cow} - \frac{\rho_w z}{144} \quad . \tag{4.28}$$

The gravity and capillary contributions to the phase pressures have been collected in the terms CG_o and CG_w:

$$CG_o = -\nabla \cdot \left(\rho_o \frac{Kk_{ro}}{\mu_o} \nabla \left(\frac{\rho_o z}{144} \right) \right) \quad ; \tag{4.29}$$

$$CG_w = -\nabla \cdot \left(\rho_w \frac{Kk_{rw}}{\mu_w} \nabla \left(\frac{\rho_w z}{144} + P_{cow} \right) \right) \quad . \tag{4.30}$$

Combining Equations (4.29) and (4.30) with Equations (4.25) and (4.26) and rearranging yields

$$\text{Oil:} \qquad \nabla \cdot \left(\rho_o \frac{Kk_{ro}}{\mu_o} \nabla P_o \right) + CG_o - q_o = \rho_o \phi S_o \left[\frac{1}{\rho_o} \frac{d\rho_o}{dt} + \frac{1}{V_p} \frac{dV_p}{dt} + \frac{1}{S_o} \frac{dS_o}{dt} \right] \quad ; \tag{4.31}$$

$$\text{Water:}\quad \nabla\cdot\left(\rho_w\frac{Kk_{rw}}{\mu_w}\nabla P_w\right)+CG_w-q_w=\rho_w\phi S_w\left[\frac{1}{\rho_w}\frac{d\rho_w}{dt}+\frac{1}{V_p}\frac{dV_p}{dt}+\frac{1}{S_w}\frac{dS_w}{dt}\right]\ . \tag{4.32}$$

The change of fluid density term $d\rho_p/\rho_p$ is rel ated to fluid compressibility by the following equations

$$c_p\nabla P_p=\frac{1}{\rho_p}\nabla\rho_p\ ; \tag{4.33}$$

$$c_p\frac{dP_p}{dt}=\frac{1}{\rho_p}\frac{d\rho_p}{dt}\ ; \tag{4.34}$$

$$-\frac{dV_p}{V_p}=-\frac{1}{V_p}\left(\frac{\partial V_p}{\partial P_d}\right)_P dP_d-\frac{1}{V_p}\left(\frac{\partial V_p}{\partial P}\right)_{P_d}dP\ . \tag{4.35}$$

Here, P_d is the differential pressure, $P_d=P_c-P$, where P_c and P are confining pressure and fluid pressure, respectively. In other words, an imposed confining pressure dP_c is considered to be the sum of two incremental pressures, dP_d and dP, i.e., $dP_c=dP_d+dP$. Differential pressure is also known as effective stress, $\sigma' = \sigma - P$.

The second partial derivative in Equation (4.35) is assumed to be the unjacketed bulk compressibility c_s $(=1/K_s)$ measured by allowing the fluid to penetrate the connected pores such that the fluid pressure acts fully on the "solid phase". Under such a condition, the change of confining pressure is equal to the change of pore-fluid pressure, i.e., dP_c-dP, and hence $dP_d=0$ or P_d=constant. Constant solid mass is assumed which implies that the fluid is chemically inert with the solid phase.

Inserting Equations (4.33), (4.34) and (4.35) into Equations (4.31) and (4.32), fluid flow equations can be written in terms of compressibilities, pore pressure and differential pressure.

Oil:
$$\rho_o \nabla \cdot \left(\frac{Kk_{ro}}{\mu_o} \nabla P_o \right) + \rho_o \frac{Kk_{ro}}{\mu_o} c_o \nabla \cdot (\nabla P_o)^2 + CG_o - q_o = \rho_o S_o \left(\phi c_o + c_b - (1+\phi) c_s + (c_b - c_s) \frac{d\sigma_m}{dP_o} \right) \frac{dP_o}{dt} + \rho_o \phi S_o \left(\frac{1}{S_o} \frac{dS_o}{dt} \right) \quad (4.36)$$

Water:
$$\rho_w \nabla \cdot \left(\frac{Kk_{rw}}{\mu_w} \nabla P_w \right) + \rho_w \frac{Kk_{rw}}{\mu_w} c_w \nabla \cdot (\nabla P_w)^2 + CG_w - q_w = \rho_w S_w \left(\phi c_w + c_b - (1+\phi) c_s + (c_b - c_s) \frac{d\sigma_m}{dP_w} \right) \frac{dP_w}{dt} + \rho_w \phi S_w \left(\frac{1}{S_w} \frac{dS_w}{dt} \right) \quad (4.37)$$

Neglecting the small quadratic term $c_p \nabla \cdot (\nabla P_p)^2$, the above equations become:

Oil:
$$\nabla \cdot \left(\frac{Kk_{ro}}{\mu_o} \nabla P_o \right) + \frac{CG_o}{\rho_o} - \frac{q_o}{\rho_o} = S_o \left\{ (\phi c_o + c_b - (1+\phi) c_s + c_b) \frac{dP_o}{dt} + (c_b - c_s) \frac{d\sigma_m}{dP_o} + \left(\frac{\phi}{S_o} \right) \frac{dS_o}{dt} \right\} \quad (4.38)$$

Water:
$$\nabla \cdot \left(\frac{Kk_{rw}}{\mu_w} \nabla P_w \right) + \frac{CG_w}{\rho_w} - \frac{q_w}{\rho_w} = S_w \left\{ (\phi c_w + c_b - (1+\phi) c_s + c_b) \frac{dP_w}{dt} + (c_b - c_s) \frac{d\sigma_m}{dP_w} + \left(\frac{\phi}{S_w} \right) \frac{dS_w}{dt} \right\} \quad (4.39)$$

4.3 Linear Poroelastic Theory:

Poroelastic theory describing fluid-solid coupling was developed in a series of papers by Biot[12,17]. Perfect elastic medium (linear, reversible and non-retarded mechanical behavior) with small strains are assumed in this study. Isothermal conditions are also assumed.

The three basic principles of poroelastic theory are: stress equilibrium, strain-displacement and strain-stress-pressure relations. They are synonymous with the mass balance, Darcy's law, and equation of state of the fluid –flow modeling. Mathematically, the porelasticity equations are:

Stress Equilibrium:

$$\sum \frac{\partial \sigma_{ij}}{\partial x_j} = 0 \quad ; \quad \sigma_{ij} = \sigma_{ji} \quad ; \tag{4.40}$$

Strain displacement relation:

$$\varepsilon_{ij} = \frac{1}{2}\left(\frac{\partial u_i}{\partial x_j} + \frac{\partial u_j}{\partial x_i} \right) \quad ; \tag{4.41}$$

Strain-stress pressure:

$$\begin{aligned} \varepsilon_{ii} &= \frac{1}{E}\left[\sigma_{ii} - \nu\left(\sigma_{jj} + \sigma_{kk}\right)\right] + \frac{\alpha}{3K_b} P \quad . \\ \varepsilon_{ij} &= \sigma_{ij} / 2G \,, \quad i \neq j \end{aligned} \tag{4.42}$$

In Equations (4.40), (4.41) and (4.42), ε_{ij} and σ_{ij} are the components of the bulk strain tensor and total stress tensor, respectively. The term u_i is the component of solid displacement vector $\boldsymbol{u}(u_x,u_y,u_z)$ and E, G (which is equal to $E/[2(1+\nu)]$), and ν are the Young's modulus, shear modulus, and Poisson's ratio for the solid skeleton under drained conditions, respectively. Finally, K_b (which is equal to $1/c_b$) is the drained jacketed bulk modulus and α is the poroelastic parameter or effective stress coefficient. A more detailed discussion of α will be given later. Body forces and inertial effects are neglected in Equation (4.40). Small strains are implied in Equation (4.41). The stress and strain are

taken positive in tension whereas fluid pressure p is positive for compression. Note that this differs from conventional geomechanics where compression is positive.

It is more convenient to express stress in terms of strain because the total stress satisfies the equilibrium equation, Equation (4.40). Solving Equation (4.42) for stress gives:

$$\sigma_{ij} = 2G\varepsilon_{ij} + \lambda e\delta_{ij} - \alpha P\delta_{ij} \quad . \tag{4.43}$$

The constants in Equation (4.43) are given below:

$$\lambda = \frac{3\nu K_b}{1+\nu} = \frac{2\nu G}{1-2\nu} = K_b - \frac{2}{3}G \quad ; \tag{4.44}$$

$$e = \frac{\sigma_m + \alpha P}{\lambda + (2/3)G} = \frac{\sigma_m + \alpha P}{K_b} \quad . \tag{4.45}$$

The term *e* is the volumetric strain which can be represented by strain tensors:

$$e = \varepsilon_{xx} + \varepsilon_{yy} + \varepsilon_{zz} \quad . \tag{4.46}$$

The term σ_m is the mean stress:

$$\sigma_m = (\sigma_{xx} + \sigma_{yy} + \sigma_{zz})/3 \quad . \tag{4.47}$$

The rate of displacement (*u*) gives the velocity of the solid:

$$v_s = \frac{\partial u}{\partial t} \quad ; \tag{4.48}$$

$$e = \nabla \cdot u \quad ; \tag{4.49}$$

$$\nabla \cdot v_s = \frac{de}{dt} = \frac{1}{V_b}\frac{dV_b}{dt} \quad ; \quad de = \frac{dV_b}{V_b} \quad . \tag{4.50}$$

The stress equilibrium can then be rewritten as:

$$\sum_{j=1}^{3} \frac{\partial}{\partial x_j}\left\{ G\left(\frac{\partial u_i}{\partial x_j} + \frac{\partial u_j}{\partial x_i} \right) \right\} = \frac{\partial(\alpha P - \lambda e)}{\partial x_i} \quad ; \tag{4.51}$$

$$G\nabla^2 u_i + (G+\lambda)\frac{\partial e}{\partial x_i} = \alpha \frac{\partial P}{\partial x_i} \quad ; \tag{4.52}$$

$$\nabla \cdot (\frac{k}{\mu}\nabla P) = \phi c_{t,II}\frac{\partial P}{\partial t} + \alpha \frac{\partial e}{\partial t} \quad ; \tag{4.53}$$

$$\phi c_{t,II} = \phi c_{t,I} - \alpha^2 c_b = \phi c + (\alpha - \phi)c_s \quad ; \tag{4.54}$$

$$G\nabla^2 u + (G+\lambda)\nabla\nabla \cdot u = \alpha \nabla P \quad ; \tag{4.55}$$

$$(\lambda + 2G)\nabla^2 e = \alpha \nabla^2 P \quad . \tag{4.56}$$

We can write the equilibrium equations in terms of the incremental displacements and incremental pore pressure. This results in:

$$\nabla \cdot \left[G\nabla(\Delta u_i) \right] + \nabla \cdot \left[G\frac{\partial(\Delta u)}{\partial x_i} \right] + \frac{\partial\left[\lambda \nabla \cdot (\Delta u)\right]}{\partial x_i} + \frac{\partial(\alpha \Delta P)}{\partial x_i} = 0 \quad ; \tag{4.57}$$

where Δu is the incremental displacement vector given by

$$\Delta u = \left(\Delta u_x, \Delta u_y \Delta u_z\right)^T \quad . \tag{4.58}$$

It is assumed that there is no incremental displacement at the boundaries. Mathematically, zero incremental boundary conditions can be expressed as:

$$\begin{aligned} \Delta u_x(x,y,z,t)_{boundary} &= 0 \\ \Delta u_y(x,y,z,t)_{boundary} &= 0 \\ \Delta u_z(x,y,z,t)_{boundary} &= 0 \end{aligned} \quad . \tag{4.59}$$

4.4 Numerical Analysis Approach

The system of nonlinear partial differential equations represented by Equations (4.38), (4.39) and (4.57) is discretized using second order finite difference approximations on a cell-centered grid in Cartesian coordinates. A fully implicit time marching procedure is adopted here for maximum numerical stability.

4.4.1 Notation Convention

The finite difference approximation of the pore pressure Equations (4.38) and (4.39) can be written in general form as the following matrix equation:

$$\begin{aligned} &\left[A_{l,\Delta P}\right]\Delta P + \left[A_{l,\Delta U_x}\right]\Delta U_x + \left[A_{l,\Delta U_y}\right]\Delta U_y + \left[A_{l,\Delta U_z}\right]\Delta U_z = F_l \\ &for \quad l = 1,2,3,4. \end{aligned} \tag{4.60}$$

In Equation (4.60), ΔP, ΔU_x, ΔU_y, ΔU_z represent the discretized approximation of the incremental pore pressure and the incremental displacements in the x-, y- and z-directions, respectively. $A_{l,\Delta X}$ is a coefficient block matrix, the first subscript, $_l$, is the equation number and the second subscript, $_{\Delta x}$, indicates the unknown vector ΔX (i.e., ΔP, ΔU_x, ΔU_y or ΔU_z) which post-multiplies the block matrix $A_{l,\Delta X}$. Due to the nonlinear behavior of Equation (4.60), the block matrix terms $A_{l,\Delta X}$ and the vectors F_l are functions of the solution.

The four matrix equations can be written in a block Gauss-Seidel fashion:

First Equation:

$$\begin{aligned} [A_{1,P}]P &= F_1 - [A_{1,\Delta U_x}]\Delta U_x - [A_{1,\Delta U_y}]\Delta U_y - [A_{1,\Delta U_z}]\Delta U_z \\ [A_{1,P}]P &= F_P \end{aligned} \quad ; \tag{4.61}$$

Second Equation:

$$\begin{aligned} [A_{2,\Delta U_x}]\Delta U_x &= F_2 - [A_{2,\Delta P}]\Delta P - [A_{2,\Delta U_y}]\Delta U_y - [A_{2,\Delta U_z}]\Delta U_z \\ [A_{2,\Delta U_x}]\Delta U_x &= F_x \end{aligned} \quad ; \tag{4.62}$$

Third Equation:

$$\begin{aligned} [A_{3,\Delta U_y}]\Delta U_y &= F_3 - [A_{3,\Delta P}]\Delta P - [A_{3,\Delta U_x}]\Delta U_x - [A_{3,\Delta U_z}]\Delta U_z \\ [A_{3,\Delta U_y}]\Delta U_y &= F_y \end{aligned} \quad ; \tag{4.63}$$

Fourth Equation:

$$\begin{aligned} [A_{4,\Delta U_z}]\Delta U_z &= F_4 - [A_{4,\Delta P}]\Delta P - [A_{4,\Delta U_x}]\Delta U_x - [A_{4,\Delta U_y}]\Delta U_y \\ [A_{4,\Delta U_z}]\Delta U_z &= F_z \end{aligned} \quad . \tag{4.64}$$

These matrix equations can be expressed as seven-point stencils of the form:

$$\begin{bmatrix} 0 & 0 & 0 \\ 0 & B_{i,j,k} & 0 \\ 0 & 0 & 0 \end{bmatrix} \Delta X_{i,j,k-1} + \begin{bmatrix} 0 & N_{i,j,k} & 0 \\ W_{i,j,k} & C_{i,j,k} & E_{i.j.k} \\ 0 & S_{i,j,k} & 0 \end{bmatrix} \Delta X_{i,j,k} + \begin{bmatrix} 0 & 0 & 0 \\ 0 & T_{i,j,k} & 0 \\ 0 & 0 & 0 \end{bmatrix} \Delta X_{i,j,k+1} = F_{i,j,k} ; \tag{4.65}$$

where the stencil elements $B_{i,j,k}$, $N_{i,j,k}$, $W_{i,j,k}$, $C_{i,j,k}$, $E_{i,j,k}$, $S_{i,j,k}$, and $T_{i,j,k}$ represent the matrix coefficients of the difference equation for $\Delta X_{i,j,k-1}$, $\Delta X_{i,j+1,k}$, $\Delta X_{i-1,j,k}$, $\Delta X_{i,j,k}$, $\Delta X_{i+1,j,k}$, $\Delta X_{i,j-}$

$_{1,k}$, and $\Delta X_{i,j,k+1}$ respectively. The values ΔX refer to elements of the unknown vector $\Delta \mathbf{X}$. The stencil coefficients and the values $F_{i,j,k}$ are functions of the unknowns, $X_{t+\Delta t} = X_t + \Delta X$.

4.5 Discretization of the Pore pressure Equation

Following the notation in Equation (4.65), the finite difference approximation of Equation (4.61) is given as:

$$B_{P_{i,j,k}} P_{i,j,k-1}^{n+1} + S_{P_{i,j,k}} P_{i,j-1,k}^{n+1} + W_{P_{i,j,k}} P_{i-1,j,k}^{n+1} + C_{P_{i,j,k}} P_{i,j,k}^{n+1} + E_{P_{i,j,k}} P_{i+1,j,k}^{n+1} + N_{P_{i,j,k}} P_{i,j+1,k}^{n+1} + T_{P_{i,j,k}} P_{i,j,k+1}^{n+1} = F_{P_{i,j,k}} \quad . \tag{4.66}$$

For the outer domain, the finite difference approximation of Equation (4.61) is given by

$$P_{i,j,k}^{n+1} = P_{i,j,k}^{n} + \frac{c_{pc_{i,j,k}}^{n+1}}{c_{bc_{i,j,k}}^{n+1}\left(c_{t_{i,j,k}}^{n+1} - c_{pc_{i,j,k}}^{n+1}\alpha_{i,j,k}^{n+1}\right)} \times \left[\left(\nabla \cdot \Delta u\right)_{i,j,k}^{n+1} - \left(\nabla \cdot \Delta u\right)_{i,j,k}^{n}\right] \quad . \tag{4.67}$$

The finite difference approximations of Equations (4.62) through (4.64) are given, respectively, as

$$B_{x_{i,j,k}} \Delta U_{x_{i,j,k-1}}^{n+1} + S_{x_{i,j,k}} \Delta U_{x_{i,j-1,k}}^{n+1} + W_{x_{i,j,k}} \Delta U_{x_{i-1,j,k}}^{n+1} + C_{x_{i,j,k}} \Delta U_{x_{i,j,k}}^{n+1} + E_{x_{i,j,k}} \Delta U_{x_{i+1,j,k}}^{n+1} + N_{x_{i,j,k}} \Delta U_{x_{i,j+1,k}}^{n+1} + T_{x_{i,j,k}} \Delta U_{x_{i,j,k+1}}^{n+1} = F_{x_{i,j,k}} \quad ; \tag{4.68}$$

$$B_{y_{i,j,k}} \Delta U_{y_{i,j,k-1}}^{n+1} + S_{y_{i,j,k}} \Delta U_{y_{i,j-1,k}}^{n+1} + W_{y_{i,j,k}} \Delta U_{y_{i-1,j,k}}^{n+1} + C_{y_{i,j,k}} \Delta U_{y_{i,j,k}}^{n+1} + E_{y_{i,j,k}} \Delta U_{y_{i+1,j,k}}^{n+1} + N_{y_{i,j,k}} \Delta U_{y_{i,j+1,k}}^{n+1} + T_{y_{i,j,k}} \Delta U_{y_{i,j,k+1}}^{n+1} = F_{y_{i,j,k}} \quad ; \tag{4.69}$$

$$B_{z_{i,j,k}} \Delta U_{z_{i,j,k-1}}^{n+1} + S_{z_{i,j,k}} \Delta U_{z_{i,j-1,k}}^{n+1} + W_{z_{i,j,k}} \Delta U_{z_{i-1,j,k}}^{n+1} + C_{z_{i,j,k}} \Delta U_{z_{i,j,k}}^{n+1} + E_{z_{i,j,k}} \Delta U_{z_{i+1,j,k}}^{n+1} + N_{z_{i,j,k}} \Delta U_{z_{i,j+1,k}}^{n+1} + T_{z_{i,j,k}} \Delta U_{z_{i,j,k+1}}^{n+1} = F_{z_{i,j,k}} \quad . \tag{4.70}$$

Discretization of the porosity equation is as follows

$$\phi_{i,j,k}^{n+1} - \phi_{i,j,k}^{n} = -\left[c_{bc_{i,j,k}}^{n+1}\left(1-\phi_{i,j,k}^{n+1}\right) - c_s\right] \times \left[\left(\sigma_{m_{i,j,k}}^{n+1} - P_{i,j,k}^{n+1}\right) - \left(\sigma_{m_{i,j,k}}^{n} - P_{i,j,k}^{n}\right)\right] . \quad (4.71)$$

Solving for $\phi_{i,j,k}^{n+1}$ gives

$$D = \phi_{i,j,k}^{n} - \left(c_{bc_{i,j,k}}^{n+1} - c_s\right)\left[\left(\sigma_{m_{i,j,k}}^{n+1} - P_{i,j,k}^{n+1}\right) - \left(\sigma_{m_{i,j,k}}^{n} - P_{i,j,k}^{n}\right)\right] ; \quad (4.72)$$

$$\phi_{i,j,k}^{n+1} = \frac{D}{1 - c_{bc_{i,j,k}}^{n+1}\left[\left(\sigma_{m_{i,j,k}}^{n+1} - P_{i,j,k}^{n+1}\right) - \left(\sigma_{m_{i,j,k}}^{n} - P_{i,j,k}^{n}\right)\right]} . \quad (4.73)$$

4.6 Numerical Solution Procedure

Due to the nonlinear behaviour of flow and stress equilibrium equations, the solution must be found iteratively[63,68]. A Picard like, block Gauss Seidel iteration method, where nonlinear terms are updated as soon as one of the dependent terms are calculated, is used. According to this method, initial values for P^{n+1}, ΔU_y^{n+1} and ΔU_z^{n+1} are guessed. Then, the coefficient matrices ($A_{l,\Delta X}$) and the vector (F_X) are calculated and solved for ΔU_x^{n+1}. Using the new values for ΔU_x^{n+1} the coefficient matrices ($A_{l,\Delta X}$) and the vector (F_y) are computed and solved for ΔU_y^{n+1}. Then using the new values for ΔU_x^{n+1} and ΔU_y^{n+1} the coefficient matrices ($A_{l,\Delta X}$) and the vector (F_z) are computed and solved for ΔU_z^{n+1}. Finally, with the new values of ΔU_x^{n+1}, ΔU_y^{n+1} and ΔU_z^{n+1} the coefficient matrices ($A_{l,\Delta X}$) are the vector F_p are updated and solved for P^{n+1}. This procedure is repeated until the convergence is reached after which the process moves to the next time step. Once the displacements and pore pressure are known, the stress state can be determined from Equation (4.41) and Equation (4.43). Then the shear modulus, bulk compressibility, rock compressibility, permeability and porosity can be found from lab-generated charts.

5 PRESSURE PULSE EQUATIONS

5.1 Background

Declining oil recovery is of major concern in the oil industry. Common EOR methods have a number of limitations, such as high cost, or possible harmful ecological consequences. Searching for new methods of stimulation is currently an urgent focus to engineers as well as geophysicists. The use of elastic wave excitation has been suggested as an alternative EOR method[4,21].

5.2 Mechanisms

5.2.1 Non-Conventional EOR Methods

During the 1970's, in Russia, earthquakes were observed to have affected the fluid levels in petroleum reservoirs[4]. In most cases, the fluid levels were reported to have increased, leading to enhanced flow from the reservoir. It has also been observed that the water/oil ratio during an earthquake swarm may change[69]. Wells with initially large water/oil ratios were observed to have lower post-earthquake-swarm water/oil ratios and vice-versa in wells with initially low water/oil ratios. Earthquakes and explosions have also been known to affect underground fluid levels (water table and oil reservoir levels) in some areas[18]. These observations led to the concept of seismic excitation enhancing the flow of (underground) fluids in porous media. The concept of seismic excitation involves applying small strain excitation, of magnitude 10^{-10} to 10^{-6}, either at the surface above the reservoir, or underground within the reservoir. However, because of the high rates of amplitude attenuation and geometric spreading associated with the application of surface excitation, very high-energy sources would be necessary to apply sufficient energy to the reservoir[4]. In addition, Spanos et al.[21] postulate the low strains that are generated by seismic excitation makes it unlikely that enough strain energy would be generated to substantially affect fluid flows.

Conventional recovery ratios in many reservoirs are as low as 20-40% of the original oil in place (OOIP). Improved recovery technologies may increase these numbers by as

much as 10-15% (i.e. to 30-50% of the OOIP). Only exceptionally is more than 60-65% of the OOIP recovered from a single conventional oil reservoir. Various physical processes (linked to Darcy flow, capillarity, viscosity, permeability, heterogeneity, and pressure gradients) dictate the amount of oil recovered by conventional methods.

Capillary blockage leads to isolation of bodies of oil because the capillary entry pressure cannot be overcome under static flow conditions. In cases of unfavorable mobility ratio (where the viscosity ratio of oil displacing to displaced fluids is far less than 1), the less viscous phase channels through the more viscous phase, even if the permeability is perfectly homogeneous. This is called viscous fingering, and is endemic in gas or water flooding of more viscous oils. Water coning and gas coning to oil wells under production are forms of viscous fingering, and they lead to sudden declines in oil production.

The presence of channels of different permeability leads to flow channelling, where most or all the displacing fluids flow to the producing well through the most permeable zone, leaving other zones undeveloped or underdeveloped. For example, residual oil saturation, a concept related to Darcy fluid flow through porous media, is the result of bypassing of oil during a water displacement test, and this value is typically between 10% and 50% of the original oil in place.

The basic physical process behind oil and gas exploitation is fluid flow. It has long been supposed that the physics of Darcy flow dictates recovery ratios that can be attained in multiphase systems. However, along with gravity drainage methods, pressure impulse flow enhancement has recently been found to be effective. This is achieved through the input of dynamic energy[70].

5.2.2 Darcy Theory and Biot Theory

There is a broad range of possible frequencies of mechanical excitation of the fluid phase or the solid phase of a liquid-saturated porous medium (Figure 5-1).

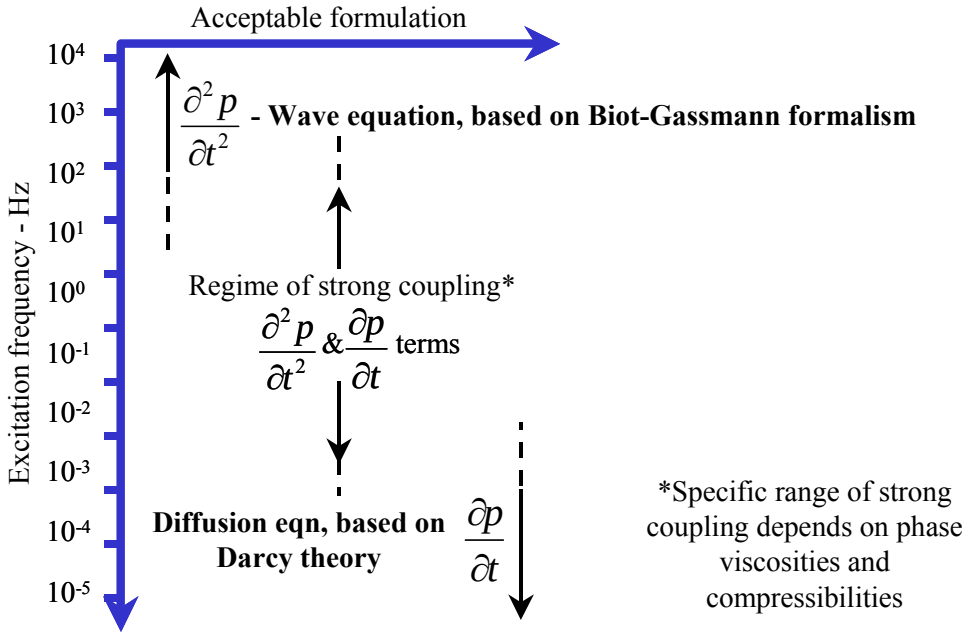

Figure 5-1: Range of frequencies for dynamic excitation[21]

Conventionally, there have been two theoretical formalisms for this broad range of excitation frequencies: for high frequencies Biot-Gassman wave mechanics theory forms the foundation of analysis, and for low frequencies ("zero frequency"), Darcy diffusion theory is the basis of analysis.

Biot theory was largely laid out in the period 1945-1965. It is a wave mechanics theory that is considered valid for excitation frequencies greater than 10Hz. Biot-Gassman theory ignores megascopic diffusion effects ($\partial P/\partial t$ terms) and deals only with inertial effects, leading to an expression of the form[70]:

$$\frac{\partial^2 P}{\partial t^2} = C \frac{\partial^2 P}{\partial z^2} \quad ; \tag{5.1}$$

where 'C' is a parameter based on the physical properties of the medium, but not including permeability and viscosity. Highly complex versions of this equation are used

to analyze dynamic behavior of porous media. Therefore, diffusion processes cannot be addressed within a Biot-Gassman context.

Biot also assumed that porosity is a scalar physical parameter. However, recent work[70] has shown that for porous media, porosity is a thermodynamic variable, similar to pressure and temperature. For a complete description of the energy state of a porous medium, the porosity must be stipulated.

Wave theory predicts the existence of many of the known strain waves in porous media, but fails to predict the existence of a slow displacement wave (v ~ 150m/s) that is often observed in earthquakes. This displacement wave arrives well after all the known strain waves, and is characterized by a low vibration frequency spectrum.

At the low end of the excitation spectrum, Darcy theory deals with flow through porous media subject to number of assumptions:

- The liquids are incompressible and the strains are small. This restriction has been modified in order to analyze gas flow to wells.

- There are no dynamic (inertial) effects; therefore all motion is described by a set of diffusion equations. For example, for the simplest one dimension case of compaction, the differential equation is of the form:

$$\frac{\partial P}{\partial t} = C \frac{\partial^2 P}{\partial z^2} \quad ;$$

where 'C' is a diffusivity parameter that describes the porous medium in terms of permeability, viscosity, and solid phase compressibility.

It is widely accepted that Darcy theory is acceptable to describe the behavior of porous systems subjected to excitation frequencies of less than ~10^{-4} – 10^{-5} Hz. The pore liquids

do in fact behave incompressibly in this dynamic range, leading to a pure displacement process through the pores.

Thus, slow excitation can be described by a diffusion equation ($\partial u/\partial t$ terms) where the liquid behaves incompressibly, whereas rapid excitation can be described by a wave equation ($\partial^2 u/\partial t^2$ terms) where the liquid undergoes strain but not displacement. This discussion, expressed diagrammatically in Figure 5-1, leads to the conclusion: there must be a range of three orders of magnitude of excitation frequency between these limits where both diffusion and dynamic aspects are of primary importance in porous media mechanics. Furthermore, there must be a transition zone where the liquid phase undergoes a transition from compressible to incompressible behavior.

5.2.3 The Porosity Dilation Wave

The shortcomings of Biot and Darcy theory have been largely overcome by the development of a set of coupled diffusion-dynamic differential equations. This was achieved in the conventional manner, satisfying all the laws of conservation. Porosity is introduced as an explicit thermodynamic variable, so that the $\partial\phi/\partial t$ and $\partial^2\phi/\partial t^2$ terms are found in the equations. The equations are mixed hyperbolic and parabolic. In our study these equations are solved numerically and coupled into BOAST. The velocity solution of these equations predicts the existence of a slow displacement wave. This wave, which is called the porosity dilation (PD) wave, is not a strain wave: it is a coupled liquid-solid displacement wave, and it has the following properties [70].

- The PD wave is a body wave of small elastic porosity dilation that propagates through a liquid-saturated porous medium. Gas was observed to dampen the PD wave.

- The wave cannot exist without liquid-solid coupling, and it is preferentially generated through excitation that is dominated by moderate frequency energy (0.1-1 Hz), in the range where the liquid evidences a transition to incompressible behavior.

- With regard to conventional strain waves such as compressional and shear waves, the PD wave is analogous to the relationship between a tsunami (a liquid displacement wave) and a liquid-transmitted compressional wave (the "P" liquid strain wave). In fact, the velocity ratios are similar (roughly $1/20^{th}$).

The theoretical[9,12,17,69], laboratory[3] and field demonstration[4,8] of the existence of the PD wave helps explain several physical phenomena that to date have escaped rigorous analysis. For example, post-earthquake flow rate enhancement in oil wells can be explained by the micromechanical effects associated with the PD wave. The unusual delay in response, which occurs long after all strain waves and surface waves have transmitted, can be linked to the low velocity of the PD wave. Similarly, delayed triggering of sympathetic earthquakes, groundwater response in low-frequency vibrations (such as storm-wave induced inland flow in porous sediments), and other phenomena can perhaps be better understood by PD wave mechanics.

5.2.4 Benefits to Flow Process

Figure 5-2 shows the change in pore volume as a porosity dilation wave passes through the matrix. This is important because the induced variations in porosity are responsible for the flow rate enhancement effect. As waves of increased and decreased porosity pass through a medium, they induce the pore fluid to flow, significantly increasing flow. In addition to increasing flow, pressure pulsing also has an associated reservoir pressurization effect that is seen in both the field and laboratory[3,4,8].

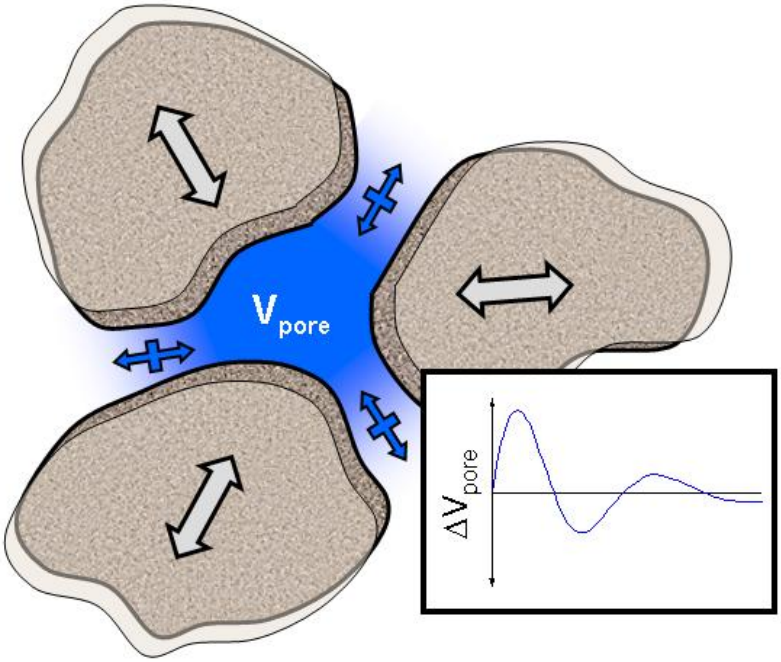

Figure 5-2: Pulsing at the pore scale.

Pressure pulsing creates the PD wave, which transits through the system, and results in the acceleration (a) of a small amount of the fluid mass (m) into and out of the pore throats (Figure 5-3). This gives rise to a force, $F = m \cdot a$, and if the force is divided by the area (A) of the pore throat that is blocking the flow, it is clear that a dynamic pressure $\Delta P = F/A$ is generated at the throat. For immiscible two-phase systems, if $ma/A > \gamma_{ow}/2r$, the dynamic ΔP can overcome the capillary barrier, and cause phase breakthrough. Once breakthrough has been achieved, fluid can flow through the pore easily and oil production can continue with fewer sources of impedance. If capillary barriers are overcome, there will be less bypassed oil in situations such as bottom-water drive: excitation in the bottom-water zone will help generate a more planar front. This process will increase the ultimate oil recovery factor in such cases.

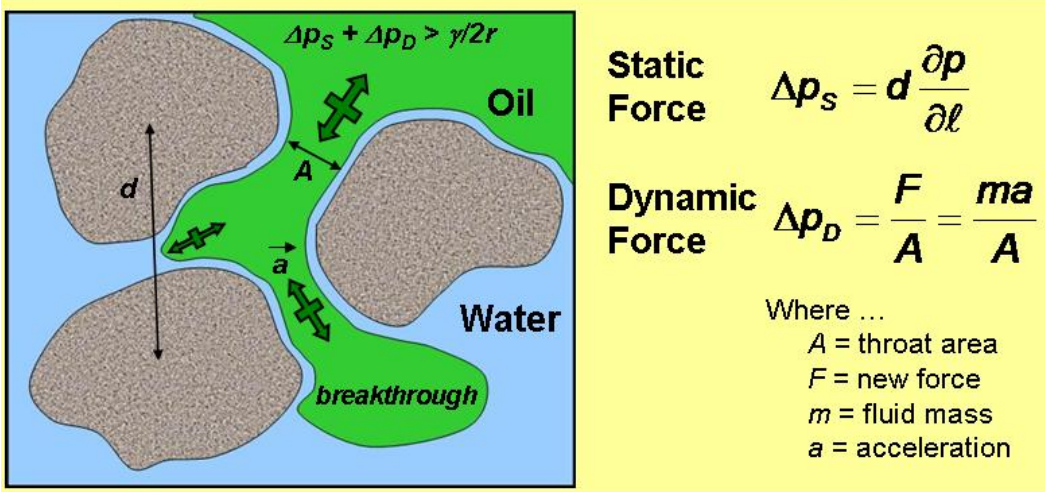

Figure 5-3: Pulsing overcomes capillarity

The diagram in Figure 5-4 represents a case of viscous fingering around a wellbore. These cases typically arise when a low viscosity liquid is injected into a porous medium containing a higher viscosity liquid; examples are water floods or chemical treatments in heavy oil reservoirs where the viscosity differences are so large that viscous fingering completely dominates the process, leading to early low-viscosity phase breakthrough, poor chemical contact with the reservoir, and so on. With pulsing, there is high dynamic energy near the wellbore to help overcome the barriers to flow that generate viscous fingering, but far from the well, the pulsing energy is diminished by geometric spreading. Thus, viscous fingering and channelling effects near the wellbore tend to be overcome, and this increases efficiency.

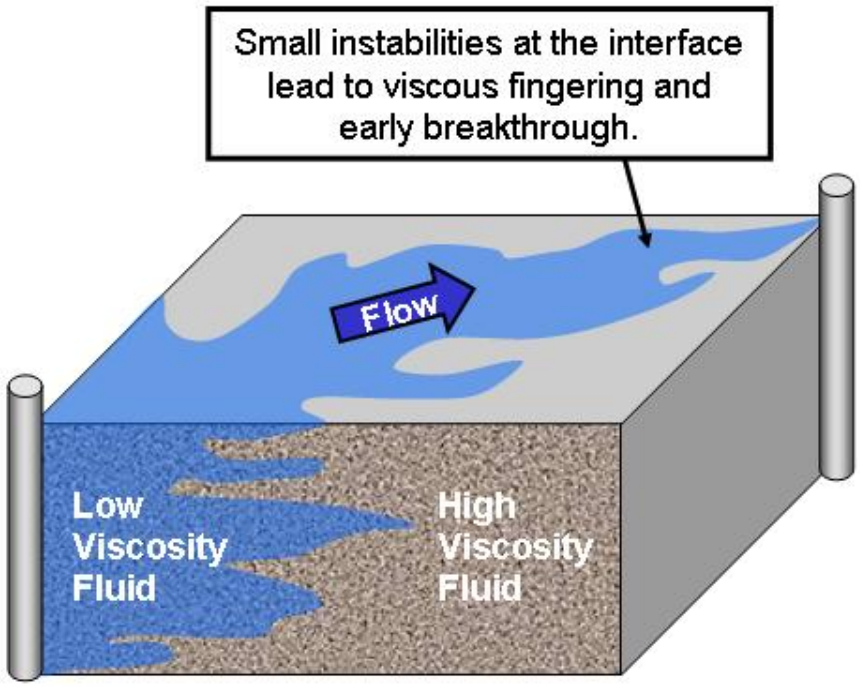

Figure 5-4: Viscous Instabilities

Pore throats accumulate fine-grained fluid-transported minerals as well as precipitates such as asphaltenes or minerals coming out of solution because of geochemical or pressure changes. The presence of these solids leads to the development of massive restrictions around producing wellbores. Many chemical treatments and technologies exist to attempt to dissolve or dislodge this material so that the well can be become a good producer again. Pressure pulsing helps loosen existing pore blockages and reduces the creation of future blockages because of the acceleration of the fluids into and out of the pores.

5.3 Theory Development

The derivation of the wave equations for porous media depends upon a set of basic equations and the equations of motion. The basic equations are the continuity equations, the pressure equations, and the porosity process equation. These equations permit the derivation of the solid dilation and porosity equations[1,2,6,7,9,21].

5.3.1 Fluid Phase Equations

5.3.1.1 Continuity

The continuity equation for the fluid is

$$\frac{\partial(\phi\rho_f)}{\partial t} + \nabla\cdot(\phi\rho_f v_f) = \dot{m}_f \quad ; \tag{5.2}$$

where the source term $\dot{m}_f = \frac{\partial m_f}{\partial t}$ is the rate of mass of fluid injected. The wave phenomena will be examined as deviations from (perturbations of) an unperturbed physical state physical state ρ_{of} (density), ϕ_o (porosity), v_{of} (velocity). The unperturbed physical state satisfies the continuity equation, i.e.

$$\frac{\partial(\phi_o\rho_{of})}{\partial t} + \nabla\cdot(\phi_o\rho_{of}v_{of}) = \dot{m}_{of} \quad ; \tag{5.3}$$

and $\dot{m}_f$ is usually set to zero. For deviations from the unperturbed state, the following equations are derived:

$$\phi = \phi_o + \delta\phi \quad ; \tag{5.4}$$

$$\rho_f = \rho_{fo} + \delta\rho_f \quad ; \tag{5.5}$$

$$v_f = v_{fo} + \delta v_f \quad ; \tag{5.6}$$

$$\dot{m}_f = \dot{m}_{fo} + \delta \dot{m}_f \quad . \tag{5.7}$$

Consequently, it is observed that

$$\phi \rho_f = \phi_o \rho_{fo} + \delta\phi \rho_{fo} + \phi_o \delta\rho_f \quad ; \tag{5.8}$$

to first order. Furthermore, we have

$$\phi \rho_f v_f = \phi_o \rho_{fo} v_{fo} + \delta\phi \rho_{fo} v_{fo} + \phi_o \delta\rho_f v_{fo} + \phi_o \rho_{fo} \delta v_f \quad . \tag{5.9}$$

The following two equations are obtained by reorganizing Equations (5.8) and (5.9) to accentuate a common factor $\phi_o \rho_{fo}$,

$$\phi \rho_f = \phi_o \rho_{fo} + \phi_o \rho_{fo} \frac{\delta\phi}{\phi_o} + \phi_o \rho_{fo} \frac{\delta\rho_f}{\rho_{fo}} \quad ; \tag{5.10}$$

$$\phi \rho_f v_f = \phi_o \rho_{fo} v_{fo} + \phi_o \rho_{fo} v_{fo} \frac{\delta\phi}{\phi_o} + \phi_o \rho_{fo} v_{fo} \frac{\delta\rho_f}{\rho_{of}} + \phi_o \rho_{fo} \delta v_f \quad . \tag{5.11}$$

Thus to first order, the continuity equation may be written as:

$$\frac{\partial(\phi_o \rho_{fo} + \phi_o \rho_{fo} \frac{\delta\phi}{\phi_o} + \phi_o \rho_{fo} \frac{\delta\rho_f}{\rho_{fo}})}{\partial t} + \nabla \cdot \left(\phi_o \rho_{fo} v_{fo} + \phi_o \rho_{fo} v_{fo} \frac{\delta\phi}{\phi_o} + \phi_o \rho_{fo} v_{fo} \frac{\delta\rho_f}{\rho_{of}} + \phi_o \rho_{fo} \delta v_f \right) = \dot{m}_{fo} + \delta \dot{m}_f \cdot \tag{5.12}$$

Rearranging terms, Equation (5.12) may be written as:

$$\frac{\partial(\phi_o \rho_{fo})}{\partial t} + \nabla \cdot (\phi_o \rho_{fo} v_{fo}) + \frac{\partial(\phi_o \rho_{fo} \frac{\delta\phi}{\phi_o} + \phi_o \rho_{fo} \frac{\delta\rho_f}{\rho_{fo}})}{\partial t} + \nabla \cdot \left(\phi_o \rho_{fo} v_{fo} \frac{\delta\phi}{\phi_o} + \phi_o \rho_{fo} v_{fo} \frac{\delta\rho_f}{\rho_{of}} + \phi_o \rho_{fo} \delta v_f \right) = \dot{m}_{fo} + \delta\dot{m}_f \quad . \tag{5.13}$$

Since the unperturbed state satisfies the equation of continuity, this equation reduces to

$$\frac{\partial(\phi_o \rho_{fo} \frac{\delta\phi}{\phi_o} + \phi_o \rho_{fo} \frac{\delta\rho_f}{\rho_{fo}})}{\partial t} + \nabla \cdot \left(\phi_o \rho_{fo} v_{fo} \frac{\delta\phi}{\phi_o} + \phi_o \rho_{fo} v_{fo} \frac{\delta\rho_f}{\rho_{of}} + \phi_o \rho_{fo} \delta v_f \right) = \delta\dot{m}_f \; ; \tag{5.14}$$

or, grouping terms,

$$\frac{\partial(\phi_o \rho_{fo} (\frac{\delta\phi}{\phi_o} + \frac{\delta\rho_f}{\rho_{fo}}))}{\partial t} + \nabla \cdot \left(\phi_o \rho_{fo} v_{fo} (\frac{\delta\phi}{\phi_o} + \frac{\delta\rho_f}{\rho_{of}}) + \phi_o \rho_{fo} \delta v_f \right) = \delta\dot{m}_f \quad . \tag{5.15}$$

Using the chain rule, Equation (5.15) can be rewritten as:

$$\phi_o \rho_{fo} \frac{\partial(\frac{\delta\phi}{\phi_o} + \frac{\delta\rho_f}{\rho_{fo}})}{\partial t} + \frac{\partial(\phi_o \rho_{fo})}{\partial t} (\frac{\delta\phi}{\phi_o} + \frac{\delta\rho_f}{\rho_{fo}}) + \phi_o \rho_{fo} v_{fo} \nabla \cdot (\frac{\delta\phi}{\phi_o} + \frac{\delta\rho_f}{\rho_{of}}) + \nabla \cdot (\phi_o \rho_{fo} v_{fo}) (\frac{\delta\phi}{\phi_o} + \frac{\delta\rho_f}{\rho_{of}}) + \nabla \cdot (\phi_o \rho_{fo} \delta v_f) = \delta\dot{m}_f \; ; \tag{5.16}$$

and which, after collecting terms, can be rewritten as:

$$\phi_o \rho_{fo} \frac{\partial(\frac{\delta\phi}{\phi_o} + \frac{\delta\rho_f}{\rho_{fo}})}{\partial t} + \phi_o \rho_{fo} v_{fo} \nabla \cdot (\frac{\delta\phi}{\phi_o} + \frac{\delta\rho_f}{\rho_{of}}) + \nabla \cdot (\phi_o \rho_{fo} \delta v_f) + (\frac{\partial(\phi_o \rho_{fo})}{\partial t} + \nabla \cdot (\phi_o \rho_{fo} v_{fo}))(\frac{\delta\phi}{\phi_o} + \frac{\delta\rho_f}{\rho_{fo}}) = \delta\dot{m}_f \quad . \tag{5.17}$$

Again, because the unperturbed state satisfies the continuity equation, this equation reduces to

$$\phi_o \rho_{fo} \frac{\partial(\frac{\delta\phi}{\phi_o} + \frac{\delta\rho_f}{\rho_{fo}})}{\partial t} + \phi_o \rho_{fo} v_{fo} \nabla \cdot (\frac{\delta\phi}{\phi_o} + \frac{\delta\rho_f}{\rho_{of}}) + \nabla \cdot (\phi_o \rho_{fo} \delta v_f) = \delta\dot{m}_f \quad . \tag{5.18}$$

Expanding and regrouping terms in Equation (5.18) provides the following:

$$\phi_o \rho_{fo} \frac{\partial(\frac{\delta\phi}{\phi_o})}{\partial t} + \phi_o \rho_{fo} \frac{\partial(\frac{\delta\rho_f}{\rho_{fo}})}{\partial t} + \phi_o \rho_{fo} \nabla \cdot (\delta v_f) + \phi_o \rho_{fo} v_{fo} \nabla \cdot (\frac{\delta\phi}{\phi_o} + \frac{\delta\rho_f}{\rho_{of}}) + \delta v_f \nabla(\phi_o \rho_{fo}) = \delta\dot{m}_f \quad . \tag{5.19}$$

If the unperturbed state is restricted to a no-flow, homogeneous and isotropic system without sources, then we have

$$\dot{m}_{fo} = 0 \qquad v_{fo} = 0 \quad ; \tag{5.20}$$

and that immediately gives

$$\frac{\partial \phi_o \rho_{fo}}{\partial t} = 0 \quad ; \tag{5.21}$$

from the equation of continuity. Additional assumptions include:

$$\nabla(\phi_o \rho_{fo}) = 0 \quad ; \tag{5.22}$$

and the unperturbed fluid density and porosity are separately independent of time:

$$\frac{\partial \phi_o}{\partial t} = 0 \qquad \frac{\partial \rho_{fo}}{\partial t} = 0 \quad . \tag{5.23}$$

With restrictions on the unperturbed state, the equation of continuity becomes:

$$\phi_o \rho_{fo} \frac{\partial(\frac{\delta\phi}{\phi_o})}{\partial t} + \phi_o \rho_{fo} \frac{\partial(\frac{\delta\rho_f}{\rho_{fo}})}{\partial t} + \phi_o \rho_{fo} \nabla \cdot (\delta v_f) = \delta \dot{m}_f \quad . \tag{5.24}$$

Dividing Equation (5.24) through by the common factor $\phi_o \rho_{fo}$:

$$\frac{\partial(\frac{\delta\phi}{\phi_o})}{\partial t} + \frac{\partial(\frac{\delta\rho_f}{\rho_{fo}})}{\partial t} + \nabla \cdot (\delta v_f) = \frac{\delta \dot{m}_f}{\phi_o \rho_{fo}} \quad ; \tag{5.25}$$

and extracting out the time independent terms, Equation (5.25) may also be written as

$$\frac{1}{\phi_o} \frac{\partial(\delta\phi)}{\partial t} + \frac{1}{\rho_{fo}} \frac{\partial(\delta\rho_f)}{\partial t} + \nabla \cdot (\delta v_f) = \frac{\delta \dot{m}_f}{\phi_o \rho_{fo}} \quad . \tag{5.26}$$

Writing the fluid velocity as the time derivative of the fluid's displacement:

$$v_f = \frac{\partial(u_f)}{\partial t} \quad . \tag{5.27}$$

The unperturbed state is $u_f = 0$. Equation (5.27) can be rewritten as:

$$\delta v_f = \frac{\partial(\delta u_f)}{\partial t} \quad . \tag{5.28}$$

The continuity equation may now be written as

$$\frac{\partial}{\partial t}\left(\frac{\delta\phi}{\phi_o} + \frac{\delta\rho_f}{\rho_{fo}} + \nabla\cdot\left(\delta u_f\right)\right) = \frac{\partial}{\partial t}\left(\frac{\delta m_f}{\phi_o\rho_{fo}}\right) \quad ; \tag{5.29}$$

which may be immediately integrated to give

$$\frac{\delta\phi}{\phi_o} + \frac{\delta\rho_f}{\rho_{fo}} + \nabla\cdot\left(\delta u_f\right) = \frac{\delta m_f}{\phi_o\rho_{fo}} \quad . \tag{5.30}$$

Replacing the terms by their definitions, this integrated form is

$$\frac{\phi-\phi_o}{\phi_o} + \frac{\rho_f-\rho_{fo}}{\rho_{fo}} + \nabla\cdot\left(u_f\right) = \frac{m_f-m_{fo}}{\phi_o\rho_{fo}} \quad . \tag{5.31}$$

Isolating the velocity and fluid displacement, these equations give

$$\nabla\cdot\delta v_f = -\frac{1}{\phi_o}\frac{\partial\delta\phi}{\partial t} - \frac{1}{\rho_{fo}}\frac{\partial\delta\rho_f}{\partial t} + \frac{\delta\dot{m}_f}{\phi_o\rho_{fo}} \quad ; \tag{5.32}$$

$$\nabla\cdot u_f = -\frac{\delta\phi}{\phi_o} - \frac{\delta\rho_f}{\rho_{fo}} + \frac{\delta m_f}{\phi_o\rho_{fo}} \quad . \tag{5.33}$$

5.3.1.2 Pressure

The density terms in Equation (5.32) and (5.33) can be written in terms of pressure. The (adiabatic) bulk modulus of the fluid is defined by

$$\frac{1}{K_f} = -\frac{1}{V_f}\frac{dV_f}{dP_f} \quad ; \tag{5.34}$$

where the specific volume of the fluid is $V_f = 1/\rho_f$. Consequently:

$$\frac{1}{K_f} = \frac{1}{\rho_f}\frac{d\rho_f}{dP_f} \quad . \tag{5.35}$$

A book keeping parameter c_f can be defined by writing the above expression as

$$\frac{c_f}{K_f} = \frac{1}{\rho_f}\frac{d\rho_f}{dP_f} \quad ; \tag{5.36}$$

c_f is called the compressibility factor. Normally, $c_f = 1$. As $K_f \to \infty$, the fluid becomes incompressible. The same limit can be achieved (in a computer program) by keeping K_f finite and letting $c_f \to 0$. Following equation can be written:

$$\frac{\delta\rho_f}{\rho_{fo}} = \frac{1}{\rho_{fo}}\frac{d\rho_f}{dP_f}\delta P_f \quad ; \tag{5.37}$$

where $\delta P_f = P_f - P_{of}$. Using the definition of the bulk modulus, the following equation can be written:

$$\frac{\delta\rho_f}{\rho_{fo}} = \frac{c_f}{K_f}\delta P_f \quad ; \tag{5.38}$$

or, using the definitions of the terms

$$\frac{\rho_f - \rho_{fo}}{\rho_{fo}} = \frac{c_f}{K_f}(P_f - P_{fo}) \quad . \tag{5.39}$$

Substituting this expression into the integrated continuity equation, the fluid's pressure equation can be obtained:

$$\frac{\phi - \phi_o}{\phi_o} + \frac{c_f}{K_f}(P_f - P_{of}) + \nabla\cdot\left(\delta u_f\right) = \frac{\delta m_f}{\phi_o \rho_{fo}} \quad . \tag{5.40}$$

A useful form of this equation is

$$\nabla\cdot\delta u_f = -\frac{\delta\phi}{\phi_o} - \frac{c_f}{K_f}\delta P_f + \frac{\delta m_f}{\phi_o\rho_{fo}} \quad . \tag{5.41}$$

The time derivative of the fluid's density-pressure relationship gives

$$\frac{1}{\rho_{fo}}\frac{\partial\delta\rho_f}{\partial t} = \frac{c_f}{K_f}\frac{\partial\delta P_f}{\partial t} \quad ; \tag{5.42}$$

or, replacing the terms by their definitions,

$$\frac{1}{\rho_{fo}}\frac{\partial \rho_f}{\partial t} = \frac{c_f}{K_f}\frac{\partial P_f}{\partial t} \quad . \tag{5.43}$$

Substituting this expression into the continuity equation gives:

$$\frac{1}{\phi_o}\frac{\partial \phi}{\partial t} + \frac{c_f}{K_f}\frac{\partial P_f}{\partial t} + \nabla \cdot v_f = \frac{\dot{m}_f}{\phi_o \rho_{fo}} \quad ; \tag{5.44}$$

which could have also been obtained by taking the partial time derivative of the pressure equation. This equation may be rewritten as:

$$\nabla \cdot v_f = -\frac{1}{\phi_o}\frac{\partial \phi}{\partial t} - \frac{c_f}{K_f}\frac{\partial P_f}{\partial t} + \frac{\dot{m}_f}{\phi_o \rho_{fo}} \quad ; \tag{5.45}$$

in the limit as $K_f \to \infty$ the following equation is obtained:

$$\nabla \cdot v_f = -\frac{1}{\phi_o}\frac{\partial \phi}{\partial t} + \frac{\dot{m}}{\phi_o \rho_{fo}} \quad . \tag{5.46}$$

This also means

$$\frac{\partial \rho_f}{\partial t} = \frac{\partial \delta \rho_f}{\partial t} = 0 \quad . \tag{5.47}$$

5.3.2 Solid Phase Equations

5.3.2.1 Continuity

The continuity equation for the solid is

$$\frac{\partial(\eta\rho_s)}{\partial t} + \nabla\cdot\left(\phi\rho_s v_s\right) = 0 \quad ; \tag{5.48}$$

where

$$\eta = 1 - \phi \quad . \tag{5.49}$$

The analysis proceeds in direct correspondence with the analysis of the fluid's equation of continuity. Deviations from an unperturbed state ρ_{os} , η_o , v_{os} that satisfies the continuity equation is examined, i.e.

$$\frac{\partial(\eta_o\rho_{os})}{\partial t} + \nabla\cdot\left(\eta_o\rho_{os}v_{os}\right) = 0 \quad . \tag{5.50}$$

The deviations from the unperturbed state are written as:

$$\eta = \eta_o + \delta\eta \quad ; \tag{5.51}$$

$$\rho_s = \rho_{os} + \delta\rho_s \quad ; \tag{5.52}$$

$$v_s = v_{os} + \delta v_s \quad ; \tag{5.53}$$

and observe that

$$\begin{aligned} \delta\eta &= \eta - \eta_o \\ &= (1-\eta) - (1-\eta_o) \\ &= -(\phi - \phi_o) \\ &= -\delta\phi \end{aligned} \quad . \tag{5.54}$$

Consequently, it is observed that

$$\eta\rho_s = \eta_o\rho_{os} + \delta\eta\rho_{os} + \eta_o\delta\rho_s \quad ; \tag{5.55}$$

to first order. Furthermore,

$$\eta\rho_s v_s = \eta_o\rho_{so}v_{so} + \delta\eta\rho_{so}v_{so} + \eta_o\delta\rho_s v_{so} + \eta_o\rho_{so}\delta v_s \quad . \tag{5.56}$$

Reorganizing these two equations to accentuate a common factor $\phi_o\rho_{fo}$, the following equations are obtained

$$\eta\rho_s = \eta_o\rho_{so} + \eta_o\rho_{so}\frac{\delta\eta}{\eta_o} + \eta_o\rho_{so}\frac{\delta\rho_s}{\rho_{so}} \quad ; \tag{5.57}$$

$$\eta\rho_s v_s = \eta_o\rho_{so}v_{so} + \eta_o\rho_{so}v_{so}\frac{\delta\eta}{\eta_o} + \eta_o\rho_{so}v_{so}\frac{\delta\rho_s}{\rho_{os}} + \eta_o\rho_{so}\delta v_s \quad . \tag{5.58}$$

Substituting these expressions into the continuity equation, the following can be obtained (omitting all of the interim calculations)

$$\eta_o\rho_{so}\frac{\partial(\frac{\delta\eta}{\eta_o})}{\partial t} + \eta_o\rho_{so}\frac{\partial(\frac{\delta\rho_s}{\rho_{so}})}{\partial t} + \eta_o\rho_{so}\nabla\cdot(\delta v_s) + \eta_o\rho_{so}v_{so}\nabla\cdot(\frac{\delta\eta}{\eta_o} + \frac{\delta\rho_s}{\rho_{os}}) + \delta v_s\nabla(\eta_o\rho_{so}) = 0 \,. \tag{5.59}$$

Now, expressing η in terms of ϕ:

$$-(1-\phi_o)\rho_{so}\frac{\partial(\frac{\delta\phi}{1-\phi_o})}{\partial t} + (1-\phi_o)\rho_{so}\frac{\partial(\frac{\delta\rho_s}{\rho_{so}})}{\partial t} + (1-\phi_o)\rho_{so}\nabla\cdot(\delta v_s) \quad .$$
$$+ (1-\phi_o)\rho_{so}v_{so}\nabla\cdot(-\frac{\delta\phi}{1-\phi_o} + \frac{\delta\rho_s}{\rho_{os}}) + \delta v_s\nabla((1-\phi_o)\rho_{so}) = 0$$

(5.60)

For porous media, the solid is normally motionless, i.e.

$$v_{so} = 0 \quad ; \tag{5.61}$$

that immediately gives

$$\frac{\partial \eta_o \rho_{so}}{\partial t} = 0 \quad ; \tag{5.62}$$

from the equation of continuity. Since

$$\frac{\partial \eta_o}{\partial t} = -\frac{\partial \phi_o}{\partial t} = 0 \quad ; \tag{5.63}$$

then

$$\frac{\partial \rho_{so}}{\partial t} = 0 \quad . \tag{5.64}$$

Assuming the unperturbed solid represents a homogeneous and isotropic system:

$$\nabla(\eta_o \rho_{so}) = 0 \quad . \tag{5.65}$$

With the restrictions to the unperturbed state, the equation of continuity is

$$\eta_o \rho_{so} \frac{\partial(\frac{\delta\eta}{\phi_o})}{\partial t} + \eta_o \rho_{so} \frac{\partial(\frac{\delta\rho_s}{\rho_{so}})}{\partial t} + \phi_o \rho_{so} \nabla \cdot (\delta v_s) = 0 \quad . \tag{5.66}$$

Dividing through by the common factor $\phi_o \rho_{fo}$:

$$\frac{\partial(\frac{\delta\eta}{\eta_o})}{\partial t} + \frac{\partial(\frac{\delta\rho_s}{\rho_{so}})}{\partial t} + \nabla \cdot (\delta v_s) = 0 \quad . \tag{5.67}$$

Extracting out the time independent terms, this equation may also be written as

$$\frac{1}{\eta_o} \frac{\partial(\delta\eta)}{\partial t} + \frac{1}{\rho_{so}} \frac{\partial(\delta\rho_s)}{\partial t} + \nabla \cdot (\delta v_s) = 0 \quad ; \tag{5.68}$$

or, replacing the deviations by their definitions,

$$\frac{1}{\eta_o} \frac{\partial\eta}{\partial t} + \frac{1}{\rho_{so}} \frac{\partial\rho_s}{\partial t} + \nabla \cdot v_s = 0 \quad . \tag{5.69}$$

Writing the solid velocity as the time derivative of the solid's displacement:

$$v_s = \frac{\partial(u_s)}{\partial t} \quad . \tag{5.70}$$

The unperturbed state is $u_s = 0$, then

$$\delta v_s = \frac{\partial(\delta u_s)}{\partial t} \quad . \tag{5.71}$$

The continuity equation may now be written as

$$\frac{\partial}{\partial t}\left(\frac{\delta\eta}{\eta_o}+\frac{\delta\rho_s}{\rho_{so}}+\nabla\cdot(\delta u_s)\right)=0 \quad ; \tag{5.72}$$

which may be immediately integrated to give

$$\frac{\delta\eta}{\eta_o}+\frac{\delta\rho_s}{\rho_{so}}+\nabla\cdot(\delta u_s)=0 \quad . \tag{5.73}$$

Replacing the terms by their definitions, this integrated form is

$$\frac{\eta-\eta_o}{\eta_o}+\frac{\rho_s-\rho_{so}}{\rho_{so}}+\nabla\cdot(u_s)=0 \quad . \tag{5.74}$$

In terms of porosity, this equation is

$$-\frac{\phi-\phi_o}{1-\phi_o}+\frac{\rho_s-\rho_{so}}{\rho_{so}}+\nabla\cdot(u_s)=0 \quad . \tag{5.75}$$

5.3.2.2 Pressure

A pressure term will be introduced in Equation (5.75). The (adiabatic) bulk modulus of the solid is defined by

$$\frac{1}{K_s}=-\frac{1}{V_s}\frac{dV_s}{dP_s} \quad ; \tag{5.76}$$

where the specific volume of the solid is $V_s = 1/\rho_s$. This definition assumes the solid is undergoing a pure compression (no shear). Consequently;

$$\frac{1}{K_s} = \frac{1}{\rho_s}\frac{d\rho_s}{dP_s} \quad . \tag{5.77}$$

To first order Equation (5.77) may be written as:

$$\frac{1}{K_s} = \frac{1}{\rho_{os}}\frac{d\rho_s}{dP_s} = \frac{1}{\rho_{os}}\frac{\rho_s - \rho_{os}}{P_s - P_{os}} \quad ; \tag{5.78}$$

so that

$$\frac{\rho_s - \rho_{os}}{\rho_{os}} = \frac{P_s - P_{os}}{K_s} \quad . \tag{5.79}$$

Substituting this result into the integral of the continuity equation, the following can be obtained:

$$\frac{\eta - \eta_o}{\eta_o} + \frac{P_s - P_{os}}{K_s} + \nabla \cdot u_s = 0 \quad . \tag{5.80}$$

Expressing this equation in terms of porosity, the pressure equation is

$$\frac{P_s - P_{os}}{K_s} - \frac{\phi - \phi_o}{1 - \phi_o} + \nabla \cdot u_s = 0 \quad ; \tag{5.81}$$

or, rearranging,

$$P_s - P_{os} = -K_s(\nabla \cdot u_s - \frac{\phi - \phi_o}{1 - \phi_o}) \quad . \tag{5.82}$$

Another useful form of this equation is

$$\nabla \cdot \delta u_s = \frac{\delta\phi}{1 - \phi_o} - \frac{\delta P_s}{K_s} \quad . \tag{5.83}$$

The time derivative of the pressure equation is

$$\frac{1}{K_s}\frac{\partial P_s}{\partial t} - \frac{1}{1 - \phi_o}\frac{\partial \phi}{\partial t} + \nabla \cdot v_s = 0 \quad ; \tag{5.84}$$

or

$$\nabla \cdot v_s = \frac{1}{1 - \phi_o}\frac{\partial \phi}{\partial t} - \frac{1}{K_s}\frac{\partial P_s}{\partial t} \quad .$$

5.3.3 Porosity

The porosity equation is needed to complete the system of equations for a porous medium. Spanos, et al.[21] showed that this equation takes the form

$$\frac{\partial \phi}{\partial t} = \delta_s \nabla \cdot v_s - \delta_f \nabla \cdot v_f \quad ; \tag{5.85}$$

where

$\delta_s > 0$ and $\delta_f > 0$.

It was assumed

$$v_{of} = 0 \quad ; \tag{5.86}$$
$$v_{os} = 0 \quad ;$$

and

$$\frac{\partial \phi_o}{\partial t} = 0 \quad ; \tag{5.87}$$

for the unperturbed state. Thus the porosity equation becomes

$$\frac{\partial \delta\phi}{\partial t} = \delta_s \nabla \cdot \delta v_s - \delta_f \nabla \cdot \delta v_f \quad . \tag{5.88}$$

This equation may be integrated. This gives us

$$\delta\phi = \delta_s \nabla \cdot \delta u_s - \delta_f \nabla \cdot \delta u_f \quad . \tag{5.89}$$

5.3.3.1 Solid Dilation

Knowing that the displacement of fluids and solids are a function of fluid pressures, the dilation of the solid can be related to the perturbations in porosity and fluid pressure. It is obtained by combining the integrated porosity equation with the fluid's pressure equation.

Combining the integrated porosity equation (5.89) and the fluid's pressure equation (5.41) gives

$$\delta\phi = \delta_s \nabla \cdot \delta u_s - \delta_f \left(-\frac{\delta\phi}{\phi_o} - \frac{c_f}{K_f}\delta P_f + \frac{\delta m_f}{\phi_o \rho_{fo}}\right) \quad . \tag{5.90}$$

Combining terms and rearranging this equation give

$$\delta_s \nabla \cdot \delta u_s = \left(\phi_o - \delta_f\right)\frac{1}{\phi_o}\delta\phi - \delta_f \frac{c_f}{K_f}\delta P_f + \delta_f \frac{\delta m_f}{\phi_o \rho_{fo}} \quad ; \tag{5.91}$$

or, dividing through by δ_s

$$\nabla \cdot \delta u_s = \frac{\left(\phi_o - \delta_f\right)}{\delta_s}\frac{1}{\phi_o}\delta\phi - \frac{\delta_f}{\delta_s}\frac{c_f}{K_f}\delta P_f + \frac{\delta_f}{\delta_s}\frac{\delta m_f}{\phi_o \rho_{fo}} \quad . \tag{5.92}$$

According to Spanos and Udey's definitions[21]

$$\alpha_\eta = \frac{\phi_o - \delta_f}{\delta_s} \quad ; \tag{5.93}$$

$$\alpha_p = \frac{\delta_f}{\delta_s} \quad . \tag{5.94}$$

Equation (5.92) becomes the solid dilation equation:

$$\nabla \cdot \delta u_s = \alpha_\eta \frac{1}{\phi_o}\delta\phi - \alpha_p \frac{c_f}{K_f}\delta P_f + \alpha_p \frac{\delta m_f}{\phi_o \rho_{fo}} \quad . \tag{5.95}$$

The time derivative of the solid dilation equation is

$$\nabla \cdot \delta v_s = \frac{\alpha_\eta}{\phi_o} \frac{\partial \delta\phi}{\partial t} - \alpha_p \frac{c_f}{K_f} \frac{\partial \delta P_f}{\partial t} + \alpha_p \frac{\delta \dot{m}_f}{\phi_o \rho_{fo}} \quad . \tag{5.96}$$

Taking the gradient of the solid dilation equations gives

$$\nabla(\nabla \cdot \delta u_s) = \frac{\alpha_\eta}{\phi_o} \nabla \delta\phi - \alpha_p \frac{c_f}{K_f} \nabla \delta P_f + \alpha_p \frac{\delta m_f}{\phi_o \rho_{fo}} \quad ; \tag{5.97}$$

or, equivalently

$$\nabla(\nabla \cdot u_s) = \frac{\alpha_\eta}{\phi_o} \nabla \phi - \alpha_p \frac{c_f}{K_f} \nabla P_f + \alpha_p \frac{m_f}{\phi_o \rho_{fo}} \quad ; \tag{5.98}$$

where we have assumed the unperturbed pressure satisfies $\nabla P_{of} = 0$.

5.3.4 Coupled Wave Equations

Spanos and Udey defined that[21]

$$\alpha_\phi = \frac{\phi_o - \delta_f}{\delta_s} \quad ; \tag{5.99}$$

$$\alpha_p = \frac{\delta_f}{\delta_s} \quad ; \tag{5.100}$$

so that

$$\delta_s = \frac{\phi_o}{\alpha_\phi + \alpha_p} \quad ; \qquad \delta_f = \frac{\alpha_p \phi_o}{\alpha_\phi + \alpha_p} = \alpha_p \delta_s \quad . \tag{5.101}$$

We employ α_ϕ and α_p as independent variables in our derivations below. The constraints

$$\delta_s > 0 \quad ; \qquad \delta_f > 0 \quad ; \qquad \frac{\delta_s}{1-\phi_o} + \frac{\delta_f}{\phi_o} < 1 \quad ; \tag{5.102}$$

leads to

$$\alpha_\phi > \frac{\phi_o}{1-\phi_o} \quad ; \qquad \alpha_p > 0 \quad . \tag{5.103}$$

5.3.5 Summary of Fluid and Solid Equations

Before introducing the equation of motion and wave equations, the following is a summary of some useful equations derived in the previous sections.

The continuity equation for the fluid equation leads to

$$\nabla \cdot \delta v_f = -\frac{1}{\phi_o}\frac{\partial \delta\phi}{\partial t} - \frac{c_f}{K_f}\frac{\partial \delta P_f}{\partial t} + \frac{\delta \dot{m}_f}{\phi_o \rho_{fo}} \quad . \tag{5.104}$$

The solid dilation equation is

$$\nabla \cdot \delta u_s = \alpha_\eta \frac{1}{\phi_o}\delta\phi - \alpha_p \frac{c_f}{K_f}\delta P_f + \alpha_p \frac{\delta m_f}{\phi_o \rho_{fo}} \quad ; \tag{5.105}$$

with time and spatial derivatives given by

$$\nabla \cdot \delta v_s = \frac{\alpha_\eta}{\phi_o}\frac{\partial \delta\phi}{\partial t} - \alpha_p \frac{c_f}{K_f}\frac{\partial \delta P_f}{\partial t} + \alpha_p \frac{\delta \dot{m}_f}{\phi_o \rho_{fo}} \quad ; \tag{5.106}$$

$$\nabla(\nabla \cdot \delta u_s) = \frac{\alpha_\eta}{\phi_o}\nabla\delta\phi - \alpha_p \frac{c_f}{K_f}\nabla\delta P_f + \alpha_p \frac{\delta m_f}{\phi_o \rho_{fo}} \quad . \tag{5.107}$$

Combining Equation (5.104) and (5.106):

$$\nabla \cdot v_f - \nabla \cdot v_s = -(\alpha_\phi + 1)\frac{1}{\phi_o}\frac{\partial \phi}{\partial t} + (\alpha_p - 1)\frac{c_f}{K_f}\frac{\partial P_f}{\partial t} - (\alpha_p - 1)\frac{\dot{m}}{\phi_o \rho_{fo}} \quad . \tag{5.108}$$

5.3.6 Wave Equation

The standard equation for a damped wave $\varphi(x,t)$ is

$$f_\varphi \rho\left(\frac{\partial^2 \varphi}{\partial t^2} + 2a\frac{\partial \varphi}{\partial t} - 2b\nabla^2\frac{\partial \varphi}{\partial t} - \upsilon_o^2\nabla^2\varphi\right) = 0 \quad ; \tag{5.109}$$

where ρ is the effective density, a is the attenuation, b is the bulk attenuation, and υ_o is the undamped wave speed. The factor f_φ is a normalization factor; a typical choice is

$$f_\varphi = \frac{1}{\varphi_o} \quad . \tag{5.110}$$

The wave operation W(f, ρ, a, b, υ_o) can be defined as

$$W(f,\rho,a,b,\upsilon_o) = f\rho\left(\frac{\partial^2}{\partial t^2} + 2a\frac{\partial}{\partial t} - 2b\nabla^2\frac{\partial}{\partial t} - \upsilon_o^2\nabla^2\right) \quad . \tag{5.111}$$

Thus, the standard wave equation may be expressed as

$$W(f_\varphi, \rho, a, b, \upsilon_o)\varphi = 0 \quad . \tag{5.112}$$

In the next sections solid and fluid wave equations will be derived.

5.3.6.1 Solid Equation of Motion

The solid's equation of motion in the isothermal case is

$$\rho_s \frac{\partial^2}{\partial t^2} u_s = K_s \nabla(\nabla \cdot v_s) - \frac{K_s}{1-\phi_o} \nabla\phi + \frac{\mu_M}{(1-\phi_o)}\left[\nabla^2 u_s + 1/3\nabla(\nabla \cdot u_s)\right] + \frac{\mu_f \phi_o^2}{K(1-\phi_o)}(v_f - v_s) ; \\ - \frac{\rho_{12}}{(1-\phi_o)} \frac{\partial}{\partial t}(v_f - v_s) + f_s \tag{5.113}$$

where f_s is the external force density and K is a macroscopic permeability term[21].

The divergence of the equation of motion Equation (5.113) produces the following equation:

$$\rho_s \frac{\partial^2 (\nabla \cdot u_s)}{\partial t^2} = K_s \nabla^2(\nabla \cdot v_s) - \frac{K_s}{1-\phi_o} \nabla^2\phi + \frac{\mu_M}{(1-\phi_o)}\left[\nabla^2(\nabla \cdot u_s) + 1/3\nabla^2(\nabla \cdot u_s)\right] ; \\ + \frac{\mu_f \phi_o^2}{K(1-\phi_o)}(\nabla \cdot v_f - \nabla \cdot v_s) - \frac{\rho_{12}}{(1-\phi_o)} \frac{\partial}{\partial t}(\nabla \cdot v_f - \nabla \cdot v_s) + \nabla \cdot f_s \tag{5.114}$$

and collecting terms, it simplifies to the following form:

$$\rho_s \frac{\partial^2(\nabla \cdot u_s)}{\partial t^2} = (K_s + \frac{4}{3}\frac{\mu_M}{(1-\phi_o)})\nabla^2(\nabla \cdot u_s) - \frac{K_s}{1-\phi_o}\nabla^2\phi + \frac{\mu_f \phi_o^2}{K(1-\phi_o)}(\nabla \cdot v_f - \nabla \cdot v_s) - \frac{\rho_{12}}{(1-\phi_o)}\frac{\partial}{\partial t}(\nabla \cdot v_f - \nabla \cdot v_s) + \nabla \cdot f_s \quad (5.115)$$

K_M the matrix bulk modulus can be defined as:

$$K_M = K_s + \frac{4}{3}\frac{\mu_M}{(1-\phi_o)} \quad (5.116)$$

Substituting K_M into Equation (5.115), the solid dilation equation becomes:

$$\rho_s \frac{\partial^2(\nabla \cdot u_s)}{\partial t^2} = K_M\nabla^2(\nabla \cdot u_s) - \frac{K_s}{1-\phi_o}\nabla^2\phi + \frac{\mu_f \phi_o^2}{K(1-\phi_o)}(\nabla \cdot v_f - \nabla \cdot v_s) - \frac{\rho_{12}}{(1-\phi_o)}\frac{\partial}{\partial t}(\nabla \cdot v_f - \nabla \cdot v_s) + \nabla \cdot f_s \quad (5.117)$$

Substituting in the expressions for $(\nabla \cdot u_s)$ and $(\nabla \cdot v_f - \nabla \cdot v_s)$ produces the following equation which includes necessary terms to form standard wave equation.

$$\rho_s \frac{\partial^2}{\partial t^2}(\alpha_\phi \frac{1}{\phi_o}\delta\phi - \alpha_p \frac{c_f}{K_f}\delta P_f + \alpha_p \frac{\delta m_f}{\phi_o \rho_{fo}}) = K_M\nabla^2\left(\alpha_\phi \frac{1}{\phi_o}\delta\phi - \alpha_p \frac{c_f}{K_f}\delta P_f + \alpha_p \frac{\delta m_f}{\phi_o \rho_{fo}}\right) - \frac{K_s}{1-\phi_o}\nabla^2\delta\phi + \frac{\mu_f \phi_o^2}{K(1-\phi_o)}\left(-(\alpha_\phi + 1)\frac{1}{\phi_o}\frac{\partial\phi}{\partial t} + (\alpha_p - 1)\frac{c_f}{K_f}\frac{\partial P_f}{\partial t} - (\alpha_p - 1)\frac{\delta\dot{m}}{\phi_o \rho_{fo}}\right) - \frac{\rho_{12}}{(1-\phi_o)}\frac{\partial}{\partial t}\left(-(\alpha_\phi + 1)\frac{1}{\phi_o}\frac{\partial\phi}{\partial t} + (\alpha_p - 1)\frac{c_f}{K_f}\frac{\partial P_f}{\partial t} - (\alpha_p - 1)\frac{\delta\dot{m}}{\phi_o \rho_{fo}}\right) + \nabla \cdot f_s \quad (5.118)$$

Furthermore, expanding terms

$$\rho_s\alpha_\phi\frac{1}{\phi_o}\frac{\partial^2\delta\phi}{\partial t^2}-\frac{\rho_{12}}{(1-\phi_o)}(\alpha_\phi+1)\frac{1}{\phi_o}\frac{\partial^2\delta\phi}{\partial t^2}+\frac{\mu_f\phi_o^2}{K(1-\phi_o)}(\alpha_\phi+1)\frac{1}{\phi_o}\frac{\partial\delta\phi}{\partial t}$$
$$-K_M\alpha_\phi\frac{1}{\phi_o}\nabla^2\delta\phi+\frac{K_s}{1-\phi_o}\nabla^2\delta\phi=$$
$$\rho_s\alpha_p\frac{c_f}{K_f}\frac{\partial^2\delta P_f}{\partial t^2}-\frac{\rho_{12}}{(1-\phi_o)}(\alpha_p-1)\frac{c_f}{K_f}\frac{\partial^2\delta P_f}{\partial t^2}$$
$$+\frac{\mu_f\phi_o^2}{K(1-\phi_o)}(\alpha_p-1)\frac{c_f}{K_f}\frac{\partial P_f}{\partial t}-K_M\alpha_p\frac{c_f}{K_f}\nabla^2\delta P_f$$
$$-\rho_s\alpha_p\frac{1}{\phi_o\rho_{fo}}\frac{\partial^2\delta m_f}{\partial t^2}+\frac{\rho_{12}}{(1-\phi_o)}(\alpha_p-1)\frac{1}{\phi_o\rho_{fo}}\frac{\partial\delta m_f}{\partial t}$$
$$-\frac{\mu_f\phi_o^2}{K(1-\phi_o)}(\alpha_p-1)\frac{1}{\phi_o\rho_{fo}}\frac{\partial\delta m_f}{\partial t}+K_M\alpha_p\frac{1}{\phi_o\rho_{fo}}\nabla^2\delta m_f+\nabla f_s\,.$$

(5.119)

Putting all porosity terms on the left and all other terms on the right and collecting terms:

$$(\rho_s\alpha_\phi-\frac{\rho_{12}}{(1-\phi_o)}(\alpha_\phi+1))\frac{1}{\phi_o}\frac{\partial^2\delta\phi}{\partial t^2}+\frac{\mu_f\phi_o^2}{K(1-\phi_o)}(\alpha_\phi+1)\frac{1}{\phi_o}\frac{\partial\delta\phi}{\partial t}-(K_M\alpha_\phi-\frac{K_s\phi_o}{1-\phi_o})\frac{1}{\phi_o}\nabla^2\delta\phi=$$
$$(\rho_s\alpha_p-\frac{\rho_{12}}{(1-\phi_o)}(\alpha_p-1))\frac{c_f}{K_f}\frac{\partial^2\delta P_f}{\partial t^2}+\frac{\mu_f\phi_o^2}{K(1-\phi_o)}(\alpha_p-1)\frac{c_f}{K_f}\frac{\partial\delta P_f}{\partial t}$$
$$-K_M\alpha_p\frac{c_f}{K_f}\nabla^2\delta P_f-\left(\rho_s\alpha_p\frac{1}{\phi_o\rho_{fo}}-\frac{\rho_{12}}{(1-\phi_o)}(\alpha_p-1)\right)\frac{1}{\phi_o\rho_{fo}}\frac{\partial^2\delta m_f}{\partial t^2}$$
$$-\frac{\mu_f\phi_o^2}{K(1-\phi_o)}(\alpha_p-1)\frac{1}{\phi_o\rho_{fo}}\frac{\partial\delta m_f}{\partial t}+K_M\alpha_p\frac{1}{\phi_o\rho_{fo}}\nabla^2\delta m_f+\nabla f_s\,.$$

(5.120)

With a few more steps Equation (5.120) can be written in standard wave form. First the effective densities $\rho_{\phi s}$ and ρ_{ps} are introduced

$$\rho_{\phi s} = (\rho_s \alpha_\phi - \frac{\rho_{12}}{(1-\phi_o)}(\alpha_\phi + 1)) \quad ; \tag{5.121}$$

$$\rho_{ps} = (\rho_s \alpha_p - \frac{\rho_{12}}{(1-\phi_o)}(\alpha_p - 1)) \quad . \tag{5.122}$$

In addition, the porosity's bulk modulus K_ϕ is defined by

$$K_\phi = K_M \alpha_\phi - \frac{K_s \phi_o}{1-\phi_o} \quad . \tag{5.123}$$

Substituting these definitions into the solid equation gives

$$\begin{aligned} \rho_{\phi s} \frac{1}{\phi_o} \frac{\partial^2 \delta\phi}{\partial t^2} + \frac{\mu_f \phi_o^2}{K(1-\phi_o)}(\alpha_\phi + 1) \frac{1}{\phi_o} \frac{\partial \delta\phi}{\partial t} - K_\phi \frac{1}{\phi_o} \nabla^2 \delta\phi = \\ \rho_{ps} \frac{c_f}{K_f} \frac{\partial^2 \delta P_f}{\partial t^2} + \frac{\mu_f \phi_o^2}{K(1-\phi_o)}(\alpha_p - 1) \frac{c_f}{K_f} \frac{\partial \delta P_f}{\partial t} - K_M \alpha_p \frac{c_f}{K_f} \nabla^2 \delta P_f \\ - \rho_{ps} \frac{1}{\phi_o \rho_{fo}} \frac{\partial^2 \delta m_f}{\partial t^2} - \frac{\mu_f \phi_o^2}{K(1-\phi_o)}(\alpha_p - 1) \frac{1}{\phi_o \rho_{fo}} \frac{\partial \delta m_f}{\partial t} + K_M \alpha_p \frac{1}{\phi_o \rho_{fo}} \nabla^2 \delta m_f + \nabla f_s \end{aligned} \quad ; \tag{5.124}$$

and then, factoring out densities and normalization factors, the following equation can be obtained

$$\rho_{\phi s}\frac{1}{\phi_o}\left(\frac{\partial^2\delta\phi}{\partial t^2}+\frac{\mu_f\phi_o^2}{K(1-\phi_o)}\frac{(\alpha_\phi+1)}{\rho_{\phi s}}\frac{\partial\phi}{\partial t}-\frac{K_\phi}{\rho_{\phi s}}\nabla^2\delta\phi\right)=$$
$$\rho_{ps}\frac{c_f}{K_f}\left(\frac{\partial^2\delta P_f}{\partial t^2}+\frac{\mu_f\phi_o^2}{K(1-\phi_o)}\frac{(\alpha_p-1)}{\rho_{ps}}\frac{\partial\delta P_f}{\partial t}-\frac{K_M\alpha_p}{\rho_{ps}}\nabla^2\delta P_f\right)$$
$$-\rho_{ps}\frac{1}{\phi_o\rho_{fo}}\left(\frac{\partial^2\delta m_f}{\partial t^2}+\frac{\mu_f\phi_o^2}{K(1-\phi_o)}\frac{(\alpha_p-1)}{\rho_{ps}}\frac{\partial\delta m_f}{\partial t}-\frac{K_M\alpha_p}{\rho_{ps}}\nabla^2\delta m_f\right)+\nabla f_s \quad . \tag{5.125}$$

Comparison with the wave standard form Equation (5.111) now permits the porosity's solid attenuation to be identified and defined as

$$a_{\phi s}=\frac{1}{2}\frac{\mu_f\phi_o^2}{K(1-\phi_o)}\frac{(\alpha_\phi+1)}{\rho_{\phi s}} \quad ; \tag{5.126}$$

the porosity's solid bulk attenuation by

$$b_{\phi s}=0 \quad ; \tag{5.127}$$

and the porosity's solid wave speed by

$$\upsilon_{\phi s}^2=\frac{K_\phi}{\rho_{\phi s}} \quad . \tag{5.128}$$

For the right hand side of the solid wave equations the pressure's solid attenuation can be identified and defined by

$$a_{ps}=\frac{1}{2}\frac{\mu_f\phi_o^2}{K(1-\phi_o)}\frac{(\alpha_p-1)}{\rho_{ps}} \quad ; \tag{5.129}$$

the pressure's solid bulk attenuation by

$$b_{ps} = 0 \quad ; \tag{5.130}$$

and the pressure's solid wave speed by

$$\upsilon_{ps}^2 = \frac{K_M \alpha_p}{\rho_{ps}} \quad . \tag{5.131}$$

Consequently, the standard form of the solid wave equation is

$$\rho_{\phi s} \frac{1}{\phi_o}\left(\frac{\partial^2 \delta\phi}{\partial t^2} + 2a_{\phi s}\frac{\partial \delta\phi}{\partial t} - \upsilon_{\phi s}^2 \nabla^2 \delta\phi\right) = \rho_{ps}\frac{c_f}{K_f}\left(\frac{\partial^2 \delta P_f}{\partial t^2} + 2a_{ps}\frac{\partial \delta P_f}{\partial t} - \upsilon_{ps}^2 \nabla^2 \delta P_f\right)$$
$$- \rho_{ps}\frac{1}{\phi_o \rho_{fo}}\left(\frac{\partial^2 \delta m_f}{\partial t^2} + 2a_{ps}\frac{\partial \delta m_f}{\partial t} - \upsilon_{ps}^2 \nabla^2 \delta m_f\right) + \nabla f_s \quad . \tag{5.132}$$

The porosity-solid wave operator can be defined by

$$W_{\phi s} = W\left(\frac{1}{\phi_o}, \rho_{\phi s}, a_{\phi s}, 0, \upsilon_{\phi s}\right) \quad ; \tag{5.133}$$

and the pressure-solid wave operator by

$$W_{ps} = W\left(\frac{c_f}{K_f}, \rho_{ps}, a_{ps}, 0, \upsilon_{ps}\right) \quad . \tag{5.134}$$

Then the solid wave equation above may be expressed as

$$W_{\phi s}\left(\frac{\delta\phi}{\phi_o}\right) = W_{ps}\left(\frac{c_f}{K_f}\delta P_f\right) - W_{ps}\left(\frac{\delta m_f}{\phi_o \rho_{fo}}\right) + \nabla f \quad . \tag{5.135}$$

5.3.6.2 Fluid Equation of Motion

The fluid equation of motion is:

$$\rho_f \frac{\partial}{\partial t} v_f = -\nabla P_f + \mu_f \nabla^2 v_f + \left(\xi_f + 1/3\mu_f\right)\nabla\left(\nabla \cdot v_f\right) + \frac{\xi_f}{\phi_o}\nabla\frac{\partial\phi}{\partial t} + \frac{(1-\phi_o)}{\phi_o}\mu_f\left(\frac{\mu_M}{(1-\phi_o)\mu_s} - 1\right)$$
$$\left(\nabla^2 \frac{\partial u_s}{\partial t} + 1/3\nabla\left(\nabla \cdot \frac{\partial u_s}{\partial t}\right)\right) - \frac{\mu_f \phi_o}{K}\left(v_f - v_s\right) + \frac{\rho_{12}}{\phi_o}\frac{\partial}{\partial t}\left(v_f - v_s\right) + f_f \quad ; \tag{5.136}$$

where μ_M is given by

$$\mu_M = (1-\phi_o)\mu_s(1+\lambda_s) \quad ; \tag{5.137}$$

and λ_s is a shear modulus enhancement factor. Defining σ_M

$$\sigma_M = \frac{(1-\phi_o)}{\phi_o}\mu_f\left(\frac{\mu_M}{(1-\phi_o)\mu_s} - 1\right) \quad ;$$
$$= \frac{(1-\phi_o)}{\phi_o}\mu_f\lambda_s \tag{5.138}$$

Substituting this expression into the wave equation and noting that

$$\frac{\partial u_s}{\partial t} = v_s \quad ; \tag{5.139}$$

now gives

$$\rho_f \frac{\partial}{\partial t} v_f = -\nabla P_f + \mu_f \nabla^2 v_f + \left(\xi_f + 1/3\mu_f\right)\nabla\left(\nabla \cdot v_f\right) + \frac{\xi_f}{\phi_o}\nabla\frac{\partial \phi}{\partial t} - \sigma_M\left(\nabla^2 v_s + 1/3\nabla\left(\nabla \cdot v_s\right)\right)$$
$$- \frac{\mu_f \phi_o}{K}\left(v_f - v_s\right) + \frac{\rho_{12}}{\phi_o}\frac{\partial}{\partial t}\left(v_f - v_s\right) + f_f$$

.

(5.140)

With a few more steps Equation (5.140) can be written in standard wave form. Taking the negative divergence $(-\nabla\cdot)$ of the equation of motion.

$$-\rho_f \frac{\partial(\nabla \cdot v_f)}{\partial t} = \nabla^2 P_f - \mu_f \nabla^2(\nabla \cdot v_f) - \left(\xi_f + 1/3\mu_f\right)\nabla^2\left(\nabla \cdot v_f\right) - \frac{\xi_f}{\phi_o}\nabla^2\frac{\partial \phi}{\partial t} + \frac{4}{3}\sigma_M \nabla^2\left(\nabla \cdot v_s\right)$$
$$+ \frac{\mu_f \phi_o}{K}\left(\nabla \cdot v_f - \nabla \cdot v_s\right) - \frac{\rho_{12}}{\phi_o}\frac{\partial}{\partial t}\left(\nabla \cdot v_f - \nabla \cdot v_s\right) - \nabla \cdot f_f$$

.

(5.141)

Now substituting for $(\nabla \cdot v_f)$, $\left(\nabla \cdot v_s\right)$ and $\left(\nabla \cdot v_f - \nabla \cdot v_s\right)$

$$-\rho_{fo}\frac{\partial}{\partial t}\left(-\frac{1}{\phi_o}\frac{\partial \delta\phi}{\partial t} - \frac{c_f}{K_f}\frac{\partial \delta P_f}{\partial t} + \frac{\delta \dot{m}_f}{\phi_o \rho_{fo}}\right) = \nabla^2 P_f - \mu_f \nabla^2\left(-\frac{1}{\phi_o}\frac{\partial \delta\phi}{\partial t} - \frac{c_f}{K_f}\frac{\partial \delta P_f}{\partial t} + \frac{\delta \dot{m}}{\phi_o \rho_{fo}}\right)$$
$$- \left(\xi_f + 1/3\mu_f\right)\nabla^2\left(-\frac{1}{\phi_o}\frac{\partial \delta\phi}{\partial t} - \frac{c_f}{K_f}\frac{\partial \delta P_f}{\partial t} + \frac{\delta \dot{m}}{\phi_o \rho_{fo}}\right) - \frac{\xi_f}{\phi_o}\nabla^2\frac{\partial \delta\phi}{\partial t}$$
$$+ \frac{4}{3}\sigma_M \nabla^2\left(\alpha_\phi \frac{1}{\phi_o}\frac{\partial \delta\phi}{\partial t} - \alpha_p \frac{c_f}{K_f}\frac{\partial \delta P_f}{\partial t} + \alpha_p \frac{\delta \dot{m}}{\phi_o \rho_{fo}}\right)$$
$$+ \frac{\mu_f \phi_o}{K}\left(-(\alpha_\phi + 1)\frac{1}{\phi_o}\frac{\partial \delta\phi}{\partial t} + (\alpha_p - 1)\frac{c_f}{K_f}\frac{\partial \delta P_f}{\partial t} - (\alpha_p - 1)\frac{\delta \dot{m}}{\phi_o \rho_{fo}}\right)$$
$$- \frac{\rho_{12}}{\phi_o}\frac{\partial}{\partial t}\left(-(\alpha_\phi + 1)\frac{1}{\phi_o}\frac{\partial \delta\phi}{\partial t} + (\alpha_p - 1)\frac{c_f}{K_f}\frac{\partial \delta P_f}{\partial t} - (\alpha_p - 1)\frac{\delta \dot{m}}{\phi_o \rho_{fo}}\right) - \nabla \cdot f_f$$

;

(5.142)

expanding terms gives

$$\rho_{fo}\frac{1}{\phi_o}\frac{\partial^2\delta\phi}{\partial t^2}+\rho_{fo}\frac{c_f}{K_f}\frac{\partial^2\delta P_f}{\partial t^2}+\rho_{fo}\frac{1}{\phi_o\rho_{fo}}\frac{\partial^2\delta m_f}{\partial t^2}=\nabla^2\delta P_f+\mu_f\frac{1}{\phi_o}\nabla^2\frac{\partial\delta\phi}{\partial t}$$
$$+\mu_f\frac{c_f}{K_f}\nabla^2\frac{\partial\delta P_f}{\partial t}-\mu_f\nabla^2\frac{\delta\dot{m}_f}{\phi_o\rho_{fo}}+\left(\xi_f+1/3\mu_f\right)\frac{1}{\phi_o}\nabla^2\frac{\partial\delta\phi}{\partial t}+\left(\xi_f+1/3\mu_f\right)\frac{c_f}{K_f}\nabla^2\frac{\partial\delta P_f}{\partial t}$$
$$-\left(\xi_f+1/3\mu_f\right)\frac{\delta\dot{m}_f}{\phi_o\rho_{fo}}-\frac{\xi_f}{\phi_o}\nabla^2\frac{\partial\delta\phi}{\partial t}+\frac{4}{3}\sigma_M\alpha_\phi\frac{1}{\phi_o}\nabla^2\frac{\partial\delta\phi}{\partial t}-\frac{4}{3}\sigma_M\alpha_p\frac{c_f}{K_f}\nabla^2\frac{\partial\delta P_f}{\partial t}$$
$$+\frac{4}{3}\sigma_M\alpha_p\nabla^2\frac{\delta\dot{m}_f}{\phi_o\rho_{fo}}-\frac{\mu_f\phi_o}{K}(\alpha_\phi+1)\frac{1}{\phi_o}\frac{\partial\delta\phi}{\partial t}+\frac{\mu_f\phi_o}{K}(\alpha_p-1)\frac{c_f}{K_f}\frac{\partial\delta P_f}{\partial t}-\frac{\mu_f\phi_o}{K}(\alpha_p-1)\frac{\delta\dot{m}_f}{\phi_o\rho_{fo}}$$
$$+\frac{\rho_{12}}{\phi_o}(\alpha_\phi+1)\frac{1}{\phi_o}\frac{\partial^2\delta\phi}{\partial t^2}-\frac{\rho_{12}}{\phi_o}(\alpha_p-1)\frac{c_f}{K_f}\frac{\partial^2\delta P_f}{\partial t^2}+\frac{\rho_{12}}{\phi_o}(\alpha_p-1)\frac{1}{\phi_o\rho_{fo}}\frac{\partial^2\delta m_f}{\partial t^2}-\nabla\cdot f_f$$

.

(5.143)

Collecting terms

$$\rho_{fo}\frac{1}{\phi_o}\frac{\partial^2\delta\phi}{\partial t^2}+\rho_{fo}\frac{c_f}{K_f}\frac{\partial^2\delta P_f}{\partial t^2}+\rho_{fo}\frac{1}{\phi_o\rho_{fo}}\frac{\partial^2\delta m_f}{\partial t^2}=$$
$$\nabla^2\delta P_f+\left(\mu_f+\left(\xi_f+1/3\mu_f\right)-\xi_f+\frac{4}{3}\sigma_M\alpha_\phi\right)\frac{1}{\phi_o}\nabla^2\frac{\partial\delta\phi}{\partial t}$$
$$+\left(\mu_f+\left(\xi_f+1/3\mu_f\right)-\frac{4}{3}\sigma_M\alpha_p\right)\frac{c_f}{K_f}\nabla^2\frac{\partial\delta P_f}{\partial t}-\left(\mu_f+\left(\xi_f+1/3\mu_f\right)-\frac{4}{3}\sigma_M\alpha_p\right)\frac{1}{\phi_o\rho_{fo}}\nabla^2\delta\dot{m}_f$$
$$-\frac{\mu_f\phi_o}{K}(\alpha_\phi+1)\frac{1}{\phi_o}\frac{\partial\delta\phi}{\partial t}+\frac{\mu_f\phi_o}{K}(\alpha_p-1)\frac{c_f}{K_f}\frac{\partial\delta P_f}{\partial t}-\frac{\mu_f\phi_o}{K}(\alpha_p-1)\frac{\delta\dot{m}_f}{\phi_o\rho_{fo}}$$
$$+\frac{\rho_{12}}{\phi_o}(\alpha_\phi+1)\frac{1}{\phi_o}\frac{\partial^2\delta\phi}{\partial t^2}-\frac{\rho_{12}}{\phi_o}(\alpha_p-1)\frac{c_f}{K_f}\frac{\partial^2\delta P_f}{\partial t^2}+\frac{\rho_{12}}{\phi_o}(\alpha_p-1)\frac{1}{\phi_o\rho_{fo}}\frac{\partial^2\delta m_f}{\partial t^2}-\nabla\cdot f_f$$

;

(5.144)

which becomes, after some minor simplifications

$$\rho_{fo}\frac{1}{\phi_o}\frac{\partial^2\delta\phi}{\partial t^2}+\rho_{fo}\frac{c_f}{K_f}\frac{\partial^2\delta P_f}{\partial t^2}+\rho_{fo}\frac{1}{\phi_o\rho_{fo}}\frac{\partial^2\delta m_f}{\partial t^2}=$$
$$\nabla^2\delta P_f+\frac{4}{3}\left(\mu_f+\sigma_M\alpha_\phi\right)\frac{1}{\phi_o}\nabla^2\frac{\partial\delta\phi}{\partial t}$$
$$+\left(\xi_f+\frac{4}{3}\left(\mu_f-\sigma_M\alpha_p\right)\right)\frac{c_f}{K_f}\nabla^2\frac{\partial\delta P_f}{\partial t}-\left(\xi_f+\frac{4}{3}\left(\mu_f-\sigma_M\alpha_p\right)\right)\frac{1}{\phi_o\rho_{fo}}\nabla^2\delta\dot{m}_f$$
$$-\frac{\mu_f\phi_o}{K}(\alpha_\phi+1)\frac{1}{\phi_o}\frac{\partial\delta\phi}{\partial t}+\frac{\mu_f\phi_o}{K}(\alpha_p-1)\frac{c_f}{K_f}\frac{\partial\delta P_f}{\partial t}-\frac{\mu_f\phi_o}{K}(\alpha_p-1)\frac{\delta\dot{m}_f}{\phi_o\rho_{fo}}$$
$$+\frac{\rho_{12}}{\phi_o}(\alpha_\phi+1)\frac{1}{\phi_o}\frac{\partial^2\delta\phi}{\partial t^2}-\frac{\rho_{12}}{\phi_o}(\alpha_p-1)\frac{c_f}{K_f}\frac{\partial^2\delta P_f}{\partial t^2}+\frac{\rho_{12}}{\phi_o}(\alpha_p-1)\frac{1}{\phi_o\rho_{fo}}\frac{\partial^2\delta m_f}{\partial t^2}-\nabla\cdot f_f$$

.

(5.145)

Rearranging so all porosity terms are on the left hand side and pressure terms are on the right hand side:

$$\rho_{fo}\frac{1}{\phi_o}\frac{\partial^2\delta\phi}{\partial t^2}-\frac{\rho_{12}}{\phi_o}(\alpha_\phi+1)\frac{1}{\phi_o}\frac{\partial^2\delta\phi}{\partial t^2}+\frac{\mu_f\phi_o}{K}(\alpha_\phi+1)\frac{1}{\phi_o}\frac{\partial\delta\phi}{\partial t}-\frac{4}{3}\left(\mu_f+\sigma_M\alpha_\phi\right)\frac{1}{\phi_o}\nabla^2\frac{\partial\delta\phi}{\partial t}=$$
$$\nabla^2\delta P_f-\rho_{fo}\frac{c_f}{K_f}\frac{\partial^2\delta P_f}{\partial t^2}-\frac{\rho_{12}}{\phi_o}(\alpha_p-1)\frac{c_f}{K_f}\frac{\partial^2\delta P_f}{\partial t^2}+\frac{\mu_f\phi_o}{K}(\alpha_p-1)\frac{c_f}{K_f}\frac{\partial\delta P_f}{\partial t}$$
$$+\left(\xi_f+\frac{4}{3}\left(\mu_f-\sigma_M\alpha_p\right)\right)\frac{c_f}{K_f}\nabla^2\frac{\partial\delta P_f}{\partial t}+\rho_{fo}\frac{1}{\phi_o\rho_{fo}}\frac{\partial^2\delta m_f}{\partial t^2}+\frac{\rho_{12}}{\phi_o}(\alpha_p-1)\frac{1}{\phi_o\rho_{fo}}\frac{\partial^2\delta m_f}{\partial t^2}$$
$$-\frac{\mu_f\phi_o}{K}(\alpha_p-1)\frac{\delta\dot{m}_f}{\phi_o\rho_{fo}}-\left(\xi_f+\frac{4}{3}\left(\mu_f-\sigma_M\alpha_p\right)\right)\frac{1}{\phi_o\rho_{fo}}\nabla^2\delta\dot{m}_f-\nabla\cdot f_f$$

.

(5.146)

Finally, collecting terms

$$\left(\rho_{fo}-\frac{\rho_{12}}{\phi_o}(\alpha_\phi+1)\right)\frac{1}{\phi_o}\frac{\partial^2\delta\phi}{\partial t^2}+\frac{\mu_f\phi_o}{K}(\alpha_\phi+1)\frac{1}{\phi_o}\frac{\partial\delta\phi}{\partial t}-\frac{4}{3}\left(\mu_f+\sigma_M\alpha_\phi\right)\frac{1}{\phi_o}\nabla^2\frac{\partial\delta\phi}{\partial t}=$$
$$\nabla^2\delta P_f-\left(\rho_{fo}+\frac{\rho_{12}}{\phi_o}(\alpha_p-1)\right)\frac{c_f}{K_f}\frac{\partial^2\delta P_f}{\partial t^2}+\frac{\mu_f\phi_o}{K}(\alpha_p-1)\frac{c_f}{K_f}\frac{\partial\delta P_f}{\partial t}$$
$$+\left(\xi_f+\frac{4}{3}\left(\mu_f-\sigma_M\alpha_p\right)\right)\frac{c_f}{K_f}\nabla^2\frac{\partial\delta P_f}{\partial t}+\left(\rho_{fo}+\frac{\rho_{12}}{\phi_o}(\alpha_p-1)\right)\frac{1}{\phi_o\rho_{fo}}\frac{\partial^2\delta m_f}{\partial t^2}$$
$$-\frac{\mu_f\phi_o}{K}(\alpha_p-1)\frac{\delta\dot{m}_f}{\phi_o\rho_{fo}}-\left(\xi_f+\frac{4}{3}\left(\mu_f-\sigma_M\alpha_p\right)\right)\frac{1}{\phi_o\rho_{fo}}\nabla^2\delta\dot{m}_f-\nabla\cdot f_f\,.$$

(5.147)

To cast the fluid equation above into the standard wave equation form, first, the effective densities are defined

$$\rho_{\phi f}=(\rho_f-\frac{\rho_{12}}{\phi_o}(\alpha_\phi+1))\;\;;\qquad\rho_{pf}=(\rho_f+\frac{\rho_{12}}{\phi_o}(\alpha_p-1))\;\;; \tag{5.148}$$

so that the fluid equation becomes

$$\rho_{\phi f}\frac{1}{\phi_o}\frac{\partial^2\phi}{\partial t^2}+\frac{\mu_f\phi_o}{K}(\alpha_\phi+1)\frac{1}{\phi_o}\frac{\partial\phi}{\partial t}-\frac{4}{3}(\mu_f+\sigma_M\alpha_\phi)\frac{1}{\phi_o}\nabla^2\frac{\partial\phi}{\partial t}=\nabla^2P_f$$
$$-\rho_{ps}\frac{c_f}{K_f}\frac{\partial^2P_f}{\partial t^2}+\frac{\mu_f\phi_o}{K}(\alpha_p-1)\frac{c_f}{K_f}\frac{\partial P_f}{\partial t}+(\xi_f+\frac{4}{3}\left(\mu_f-\sigma_M\alpha_p\right))\frac{c_f}{K_f}\nabla^2\frac{\partial P_f}{\partial t}$$
$$\rho_{ps}\frac{1}{\phi_o\rho_{fo}}\frac{\partial^2\delta m_f}{\partial t^2}-\frac{\mu_f\phi_o}{K}(\alpha_p-1)\frac{\delta\dot{m}_f}{\phi_o\rho_{fo}}-\left(\xi_f+\frac{4}{3}\left(\mu_f-\sigma_M\alpha_p\right)\right)\frac{1}{\phi_o\rho_{fo}}\nabla^2\delta\dot{m}_f-\nabla\cdot f_f\,.$$

(5.149)

Factoring out the density and normalization terms now produces

$$\frac{\rho_{\phi f}}{\phi_o}\left(\frac{\partial^2\phi}{\partial t^2}+\frac{\mu_f\phi_o}{K\rho_{\phi f}}(\alpha_\phi+1)\frac{\partial\phi}{\partial t}-\frac{4}{3}\frac{(\mu_f+\sigma_M\alpha_\phi)}{\rho_{\phi f}}\nabla^2\frac{\partial\phi}{\partial t}\right)$$
$$=\nabla^2 P_f-\rho_{pf}\frac{c_f}{K_f}\left(\frac{\partial^2 P_f}{\partial t^2}-\frac{\mu_f\phi_o}{K\rho_{pf}}(\alpha_p-1)\frac{\partial P_f}{\partial t}-\frac{1}{\rho_{pf}}\left(\xi_f+\frac{4}{3}\left(\mu_f-\sigma_M\alpha_p\right)\right)\nabla^2\frac{\partial P_f}{\partial t}\right)$$
$$\rho_{pf}\frac{1}{\phi_o\rho_{fo}}\left(\frac{\partial^2\delta m_f}{\partial t^2}-\frac{\mu_f\phi_o}{K}\frac{(\alpha_p-1)}{\rho_{pf}}\delta\dot{m}_f-\frac{1}{\rho_{pf}}\left(\xi_f+\frac{4}{3}\left(\mu_f-\sigma_M\alpha_p\right)\right)\nabla^2\delta\dot{m}_f\right)-\nabla\cdot f_f \quad . \tag{5.150}$$

Comparing terms in the fluid equation to the standard form Equation (5.111) permits to identify the standard coefficients. For the left hand of the fluid equation the porosity's fluid attenuation is defined by

$$a_{\phi f}=\frac{1}{2}\frac{\mu_f\phi_o}{K\rho_{\phi f}}(\alpha_\phi+1) \quad ; \tag{5.151}$$

the porosity's bulk attenuation by

$$b_{\phi f}=\frac{2}{3}\frac{(\mu_f+\sigma_M\alpha_\phi)}{\rho_{\phi f}} \quad ; \tag{5.152}$$

and the porosity's fluid wave speed by

$$\upsilon_{\phi f}^2=0 \quad . \tag{5.153}$$

For the right hand side of the fluid equation the pressure's fluid attenuation (actually a gain) is defined by

$$a_{pf} = -\frac{1}{2}\frac{\mu_f \phi_o}{K \rho_{pf}}(\alpha_p - 1) \quad ; \tag{5.154}$$

and the pressure's fluid bulk attenuation by

$$b_{pf} = \frac{1}{2}\frac{1}{\rho_{pf}}(\xi_f + \frac{4}{3}\left(\mu_f - \sigma_M \alpha_p\right) \quad . \tag{5.155}$$

With these definitions, the fluid equation in standard form is given by

$$\frac{\rho_{\phi f}}{\phi_o}(\frac{\partial^2 \phi}{\partial t^2} + 2a_{\phi f}\frac{\partial \phi}{\partial t} - 2b_{\phi f}\nabla^2 \frac{\partial \phi}{\partial t}) = \nabla^2 P_f - \rho_{pf}\frac{c_f}{K_f}(\frac{\partial^2 P_f}{\partial t^2} + 2a_{pf}\frac{\partial P_f}{\partial t} - 2b_{pf}\nabla^2 \frac{\partial P_f}{\partial t}) + \rho_{pf}\frac{1}{\phi_o \rho_{fo}}\left(\frac{\partial^2 \delta m_f}{\partial t^2} + 2a_{pf}\delta \dot{m}_f - 2b_{pf}\nabla^2 \delta \dot{m}_f\right) - \nabla \cdot f_f \quad . \tag{5.156}$$

When the fluid is incompressible, the fluid's wave speed (the speed of sound in the fluid) is defined by

$$\upsilon_{pf}^2 = \frac{K_f}{\rho_{pf}} \quad . \tag{5.157}$$

Defining the porosity-fluid wave operator by

$$W_{\phi f} = W(\frac{1}{\phi_o}, \rho_{\phi f}, a_{\phi f}, b_{\phi f}, 0) \quad ; \tag{5.158}$$

and the pressure-fluid wave operator by

$$W_{pf} = W(\frac{c_f}{K_f}, \rho_{pf}, a_{pf}, b_{pf}, 0) \quad . \tag{5.159}$$

Then the fluid wave equation above may be expressed as

$$W_{\phi f}\left(\frac{\delta\phi}{\phi_o}\right) = \nabla^2 P - W_{pf}\left(\frac{c_f}{K_f}\delta P_f\right) + W_{ps}\left(\frac{\delta m_f}{\phi_o \rho_{fo}}\right) - \nabla f \quad . \tag{5.160}$$

5.3.7 The Porosity Wave

The incompressible limit is taken by letting $K_f \to \infty$. In a computer program this can be achieved by setting $c_f = 0$. In this limit, the solid wave equation becomes

$$\rho_{\phi s}\frac{1}{\phi_o}(\frac{\partial^2\phi}{\partial t^2} + 2a_{\phi s}\frac{\partial\phi}{\partial t} - \upsilon_{\phi s}^2\nabla^2\phi) = -\rho_{ps}\frac{1}{\phi_o\rho_{fo}}\left(\frac{\partial^2\delta m_f}{\partial t^2} + 2a_{ps}\frac{\partial\delta m_f}{\partial t} - \upsilon_{ps}^2\nabla^2\delta m_f\right) - \nabla f \quad . \tag{5.161}$$

If there are no source terms or only point source terms then this equation reduces to

$$\frac{\partial^2\phi}{\partial t^2} + 2a_{\phi s}\frac{\partial\phi}{\partial t} - \upsilon_{\phi s}^2\nabla^2\phi = 0 \quad . \tag{5.162}$$

This equation describes an undamped porosity wave. Without attenuation it would travel with speed $\upsilon_{\phi s}$. Under conditions where the inertial term (the second time derivative) is very small, this equation reduces to a diffusion equation.

$$2a_{\phi s}\frac{\partial \phi}{\partial t}-\upsilon_{\phi s}^{2}\nabla^{2}\phi=0 \quad ; \tag{5.163}$$

which can be rewritten as

$$\frac{\partial \phi}{\partial t}=D_{\phi s}\nabla^{2}\phi \quad ; \tag{5.164}$$

where the diffusion coefficient $D_{\phi s}$ is

$$D_{\phi s}=\frac{\upsilon_{\phi s}^{2}}{2a_{\phi s}} \quad ; \tag{5.165}$$

in the incompressible limit, the fluid wave equation becomes

$$\frac{\rho_{\phi f}}{\phi_o}\left(\frac{\partial^{2}\phi}{\partial t^{2}}+2a_{\phi f}\frac{\partial \phi}{\partial t}-2b_{\phi f}\nabla^{2}\frac{\partial \phi}{\partial t}\right)=\nabla^{2}P_{f}+\rho_{pf}\frac{1}{\phi_o\rho_{fo}}\left(\frac{\partial^{2}\delta m_{f}}{\partial t^{2}}+2a_{pf}\delta \dot{m}_{f}-2b_{pf}\nabla^{2}\delta \dot{m}_{f}\right)-\nabla\cdot f_{f}\,. \tag{5.166}$$

Isolating the fluid pressure gives

$$\begin{aligned}\nabla^{2}P_{f}=&\frac{\rho_{\phi f}}{\phi_o}\left(\frac{\partial^{2}\phi}{\partial t^{2}}+2a_{\phi f}\frac{\partial \phi}{\partial t}-2b_{\phi f}\nabla^{2}\frac{\partial \phi}{\partial t}\right)\\&-\rho_{pf}\frac{1}{\phi_o\rho_{fo}}\left(\frac{\partial^{2}\delta m_{f}}{\partial t^{2}}+2a_{pf}\delta \dot{m}_{f}-2b_{pf}\nabla^{2}\delta \dot{m}_{f}\right)-\nabla\cdot f_{f}\,.\end{aligned} \tag{5.167}$$

This equation shows how the fluid pressure responds to the porosity wave. It is observed that as the wave propagates (either as a wave or diffusively) it loses energy to the porous medium, and the pressure (typically increases) in response to this energy loss.

5.4 Discretization of the Fluid and Solid Wave Equations

5.4.1 Discretization of the Fluid Wave Equations

Assuming the injected mass rate is constant and it is a point source then the fluid wave equation (5.167) reduces to

$$\nabla^2 P_f = \frac{\rho_{\phi f}}{\phi_o}\left(\frac{\partial^2 \phi}{\partial t^2} + 2a_{\phi f}\frac{\partial \phi}{\partial t} - 2b_{\phi f}\nabla^2\frac{\partial \phi}{\partial t}\right) \quad ; \tag{5.168}$$

$$\begin{aligned}\frac{P^{n+1}_{i+1,j,k} - 2P^{n+1}_{i,j,k} + P^{n+1}_{i-1,j,k}}{\Delta x^2} + \frac{P^{n+1}_{i,j+1,k} - 2P^{n+1}_{i,j,k} + P^{n+1}_{i,j-1,k}}{\Delta y^2} + \frac{P^{n+1}_{i,j,k+1} - 2P^{n+1}_{i,j,k} + P^{n+1}_{i,j,k-1}}{\Delta z^2} = \\ \frac{\rho_{\phi f}}{\phi_o}\left(\frac{\phi^{n+1}_{i,j,k} - 2\phi^{n}_{i,j,k} + \phi^{n-1}_{i,j,k}}{\Delta t^2} + 2a_{\phi f}\frac{\phi^{n+1}_{i,j,k} - \phi^{n}_{i,j,k}}{\Delta t}\right. \qquad ; \\ \left. - 2b_{\phi f}\left(\frac{Z^{n+1}_{i+1,j,k} - 2Z^{n+1}_{i,j,k} + Z^{n+1}_{i-1,j,k}}{\Delta x^2} + \frac{Z^{n+1}_{i,j+1,k} - 2Z^{n+1}_{i,j,k} + Z^{n+1}_{i,j-1,k}}{\Delta y^2} + \frac{Z^{n+1}_{i,j,k+1} - 2Z^{n+1}_{i,j,k} + Z^{n+1}_{i,j,k-1}}{\Delta z^2}\right)\right)\end{aligned} \tag{5.169}$$

where

$$Z^{n+1}_{i,j,k} = \frac{\phi^{n+1}_{i,j,k} - \phi^{n}_{i,j,k}}{\Delta t} \quad ; \tag{5.170}$$

$$Z^{n+1}_{i-1,j,k} = \frac{\phi^{n+1}_{i-1,j,k} - \phi^{n}_{i-1,j,k}}{\Delta t} \quad ; \tag{5.171}$$

$$Z_{i,j+1,k}^{n+1} = \frac{\phi_{i,j+1,k}^{n+1} - \phi_{i,j+1,k}^{n}}{\Delta t} \quad ; \tag{5.172}$$

$$Z_{i,j-1,k}^{n+1} = \frac{\phi_{i,j-1,k}^{n+1} - \phi_{i,j-1,k}^{n}}{\Delta t} \quad ; \tag{5.173}$$

$$Z_{i,j,k+1}^{n+1} = \frac{\phi_{i,j,k+1}^{n+1} - \phi_{i,j,k+1}^{n}}{\Delta t} \quad ; \tag{5.174}$$

$$Z_{i,j,k-1}^{n+1} = \frac{\phi_{i,j,k-1}^{n+1} - \phi_{i,j,k-1}^{n}}{\Delta t} \quad . \tag{5.175}$$

Writing Equation (5.169) in a matrix form:

$$\begin{bmatrix} 0 & 0 & 0 \\ 0 & tc & 0 \\ 0 & 0 & 0 \end{bmatrix} \begin{bmatrix} 0 & n & 0 \\ w & c & e \\ 0 & s & 0 \end{bmatrix} \begin{bmatrix} 0 & 0 & 0 \\ 0 & bc & 0 \\ 0 & 0 & 0 \end{bmatrix} P_{i,j,k}^{n+1} = F \quad ; \tag{5.176}$$

where

$$tc = \frac{1}{\Delta z^2} \quad ; \tag{5.177}$$

$$n = \frac{1}{\Delta y^2} \quad ; \tag{5.178}$$

$$w = \frac{1}{\Delta x^2} \quad ; \tag{5.179}$$

$$e = \frac{1}{\Delta x^2} \quad ; \tag{5.180}$$

$$s = \frac{1}{\Delta y^2} \quad ; \tag{5.181}$$

$$bc = \frac{1}{\Delta z^2} \quad ; \tag{5.182}$$

$$c = 2\left(-\frac{1}{\Delta x^2} - \frac{1}{\Delta y^2} - \frac{1}{\Delta z^2} \right) \quad . \tag{5.183}$$

F includes rest of the terms which is a function of porosity.

5.4.2 Discretization of the Solid Wave Equations

Assuming the injected mass rate is constant and it is a point source then the solid wave equation reduces to

$$\rho_{\phi s} \frac{1}{\phi_o} \left(\frac{\partial^2 \phi}{\partial t^2} + 2a_{\phi s} \frac{\partial \phi}{\partial t} - \upsilon_{\phi s}^2 \nabla^2 \phi \right) = 0 \quad ; \tag{5.184}$$

$$\begin{aligned} &\frac{\phi_{i,j,k}^{n+1} - 2\phi_{i,j,k}^{n} + \phi_{i,j,k}^{n-1}}{\Delta t^2} + 2a_{\phi s} \frac{\phi_{i,j,k}^{n+1} - \phi_{i,j,k}^{n}}{\Delta t} \\ &\quad - \upsilon_{\phi s}^2 \left(\frac{\phi_{i+1,j,k}^{n+1} - 2\phi_{i,j,k}^{n+1} + \phi_{i-1,j,k}^{n+1}}{\Delta x^2} + \frac{\phi_{i,j+1,k}^{n+1} - 2\phi_{i,j,k}^{n+1} + \phi_{i,j-1,k}^{n+1}}{\Delta y^2} + \frac{\phi_{i,j,k+1}^{n+1} - 2\phi_{i,j,k}^{n+1} + \phi_{i,j,k-1}^{n+1}}{\Delta z^2} \right); \\ &\quad = 0 \end{aligned} \tag{5.185}$$

where

$$\begin{bmatrix} 0 & 0 & 0 \\ 0 & tc & 0 \\ 0 & 0 & 0 \end{bmatrix}$$
$$\begin{bmatrix} 0 & n & 0 \\ w & c & e \\ 0 & s & 0 \end{bmatrix} \quad \phi_{i,j,k}^{n+1} \quad = \quad F \quad ; \tag{5.186}$$
$$\begin{bmatrix} 0 & 0 & 0 \\ 0 & bc & 0 \\ 0 & 0 & 0 \end{bmatrix}$$

and where

$$tc = \frac{\upsilon_{\phi s}^2}{\Delta z^2} \quad ; \tag{5.187}$$

$$n = \frac{\upsilon_{\phi s}^2}{\Delta y^2} \quad ; \tag{5.188}$$

$$w = \frac{\upsilon_{\phi s}^2}{\Delta x^2} \quad ; \tag{5.189}$$

$$e = \frac{\upsilon_{\phi s}^2}{\Delta x^2} \quad ; \tag{5.190}$$

$$s = \frac{\upsilon_{\phi s}^2}{\Delta y^2} \quad ; \tag{5.191}$$

$$bc = \frac{\upsilon_{\phi s}^2}{\Delta z^2} \quad ; \tag{5.192}$$

$$c = -\frac{1}{\Delta t^2} - \frac{2a_{\phi s}}{\Delta t} - 2\upsilon_{\phi s}^2 \left(\frac{1}{\Delta x^2} + \frac{1}{\Delta y^2} + \frac{1}{\Delta z^2} \right) \quad . \tag{5.193}$$

5.5 Summary

In this chapter porosity wave equation, both for the solid and fluid, is derived. The process of derivation started with the basic equations, continuity equations, pressure equation, porosity equation and equation of motions. Terms as porosity, density, velocity and source, at a given time, are written as a function of deviations from unperturbed state. Using the definition of the fluid bulk modulus, pressure equation is derived from the solid and fluid continuity equations. Also, fluid and solid phase displacements as a function of pressure is derived to obtain solid dilation equation. Next, combining solid dilation equation with equations of motion (fluid and solid) wave equations, propagating solid and fluid, are developed. Finally, assuming incompressible limit, porosity wave equations are derived from wave equations. These equations relate porosity to fluid pressure. It is these equations which are coupled with fluid flow equations in BOAST to estimate effects of pressure pulsing on fluid flow. Coupling procedure will be discussed in the next chapter.

6 COUPLING GEOMECHANICS AND PRESSURE PULSES IN BOAST

6.1 Methodology

A diagram of the relation of the BOAST algorithm to the decoupled pressure pulsing and geomechanical model is presented in Figure 6-1. During each timestep, the pressure pulse subroutine (PPS) obtains the initial value of the pressure, saturation, porosity and fluid/solid properties from BOAST as input. It then solves the wave equations and calculates the pressure disturbance and the new porosity distribution as a result of the porosity wave propagation (dynamic porosity change). At the same time step, the BOAST algorithm solves for the pressure distribution due to static injection or production. The new reservoir pressure at the end of the timestep is then determined by adding the pressure disturbance from the PPS to the BOAST solution (Figure 6-3).

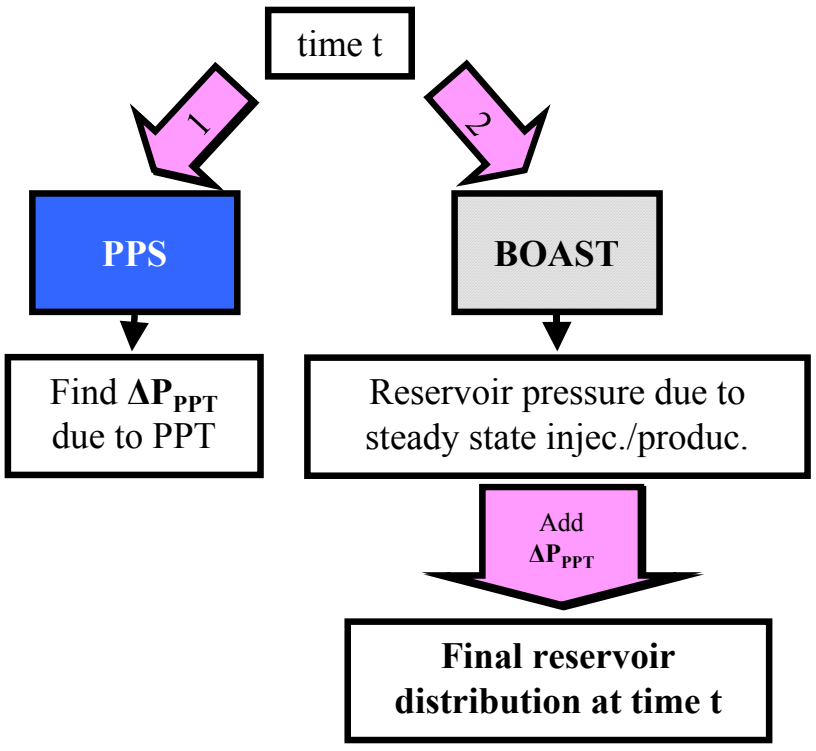

Figure 6-1: BOAST with Geomechanics and PPT Algorithm

PPS takes the initial value of phase pressures, phase saturations, porosity from BOAST, solves the wave equations and calculates the new porosity due to wave propagation. The equations required for this were presented in Chapter 5 (Pressure Pulse Equations). However, a mass source term, pulse source term and seismic source term should be included in the fluid continuity equation, fluid equation of motion and solid equation of motion, respectively.

Adding a mass source term, $\dot{m}$, in the fluid continuity equation gives

$$\frac{\partial(\phi\rho_f)}{\partial t} + \nabla\cdot\left(\phi\rho_f v^f\right) = \dot{m} \quad . \tag{6.1}$$

Having the mass source term, the pressure equation and solid dilation equation will be modified. Adding source terms, f_1 and f_2, into fluid and solid equations of motion:

$$\rho_f \frac{\partial}{\partial t} v_f = -\nabla P_f + \left[\mu_f \nabla^2 v_f + \left(\xi_f + 1/3\mu_f\right)\nabla\left(\nabla\cdot v_f\right)\right] + \frac{\xi_f}{\phi_o}\nabla\frac{\partial\phi}{\partial t} + \frac{(1-\phi_o)}{\phi_o}\mu_f\left(\frac{\mu_M}{(1-\phi_o)\mu_s} - 1\right); \\ \left[\nabla^2\frac{\partial u_s}{\partial t} + 1/3\nabla\left(\nabla\cdot\frac{\partial u_s}{\partial t}\right)\right] - \frac{\mu_f\phi_o}{K}\left(v_f - v_s\right) + f_1 \tag{6.2}$$

$$\rho_s\frac{\partial^2}{\partial t^2}u_s + \frac{\rho_{12}}{(1-\phi_o)}\frac{\partial}{\partial t}\left(v_f - v_s\right) = K_s\nabla\left(\nabla\cdot v_s\right) - \frac{K_s}{1-\phi_o}\nabla\phi + \frac{\mu_f\phi_o^2}{K(1-\phi_o)}\left(v_f - v_s\right) + \\ \frac{\mu_M}{(1-\phi_o)}\left[\nabla^2 u_s + 1/3\nabla\left(\nabla\cdot u_s\right)\right] + f_2 \tag{6.3}$$

Re-substituting the modified fluid continuity equation and solid dilation equation into these equations the new fluid and solid wave equations are developed.

Pressure pulsing causes a number of changes in fluid and solid properties which should be calculated along with pressure and porosity. Initially, pore is filled with water and oil, with initial saturations of S_1 and S_2 (1- S_1) for water and oil, respectively. Assuming that

all the porosity change will be filled by water, the initial saturations S_1 and S_2 are updated to modified saturations, S_1' and S_2'. It can be argued that not all of the new void space would be filled by water. However, assuming that the majority of the porosity disturbance occurs near the water injection wellbore, it is a valid assumption.

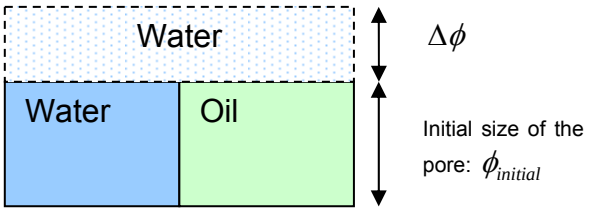

Figure 6-2: Diagram of the Relation of Increasing Porosity and Fluid Saturation

Redistribution of saturations in gridblocks will cause modifications in capillary pressures, the pressure difference between the phases. Capillary pressure is directly related to phase saturations. Using the equation developed by Spanos[21], capillary pressure is updated both for static pressure changes and dynamic changes.

$$\frac{\partial P_c}{\partial t} = -\beta \frac{\partial S_1}{\partial t} + \beta' \frac{\partial^2 S_1}{\partial t^2} \tag{6.4}$$

The first order time derivative of saturation in Equation (6.4) represents saturation changes due to pressure change across the porous media and the second order derivative represents dynamic changes due to acceleration effects, i.e. pressure pulsing. Ultimately the capillary pressure curves for each porosity-modified gridblock should be updated using Equation (6.4).

Changes in the porosity can drastically affect the absolute permeability of the porous medium. Various models exist for the porosity-permeability relationship with the

predicted permeability varying depending on the model selected. Rock permeabilities will be recalculated using Carmen-Kozeny equation and focus will be given to the sensitivity of parameters:

$$k_{abs} = k_o \frac{\phi^3}{(1-\phi)^2} \quad . \tag{6.5}$$

Relative permeabilities, which modify the absolute permeability in multi fluid system, will also be modified with the changes in the saturations. The relation of the relative permeability to saturations is given with the following equations [21]:

$$K_{11} = \frac{1}{R_\Delta} \frac{S_1^{\,2}}{R_{11}} \quad ; \tag{6.6}$$

$$K_{12} = \frac{1}{R_\Delta} \frac{R_{12}}{R_{11}} \frac{S_1 S_2}{R_{22}} \quad ; \tag{6.7}$$

$$K_{21} = \frac{1}{R_\Delta} \frac{R_{21}}{R_{22}} \frac{S_1 S_2}{R_{11}} \quad ; \tag{6.8}$$

$$K_{22} = \frac{1}{R_\Delta} \frac{S_2^{\,2}}{R_{22}} \quad . \tag{6.9}$$

The injectivity of the well is directly related to formation porosity and permeability. When changing the porosity the new injection rate is calculated.

$$\nabla \frac{\bar{K}\lambda_w}{B_w} \nabla P_o - \nabla \frac{\bar{K}\lambda_w}{B_w} \nabla \left(\frac{\rho_w z}{144} + P_{COW} \right) + \frac{q_w}{\rho_{wsc}} = \frac{\partial}{\partial t} \left(\frac{\phi S_w}{B_w} \right) \quad . \tag{6.10}$$

The porosity change, ϕ, in the right hand side of Equation (6.10) requires pressure change, ∇P_o, or injection rate change, q_w, on the left hand side. As the pressure difference between across the porous media is assumed constant in pressure, only the injection rate will be modified.

As discussed above, after modifying saturations, porosity and injection rate, PPS then submits these modified values to BOAST to solve pressures and saturations at the next time step. In addition to this, porosity will again be updated with geotechnical coupling.

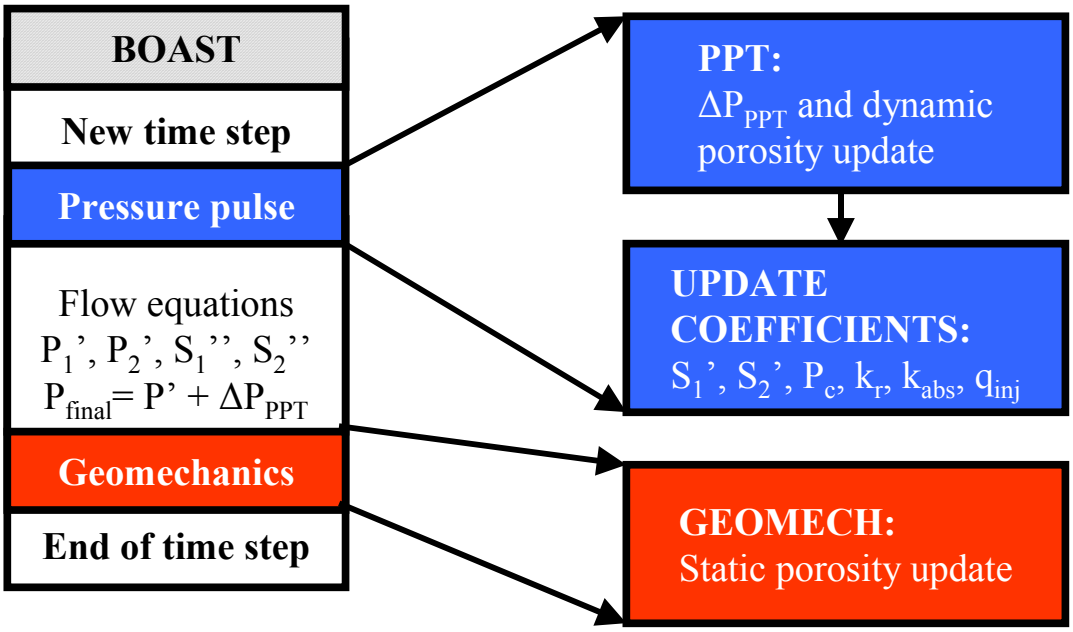

Figure 6-3: PPT and BOAST

6.2 A 1D Validation of the Pressure Pulse Model

The pressure pulse model was validated against the results of laboratory core flood tests conducted by Davidson, et al.[3]. A schematic of the laboratory setup used by these researchers is shown in Figure 6-4.

In these tests a cylindrical cell with a diameter of 6 cm and a length of 30 cm was used. Sand was poured into the cell, compacted using vibrodensification and sealed. A 1 MPa axial stress was then applied to the dense sand pack through a piston. The cell was equipped with pressure transducers along the axis of the cylinder. All walls were impermeable (no flow boundary condition) and the entry regions in the cylindrical cell were small in order to ensure the flow was one-dimensional along the axis of the cylinder.

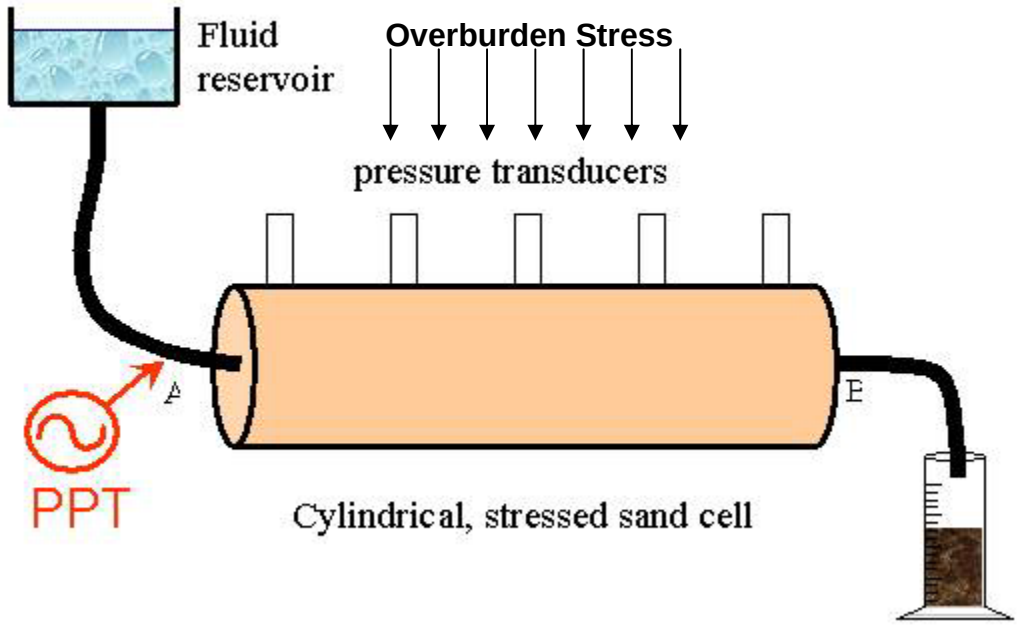

Figure 6-4: Experimental setup used in the pressure pulse test of Davidson, et al. [3]

In this particular experiment, ~35% porosity and 5-8 D permeability sand was used. The sand was initially saturated with 35 cP oil and displaced with water. Initially a constant head delta P, 0.35 psi, was established across the cell and flow was allowed to come to a

steady state rate. The sand pack was then excited by pressure pulsing near the inlet port every 1.5-2 sec, typically for 3-7 minutes. Pulsing was stopped for a similar interval, started again, and a number of cycles were carried out followed by a quiet period without excitation.

Excitation of the porous medium was created by a sudden manual squeeze or impact with a hammer on the inlet tube just before the inlet port. The impulse entered the porous medium and was converted largely to a porosity diffusion wave that was accompanied by a small pressure change. Because there was no change in the reservoir and exit tube level, the macroscopic pressure change across the cell remained constant while the short term impulses were applied periodically for several minutes.

Figure 6-5 shows the experimentally measured results from monitoring three pressure transducers, "A", "B" and "C", at different locations along the axis of the cylindrical cell. The y-axis represents the measured pressure difference between the inlet and the location of the pressure transducer. At the transducer just adjacent to the inlet orifice ("A"), there is a sharp pressure accumulation occurring with each pulse. This continues with time but begins to increase less rapidly until pulsing is stopped, at which point the system almost immediately enters into a classical pressure decay response. The next two transducers, "B" and "C", each successively further from the inlet orifice, showed a slower response and a delayed peak pressure. This occurred as the "pressure bulb" diffused along the cylinder axis even after excitation ceased.

In order to mimic this laboratory experiment, a 1D simulation model was constructed. The model consisted of 262 gridblocks in the x dimension with each gridblock measuring 0.2 ft in the x, y and z directions. A large number of gridblocks were used in order to eliminate pressure build up due to boundary effects. The porosity was 35% and permeability was 5 D. The model was saturated with 35 cP oil at an initial pressure of 1 MPa and was then displaced with water.

This model was then simulated using the pressure pulse model developed in this work. Flow within the model was allowed to come to steady state after which pulsing began at six minutes and continued for five minutes.

Figure 6-6 shows the pressure response predicted by this simulation. The x axis is in terms of 1/6 minutes and the y axis is the pressure difference between the inlet and the measured point. Three different measured points were examined similar to the three tranducers used in the experimental apparatus: "P1" represented a point near the injection point while "P2" and "P3" were each successively further away from the inlet.

A comparison of Figure 6-5 and Figure 6-6 shows that there is good agreement between the lab data and the simulation result. The predicted pressure increase at each point in the porous medium is nearly identical to the measured results. Additionally, the maximum pressure at each point, labelled "2", "3" and "4" in Figure 6-5 ("1" denotes the onset of pulsing), is reached at the same time in both the simulated and measured results.

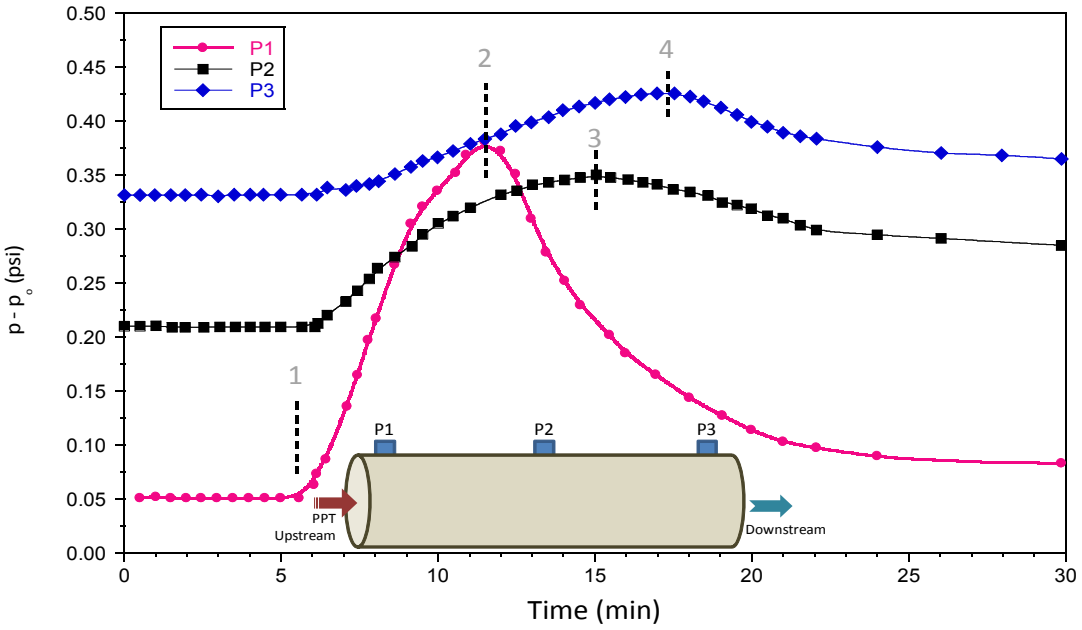

Figure 6-5: Experimentally measured pressure drops at three locations in the porous medium (reproduced from the work of Davidson, et al.[3]).

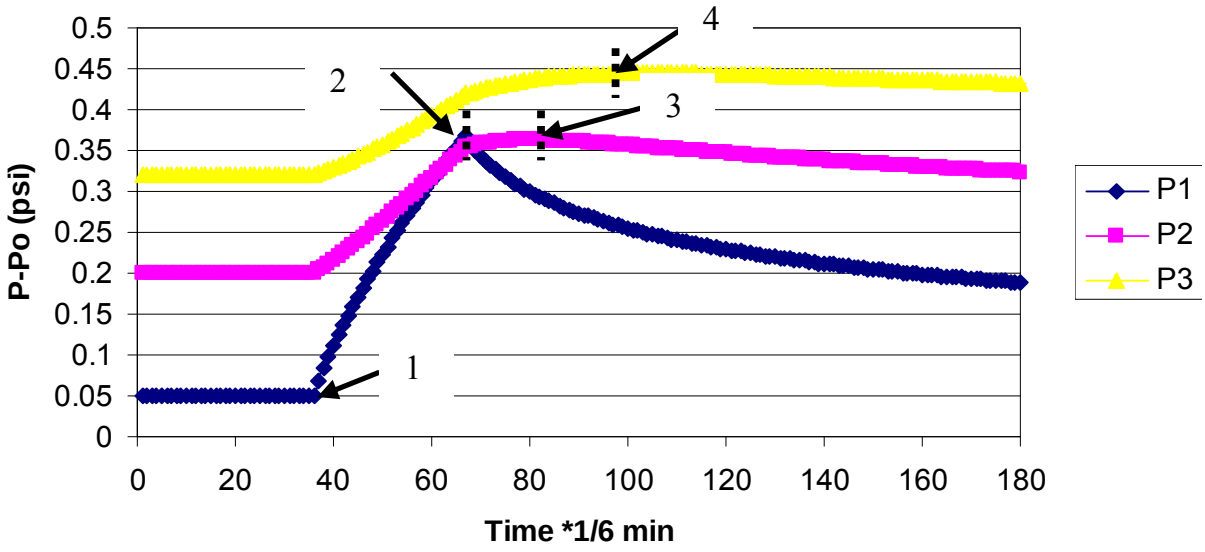

Figure 6-6: Predicted pressure drops at three locations in the porous medium

Additionally, Figure 6-7 and Figure 6-8 show the experimentally measured and the simulated production volumes, respectively. In each figure two curves are shown: one resulting from a test with a steady state flowrate and the other with the added effects of pressure pulsing. Again, good agreement is seen between the measured and simulated results. After 30 minutes of flow, the experimentally measured produced volume is around 100 cc while the results of the simulation using the PPT model show a total produced volume of around 95 cc. The produced volume using the steady state injection rate was around 70 cc for both the experiment and the simulation. The incremental recoveries for lab and simulation are, 43% and 36%, respectively.

This good agreement between measurements and simulated results validated the pressure pulse model.

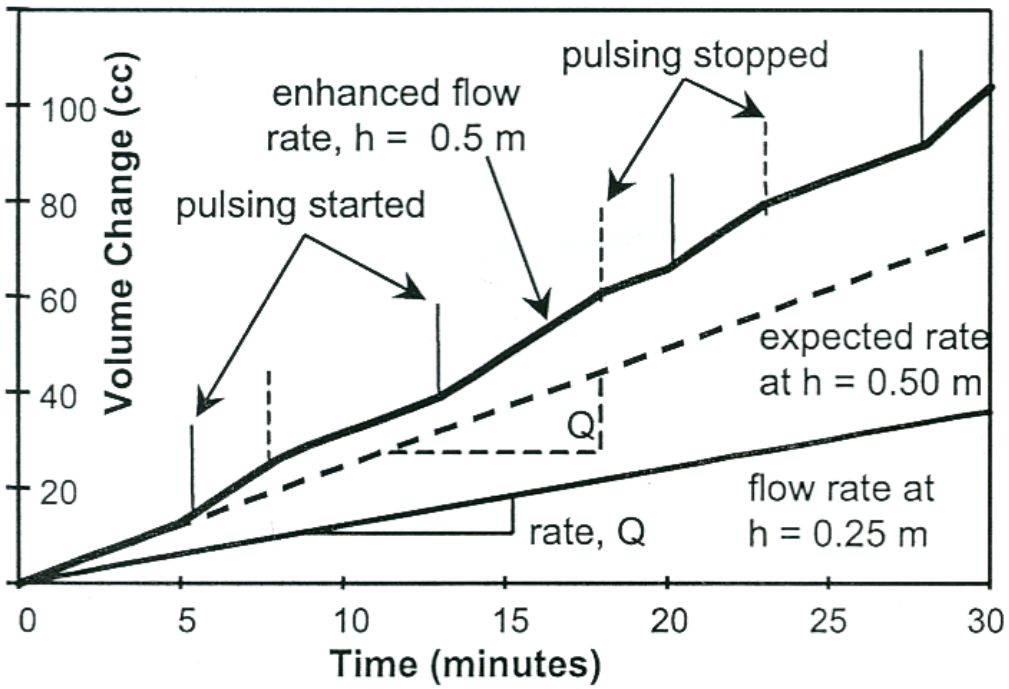

Figure 6-7: Experimentally measured cumulative production for cases with and without pressure pulsing (reproduced from the work of Davison, et al.3)

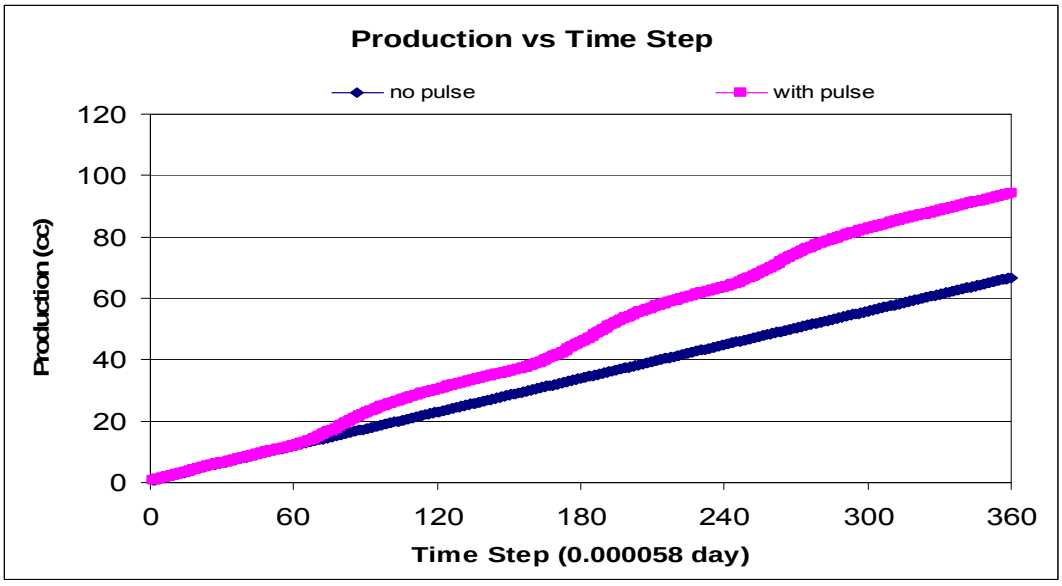

Figure 6-8: Predicted cumulative production for cases with and without pressure pulsing

An additional set of experimental results was compared to simulation results in order to provide a second independent validation of the pressure pulse code developed in this work. Details can be found in Appendix B.

6.3 Validation of the 3D Geomechanics Model

The geomechanics model presented in an earlier section of this work and implemented into the code was then validated versus previous studies. For this an oil reservoir was simulated using the model by two different approaches. In the first approach (Case 1) the reservoir permeability was assumed to be a function of only the pore pressure (the total stress being constant) while in the second (Case 2) the reservoir permeability was considered to be a function of both the pore pressure and total stress. The results of these simulations were then compared to the work of J.G. Osario, et al. [63, 68]

The discretized grid used in each approach consisted of 65 blocks with 300 ft grid spacing in each of the x and y directions and 25 blocks with 40 ft grid spacing in the z direction. The grid was divided into an inner domain representing the reservoir and an outer domain representing the boundary. The inner domain consisted of gridblocks 27 through 39 in the x and y directions and gridblocks 11 through 15 in the z direction (i.e., the ratio of the outer:inner:outer domain in each direction is 2:1:2). One well was producing from layers 11 through 15 at a constant flow rate of 1,500 STB/D. The initial reservoir pore pressure and total vertical stress were 7000 psia and 9000 psia, respectively. The ratio of initial total stress in the both x and y directions to the initial total stress in the z direction was 0.9. Other parameters of this model are presented in Table 6.1.

Table 6.1: Additional parameters used in simulations validating the geomechanics model

Bulk compressibility in the outer domain, 1/psi	2.5×10^{-6}
Shear modulus in the outer domain, psi	3.0×10^{5}
Solid compressibility, 1/psi	1.0×10^{-7}
Dt, days	100
Reference layer	11
Oil, API	35.8
Bubble Point pressure, psi	1200
Solution gas-oil ratio, SCF/STB	238
Initial porosity	0.3

Non-deformable lateral and bottom boundaries and constant vertical stress on the top boundary were used as boundary conditions[63,68].

These parameters were used to calculate the mean effective stress on the model porous medium at different times and locations. Then using Figure 6-9, Figure 6-10, and Figure 6-11 (reproduced from the work of Osorio[68]) the bulk compressibility, shear modulus initial permeability of the porous medium were determined.

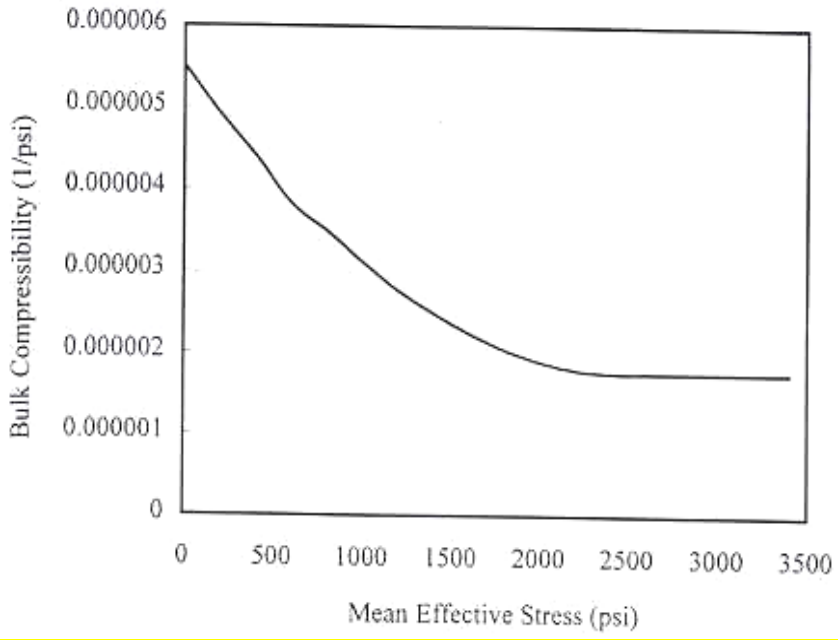

Figure 6-9: Bulk compressibility versus mean effective stress (Osorio[68])

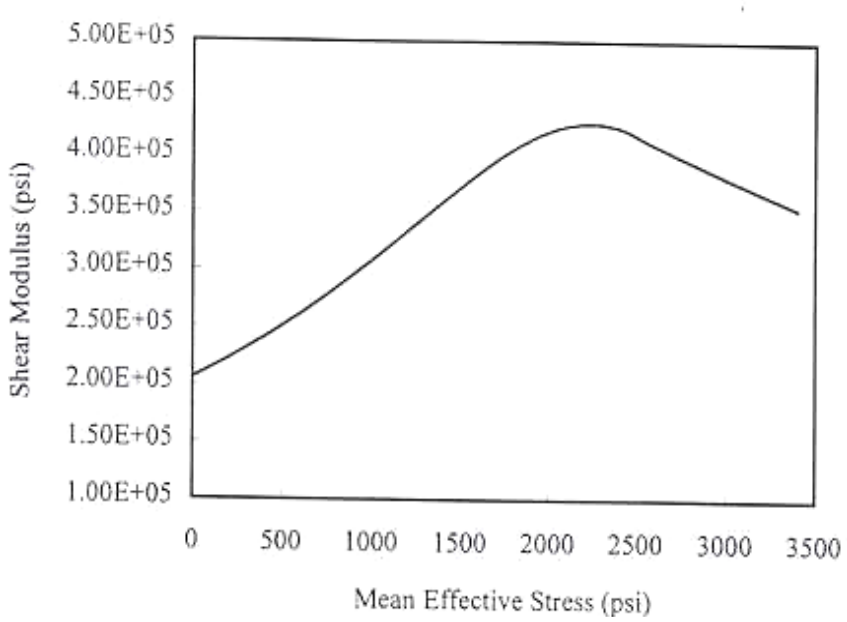

Figure 6-10: Shear modulus versus mean effective stress (Osorio[68])

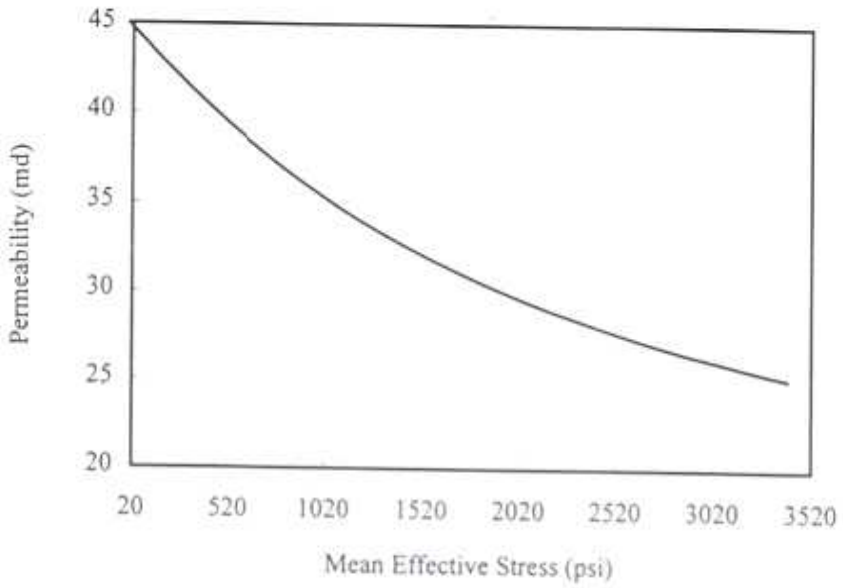

Figure 6-11: Permeability versus mean effective stress (Osorio[68])

Figure 6-12 and Figure 6-13 show the PPT-BOAST simulated permeability distribution at the intersection of the mid layer and the vertical plane containing the well after 100, 500, 1000, 2000, 3000 and 4000 days of production for Cases 1 and 2, respectively. As can be seen in these figures, the permeability reduction is greater when the permeability is assumed to be function of only the pore pressure (Case 1) than when it is considered to be a function of both the pore pressure and total stress (Case 2). This result is confirmed when considering that as pore pressure declines with time, the total stress on the porous medium should also decrease. For Case 1, holding the total stress constant leads to a calculated mean effective stress that is greater than that for Case 2. As shown in Figure 6-12, this greater mean effective stress leads to a greater reduction in the reservoir permeability.

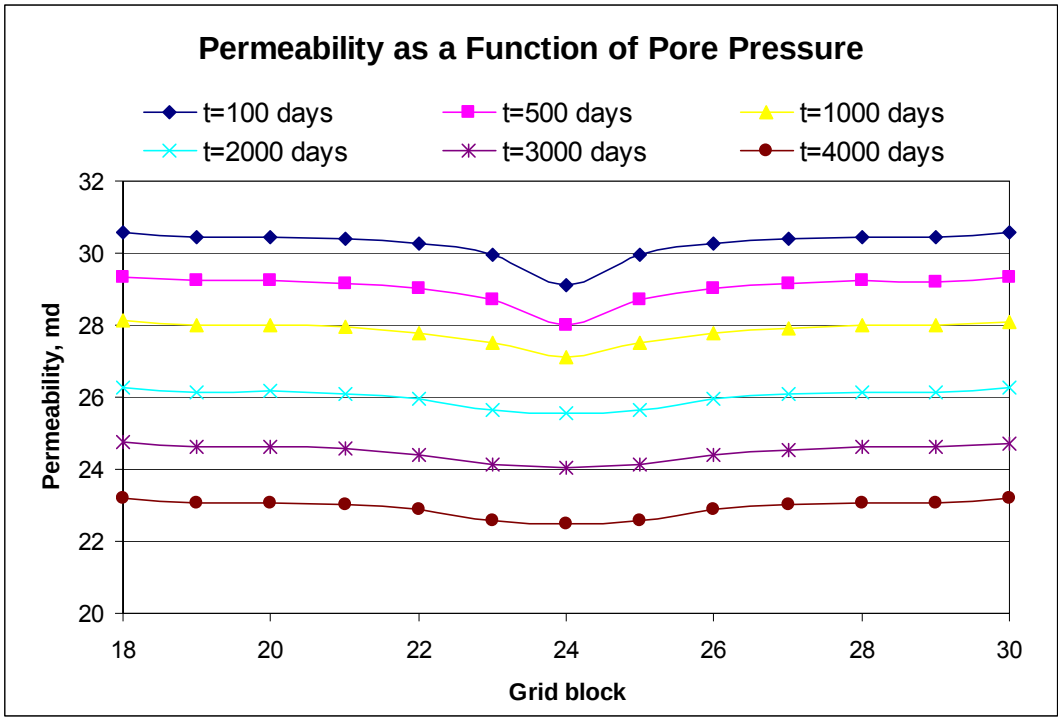

Figure 6-12: Predicted permeability profile at various times for Case 1 (permeability is a function of only pore pressure)

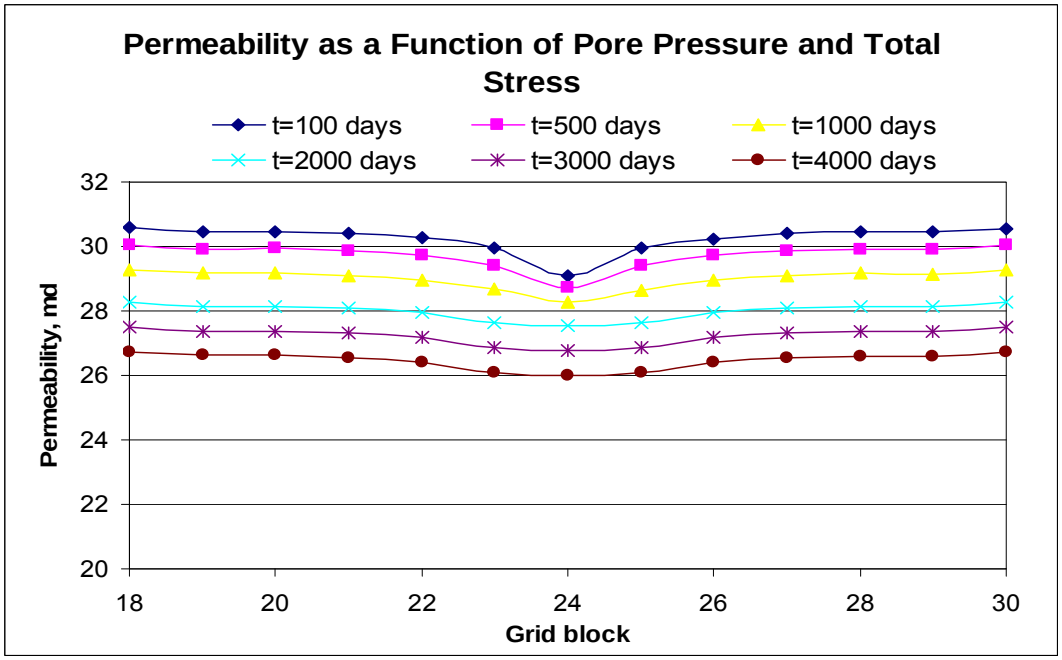

Figure 6-13: Predicted permeability profile at various times for Case 2 (permeability is a function of both pore pressure and total stress)

This result agrees with Osorio's results as shown in Figure 6-14 and Figure 6-15.

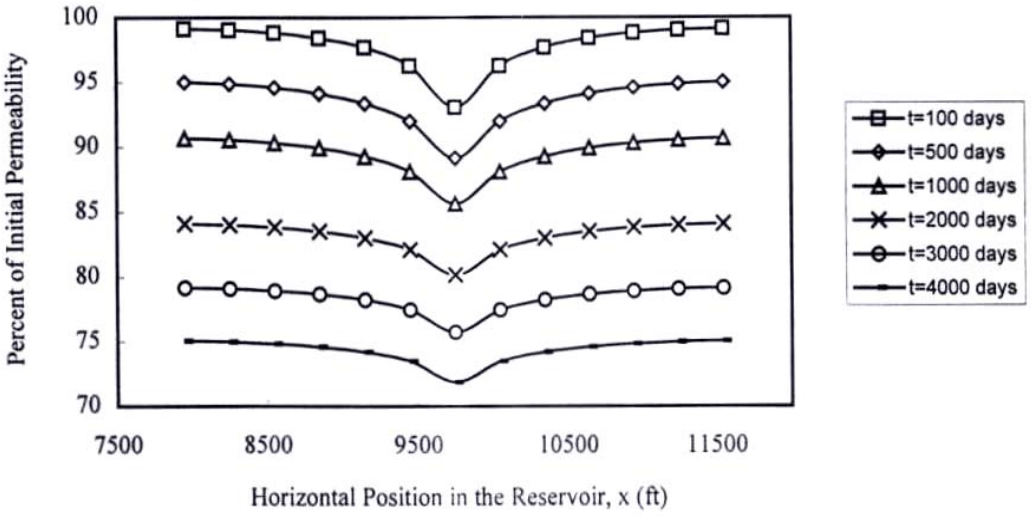

Figure 6-14: Predicted permeability profile at various times and where permeability is a function of only pore pressure (reproduced from Osorio)

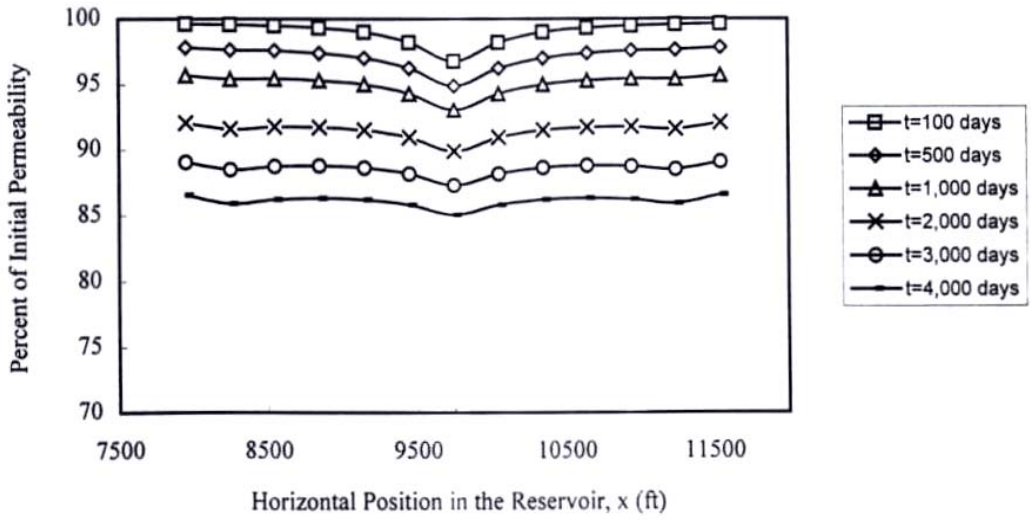

Figure 6-15: Predicted permeability profile at various times and where permeability is a function of both pore pressure and total stress (Osorio[68])

6.4 Sensitivity Analysis of the Geomechanics Model

A sensitivity analysis was performed to examine the effects of four variables of the geomechanics model on the predicted permeability behaviour. These four variables were: 1- Outer boundary conditions, 2- Layer locations with respect to the layer boundary, 3- The elastic moduli of the outer domain, and 4- Using a single domain instead of a two-domain model.

6.4.1 Outer Boundary Conditions

Three different sets of boundary conditions were investigated:

Case 1: Non-deformable lateral boundaries (zero incremental displacement) and constant vertical stress on the top and bottom boundaries equal to the overburden and underburden, respectively (zero incremental stress).

Case 2: Non-deformable lateral and bottom boundaries (zero incremental displacement) and constant vertical stress on the top boundary equal to the overburden (zero incremental stress).

Case 3: Non-deformable bottom boundary (zero incremental displacement), zero incremental horizontal displacements on the lateral boundaries and constant vertical stress on the lateral and top boundaries.

Figure 6-16 shows the permeability reduction at the intersection of mid layer and the vertical plane containing the well after 300 and 4000 days of production while Figure 6-17 shows the same information for the upper and lower layers. The results presented in these figures indicate that the set of boundary conditions associated with Case 2 and Case 3 yield the same permeability reduction. However, the boundary conditions of Case 1 yield a greater permeability reduction than the boundary conditions of Cases 2 and 3. This difference is insignificant at early times, but increases as production time increases.

This result indicates that for cases with non-deformable boundaries, less compaction occurs due to decreases in reservoir pressure. This results in a lower reduction in the reservoir permeability versus cases with deformable boundaries.

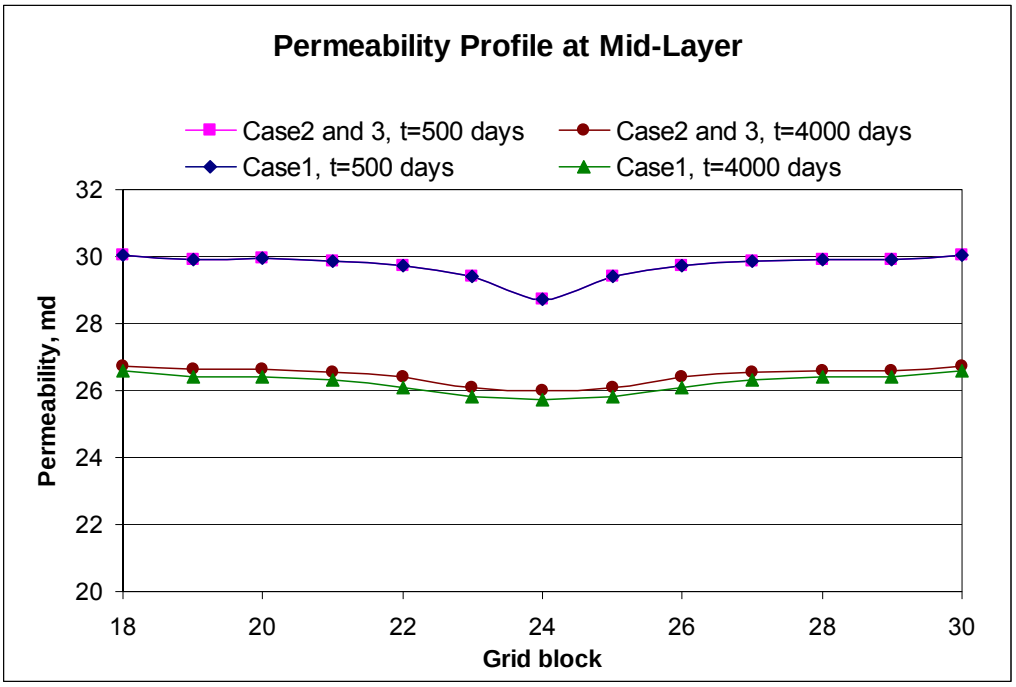

Figure 6-16: Predicted permeability profile at the intersection of mid layer with the vertical plane containing the well after 500 and 4000 days of production for Cases 1, 2, and 3

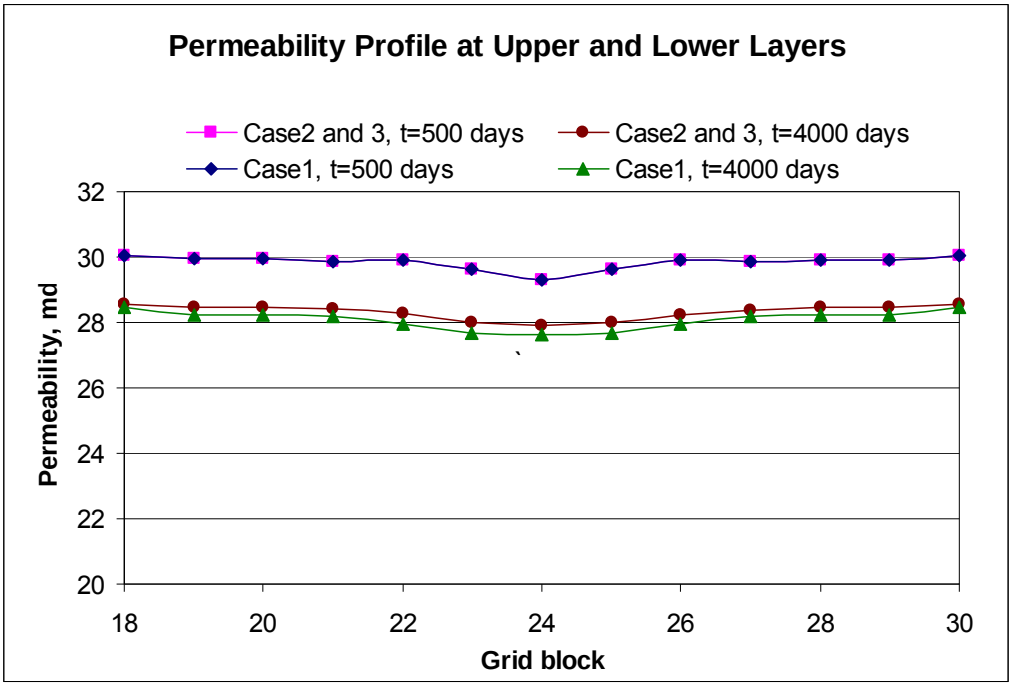

Figure 6-17: Predicted permeability profile at the intersection of the upper and lower layers with the vertical plane containing the well after 500 and 4000 days of production for Cases 1, 2, and 3

6.4.2 Layer Locations with Respect to the Layer Boundary

Figure 6-16 and Figure 6-17 also show that for each of the boundary condition cases, the reduction is the permeability is maximized at the middle layer. The explanation for this behaviour may be that the rock deformation is at its maximum in the mid-layer, where fluid flow occurs in all directions, and at a minimum in the upper and lower layers, where fluid flow is constrained by the non-permeable layers of the outer domain. This argument can be proved by examining the volumetric strains at the intersection of the middle, upper and lower layers with the vertical plane containing the well. Figure 6-18 clearly shows the volumetric strain is at its maximum at the mid-layer and minimized at the upper and lower layers.

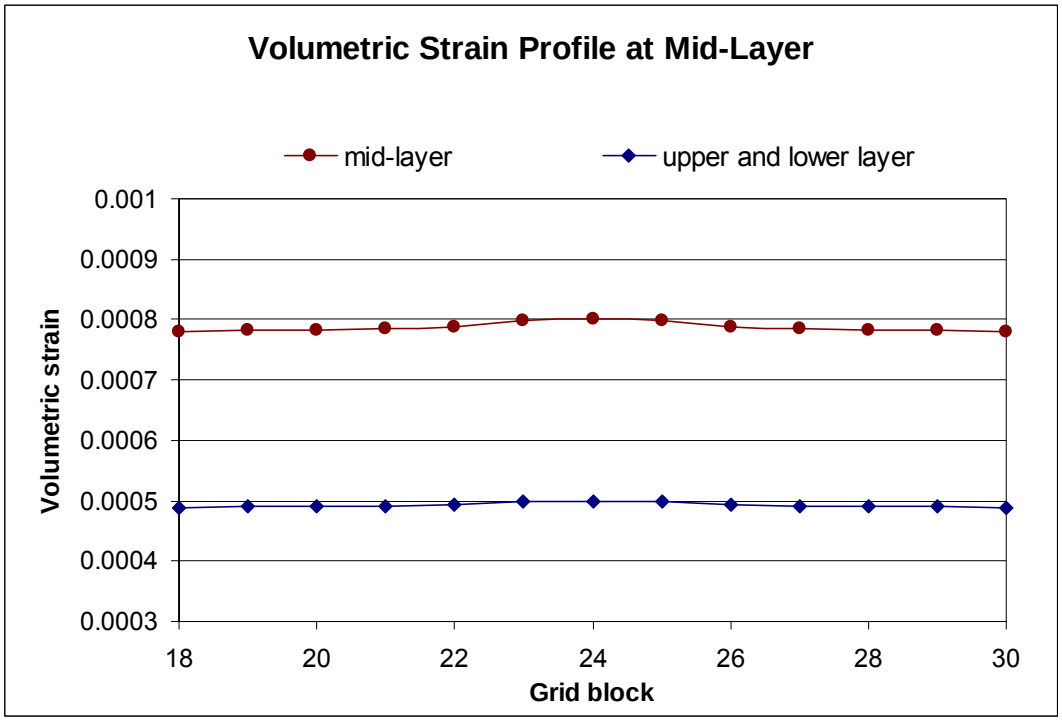

Figure 6-18: Predicted volumetric strain profile at the intersection of the mid layer and the upper and lower layers with the vertical plane containing the well

6.4.3 Elastic Moduli of the Outer Domain

The effect of the outer boundary conditions on the reservoir permeability depends upon the mechanical properties of the rock in the outer domain. This effect can be observed by varying the Young's modulus (E_o) of the outer domain. Figure 6-19 shows the permeability profile at the intersection of the mid-layer with the vertical plane containing the well for two cases where the Young's modulus equalled 72,000 psi and 720,000 psi. In this figure, the permeability is examined for each case at 500 and 4000 days.

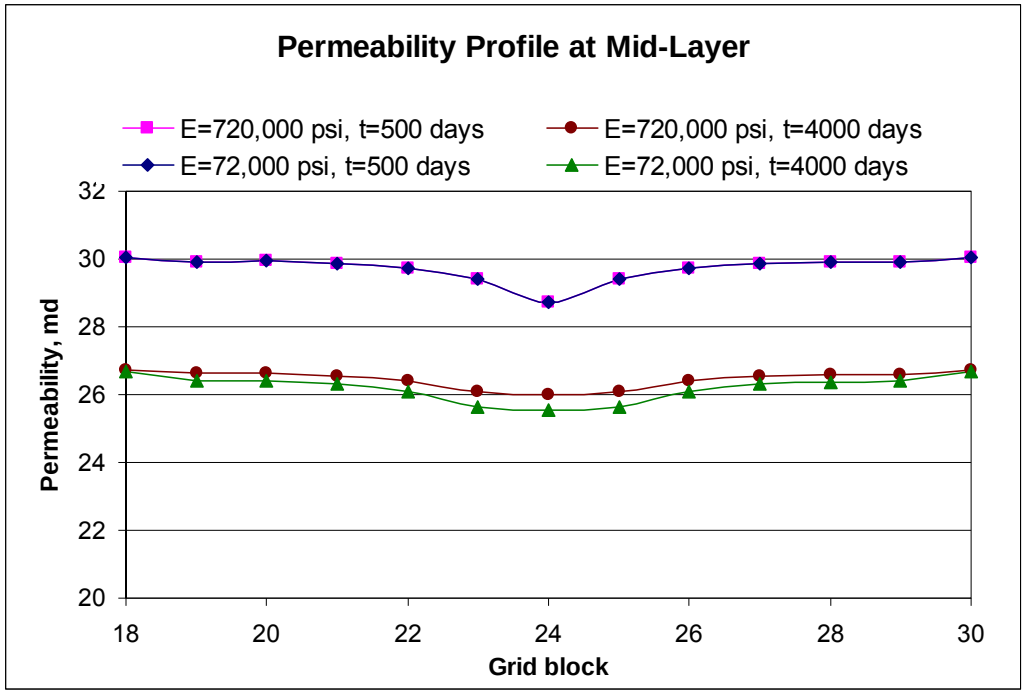

Figure 6-19: Predicted permeability profile at the intersection of the mid layer with the vertical plane containing the well after 500 and 4000 days of production for Young's moduli of 72,000 and 720,000 psi

These results indicate that the reservoir permeability decreases less with time as the rock elastic moduli of the outer domain increases. This behaviour is a reflection of the fact that the higher the Young's modulus, the lower the ability of the outer domain to deform. As the outer domain loses its ability to deform, it imparts less compaction on the reservoir and therefore less reduction in the reservoir permeability.

6.4.4 Using a Single Domain Instead of a Two-Domain Model

The inclusion of the outer domain dramatically increases both the computer storage requirements and program execution time. This issue raises the question of how much the solution would change if the outer domain were not included in the model.

Figure 6-20 and Figure 6-21 show the permeability profile at the intersection of the mid-layer and the vertical plane containing the well as a function of time. The curves in Figure 6-20 were obtained by solving the governing equations for the inner domain only

while the curves in Figure 6-21 were obtained by running the model including both the inner and the outer domains. For the purpose of comparison, both figures were plotted on same scale. When the inner and outer domains are taken into account, the geomechanical boundary conditions are applied far from the reservoir boundaries. When only the inner domain is simulated, the geomechanical boundary conditions must be applied at the reservoir boundaries.

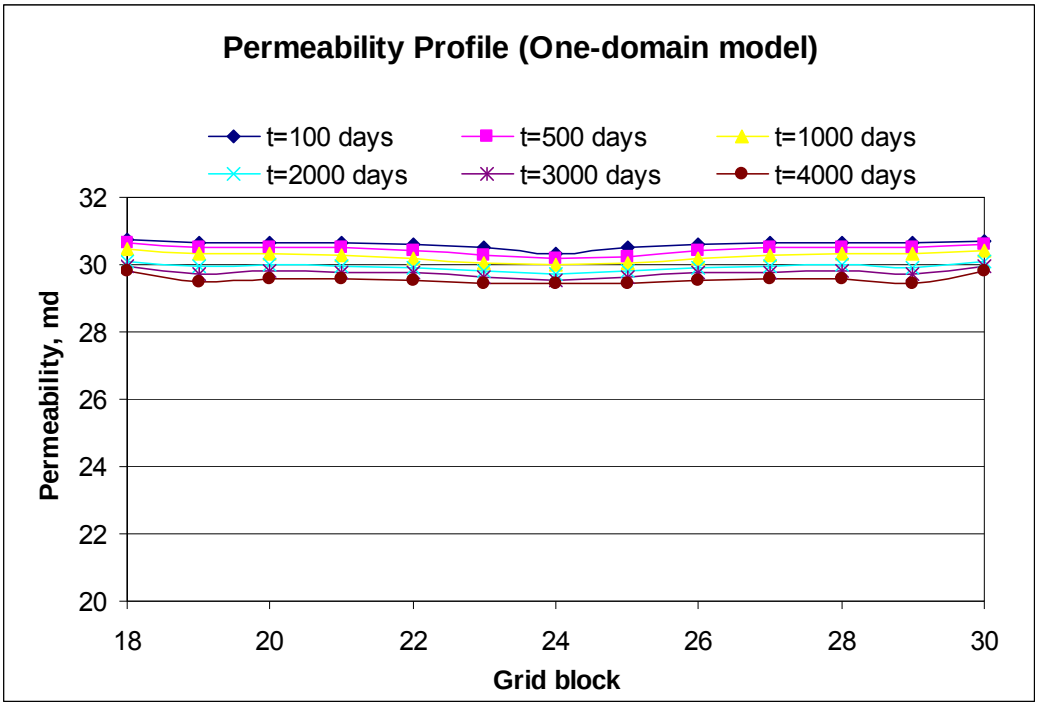

Figure 6-20: Predicted permeability profile at the intersection of the mid layer with the vertical plane containing the well for various times for a one domain model

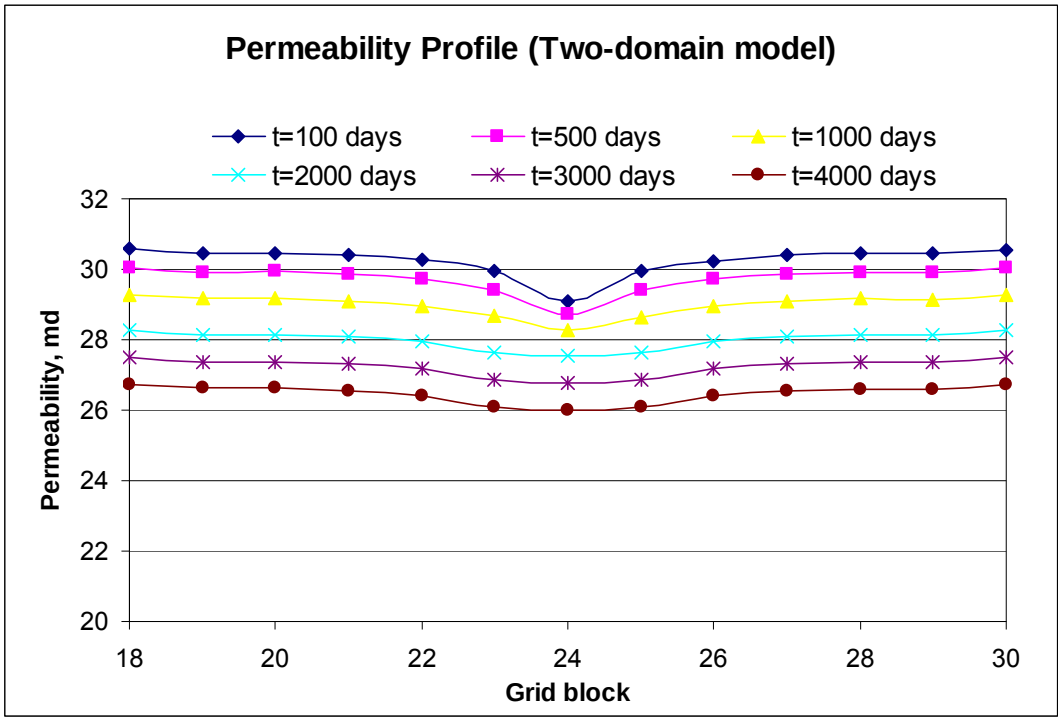

Figure 6-21: Predicted permeability profile at the intersection of the mid layer with the vertical plane containing the well for various times for a two domain model

Figure 6-20 and Figure 6-21 clearly show that the permeability profile curves obtained from the two-domain and the single-domain models differ considerably. At all times, the two-domain model yields a greater change in the permeability profile with time versus the single-domain model. This behaviour can be explained by the fact that as the pore pressure at the reservoir boundaries declines, the geomechanical conditions at the reservoir boundaries change in two ways: 1) incremental displacements at the boundaries become different than zero, and 2) due to rock expansion or compression, the local stress state at the boundaries may vary with time. These reservoir boundary deformation effects included in the two-domain model but not in the single-domain model are translated into an extra permeability decrease.

6.5 Sensitivity Analysis of the Pressure Pulse Model

As can be seen in the pressure pulse theory development section, the most important parameters in determining the porosity and pressure profiles are:

porosity's fluid attenuation: $$a_{\phi f} = \frac{1}{2}\frac{\mu_f \phi_o}{K\rho_{\phi f}}(\alpha_\phi + 1) \quad ; \tag{6.11}$$

porosity's bulk attenuation: $$b_{\phi f} = \frac{2}{3}\frac{(\mu_f + \sigma_M \alpha_\phi)}{\rho_{\phi f}} \quad ; \tag{6.12}$$

porosity's solid attenuation: $$a_{\phi s} = \frac{1}{2}\frac{\mu_f \phi_o^2}{K(1-\phi_o)}\frac{(\alpha_\phi + 1)}{\rho_{\phi s}} \quad ; \tag{6.13}$$

porosity's solid wave speed: $$\upsilon_{\phi s}^2 = \frac{K_\phi}{\rho_{\phi s}} \quad . \tag{6.14}$$

According to the derivations presented in Chapter 6, these parameters are functions of the following reservoir and fluid properties: (1) Permeability, (2) Viscosity, (3) Porosity, (4) Rock compressibility, and (5) Pulse frequency.

In order to investigate how these reservoir and fluid properties affect the impact of pressure pulsing on the reservoir pressure and production, over 50 simulation cases were run. The base model used in this study had a grid size of 262×11×11 gridblocks with each grid block measuring 0.2 ft in each direction. Initially a constant head pressure drop was established across the model and the flow was allowed to come to a steady state rate. Pressure pulsing was then applied at times 6, 15 and 22 minutes near the inlet port every 1.5-2 sec for 3 minutes. Each of these three cycles was then followed by a quiet period without excitation.

Volumetric strain was used as a wellbore boundary condition (source). One can define the pulse tool and amplitude in terms of pressure and convert this into volumetric strain. However, for the sake of simplicity, the reservoir is decoupled from the wellbore and the

strain is taken as a pulse source. The size of the pulse is represented by $8x10^{-5}$ pore volumes per timestep. Other inputs are shown in Table 6.2.

Table 6.2: Input data for sensitivity analysis

Parameter	Value*	Parameter	Value*
α_ϕ	1 (I)	λ_s	0.05 (I)
α_p	0.1 (I)	μ_s [GPa]	2.3×10^{10} (I)
$a_{\phi s}$, Q^{-1}	48.5×10^{3} (C)	μ_f [GPa]	0.001 (I)
a_{ps}, Q^{-1}	-21.8×10^{4} (C)	μ_m [GPa]	1.7×10^{10} (C)
$a_{\phi f}$, Q^{-1}	30×10^{4} (C)	ρ_s, kg/m^3	2650 (I)
a_{pf}, Q^{-1}	13.5×10^{4}	ρ_f, kg/m^3	1000 (I)
b_{ps}, Q^{-1}	0.0 (C)	ρ_{12}, kg/m^3	0 (I)
$b_{\phi s}$, Q^{-1}	0.0 (C)	$\rho_{\phi s}$, kg/m^3	2650 (C)
b_{pf}, Q^{-1}	2×10^{-6} (C)	ρ_{ps}, kg/m^3	265 (C)
$b_{\phi f}$, Q^{-1}	7.4×10^{7} (C)	$\rho_{\phi f}$, kg/m^3	1000 (C)
δ_s	0.27 (C)	ρ_{pf}, kg/m^3	1000 (C)
δ_f	0.03 (C)	σ_m, Pa	1.2×10^{-4} (C)
ϕ_o	0.3 (I)	$V_{\phi f}^2$, m^2/s^2	0.0 (C)
K_s, Pa	3.3×10^{10} (I)	v_{pf}^2, m^2/s^2	2.2×10^{6} (C)
K_f, Pa	2.2×10^{9} (I)	$V_{\phi s}^2$, m^2/s^2	1.9×10^{6} (C)
K, mD	1000 (I)	v_{ps}^2, m^2/s^2	2.5×10^{6} (C)
K_ϕ, Pa	5.1×10^{10} (C)	ξ_f, Pa	0.0028 (I)
K_m, Pa	6.5×10^{10} (C)		

* I = input variable, C = computed variable

One should be cautious when interpreting the sensitivity results from this small-scale model. The models should be scaled up appropriately to investigate field scale recoveries and sensitivities. Additionally, the field scale frequency, pulse duration, and amplitude will likely be different than the ones applied at the lab scale.

6.5.1 Permeability Sensitivity

In order to investigate the impact of permeability on the pressure pulsing process, nine simulation cases were run with isotropic permeabilities of 7000 mD (Run1), 5000 mD (Run2), 3000 mD (Run3), 1000 mD (Run4), 500 mD (Run5), 300 mD (Run6), 200 mD (Run7), 100 mD (Run8) and 50 mD (Run9). In each of these cases, the fluid viscosity

was 2000 cP, the porosity was 35%, the rock compressibility was 3×10^{-6} psi^{-1} and the pulse frequency was 0.25 Hz.

Figure 6-22 to Figure 6-30 show the cumulative production volume results for Runs 1 to 9, respectively. In each figure, one curve shows the predicted volumes from a case with steady-state injection while the other shows the effects of adding pressure pulsing. The plots show that pressure pulsing increased the production in each case.

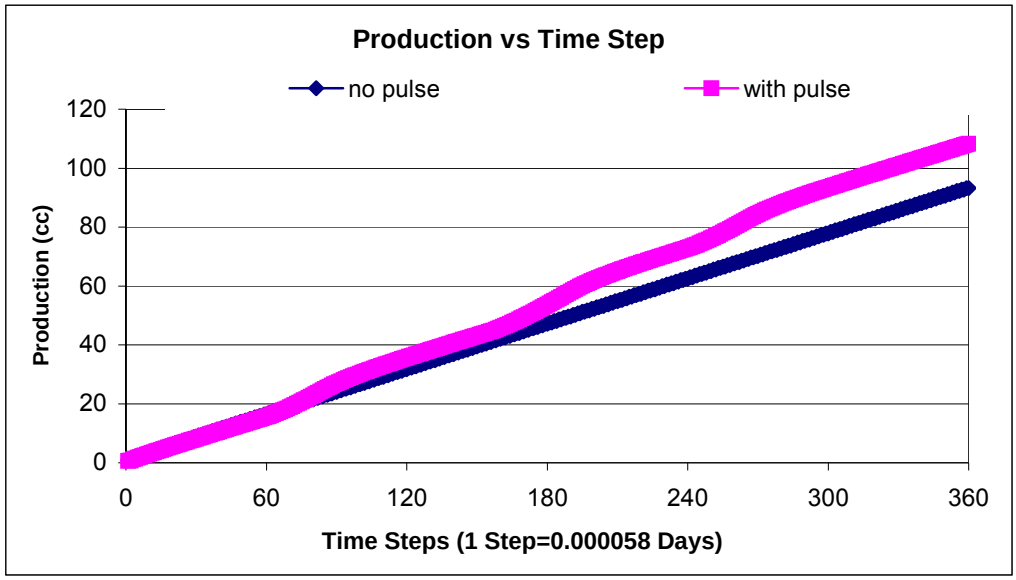

Figure 6-22: Predicted cumulative production for cases with and without pressure pulsing for a model with a permeability of 7000 mD (Run1)

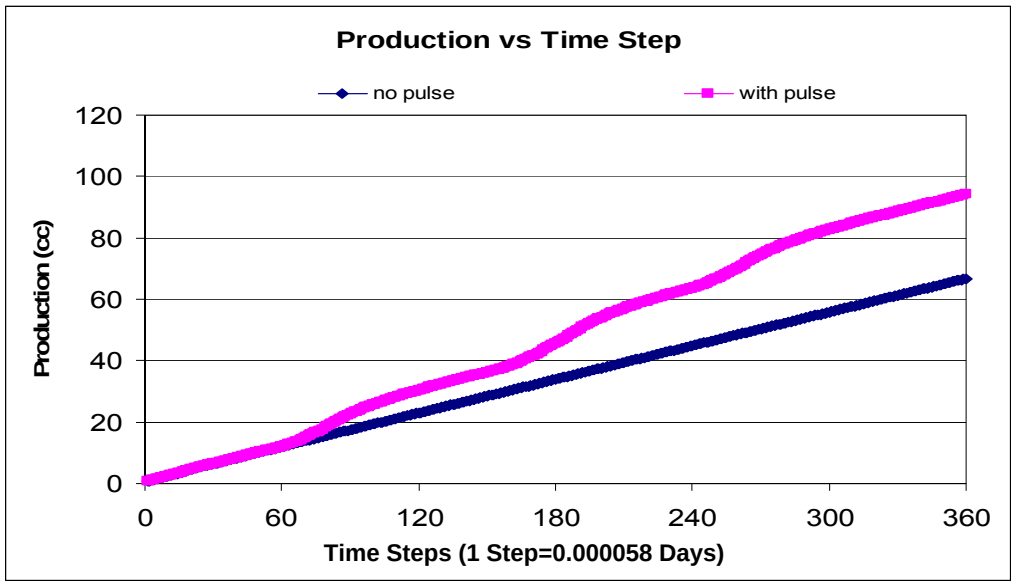

Figure 6-23: Predicted cumulative production for cases with and without pressure pulsing for a model with a permeability of 5000 mD (Run2)

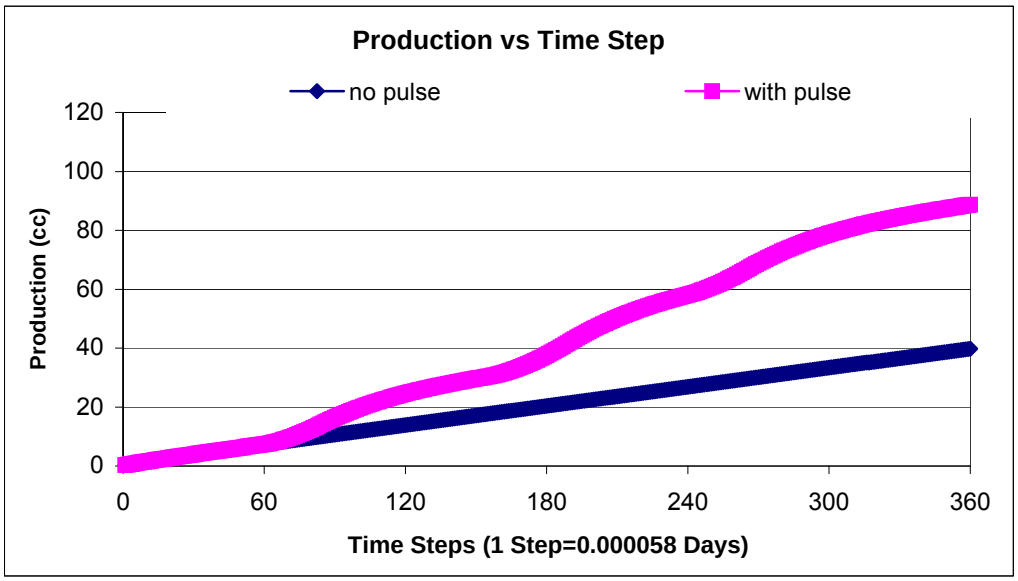

Figure 6-24: Predicted cumulative production for cases with and without pressure pulsing for a model with a permeability of 3000 mD (Run3)

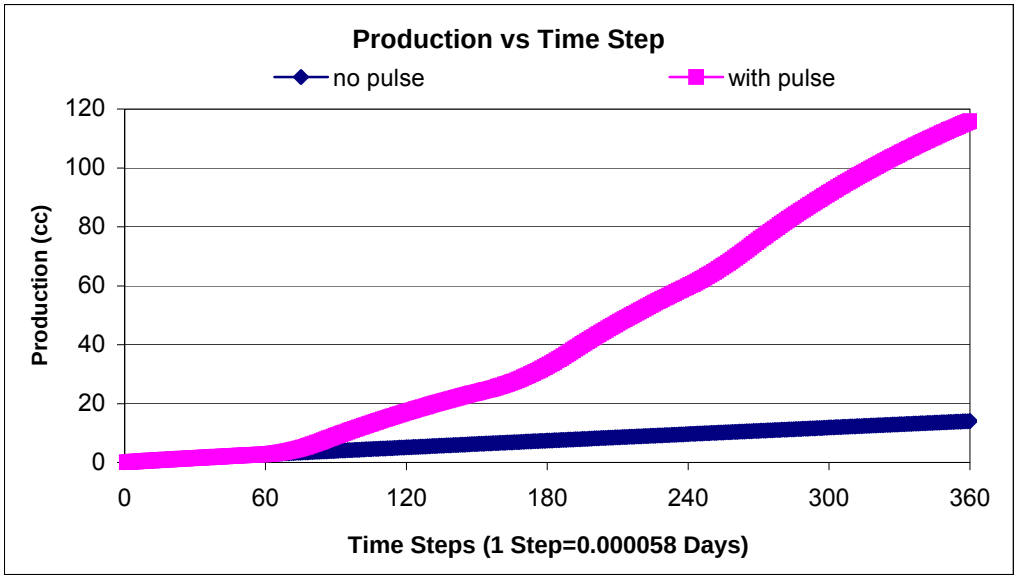

Figure 6-25: Predicted cumulative production for cases with and without pressure pulsing for a model with a permeability of 1000 mD (Run4)

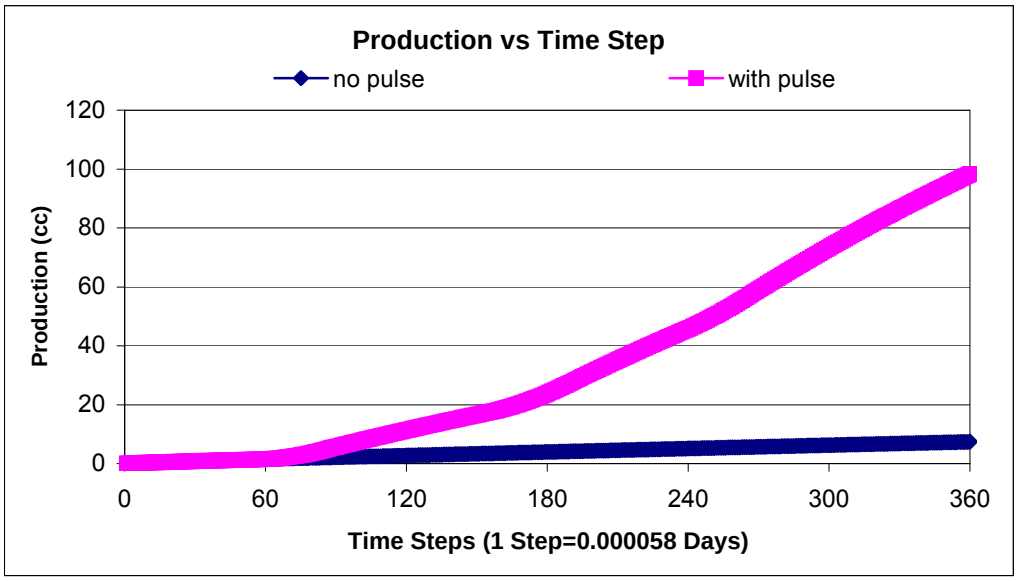

Figure 6-26: Predicted cumulative production for cases with and without pressure pulsing for a model with a permeability of 500 mD (Run5)

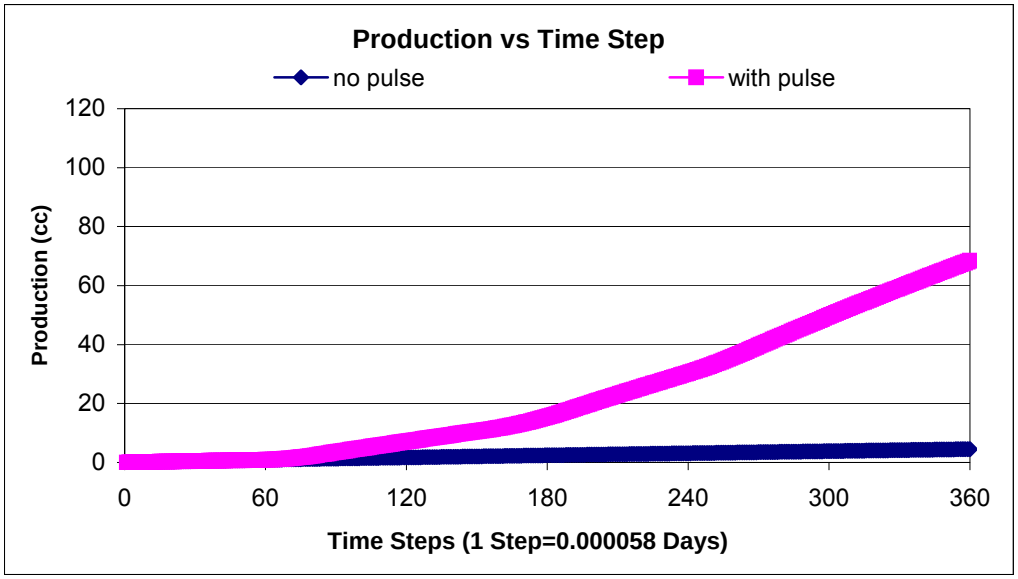

Figure 6-27: Predicted cumulative production for cases with and without pressure pulsing for a model with a permeability of 300 mD (Run6)

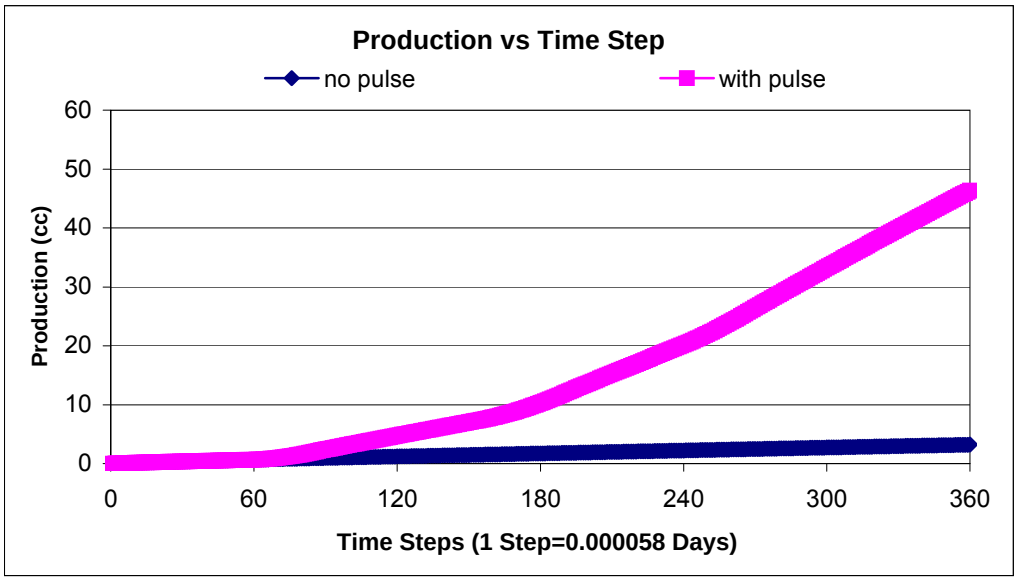

Figure 6-28: Predicted cumulative production for cases with and without pressure pulsing for a model with a permeability of 200 mD (Run7)

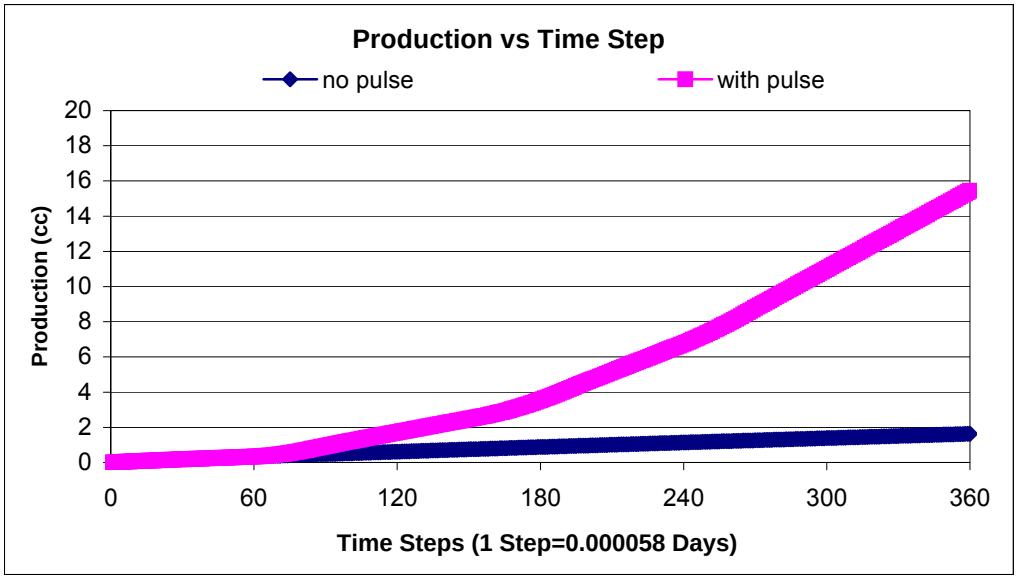

Figure 6-29: Predicted cumulative production for cases with and without pressure pulsing for a model with a permeability of 100 mD (Run8)

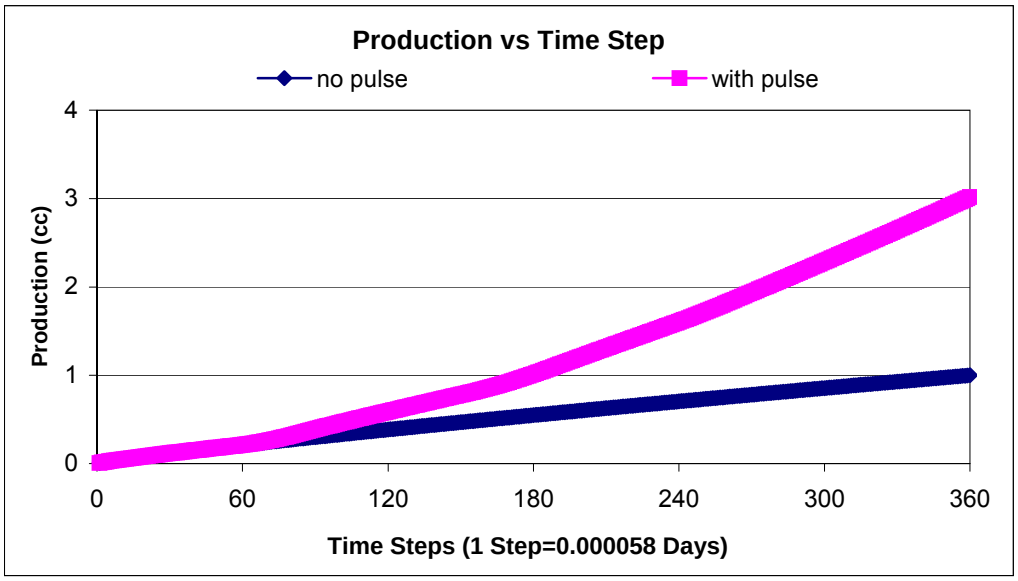

Figure 6-30: Predicted cumulative production for cases with and without pressure pulsing for a model with a permeability of 50 mD (Run9)

Figure 6-31 summarizes the results of these cases by plotting the cumulative volume produced from pressure pulsing in 30 minutes versus permeability. As can be seen in Figure 6-22 to Figure 6-30, the relationship between permeability and the cumulative

production at 30 minutes is not linear. This is highlighted by the results shown in Figure 6-31. It shows that the cumulative volume produced at 30 minutes from pulsing decreases with decreasing permeability but then begins increasing, reaching a local maximum around 1000 mD, after which it begins decreasing once again. Figure 6-32 then plots the ratio of the cumulative volume produced from pulsing to that produced by steady-state injection versus permeability. Figure 6-32 shows that the maximum benefit due to pulsing (measured as a ratio of the cumulative production due to pressure pulsing to the cumulative production without pressure pulsing) occurs at a permeability of 300 mD.

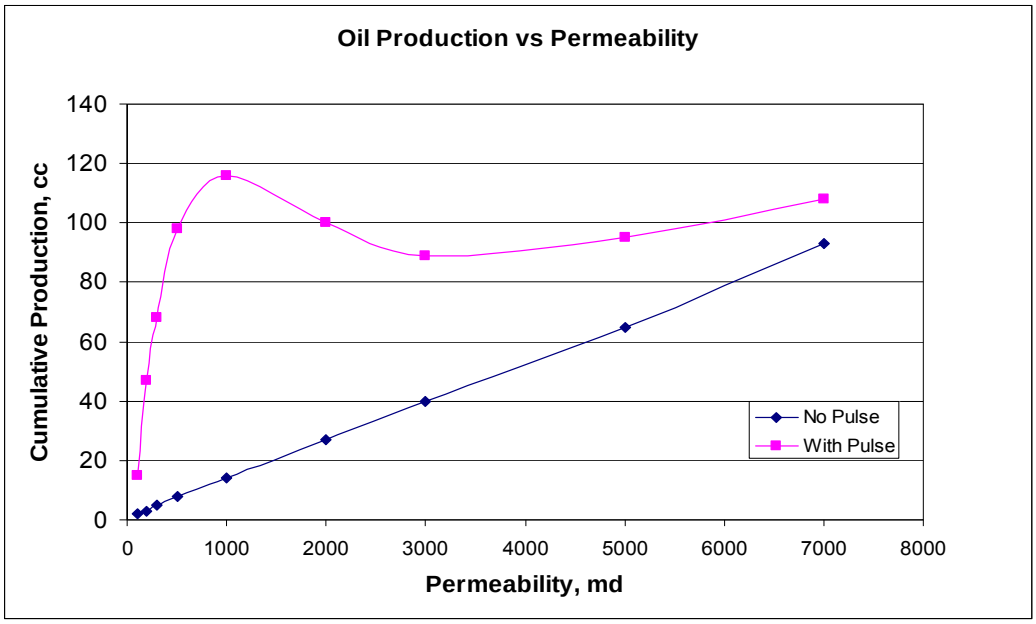

Figure 6-31: Predicted cumulative production at 30 minutes versus permeability for cases with and without pressure pulsing

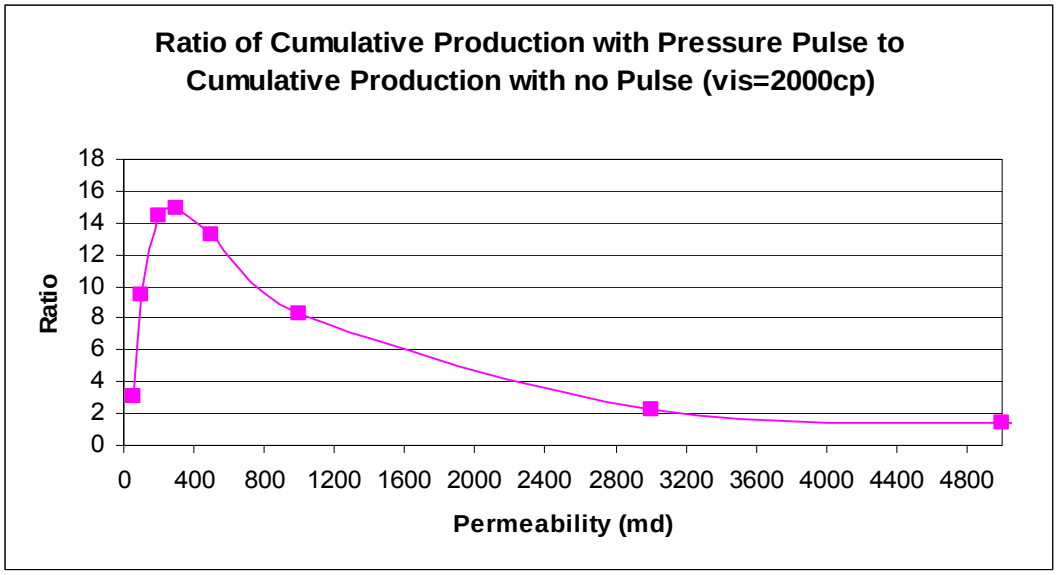

Figure 6-32: Predicted ratio of cumulative production with pressure pulsing to cumulative production without pressure pulsing versus permeability

Both of these figures indicate the existence of an optimum permeability at which pressure pulsing is most effective. This behaviour can be explained by considering that when the reservoir permeability is high, the pulse attenuation is small. At very small attenuations, energy from one point to another is released very fast and the pulse diffuses very quickly through the reservoir. This does not allow a significant pressure gradient to develop and, therefore, flow is not enhanced. At very low permeabilities, though, the pulse attenuation is high and the pressure builds only near the injection point. Because of the slow velocity, the pulse is not able to propagate far into the reservoir in order to stimulate flow.

In order to test this argument, pressure profiles due to pressure pulsing for each of the permeability cases are presented in Figure 6-33 to Figure 6-41. In these plots, "A" represents a point near the injector while "B", "C" and "D" represent points successively further away.

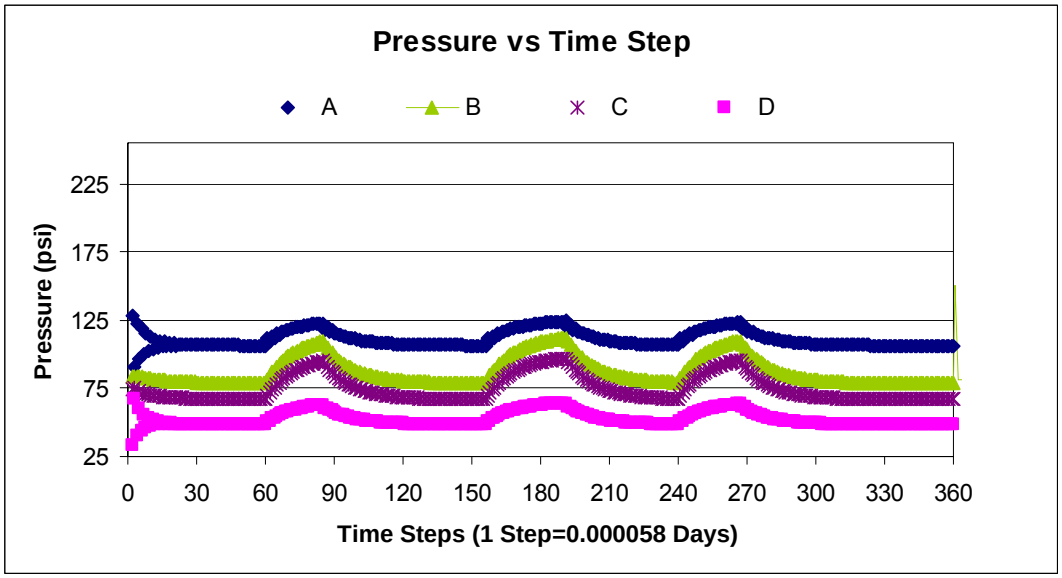

Figure 6-33: Predicted pressure profile at four locations for a model with a permeability of 7000 mD (Run1)

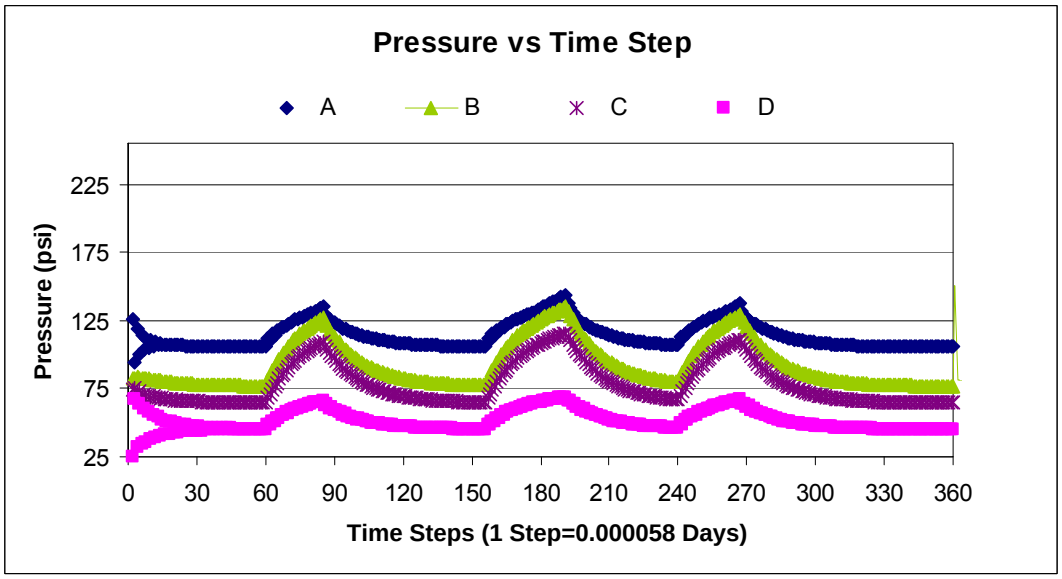

Figure 6-34: Predicted pressure profile at four locations for a model with a permeability of 5000 mD (Run2)

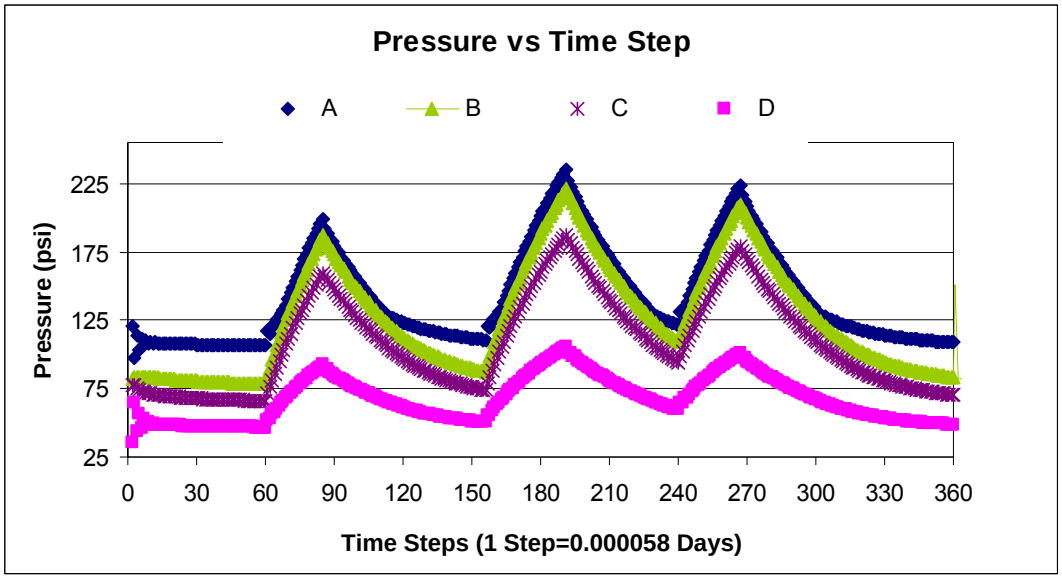

Figure 6-35: Predicted pressure profile at four locations for a model with a permeability of 3000 mD (Run3)

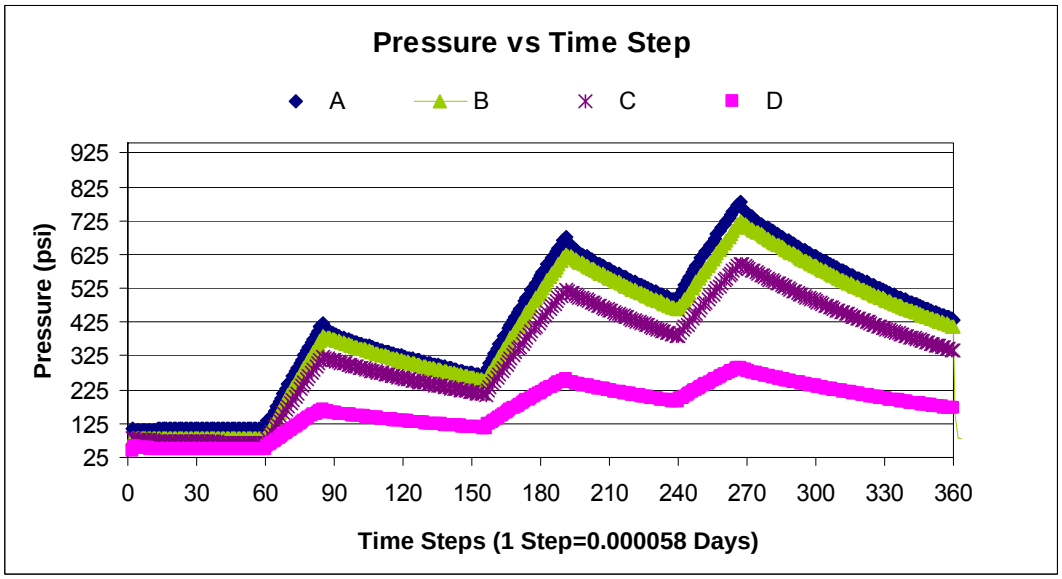

Figure 6-36: Predicted pressure profile at four locations for a model with a permeability of 1000 mD (Run4)

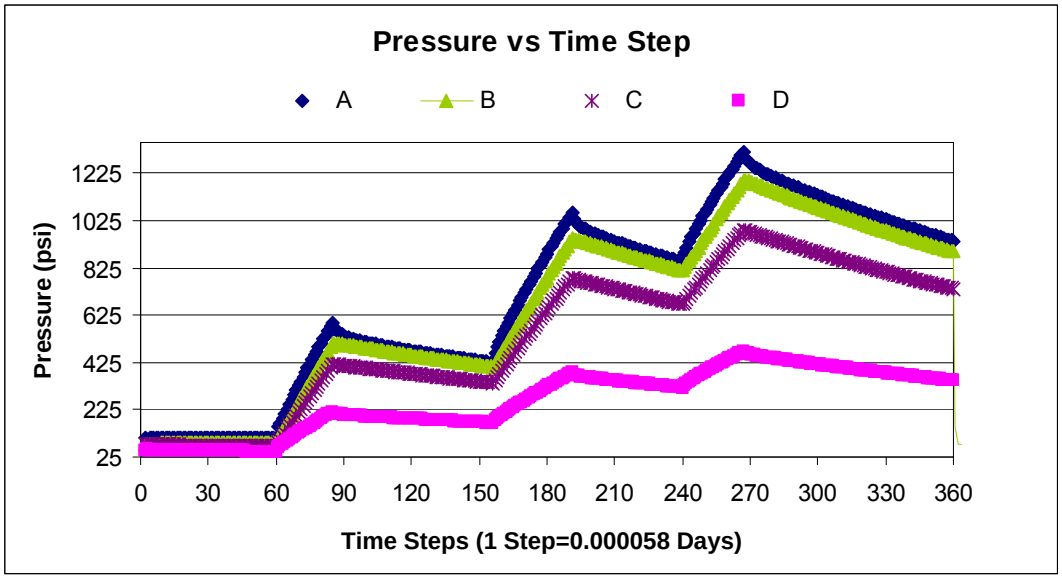

Figure 6-37: Predicted pressure profile at four locations for a model with a permeability of 500 mD (Run5)

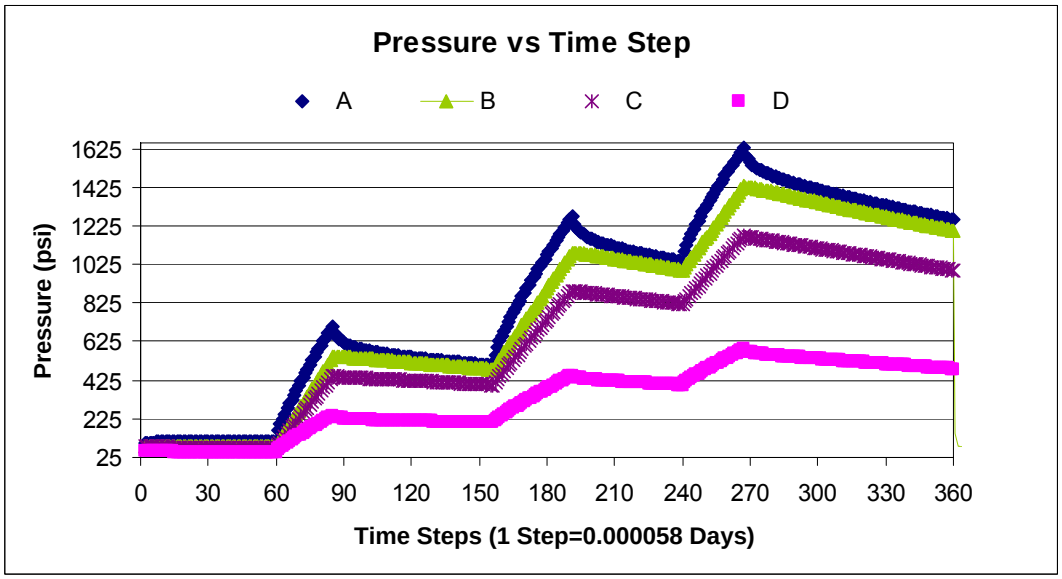

Figure 6-38: Predicted pressure profile at four locations for a model with a permeability of 300 mD (Run6)

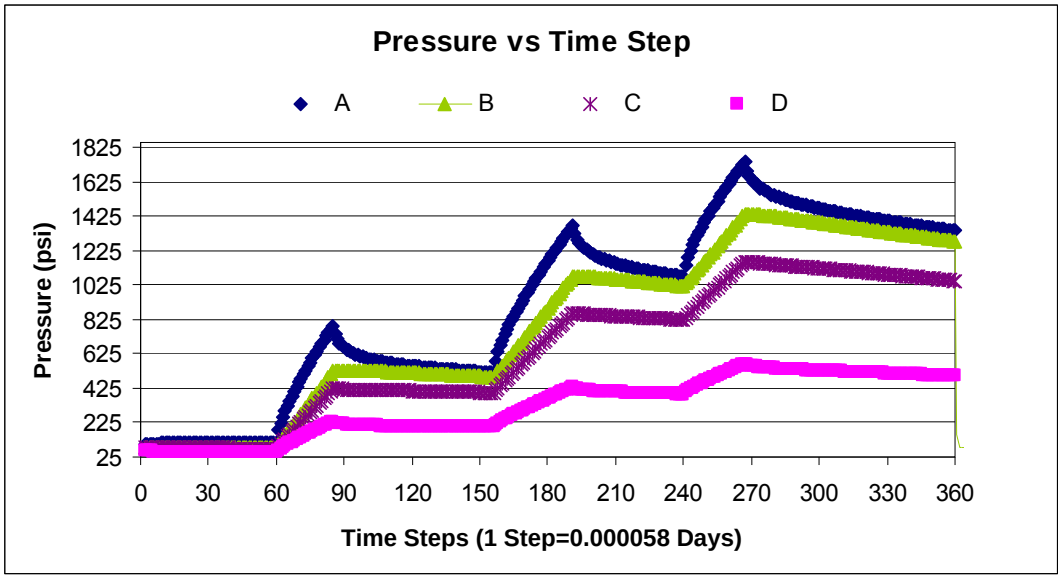

Figure 6-39: Predicted pressure profile at four locations for a model with a permeability of 200 mD (Run7)

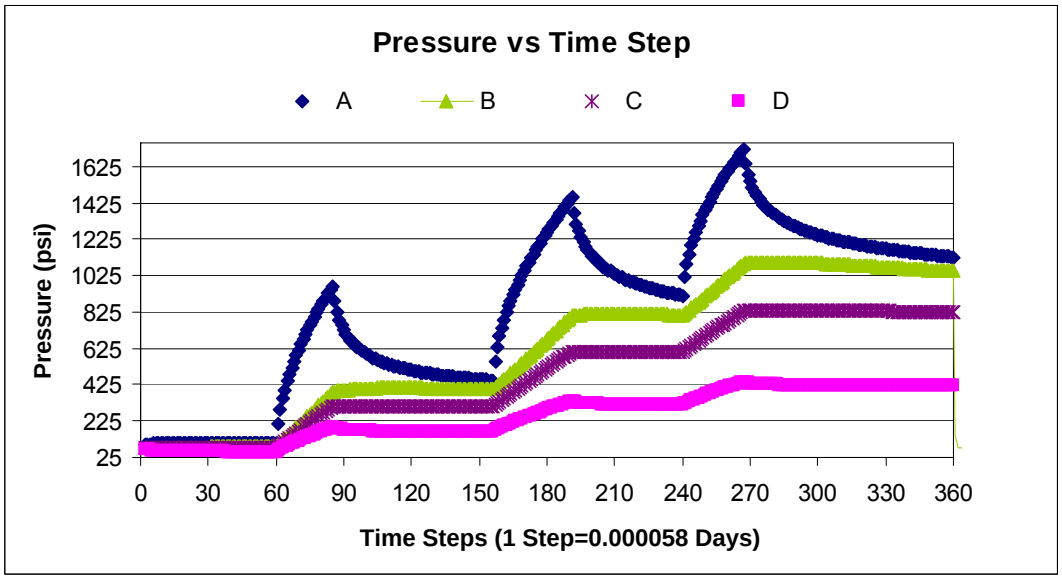

Figure 6-40: Predicted pressure profile at four locations for a model with a permeability of 100 mD (Run8)

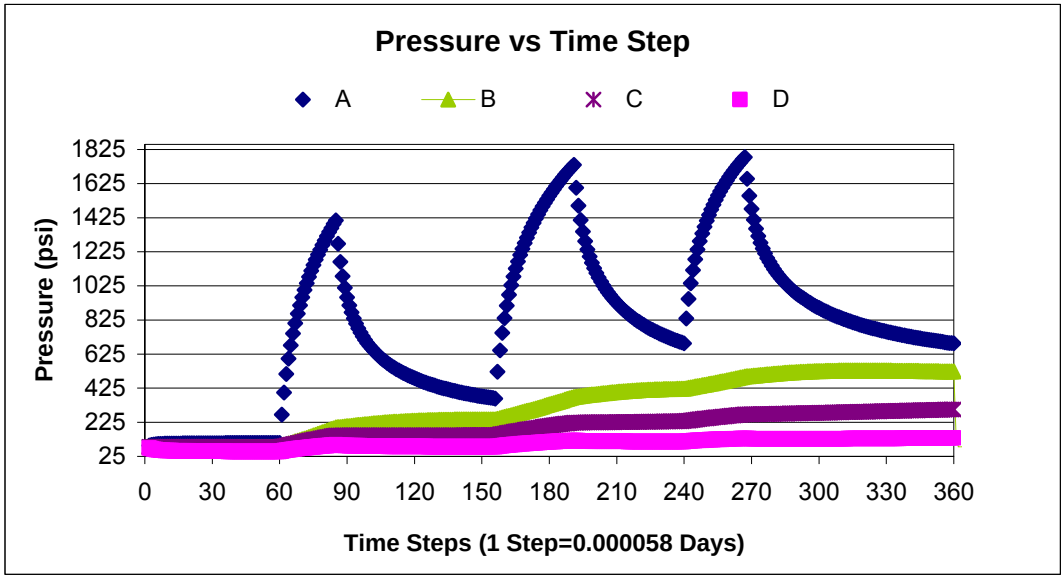

Figure 6-41: Predicted pressure profile at four locations for a model with a permeability of 50 mD (Run9)

Figure 6-33 and Figure 6-41 show the pressure profiles due to pressure pulsing for the reservoirs with the highest and the lowest permeabilities, 7000 mD and 50 mD, respectively. Note that where the permeability is very high, the pressure increases the same amount everywhere in the reservoir and the sharp pressure gradient needed to increase fluid rate is not created. However, for low permeabilities pressurization occurs only around the injection well and areas far from the injection wells remain unpressurized and flow is not stimulated by the pulses. Therefore, an examination of the pressure profiles show that for a given frequency there is an optimum permeability where we achieve the maximum ratio of cumulative production with pulse to cumulative production with no pulse.

6.5.2 Viscosity Sensitivity

In order to investigate the impact of fluid viscosity on pressure pulsing, nine simulation cases were run with viscosities of 4000 cP (Run10), 2000 cP (Run11), 1000 cP (Run12), 700 cP (Run13), 300 cP (Run14), 50 cP (Run15) and 5 cP (Run16). In each of these cases, the permeability was 200 mD, the porosity was 35%, the rock compressibility was 3×10^{-6} psi^{-1} and the pulse frequency was 0.25 Hz.

Figure 6-42 to Figure 6-48 show the cumulative production volumes for Runs 10 to 16, respectively, and Figure 6-49 and Figure 6-50 summarize these results. Figure 6-49 plots the cumulative volume produced through 30 minutes for both the steady-state and pressure-pulse tests versus fluid viscosity. Figure 6-50 then plots the ratio of the cumulative production due to pressure pulsing to that produced by steady-state injection versus fluid viscosity. Following are the figures followed by discussion of the results:

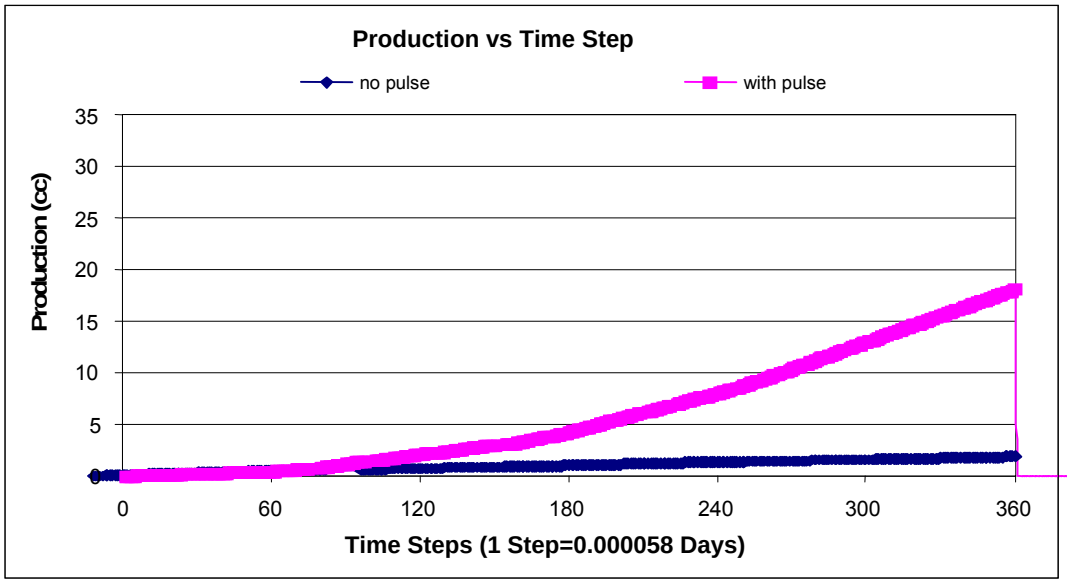

Figure 6-42: Predicted cumulative production for cases with and without pressure pulsing for a model with a fluid viscosity of 4000 cP (Run10)

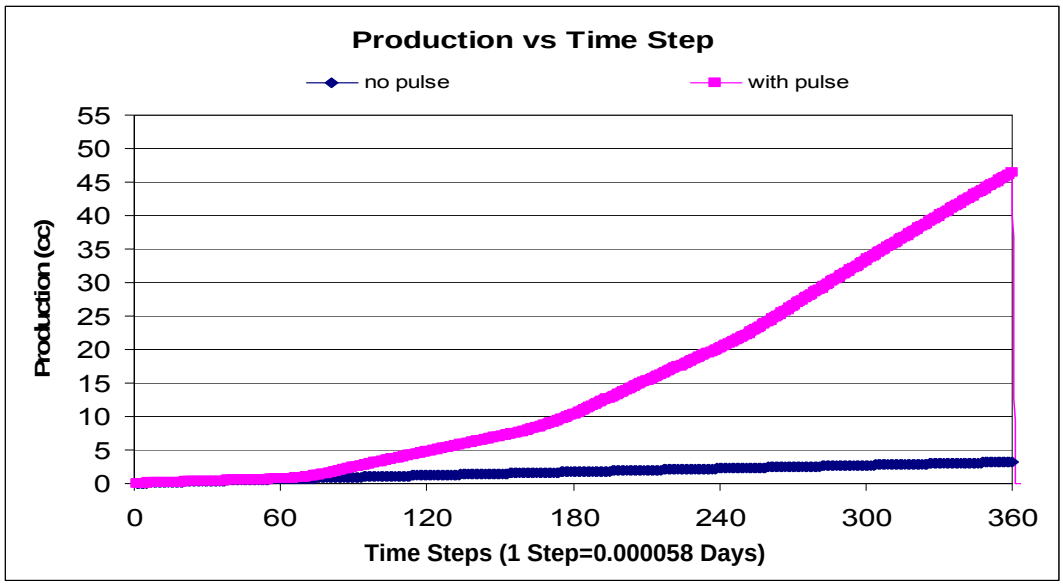

Figure 6-43: Predicted cumulative production for cases with and without pressure pulsing for a model with a fluid viscosity of 2000 cP (Run11)

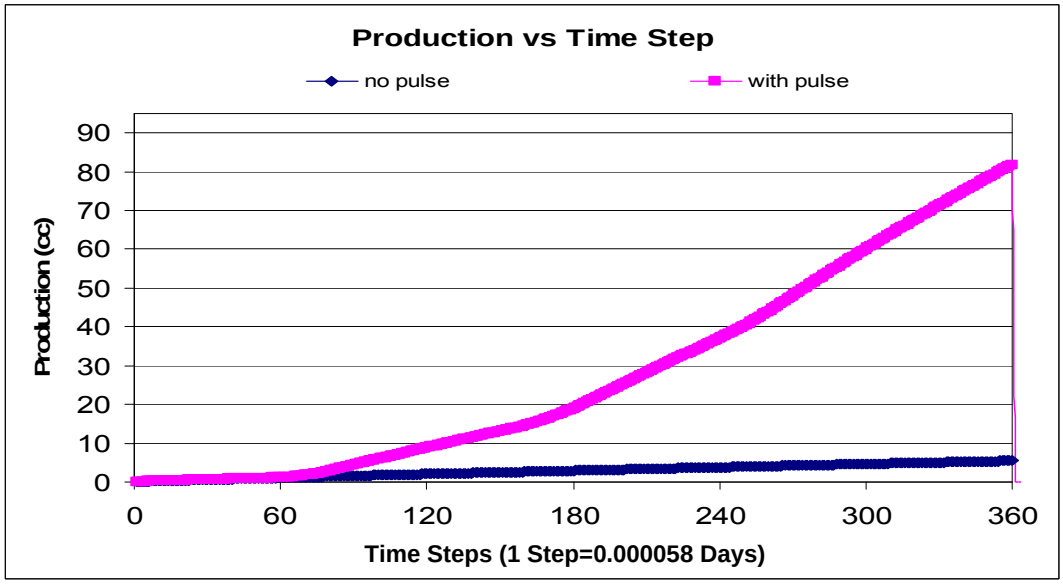

Figure 6-44: Predicted cumulative production for cases with and without pressure pulsing for a model with a fluid viscosity of 1000 cP (Run12)

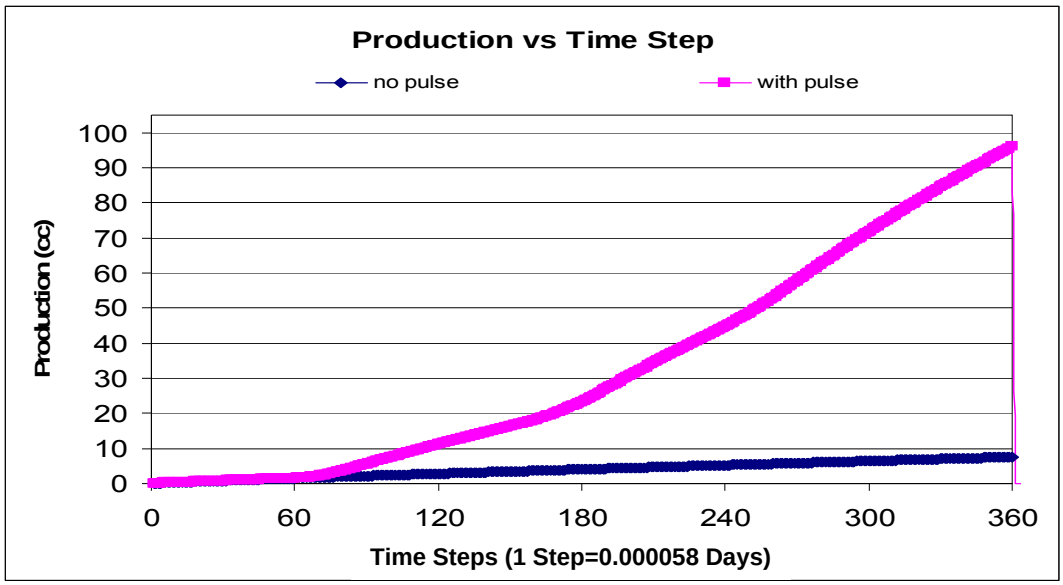

Figure 6-45: Predicted cumulative production for cases with and without pressure pulsing for a model with a fluid viscosity of 700 cP (Run13)

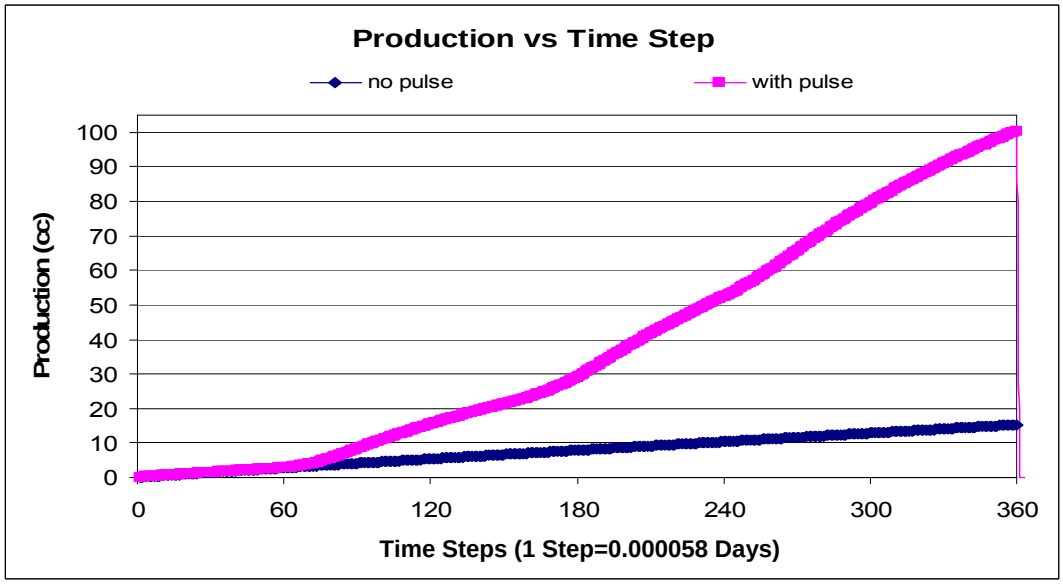

Figure 6-46: Predicted cumulative production for cases with and without pressure pulsing for a model with a fluid viscosity of 300 cP (Run14)

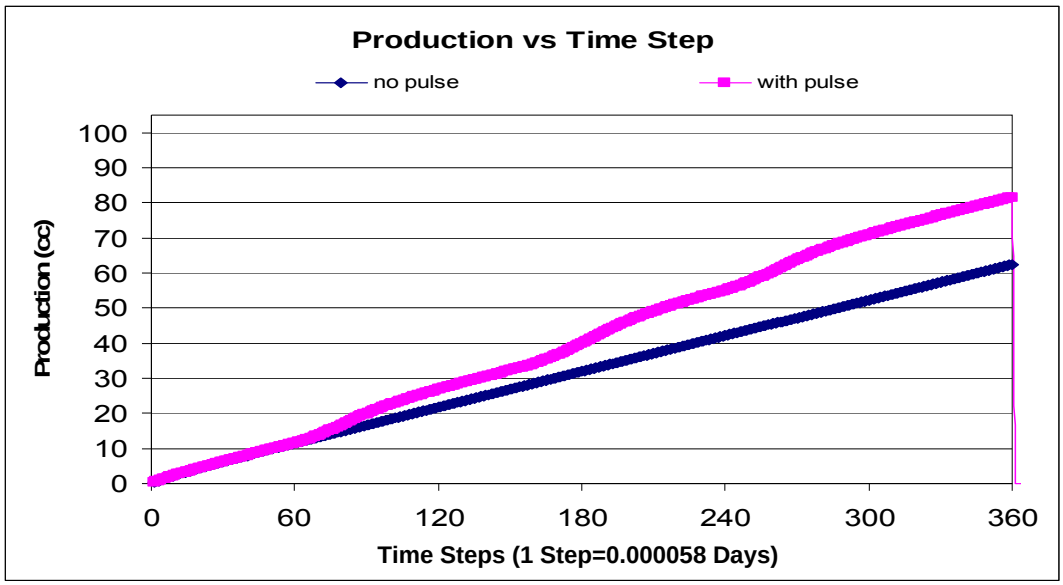

Figure 6-47: Predicted cumulative production for cases with and without pressure pulsing for a model with a fluid viscosity of 50 cP (Run15)

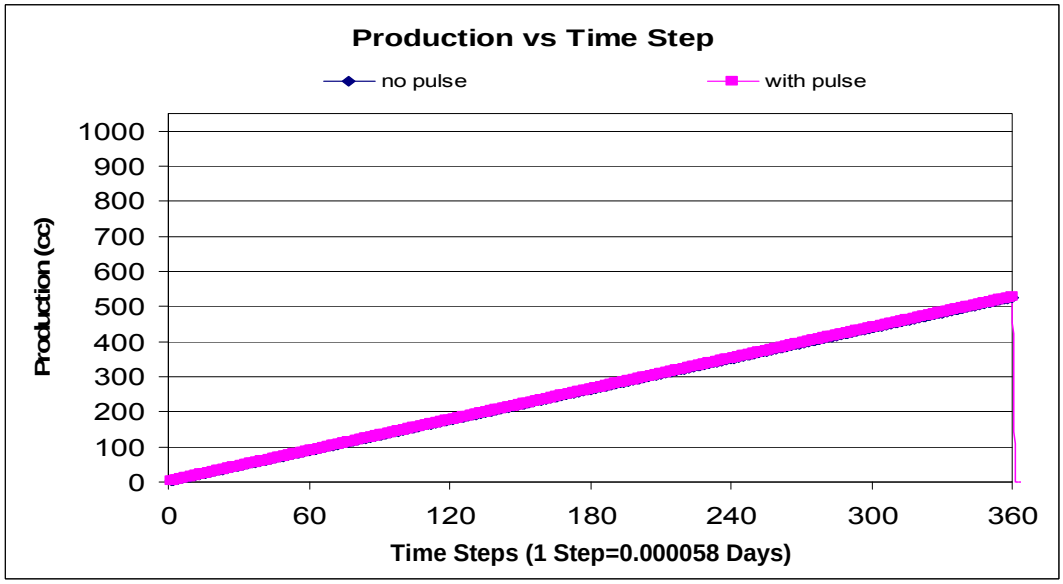

Figure 6-48: Predicted cumulative production for cases with and without pressure pulsing for a model with a fluid viscosity of 5 cP (Run16)

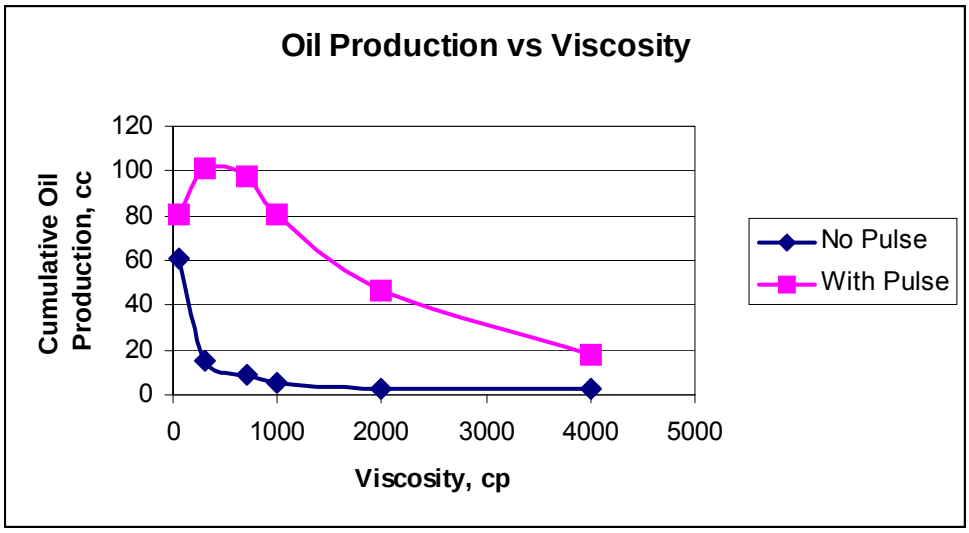

Figure 6-49: Predicted cumulative production at 30 minutes versus fluid viscosity for cases with and without pressure pulsing

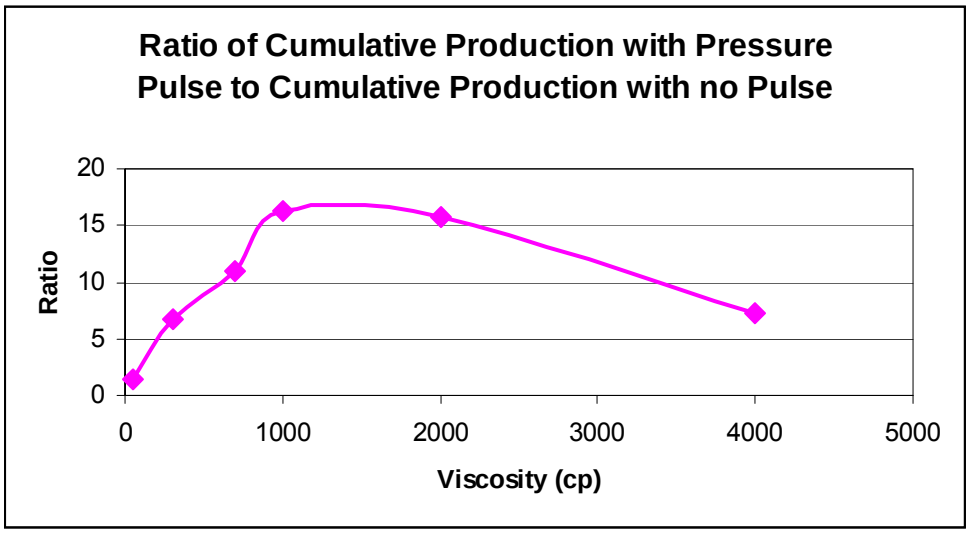

Figure 6-50: Predicted ratio of cumulative production with pressure pulsing to cumulative production without pressure pulsing versus fluid viscosity

According to Darcy's Law, changes in the fluid viscosity have an inversely-proportional effect on the fluid flow rate. This trend is apparent in the steady-state results of Figure 6-49 which show that the cumulative production at 30 minutes increases with decreasing fluid viscosity. However, for cases with pressure pulsing, these figures show that as the viscosity decreases from 4000 cP, the cumulative production increases, peaks around 300 cP and then decreases. Figure 6-50 meanwhile shows that the maximum benefit due to

pulsing occurs at a viscosity of 1000 cP. This figure also shows that for fluids with a viscosity of 5 cP, there is no benefit gained from pressure pulsing.

As was observed with changes in permeability, these results indicate the existence of an optimum viscosity at which pressure pulsing is beneficial. Once again, this fluid enhancement effect can be attributed to the internal pressure build-up. In order to test this argument, pressure profiles due to pressure pulsing for each of the viscosity cases are presented in Figure 6-51 to Figure 6-57.

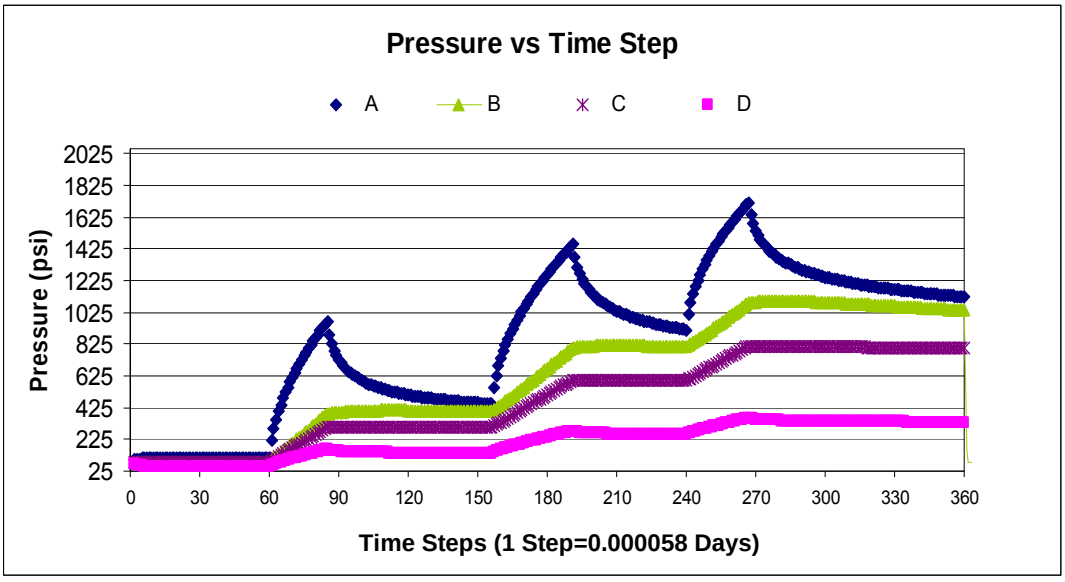

Figure 6-51: Predicted pressure profile at four locations for a model with a fluid viscosity of 4000 cP (Run10)

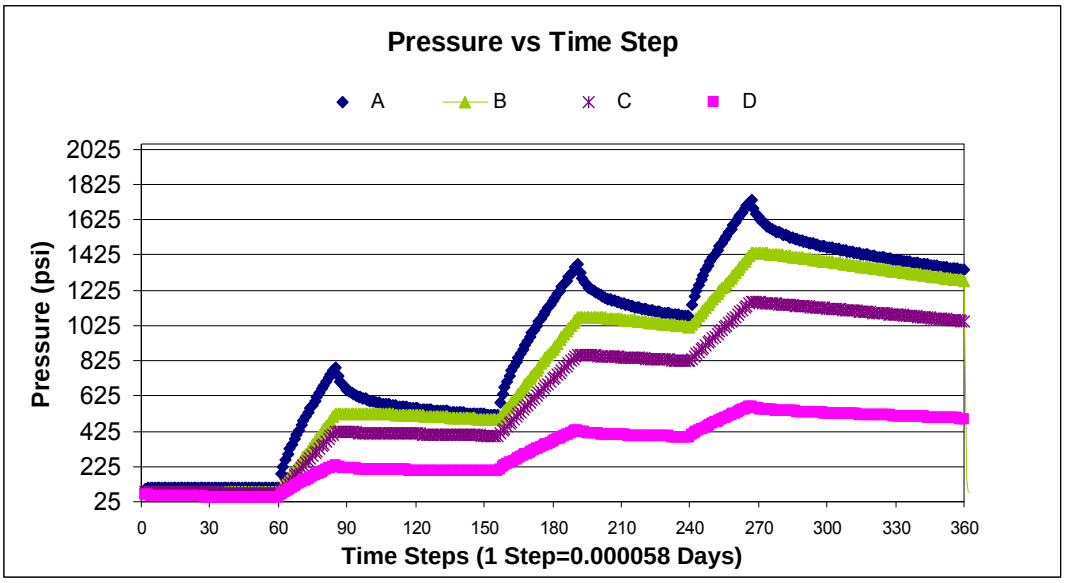

Figure 6-52: Predicted pressure profile at four locations for a model with a fluid viscosity of 2000 cP (Run11)

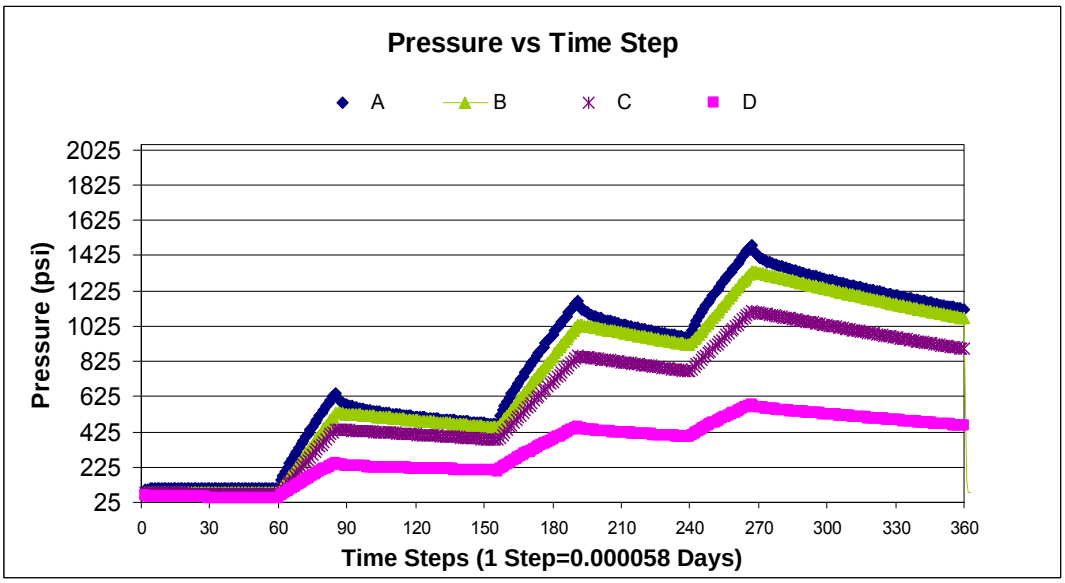

Figure 6-53: Predicted pressure profile at four locations for a model with a fluid viscosity of 1000 cP (Run11)

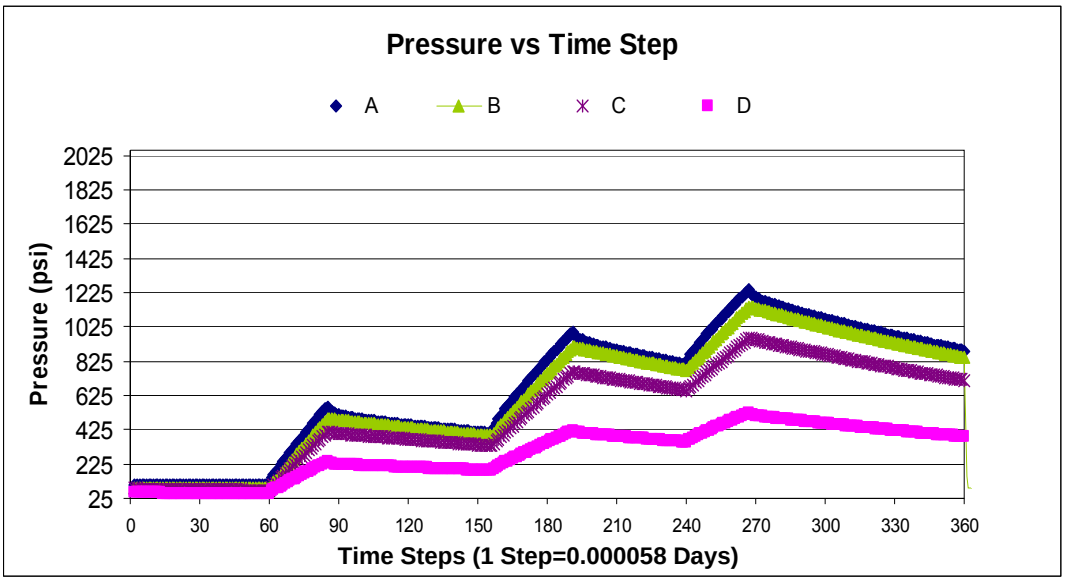

Figure 6-54: Predicted pressure profile at four locations for a model with a fluid viscosity of 700 cP (Run13)

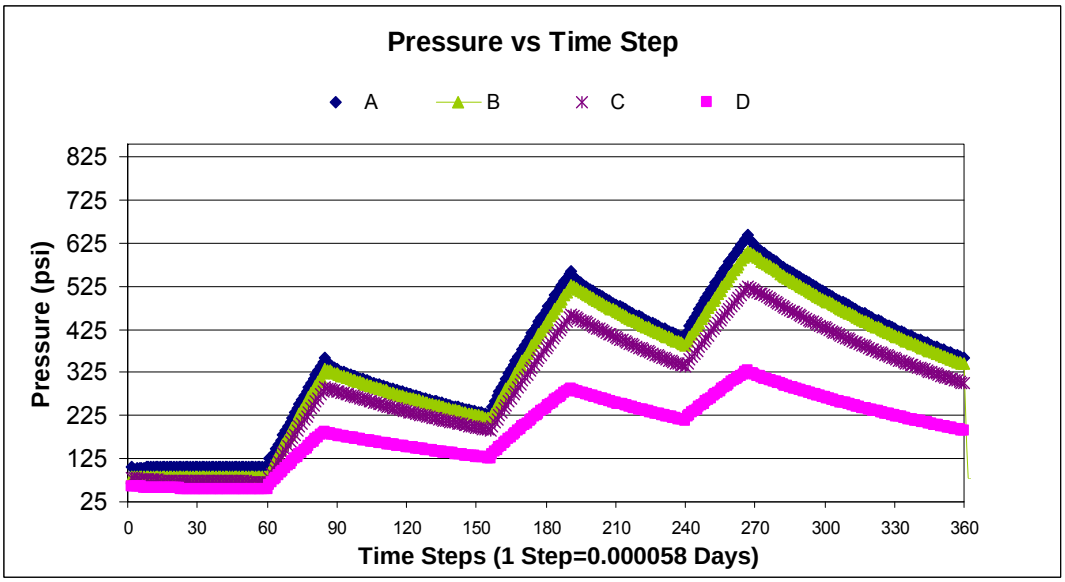

Figure 6-55: Predicted pressure profile at four locations for a model with a fluid viscosity of 300 cP (Run14)

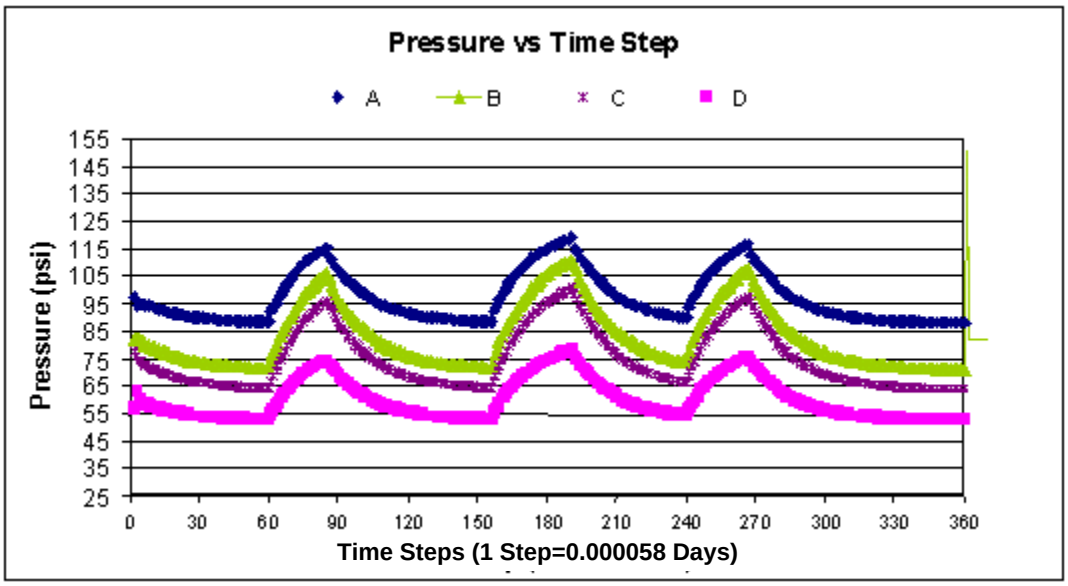

Figure 6-56: Predicted pressure profile at four locations for a model with a fluid viscosity of 50 cP (Run15)

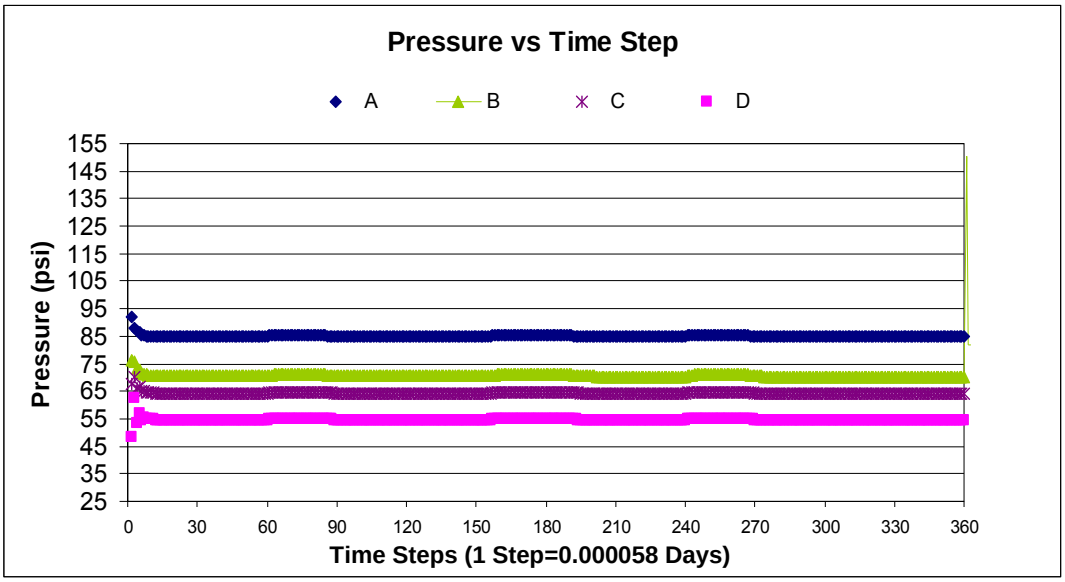

Figure 6-57: Predicted pressure profile at four locations for a model with a fluid viscosity of 5 cP (Run16)

Figure 6-51 and Figure 6-57 show the pressure profile for the reservoirs with the highest and the lowest viscosities, 4000 cP and 5 cP, respectively. Note that when the viscosity is very low the magnitude of the pressure increase is small and propagates through the

porous media quickly. A sharp pressure gradient is not achieved which is necessary to increase the fluid flowrate. However, for high viscosities pressurization occurs only around the injection well and areas far from the injection well remains unpressurized. It can be concluded that, generally, the energy-preserving ability of light oil is weaker than that of viscous oil. If the frequency of light oil is too low, the previous pulse drops too much before the next pulse is added, leading to a poor build up effect. For a given frequency there is an optimum viscosity where we achieve the maximum ratio of cumulative production with pulse to cumulative production with no pulse.

As can be seen from both the permeability and viscosity sensitivity analyses, for a given frequency, the incremental oil recovery reaches a maximum at some intermediate value of both the permeability and viscosity. Therefore, an additional sensitivity analysis consisting of 49 simulation runs was conducted to determine, for a given viscosity, the optimum permeability at which the incremental recovery is maximized. Figure 6-58 to Figure 6-64 plot the ratio of the cumulative production with pressure pulsing to the cumulative production without pressure pulsing at various permeabilities for fluid viscosities of 4000, 2000, 1000, 700, 300, 50 and 5 cP, respectively. Each of these cases uses a porosity of 35%, rock compressibility of 3×10^{-6} psi^{-1} and a pulse frequency of 0.25 Hz.

These figures show that the higher the viscosity, the greater the permeability at which incremental recovery is maximized. This shows that it is both permeability and viscosity which determine the maximum efficiency for a given frequency.

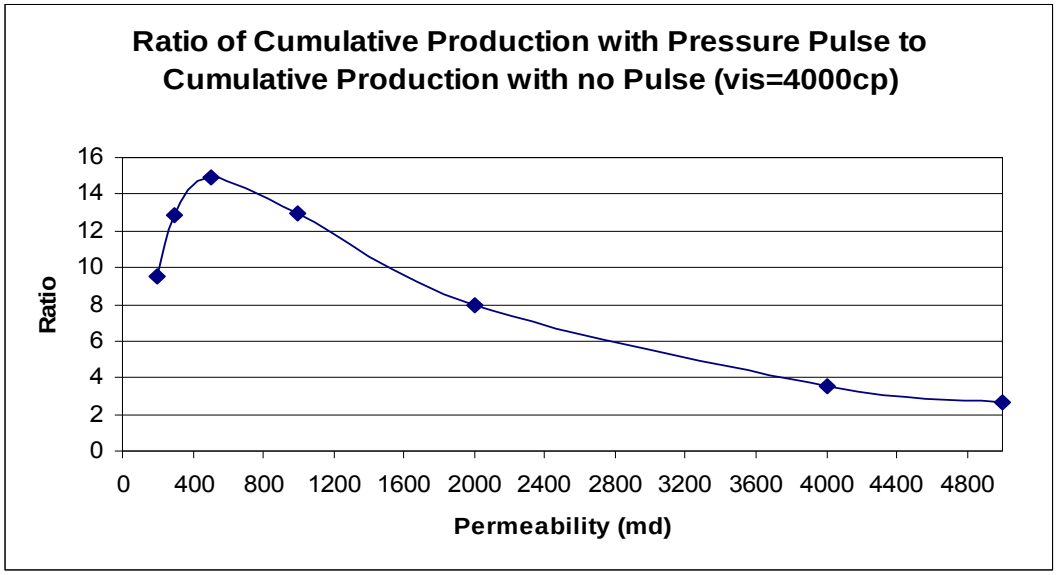

Figure 6-58: Predicted ratio of cumulative production with pressure pulsing to cumulative production without pressure pulsing versus permeability for a model with a fluid viscosity of 4000 cP

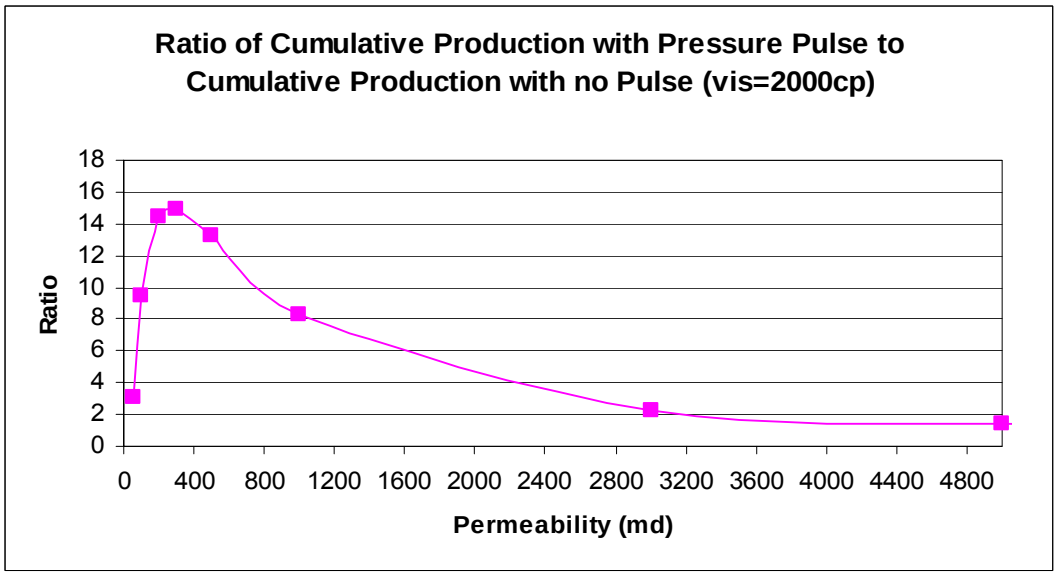

Figure 6-59: Predicted ratio of cumulative production with pressure pulsing to cumulative production without pressure pulsing versus permeability for a model with a fluid viscosity of 2000 cP

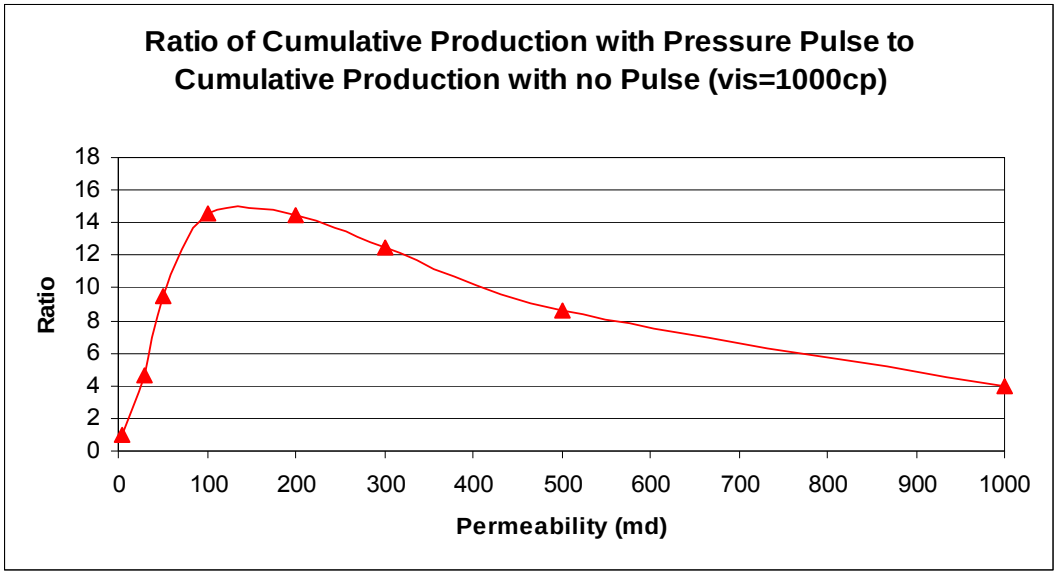

Figure 6-60: Predicted ratio of cumulative production with pressure pulsing to cumulative production without pressure pulsing versus permeability for a model with a fluid viscosity of 1000 cP

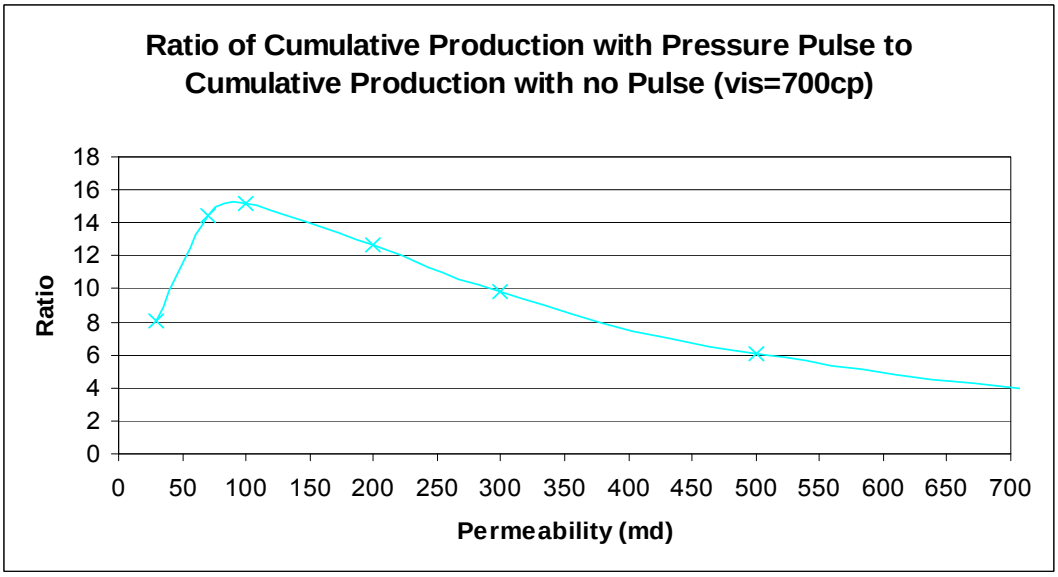

Figure 6-61: Predicted ratio of cumulative production with pressure pulsing to cumulative production without pressure pulsing versus permeability for a model with a fluid viscosity of 700 cP

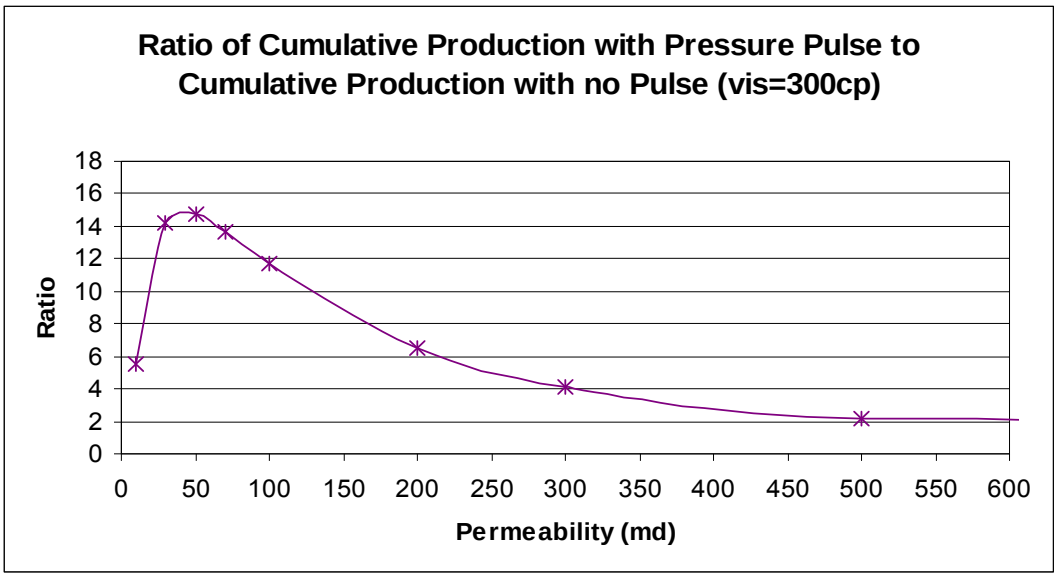

Figure 6-62: Predicted ratio of cumulative production with pressure pulsing to cumulative production without pressure pulsing versus permeability for a model with a fluid viscosity of 300 cP

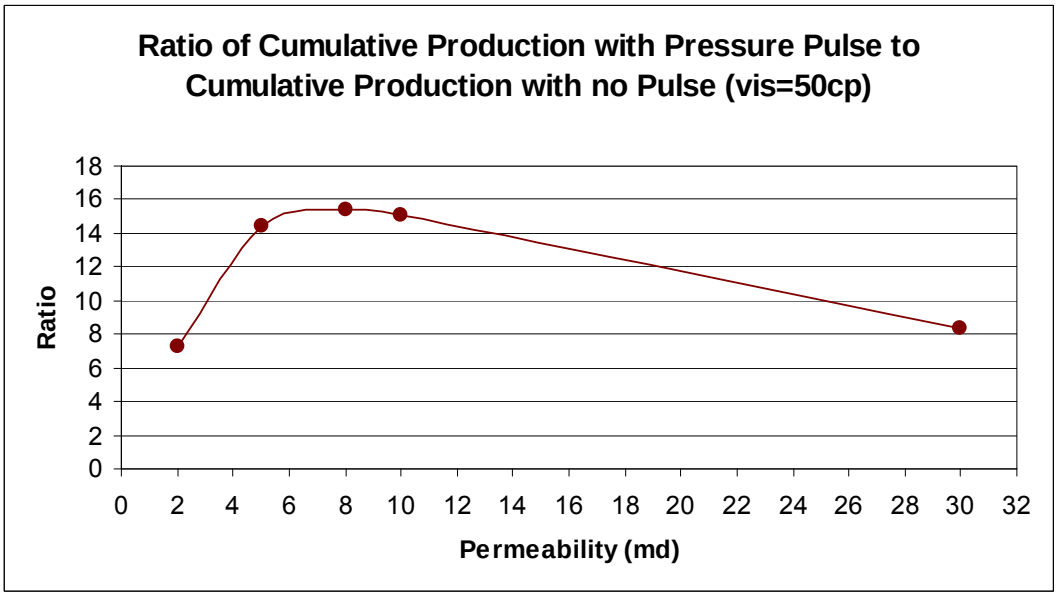

Figure 6-63: Predicted ratio of cumulative production with pressure pulsing to cumulative production without pressure pulsing versus permeability for a model with a fluid viscosity of 50 cP

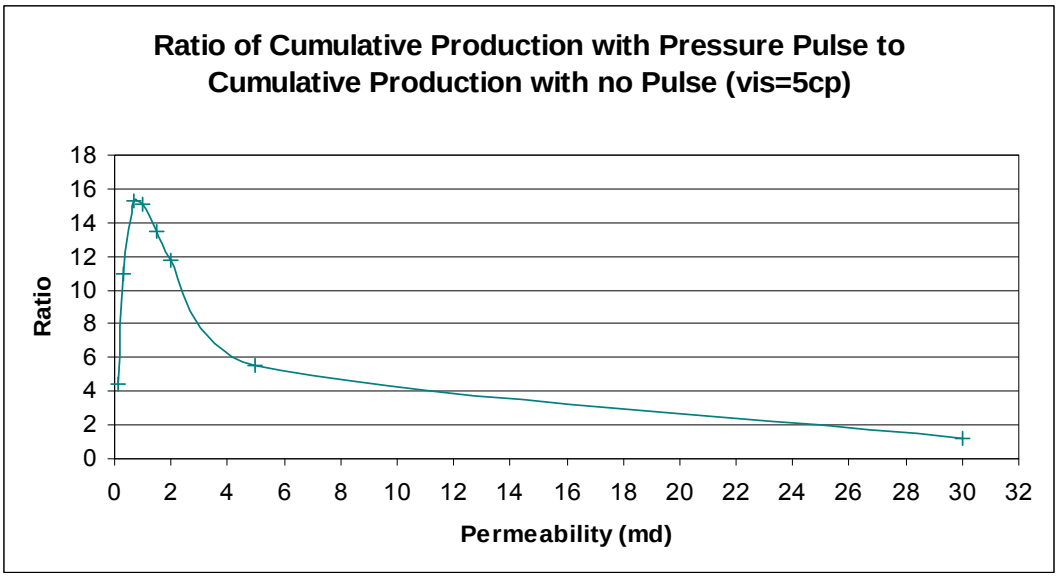

Figure 6-64: Predicted ratio of cumulative production with pressure pulsing to cumulative production without pressure pulsing versus permeability for a model with a fluid viscosity of 5 cP

Figure 6-65 summarizes the incremental oil recoveries for each fluid viscosity and plots them versus permeability on a log scale. Interestingly, at the optimum permeability for each viscosity, the incremental recovery is constant and equal to 15 (meaning that the cumulative production due to pressure pulsing was 15 times the cumulative production due to steady-state injection). There are a few points to consider when interpreting these results:

- The incremental recovery of 15 times the base recovery is specific to this example, as the geometry, frequency, source change incremental recovery will vary depending on the application.
- The incremental recovery obtained in simulating lab scale should not be applied to field scale applications. In the field scale, the efficiency would not be as high as that at the lab scale, i.e., it is harder to stack up waves on top of each other as the energy will dissipate radially. Moreover, it would require much higher frequencies and amplitudes to pressurize the reservoir and these might be limited by the constraints of the pulsing tool.
- A typical Alberta heavy oil field has a permeability of 10 D and oil viscosity of 4000 cp. According to Figure 6-70, a sample core from Alberta heavy oil field

would have only 2 times the incremental oil recovery with a pulse frequency of 0.25 Hz.

Assuming the frequency of the pulsing tool is fixed, for a given permeability there is only a small range of viscosities where very high recoveries can be achieved. Outside that range, the incremental recovery will be limited.

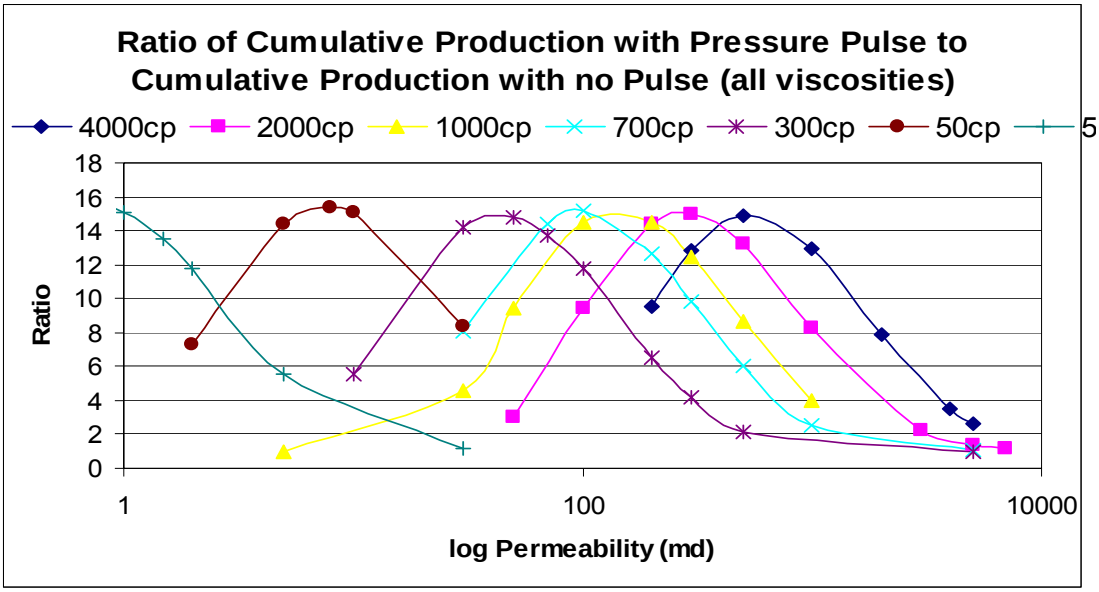

Figure 6-65: Summary of the effect of fluid viscosity on the predicted ratio of cumulative production with pressure pulsing to cumulative production without pressure pulsing versus permeability

6.5.3 Porosity Sensitivity

Generally speaking, the porosity of real petroleum reservoirs is about 20-30% or less. In order to analyze the effect of porosity, simulation runs were conducted for porosities of 20, 35 and 45%. Because many factors can affect the fluid rates, simulation runs were conducted for various viscosity and permeability values at each porosity, rather than changing only the porosity values. This provided an opportunity to simultaneously investigate the effects of permeability, viscosity and porosity.

For the three tested porosities, Figure 6-66 to Figure 6-94 present the results for various combinations of viscosity (ranging between 4000 and 50 cP) and permeability (ranging

between 1000 and 8 mD). In each case, the rock compressibility was 3×10^{-6} psi^{-1} and the pulse frequency was 0.25 Hz.

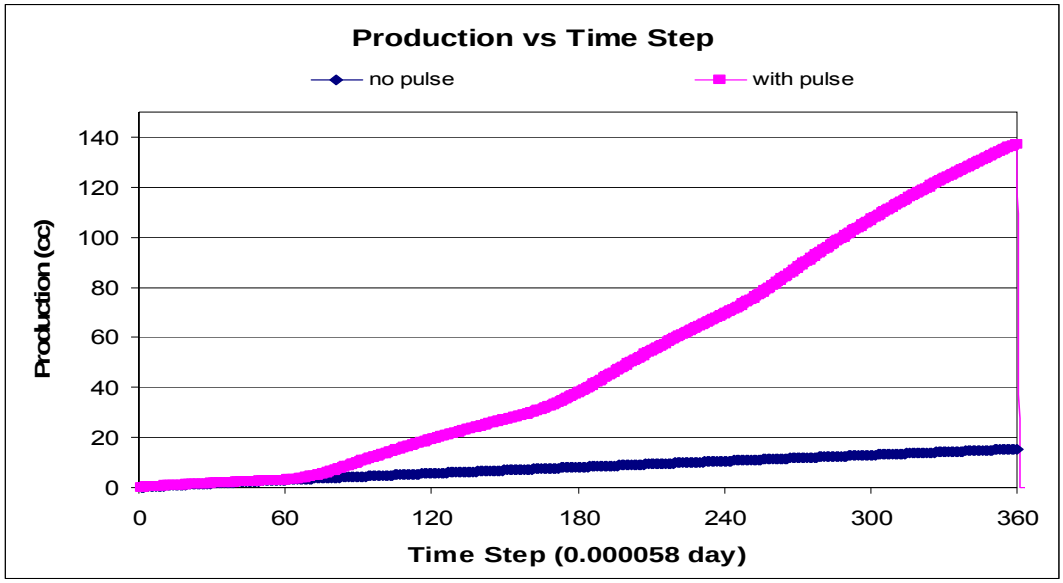

Figure 6-66: Predicted cumulative production for cases with and without pressure pulsing for a model with a fluid viscosity of 4000 cP, a porosity of 0.45 and a permeability of 2000 mD

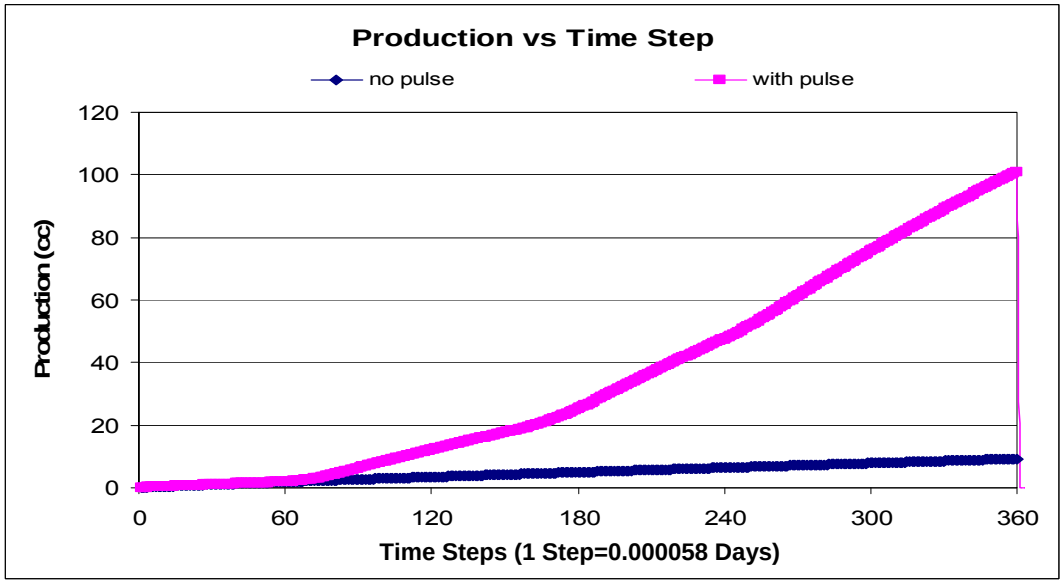

Figure 6-67: Predicted cumulative production for cases with and without pressure pulsing for a model with a fluid viscosity of 4000 cP, a porosity of 0.45 and a permeability of 1150 mD

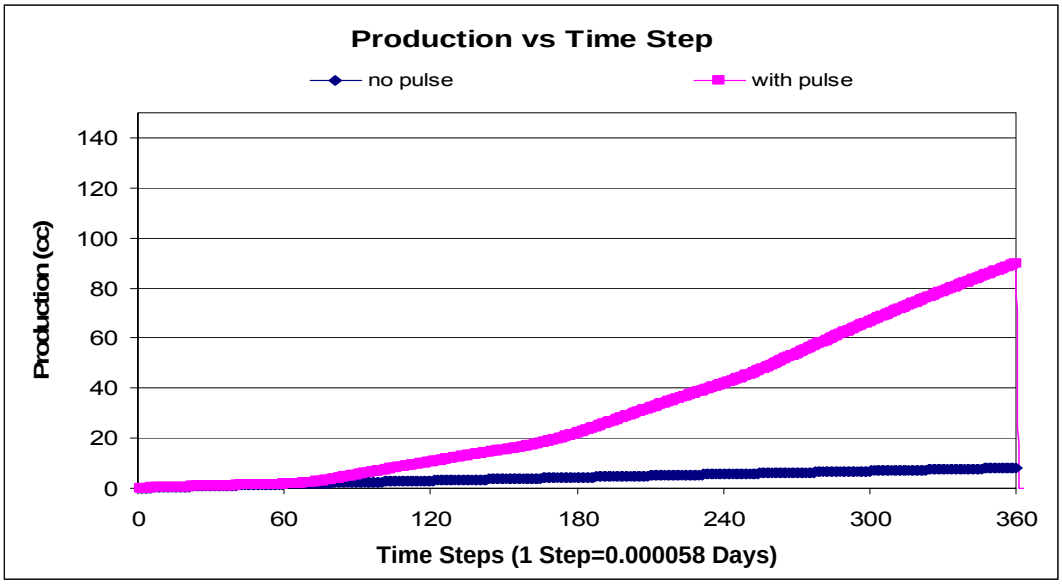

Figure 6-68: Predicted cumulative production for cases with and without pressure pulsing for a model with a fluid viscosity of 4000 cP, a porosity of 0.45 and a permeability of 1000 mD

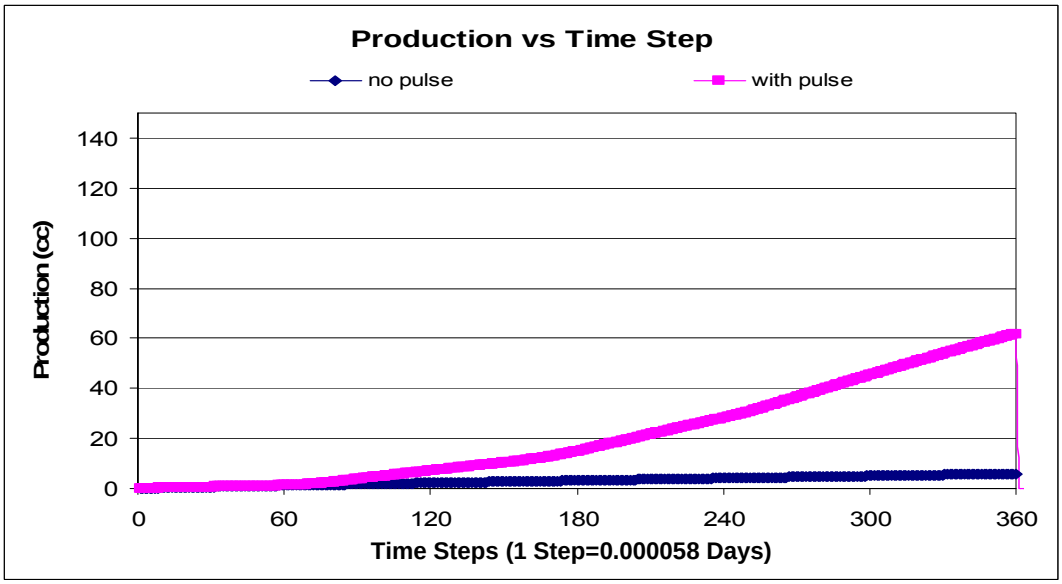

Figure 6-69: Predicted cumulative production for cases with and without pressure pulsing for a model with a fluid viscosity of 4000 cP, a porosity of 0.45 and a permeability of 700 mD

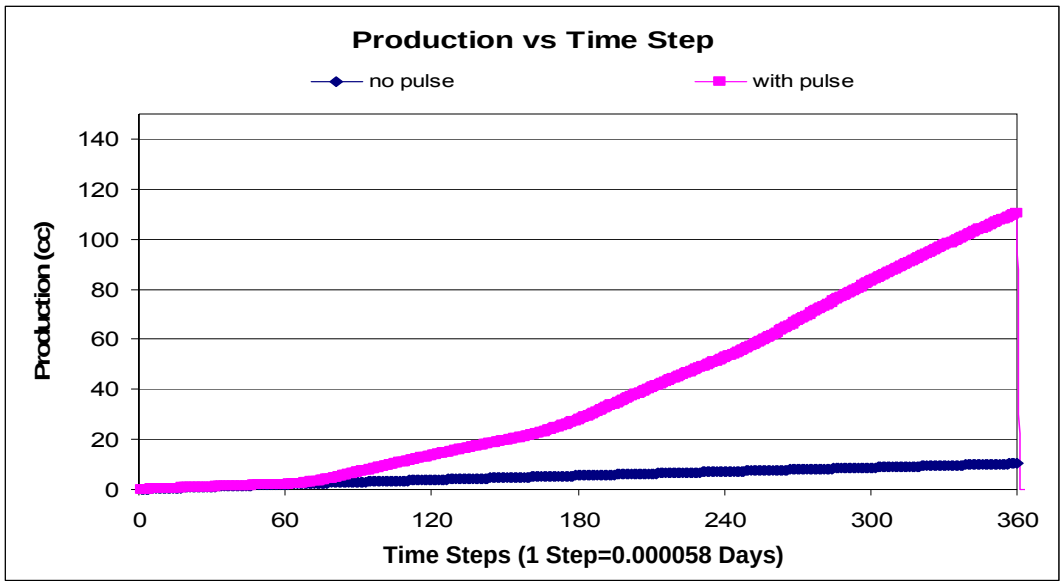

Figure 6-70: Predicted cumulative production for cases with and without pressure pulsing for a model with a fluid viscosity of 2000 cP, a porosity of 0.45 and a permeability of 700 mD

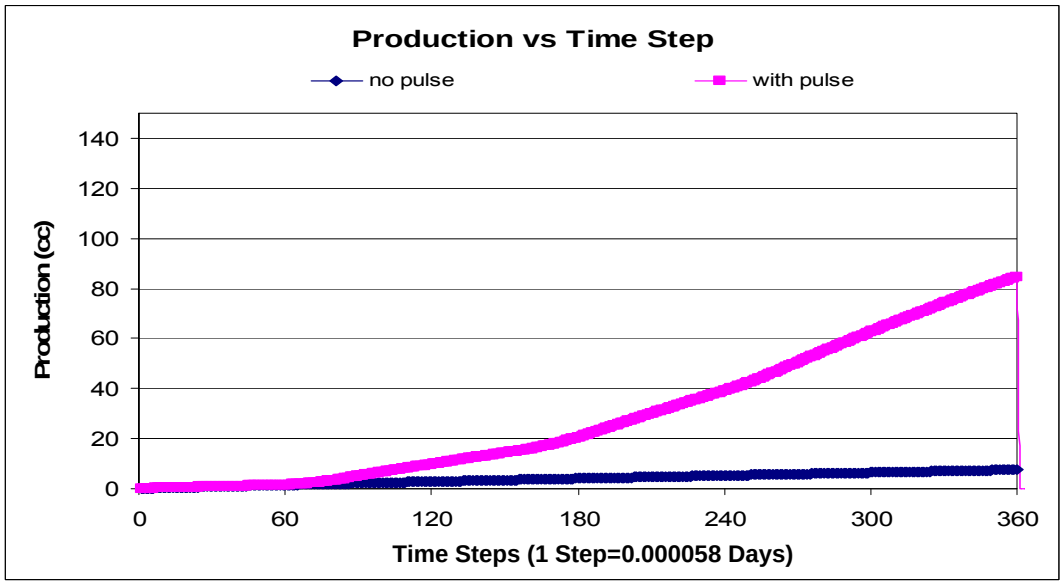

Figure 6-71: Predicted cumulative production for cases with and without pressure pulsing for a model with a fluid viscosity of 2000 cP, a porosity of 0.45 and a permeability of 500 mD

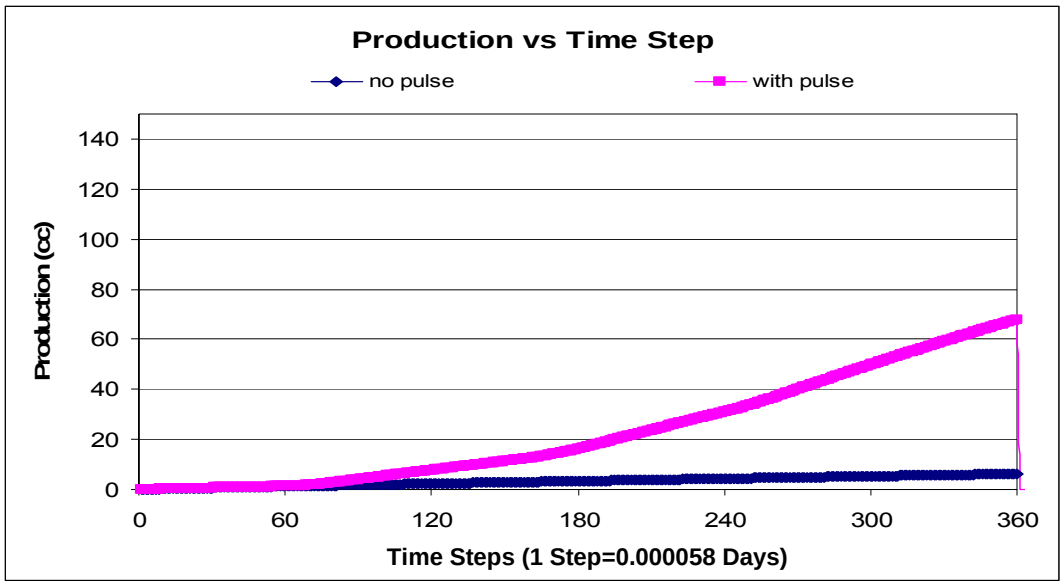

Figure 6-72: Predicted cumulative production for cases with and without pressure pulsing for a model with a fluid viscosity of 2000 cP, a porosity of 0.45 and a permeability of 400 mD

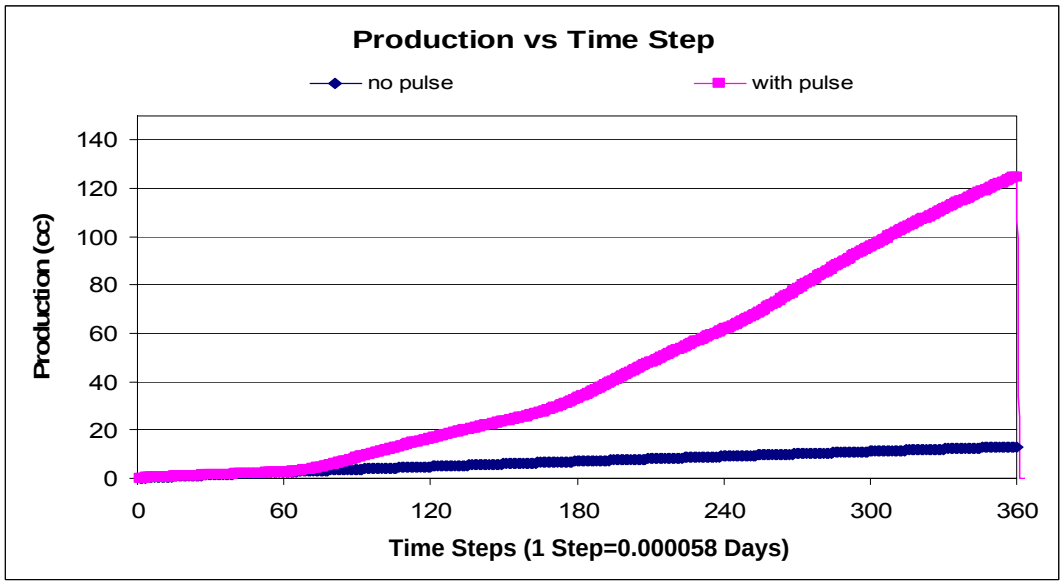

Figure 6-73: Predicted cumulative production for cases with and without pressure pulsing for a model with a fluid viscosity of 1000 cP, a porosity of 0.45 and a permeability of 500 mD

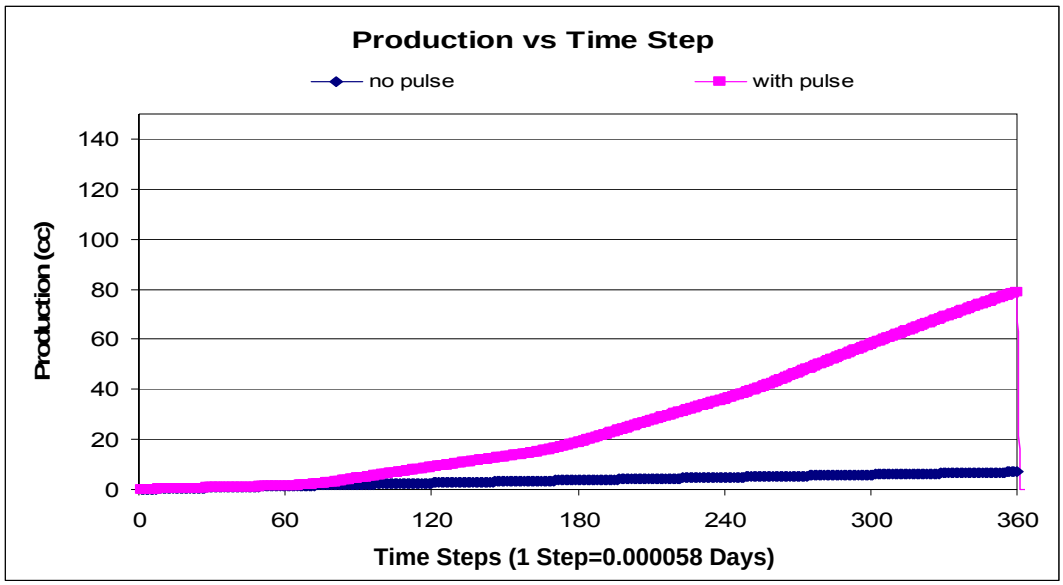

Figure 6-74: Predicted cumulative production for cases with and without pressure pulsing for a model with a fluid viscosity of 1000 cP, a porosity of 0.45 and a permeability of 250 mD

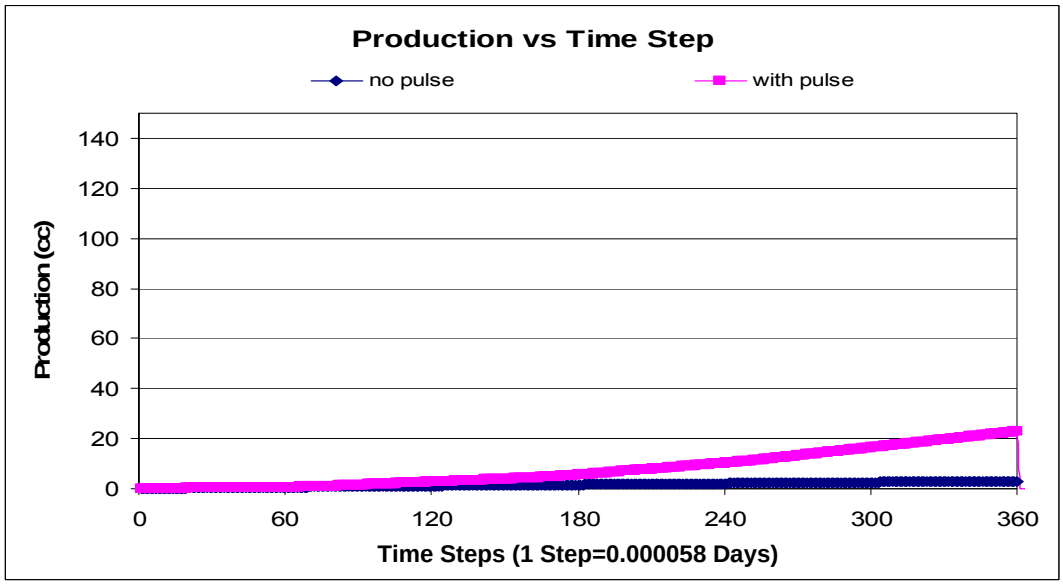

Figure 6-75: Predicted cumulative production for cases with and without pressure pulsing for a model with a fluid viscosity of 1000 cP, a porosity of 0.45 and a permeability of 100 mD

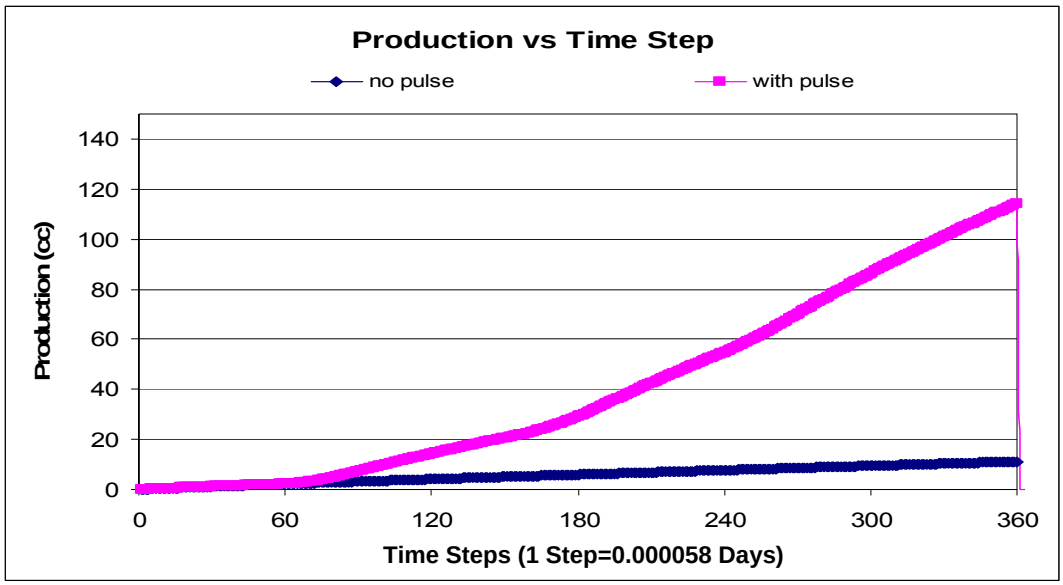

Figure 6-76: Predicted cumulative production for cases with and without pressure pulsing for a model with a fluid viscosity of 700 cP, a porosity of 0.45 and a permeability of 300 mD

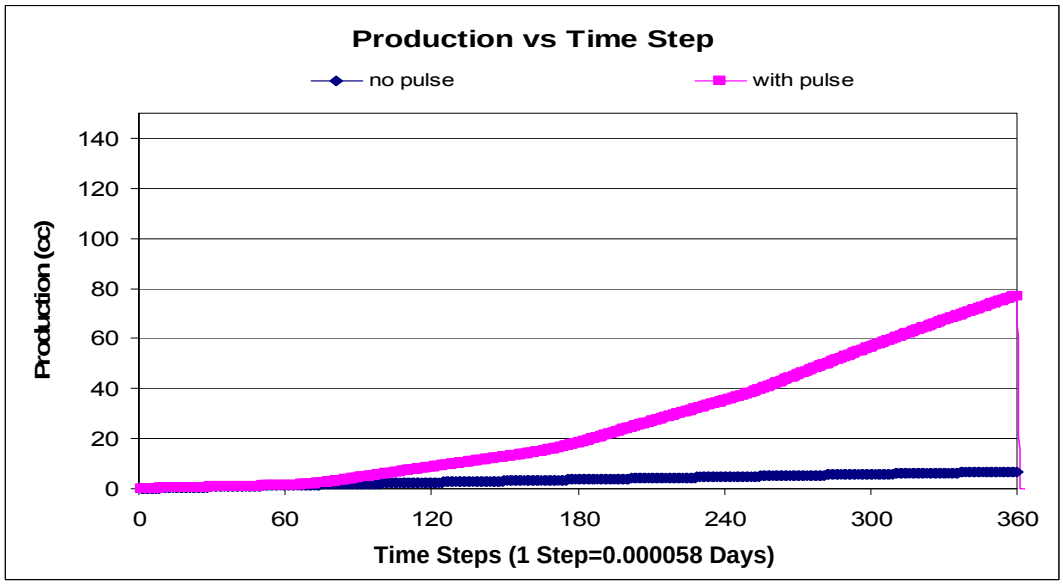

Figure 6-77: Predicted cumulative production for cases with and without pressure pulsing for a model with a fluid viscosity of 700 cP, a porosity of 0.45 and a permeability of 175 mD

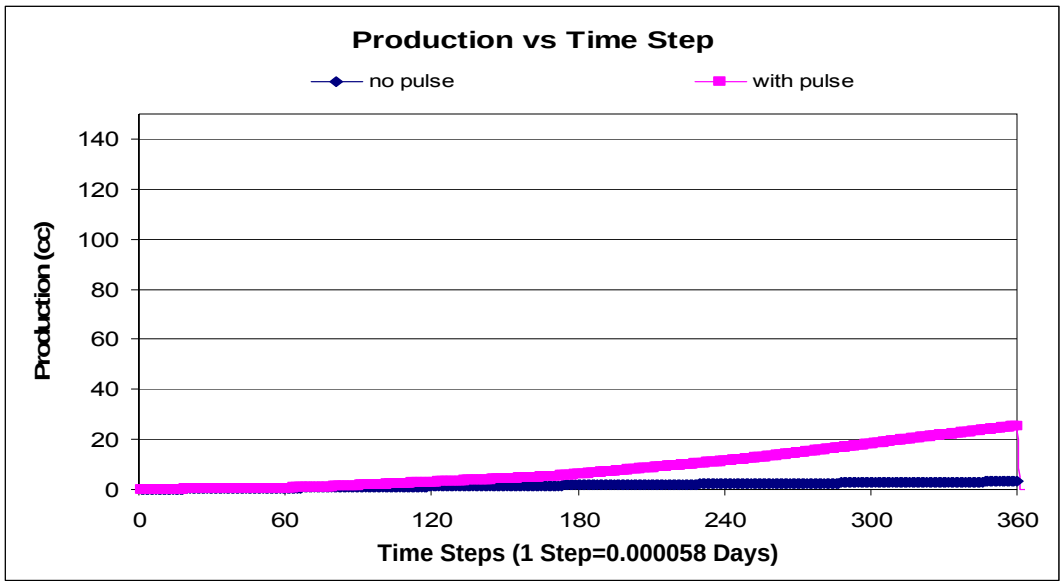

Figure 6-78: Predicted cumulative production for cases with and without pressure pulsing for a model with a fluid viscosity of 700 cP, a porosity of 0.45 and a permeability of 75 mD

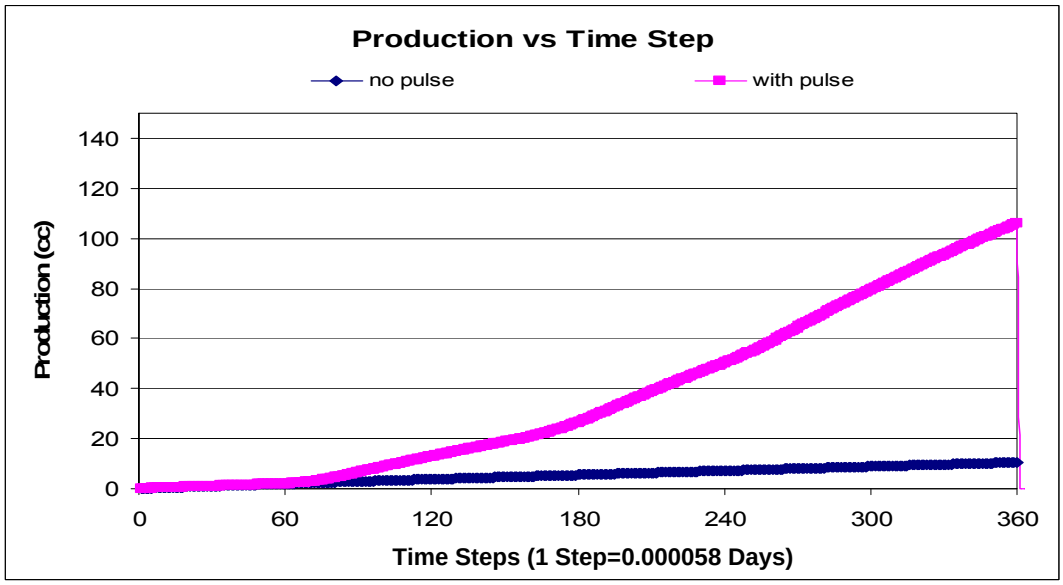

Figure 6-79: Predicted cumulative production for cases with and without pressure pulsing for a model with a fluid viscosity of 300 cP, a porosity of 0.45 and a permeability of 130 mD

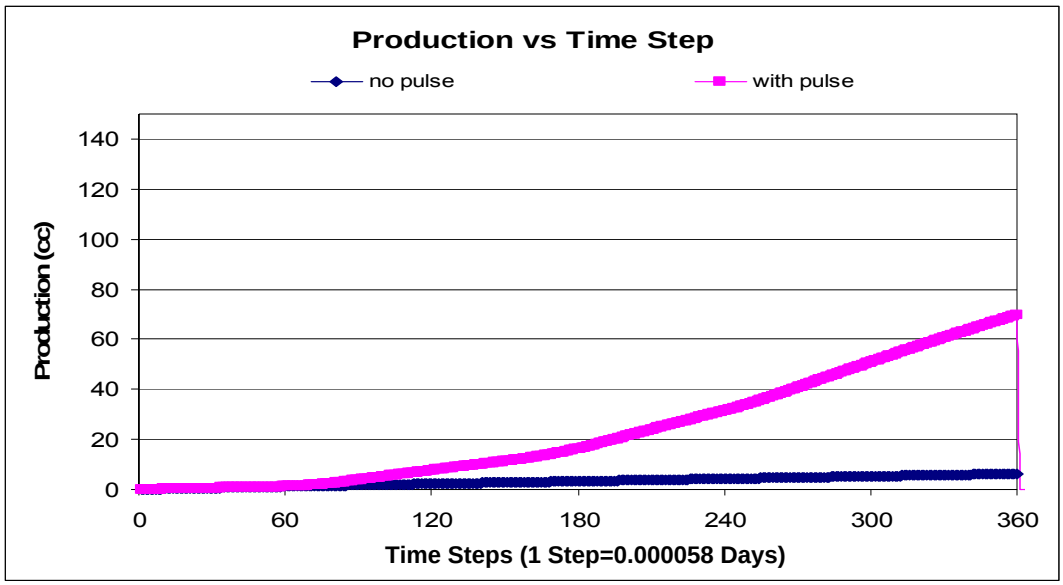

Figure 6-80: Predicted cumulative production for cases with and without pressure pulsing for a model with a fluid viscosity of 300 cP, a porosity of 0.45 and a permeability of 75 mD

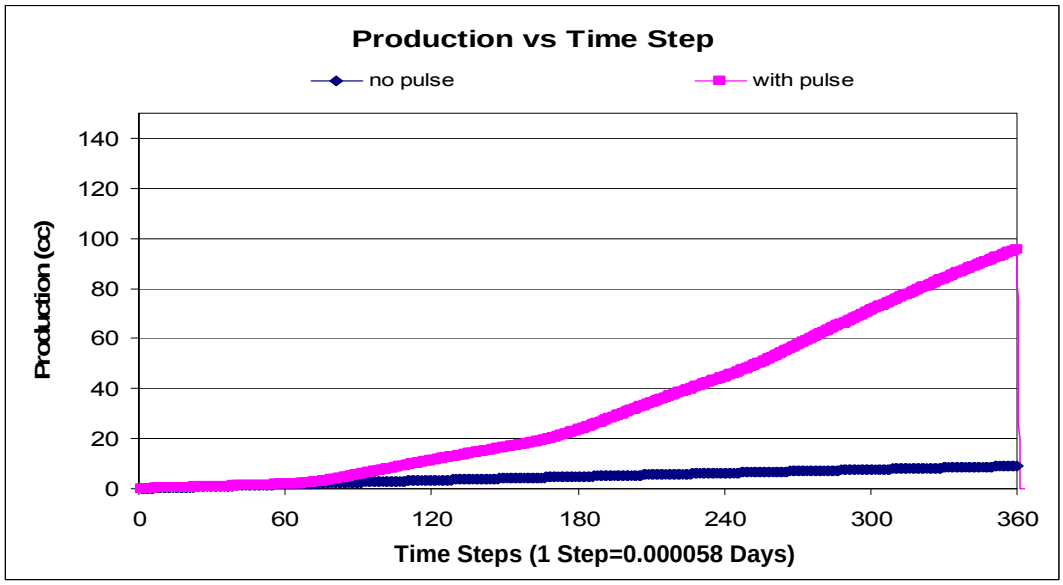

Figure 6-81: Predicted cumulative production for cases with and without pressure pulsing for a model with a fluid viscosity of 50 cP, a porosity of 0.45 and a permeability of 25 mD

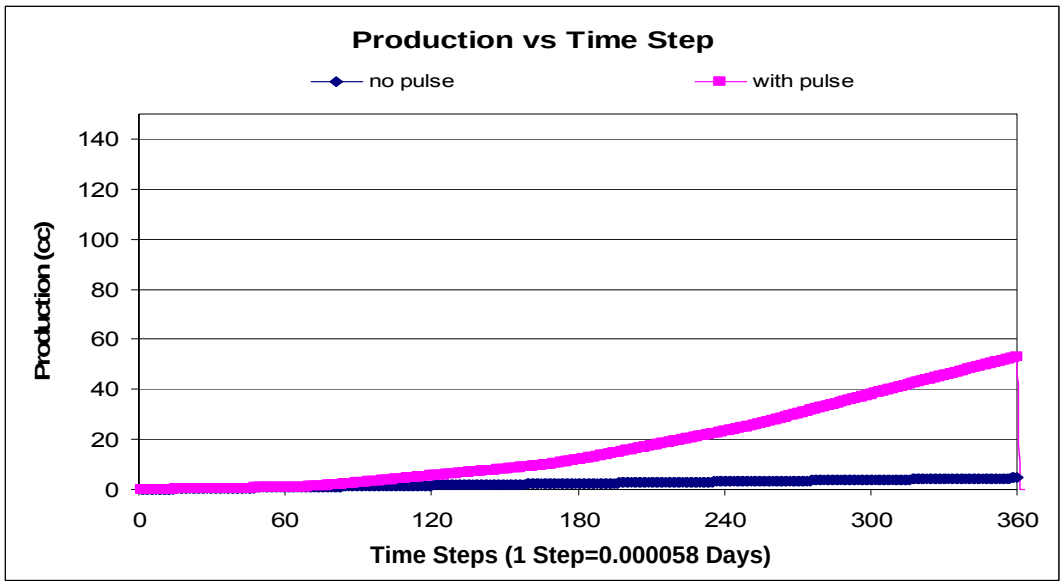

Figure 6-82: Predicted cumulative production for cases with and without pressure pulsing for a model with a fluid viscosity of 50 cP, a porosity of 0.45 and a permeability of 12 mD

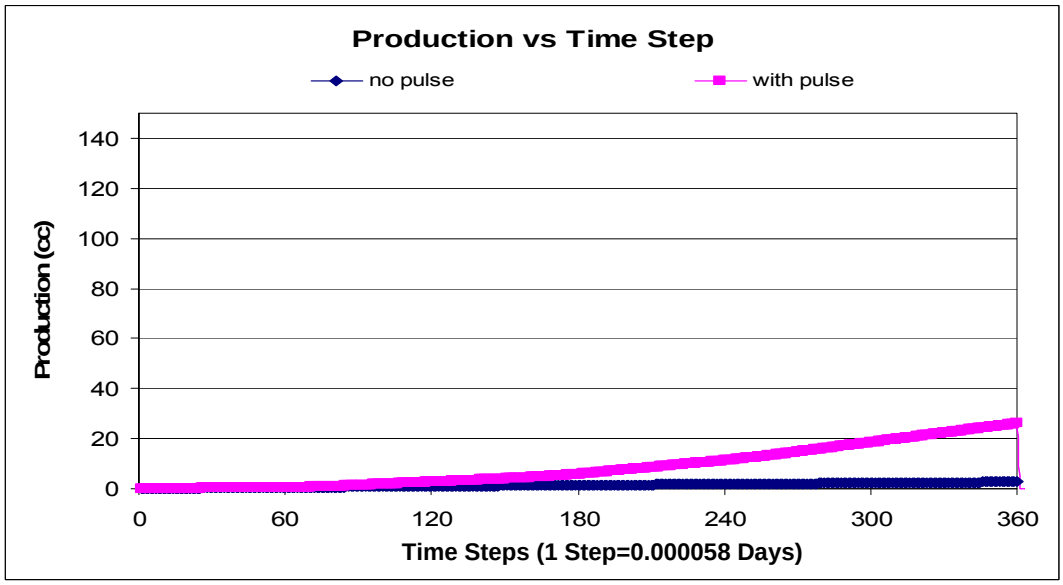

Figure 6-83: Predicted cumulative production for cases with and without pressure pulsing for a model with a fluid viscosity of 50 cP, a porosity of 0.45 and a permeability of 7 mD

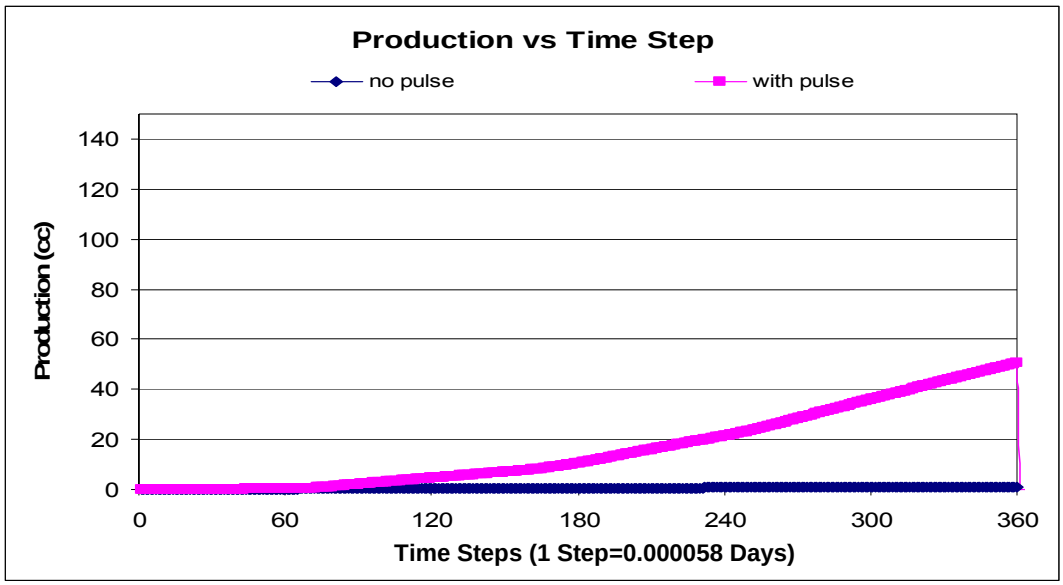

Figure 6-84: Predicted cumulative production for cases with and without pressure pulsing for a model with a fluid viscosity of 2000 cP, a porosity of 0.2 and a permeability of 90 mD

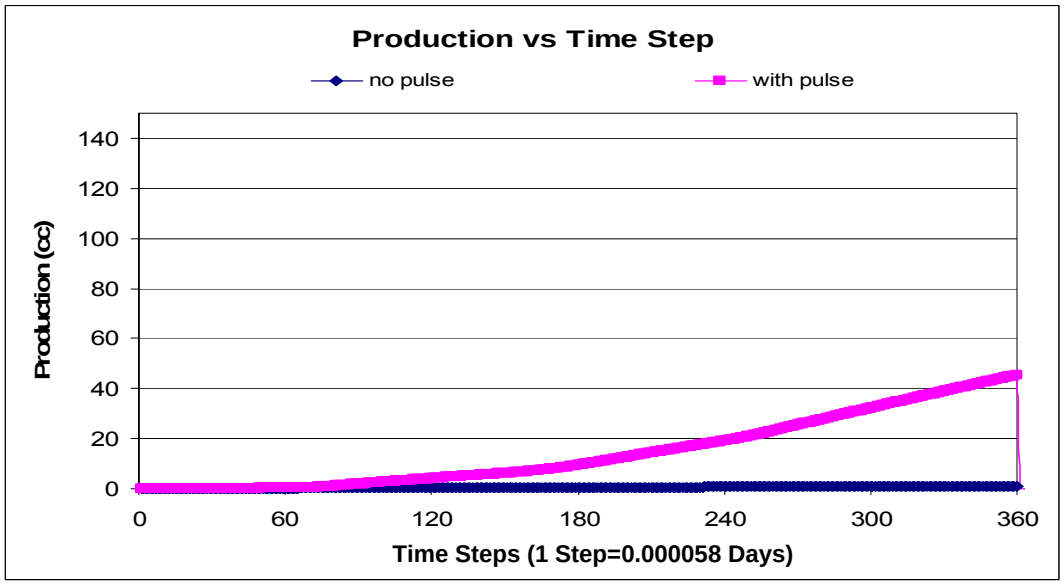

Figure 6-85: Predicted cumulative production for cases with and without pressure pulsing for a model with a fluid viscosity of 2000 cP, a porosity of 0.2 and a permeability of 80 mD

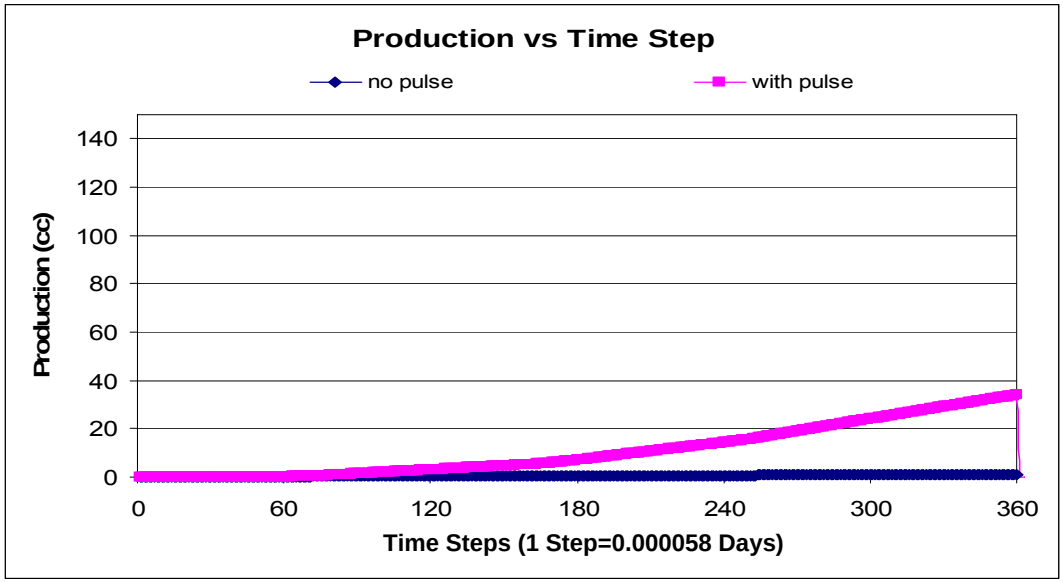

Figure 6-86: Predicted cumulative production for cases with and without pressure pulsing for a model with a fluid viscosity of 2000 cP, a porosity of 0.2 and a permeability of 60 mD

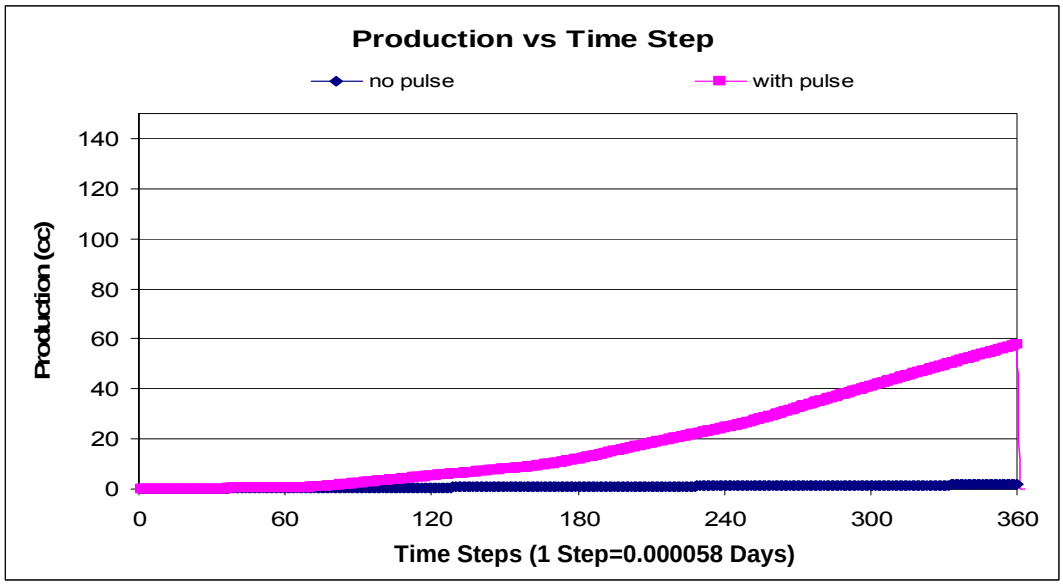

Figure 6-87: Predicted cumulative production for cases with and without pressure pulsing for a model with a fluid viscosity of 1000 cP, a porosity of 0.2 and a permeability of 60 mD

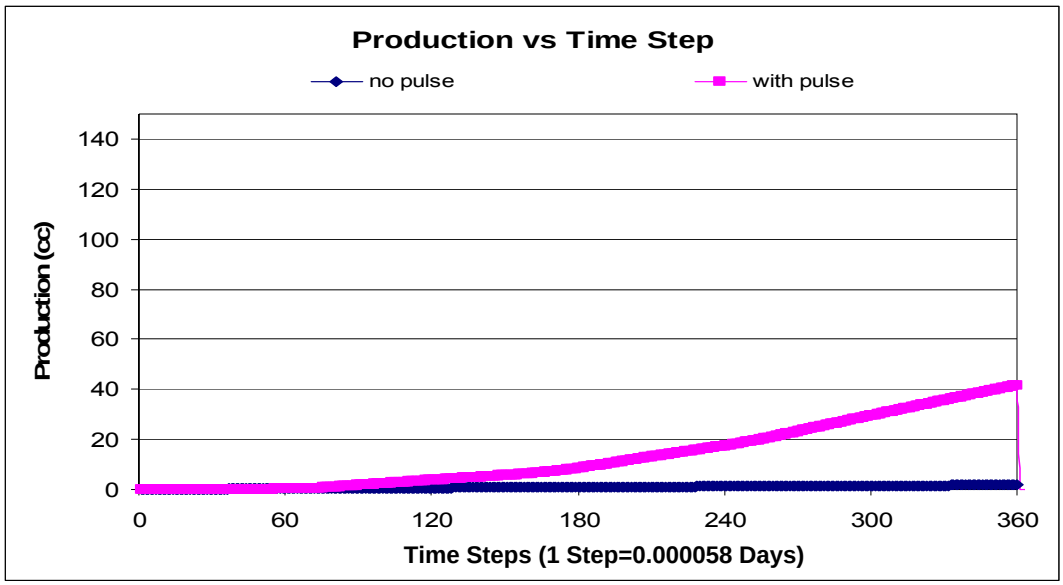

Figure 6-88: Predicted cumulative production for cases with and without pressure pulsing for a model with a fluid viscosity of 1000 cP, a porosity of 0.2 and a permeability of 40 mD

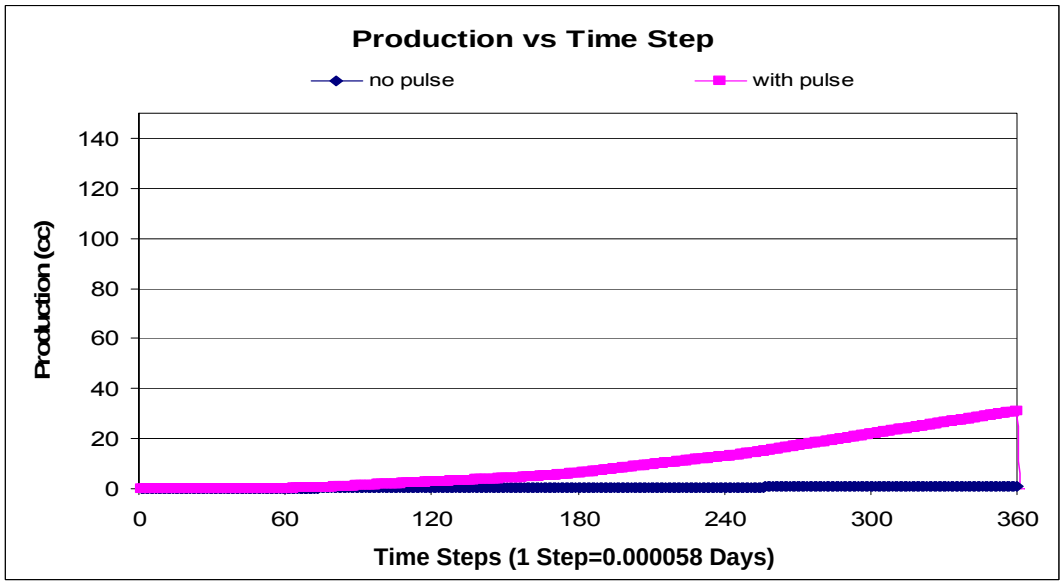

Figure 6-89: Predicted cumulative production for cases with and without pressure pulsing for a model with a fluid viscosity of 1000 cP, a porosity of 0.2 and a permeability of 30 mD

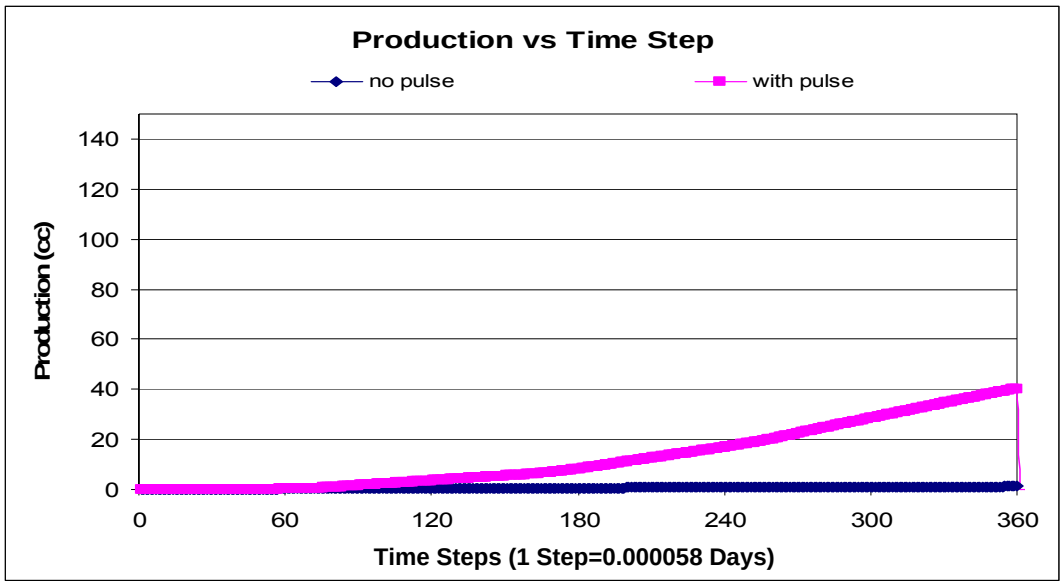

Figure 6-90: Predicted cumulative production for cases with and without pressure pulsing for a model with a fluid viscosity of 700 cP, a porosity of 0.2 and a permeability of 28 mD

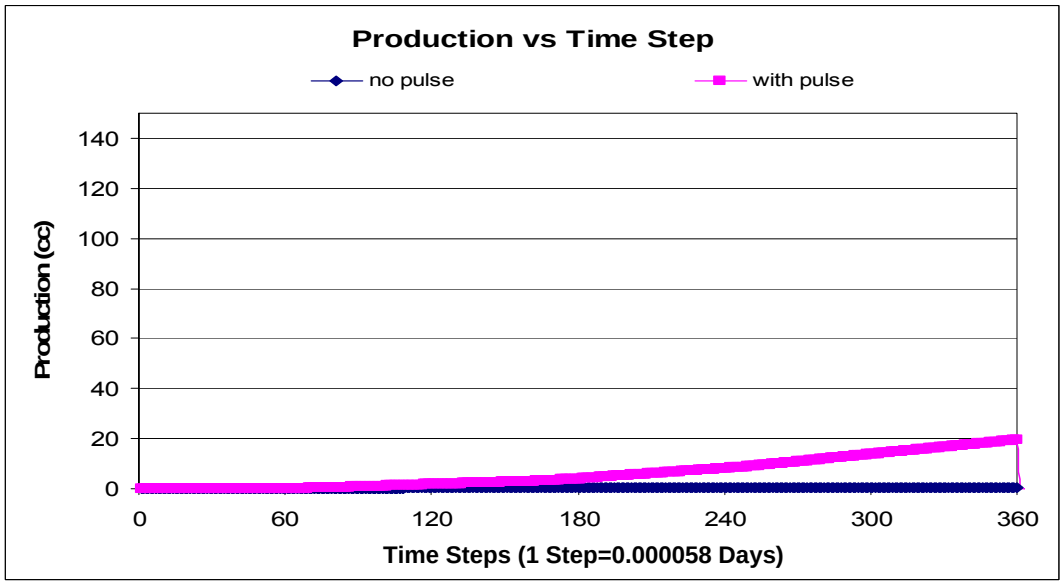

Figure 6-91: Predicted cumulative production for cases with and without pressure pulsing for a model with a fluid viscosity of 700 cP, a porosity of 0.2 and a permeability of 15 mD

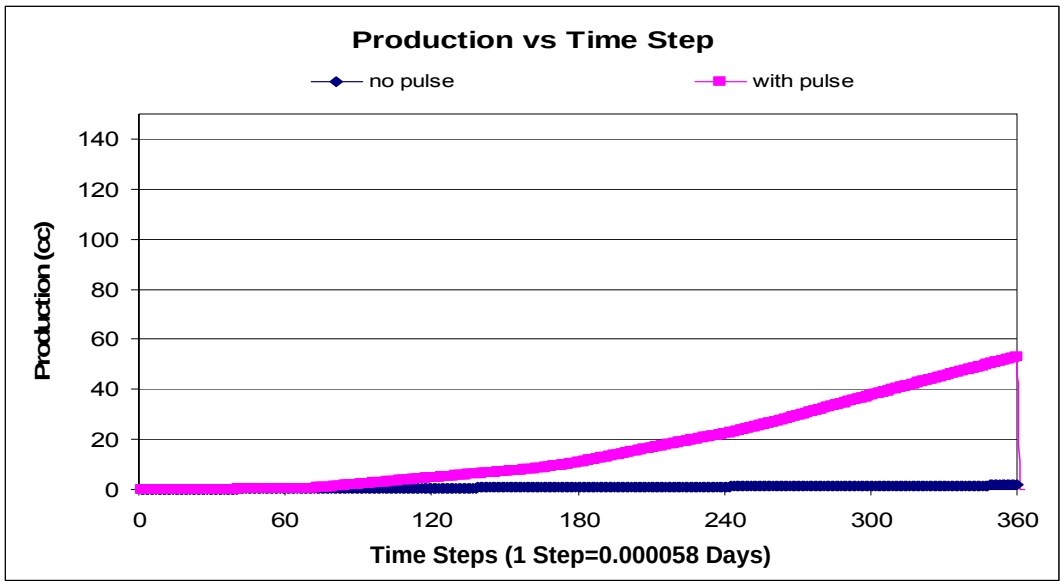

Figure 6-92: Predicted cumulative production for cases with and without pressure pulsing for a model with a fluid viscosity of 300 cP, a porosity of 0.2 and a permeability of 20 mD

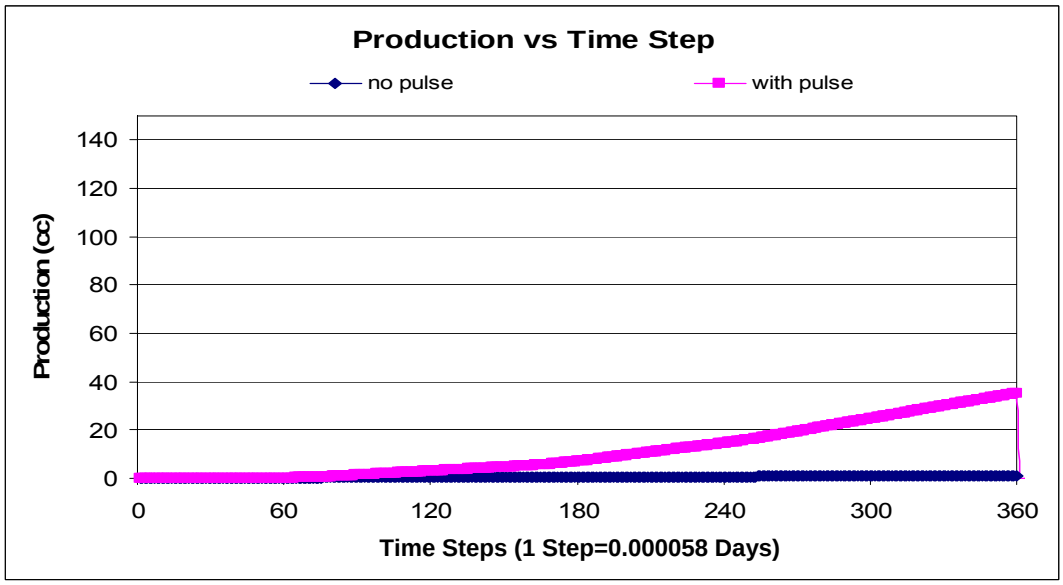

Figure 6-93: Predicted cumulative production for cases with and without pressure pulsing for a model with a fluid viscosity of 300 cP, a porosity of 0.2 and a permeability of 12 mD

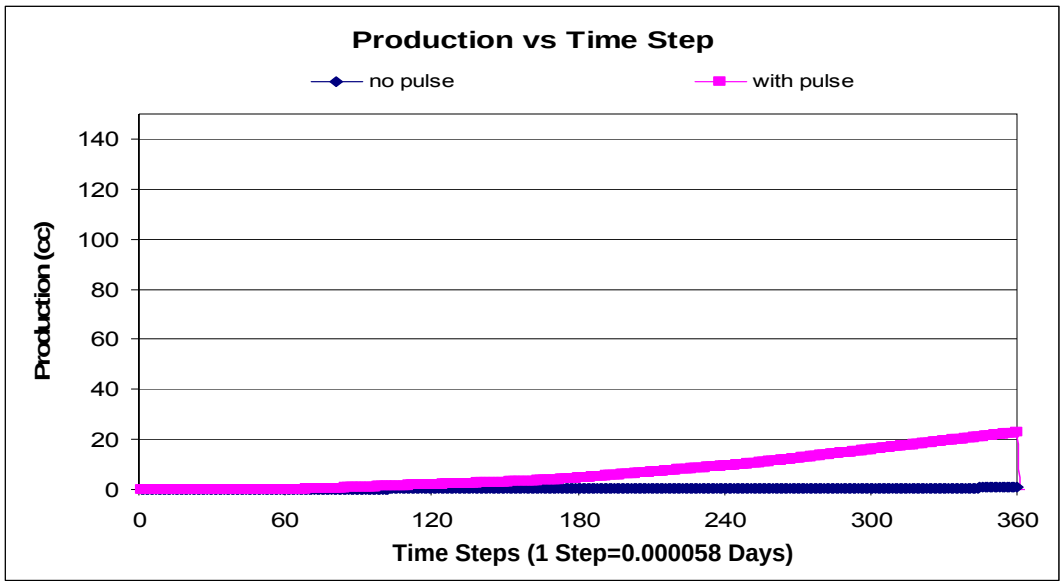

Figure 6-94: Predicted cumulative production for cases with and without pressure pulsing for a model with a fluid viscosity of 300 cP, a porosity of 0.2 and a permeability of 8 mD

The optimum permeability (the permeability at which the incremental recovery of pressure pulsing over steady-state injection is maximized) is then summarized in Figure 6-95 and Figure 6-96 for porosities of 20, 35, and 45% and for viscosities of 4000, 2000, 1000, 700, 300 and 50 cP. These figures show that the higher the porosity, the greater the optimum permeability at that viscosity. This indicates that the low attenuation associated with high permeability levels is rebuilt with high porosities. In other words, for the higher porosity levels, the energy is maintained in the pores and not let go. Also, the higher the porosity, the lower the optimum viscosity for a given frequency.

Given basic information about a reservoir, these figures could allow an engineer to quickly evaluate the effectiveness of pressure pulsing technology.

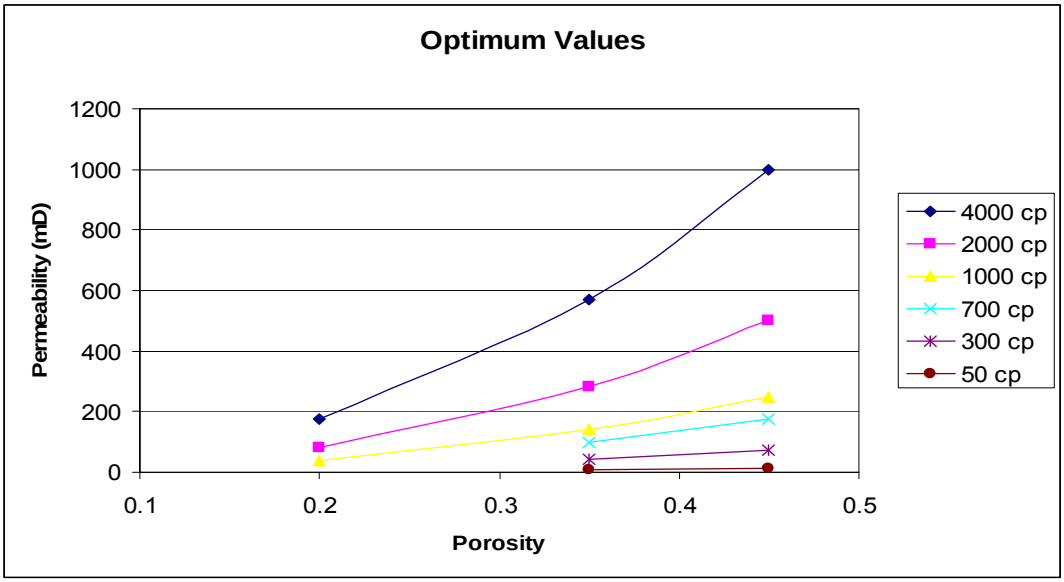

Figure 6-95: Summary of the optimum permeabilities at which pressure pulsing is beneficial versus porosity for various values of fluid viscosity

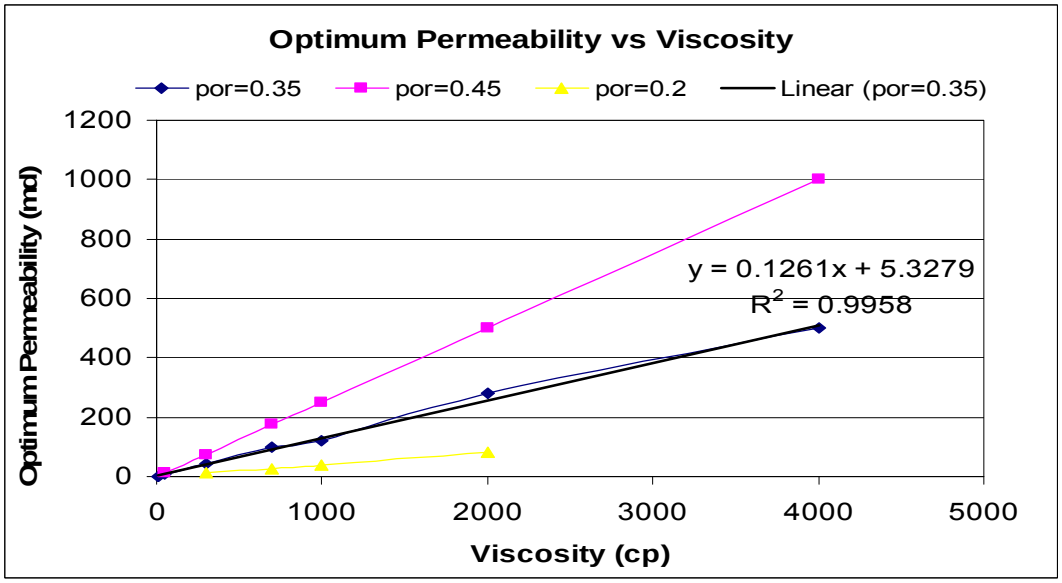

Figure 6-96: Summary of the optimum permeabilities at which pressure pulsing is beneficial versus fluid viscosity for various values of porosity

6.5.4 Compressibility Sensitivity

It has been shown previously that the porosity diffusion wave is a result of the interactions and deformations between the fluid and solid matrix in the porous media.

The porosity diffusion wave refers to a spreading front of porosity that accompanies a traveling pulse of pressure generated within a fluid-saturated porous media. Thus, it is the porosity variations in the reservoir which cause the pressure build-up and flow enhancement seen in pressure pulsing. Porosity dilation theory states that porosity diffusion is a function of wave speed and that the speed of the wave is determined by the compressibility of the solid matrix. Therefore, higher rock compressibilities lead to slower wave speeds and greater porosity variation. At very small rock compressibilities (i.e. high wave speeds), pulse energy is transferred very fast such that no change in porosity takes place. Therefore at high wave speeds no flow enhancement occurs. This argument can be summarized as below:

High comp -> Low attenuation : wave travels long distances at low velocity

Low comp -> High attenuation : wave travels fast and dies off very quickly

Three simulation runs presented here demonstrate the arguments above. Figure 6-97, Figure 6-98 and Figure 6-99 show the cumulative production plots for porous media with solid compressibilities of 3×10^{-7}, 3×10^{-5} and 3×10^{-4} psi^{-1}, respectively. For each case, the fluid viscosity was 2000 cP, the permeability was 200 mD, the porosity was 35% and the pulse frequency was 0.25 Hz.

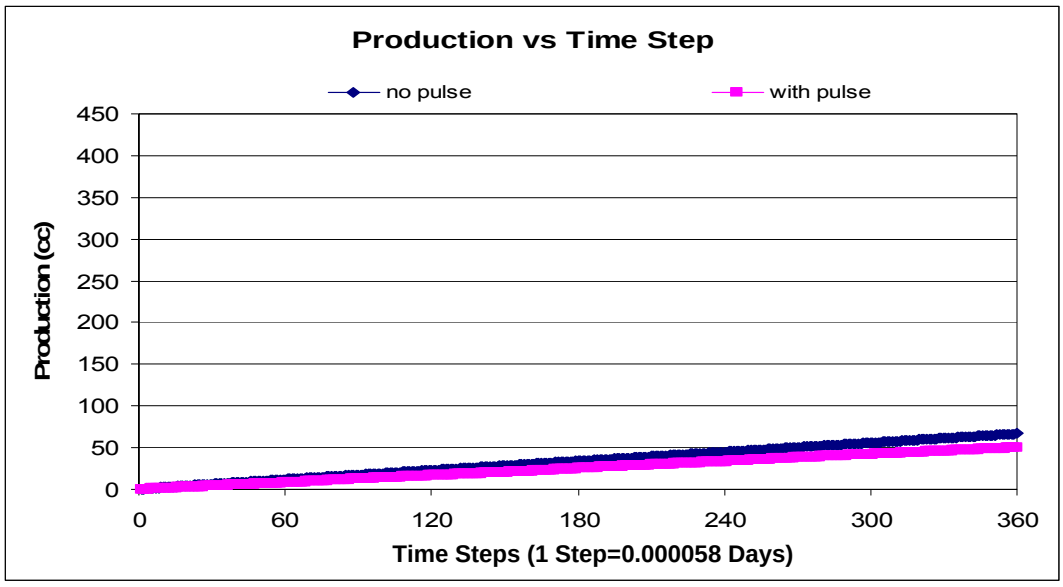

Figure 6-97: Predicted cumulative production for cases with and without pressure pulsing for a model with a rock compressibility of $3x10^{-7}$ psi^{-1}

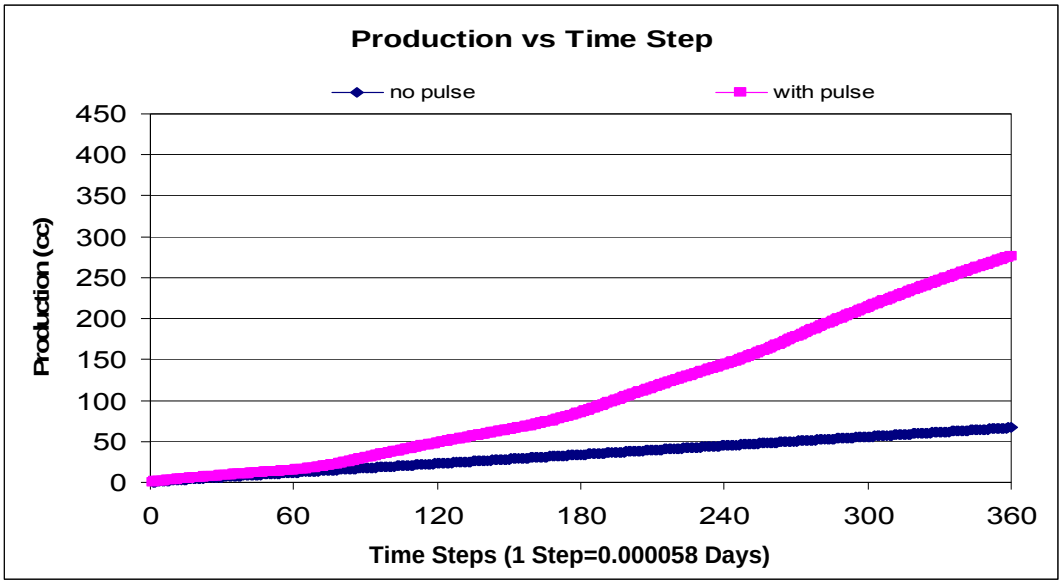

Figure 6-98: Predicted cumulative production for cases with and without pressure pulsing for a model with a rock compressibility of $3x10^{-5}$ psi^{-1}

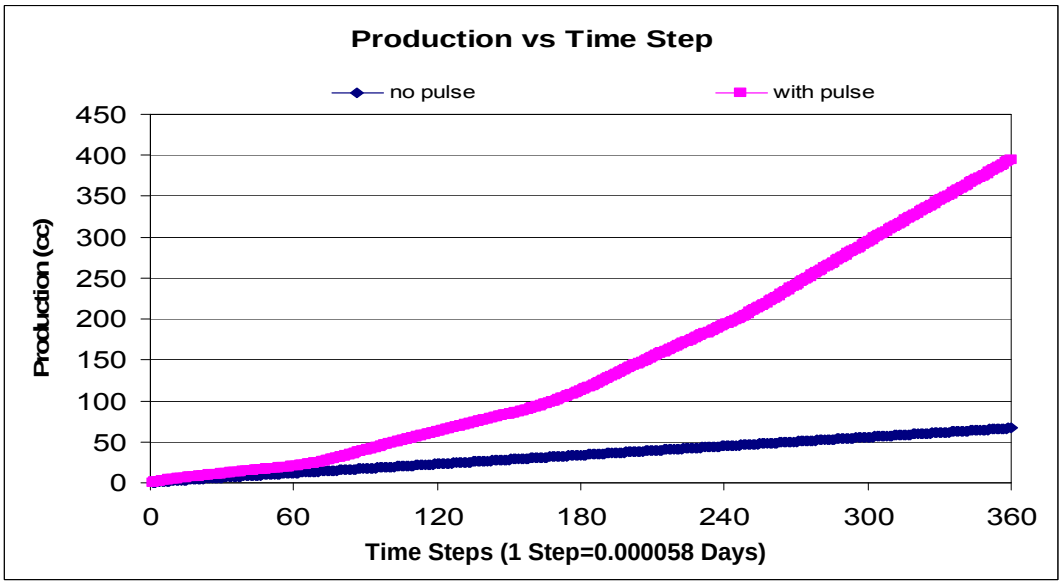

Figure 6-99: Predicted cumulative production for cases with and without pressure pulsing for a model with a rock compressibility of $3x10^{-4}$ psi^{-1}

These figures show that flow enhancement is improved with higher compressibility formations. This result agrees with the BP lab experiment that utilized a highly compressible membrane to stabilize the core sample. In that experiment, the porosity

wave “chose” to go through the highly compressible membrane leaving the relatively low compressible sample unpressurized.

6.5.5 Frequency Sensitivity

To this point, the sensitivity analysis of the pressure pulse model has focused on parameters that for a particular reservoir are unchangeable properties: rock permeability, porosity, compressibility and fluid viscosity. This analysis so far is only useful for identifying reservoirs which could have successful implementations of pressure pulse technology. It has not been useful in providing any tuneable parameters which could make pressure pulse technology successful for any particular reservoir.

A basic property of a pulse is the application frequency. Frequency, as defined here, is the time interval between two pulses. Most importantly, the frequency of a pulse is an operational parameter that can be controlled independent of the reservoir rock and fluid properties.

The simulation runs conducted in the previous sections of this work were mainly at a frequency of 0.25 Hz. Because different frequencies may have different pulse enhancement effects, some sensitivity analysis of excitation frequency is necessary to find the impact of frequency on fluid recovery. Six different application frequencies were selected for this sensitivity analysis: 0.1, 0.25, 0.4, 0.8, 1.0, and 2 Hz. The incremental cumulative production for two different viscosity fluids (4000 and 50 cP) is shown in Table 6.3 below. In each of these cases, the permeability was 200 mD, the porosity was 35% and the compressibility was 3×10^{-6} psi^{-1}.

Table 6.3: Incremental cumulative production versus pulse frequency for fluid viscosities of 4000 and 50 cP

Frequency (Hz)	Incremental Cumulative Production (%)	
	4000 cP	50 cP
0.1	39	0
0.25	115	0
0.4	101	16
0.8	83	82
1	79	108
2	74	61

The results show that, as with other parameters, the incremental cumulative production achieves a maximum at a certain frequency. This behaviour can be explained that if the pressure pulse is generated in a porous medium, it will take some time for the pressure to dissipate because of viscous effects. If the frequency is very low the next pulse is applied after the previous one dies-off, so no synergy is created to enhance the flow. However, for very high frequencies, pulses are applied too rapidly that it doesn't allow pressure to dissipate. Also, in the field applications, this pressurization should be observed carefully as high pressure build ups might cause reservoir rock to fracture.

It is also observed that a low viscosity fluid requires a higher frequency pulse to maximize the enhance flow whereas a higher viscosity fluid requires a lower frequency pulse.

As it is seen from the previous sensitivity analysis, pressure pulsing was not successful at very low viscosity fluids and high permeability reservoirs. Looking at the pressure profiles at these two cases, it is observed that there was no internal pressure build up to enhance the fluid flow. This was because the pressure from each pulse would return to the initial pressure in the medium before the next pulse was added, leading to a poor build-up effect. If the frequency was too low, the wave length would become too large, making the start of the next pulse out of the best range. This situation is shown in Figure

6-100. We can see that there is almost no pressure build up effect with a very low frequency of liquid pulsing.

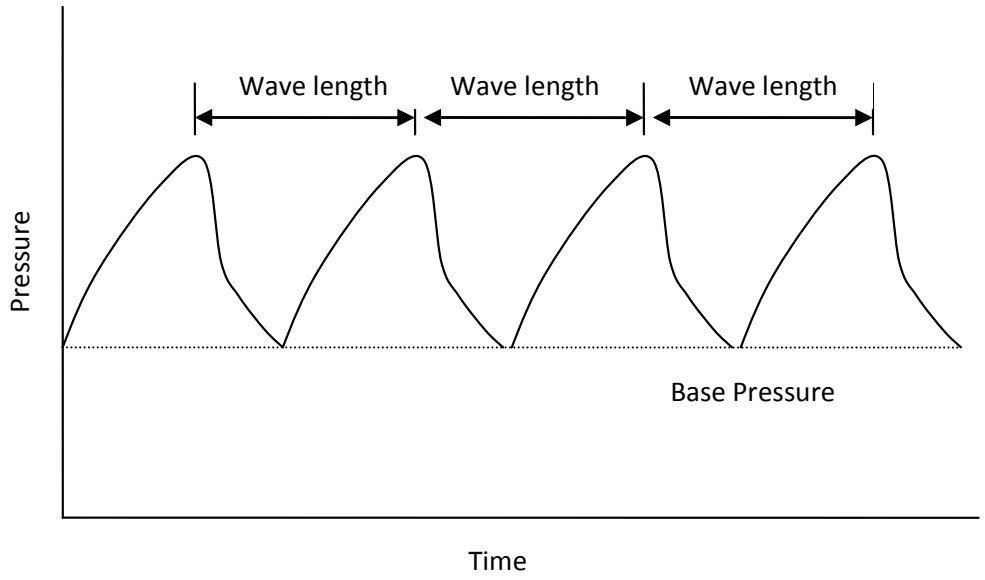

Figure 6-100: Schematic showing the undesired behavior of low frequency pressure pulses

The frequency of pressure pulsing has to be in right range to achieve a good recovery. Figure 6-101 shows higher frequency pressure pulsing.

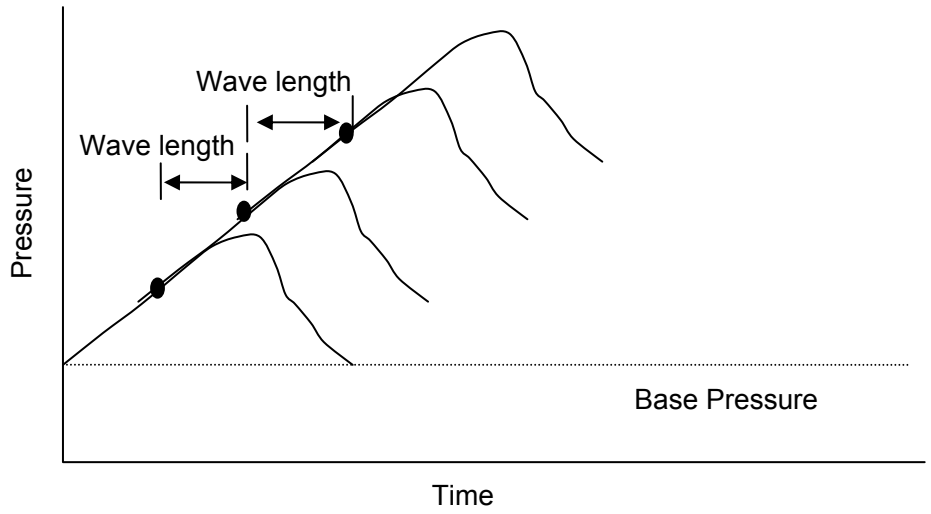

Figure 6-101: Schematic showing the desired behavior of optimal frequency pressure pulses

The next pulse is applied before the full decay of the previous pulse, so the synergism will build up a high gradient of hydraulic head, forcing the liquid to flow more quickly. It is clear that the frequency plays an important part in achieving the pressure build-up effect. The frequency determines if the next pulse is applied in the best range of the previous pulse.

In Chapter 6 the sensitivity of the output of pressure pulsing on simulation models is investigated at the lab scale. One should be cautious when interpreting sensitivity results from these small scale models. Flow rate is proportional to $\Delta P/\Delta l$, where P is pressure and l is distance from the inlet to the outlet. At the lab scale, a small ΔP across the core is required to achieve a certain flow rate. However, at the field scale, a greater ΔP is necessary to attain the same magnitude of flow rate. Moreover, in order to match the recoveries, even higher flow rates and ΔP will be required at the field scale. Therefore, one can argue that pressurization due to pressure pulsing should be greater at the field scale versus the lab scale meaning a large amplitude source is required in practice. A higher frequency and longer duration of pulses should also be achieved in the field in order to propagate sharp pressure gradients further into the reservoir, closer to the production well. However, these amplitudes and frequencies may not be reasonable due to the fracture pressure and tool capacity constraints. Therefore, lab scale recovery factors should not be applied to the field scale. It should also be noted that consolidated versus unconsolidated formations will have different recovery factors for a given amplitude-frequency pressure pulsing. The lab scale models should be scaled up by "tuning" certain parameters to investigate field scale recoveries and sensitivities. The selection of the appropriate tuning parameters deserves further research.

7 CONCLUSIONS

This dissertation has introduced the concept of pressure pulsing and geomechanics in the reservoir and addressed how to represent these physical phenomena in reservoir simulations. The research has focused on developing an iterative, fully coupled procedure that permits the analysis of porosity changes, both dynamic (propagation of porosity waves in the reservoir) and static (effective stress changes). The effects of pressure pulses on the fluid flow and production has been analyzed. In addition to pressure pulses, the combined effect of stress changes, fluid flow and reservoir property changes on oil recovery has also been evaluated by a fully coupled procedure that integrates pressure pulsing, geomechanics and reservoir simulation (BOAST, Black Oil Applied Simulation Tool). On the basis of the results from this investigation, the following conclusions are derived:

(i) The study indicates the existence of an optimum set of reservoir parameters for a given frequency at which pressure pulsing is most effective. The optimum point changes for different reservoirs and varies with each of the input parameters. For instance, in the example used in the sensitivity analysis (2000 cp, porosity 35%, rock compressibility 3x10-6 psi-1, frequency 0.25 Hz) the optimum permeability was 1000 mD. Little to no benefit was observed for permeabilities less than or greater than 1000 mD. This behaviour can be explained by considering that when the reservoir permeability is high, the pulse attenuation is small. At very small attenuations, energy from one point to another is released very fast and the pulse diffuses very quickly through the reservoir. This does not allow a significant pressure gradient to develop and, therefore, flow is not enhanced. It is observed that where the permeability is very high, the pressure increases the same amount everywhere in the reservoir and the sharp pressure gradient needed to increase fluid rate is not created. At very low permeabilities, though, the pulse attenuation is high and the pressure builds only near the injection point. Because of the slow velocity, the pulse is not able to propagate far into the reservoir in order to stimulate flow. Pressurization occurs only around the injection well and areas far

from the injection wells remain unpressurized and flow is not stimulated by the pulses. Therefore, an examination of the pressure profiles show that for a given frequency there is an optimum permeability where we achieve the maximum ratio of cumulative production with pulse to cumulative production with no pulse.

(ii) It is concluded that, generally, the energy-preserving ability of light oil is weaker than that of viscous oil. If the frequency used in the case of a light oil is too low, the previous pulse dissipates too much before the next pulse is added, leading to a poor build up effect. For a given frequency there is an optimum viscosity where the maximum ratio of cumulative production with pulse to cumulative production with no pulse is achieved.

(iii) The results from the study indicate that the low attenuation associated with high permeability levels is rebuilt with high porosities. In other words, for the higher porosity levels, the energy is maintained in the pores and not allowed to release. Also, the higher the porosity, the lower the optimum viscosity for a given frequency.

(iv) Porosity dilation theory states that porosity diffusion is a function of wave speed and that the speed of the wave is determined by the compressibility of the solid matrix. Therefore, higher rock compressibilities lead to slower wave speeds and greater porosity variation. At very small rock compressibilities (i.e. high wave speeds), pulse energy is transferred very fast such that no change in porosity takes place. Therefore at high wave speeds no flow enhancement occurs.

(v) The results show that, as with other parameters, the incremental cumulative production achieves a maximum at a certain frequency. This behaviour can be explained that if the pressure pulse is generated in a porous medium, it will take some time for the pressure to dissipate because of viscous effects. If the frequency is very low the next pulse is applied after the previous one dies-off, so no synergy is created to enhance the flow. However, for very high frequencies,

pulses are applied too rapidly such that pressure isn't allowed to dissipate. Also, in the field applications, this pressurization should be observed carefully as high pressure build-ups might cause the reservoir rock to fracture.

(vi) Three sets of boundary conditions were investigated in this study. It is observed that bottom the boundary condition is the most important factor determining permeability variation. This result indicates that for cases with non-deformable boundaries, less compaction occurs due to decreases in reservoir pressure. This results in a lower reduction in the reservoir permeability versus cases with deformable boundaries.

(vii) For each of the boundary condition cases studied, the reduction in the permeability is maximized at the middle layer. The explanation for this behaviour may be that the rock deformation is at its maximum in the mid-layer, where fluid flow occurs in all directions, and at a minimum in the upper and lower layers, where fluid flow is constrained by the non-permeable layers of the outer domain. This argument is proved by our study showing the volumetric strain is at its maximum at the mid-layer and minimized at the upper and lower layers.

(viii) The results indicate that the reservoir permeability decreases less with time as the rock elastic moduli of the outer domain increases. This behaviour is a reflection of the fact that the higher the Young's modulus, the lower the ability of the outer domain to deform. As the outer domain loses its ability to deform, it imparts less compaction on the reservoir and therefore less reduction in the reservoir permeability.

(ix) The inclusion of the outer domain dramatically increases both the computer storage requirements and program execution time. However, the study shows that the permeability profile curves obtained from the two-domain and the single-domain models differ considerably. At all times, the two-domain model yields a greater change in the permeability profile with time versus the single-domain

model. This behaviour can be explained by the fact that as the pore pressure at the reservoir boundaries declines, the geomechanical conditions at the reservoir boundaries change in two ways: 1) incremental displacements at the boundaries become different than zero, and 2) due to rock expansion or compression, the local stress state at the boundaries may vary with time. These reservoir boundary deformation effects included in the two-domain model but not in the single-domain model are translated into an extra permeability decrease.

8 RECOMMENDATIONS

The model developed in this study represents an advancement in the simulation of oil reservoirs with an iterative, fully coupled procedure that permits the analysis of pressure pulsing by modeling the propagation of porosity waves in a reservoir. In addition to a model of pressure pulsing, a 3D finite difference, fully implicit geomechanical model is developed to simulate the physical phenomena occuring during the production from reservoirs with stress-sensitive mechnical and fluid-flow properties. Although the model is verified by lab tests some additional features must be investigated or modified to use the model for more complicated situations. A few aspects to be considered for future research are:

(i) Applying pressure pulsing as EOR is a very new technique in the industry. There is very few field data which has been released to the public knowledge. Due to the lack of field data, the pressure pulse model is verified with only lab experiments. However, large scale field results could be different from small scale lab results as waves propagate 3D rather than 2D. It is highly recommended to collabrate with industry to obtain field data and compare them with the pressure pulse model developed in this research.

(ii) The theory developed in this study shows that as porosity wave propagates it causes porosity and saturation changes. The dynamic saturation changes are in addition to the saturation changes due to injection and/or production. It is caused by inertial effects due to pressure pulsing. As is widely known, capillary pressure is a function of saturation. The equations developed in this dissertation link capillary pressure changes to the dynamic saturation changes, however, only the static capillary pressure is taken into account in the simulation developed. It is recommended that future work incorporate dynamic capillary pressure changes into the simulator.

(iii) Pore structure has long been recognised as one of the key factors determining the shape of relative permeability curves. The permeability of a phase relates to pore throat size and hence to saturation at a given capillary pressure. In many data sets, there is a strong relationship between permeability and mobile oil saturation. For instance, the small permeability sandstone has much higher end point saturations than high permeability sand. Our study shows that as the porosity wave propagates in the rock, porosity and permeability changes. Additional work is still required to update relative permeability curves in the simulation as the rock permeability changes in a grid block.

(iv) Volumetric strain was used as wellbore boundary condition (source). One can define the pulse tool and amplitude in terms of pressure and convert this into volumetric strain. However, for the sake of simplicity, reservoir is decoupled from the wellbore and the strain is taken as a pulse source. There are two basic options for pulse generation: use of the entire tubing string as a drop weight, forcing all the casing liquid below the pressure pulse tool throught the perforations; and, use of a bottom hole independent piston driven by mechanical hydraulic means. In our equations the pressure pulse source term is an input in the equations. Research is required to define the pressure pulse source term as a function of the pulse generating tool. This would allow including drop weight, wellbore length, perforation size and intervals in the calculation of source term in the simulation tool.

(v) In this study the primary focus was the lab scale. However, it is important to investigate the large scale, both spatially and with time, in applying this simulation tool to field scale processes. Additional effort should be put to understanding the scaling parameters.

(vi) The success of pressure pulsing in the laboratory depends on right boundary conditions. Spacing between the rubber membrane and the core can act as a thief zone which would become a preferential path for dilation waves. Another set of

experiments using proper boundary conditions should be conducted and the results should be compared with the existing lab results (which used the improper boundary conditions).

(vii) This study assumes permeability is a function of mean effective stress, meaning that it changes in the same amount in every direction. However, it is known that fractures occur in the direction of maximum principal stress and perpendicular to the minimum principal stress. It should be further investigated if the permeability change in the minimum and maximum axes behave differently.

(viii) The geomechanical model developed in this study was validated with the results from literature. The results clearly show that permeability of stress-sensitive reservoirs may significantly change through the reservoir production life. This change is highly dependent on reservoir conditions and production scenarios. It is recommended that the results of our model be validated with field data and investigate the impact of permeability changes on actual reservoir production and compare with our model.

(ix) This study uses only fluid-flow analytical solutions as the well inflow equations. The geomechanical coupling effects are considered through the permeability changes. It should be investigated if the well productivity might be influenced by the stress-induced permeability change. Also, it is recommended to study the effects of well radius change due to geomechanics on the skin factor.

(x) In this study cartesian coordinates are used because of the restrictions of the oil simulator. Multi noded quadrilateral grids might allow for higher order of shape functions and a finer mesh near the wellbore and near the reservoir-sideburden interface to better capture the larger stress and strain gradients in these areas. To deal with large scale processes, such as far-field stress chages, coarser grids can be used at areas where stress and strain change slowly.

APPENDIX A – IMPES PROCEDURE

The method by which the pressure and saturation equations are built and solved by the IMPES procedure is explained below:

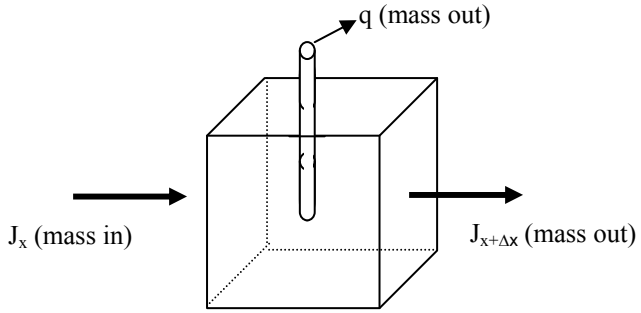

Figure A-1: Conservation of mass

Figure A-1 shows the conservation of mass in a unit volume of reservoir. 'J_x' represents the flux of mass into the unit volume in x-direction, 'q' is the mass injected or produced from the unit volume of reservoir and '$J_{x+\Delta x}$' is the flux of mass leaving the unit volume. According to this, mass in and mass out can be written as:

$$\text{Mass in} \quad = \left[\left(J_x\right)_x \Delta y \Delta z + \left(J_y\right)_y \Delta x \Delta z + \left(J_z\right)_z \Delta x \Delta y\right] \Delta t \quad ; \tag{A.1}$$

$$\text{Mass out} \quad = -\left[\left(J_x\right)_{x+\Delta x} \Delta y \Delta z + \left(J_y\right)_{y+\Delta y} \Delta x \Delta z + \left(J_z\right)_{z+\Delta z} \Delta x \Delta y\right] \Delta t - q \Delta x \Delta y \Delta z \Delta t \; . \tag{A.2}$$

Also, the mass difference between one time step and another is given as:

$$\begin{matrix}\text{Mass} \\ \text{accumulation}\end{matrix} \quad = \left[\left(C_p\right)_{t+\Delta t} - \left(C_p\right)_t\right] \Delta x \Delta y \Delta z \quad . \tag{A.3}$$

Here, 'J' is mass flux, 'q' is a sink or source term and 'C_p' is the concentration of phase p. Dividing the equation by $\Delta x\, \Delta y\, \Delta z\, \Delta t$ and rearranging gives:

$$-\frac{(J_x)_{x+\Delta x}-(J_x)_x}{\Delta x}-\frac{(J_y)_{y+\Delta y}-(J_y)_y}{\Delta y}-\frac{(J_z)_{z+\Delta z}-(J_z)_z}{\Delta z}-q=\frac{(C_p)_{t+\Delta t}-(C_p)_t}{\Delta t}. \quad \text{(A.4)}$$

As Δx, Δy, Δz and Δt goes to zero:

$$-\frac{\partial J_x}{\partial x}-\frac{\partial J_y}{\partial y}-\frac{\partial J_z}{\partial z}-q=\frac{\partial C_p}{\partial t} \quad . \quad \text{(A.5)}$$

The mass flux, 'J', is described as followed:

$$J_p=\frac{\rho_{psc}}{B_p}\vec{v}_p \quad ; \quad \text{(A.6)}$$

where the 'ρ' is density, 'B' is formation volume factor, and 'v' is velocity. The subscript 'p' refers to the fluid phase (oil, water or gas) and 'sc' refers to standard conditions. In the case of a gas reservoir, solution gas ratios are also included in the equations (more information on this case can be seen in the BOAST manual[53]).

The fluid concentrations are defined as:

$$C_p=\frac{\phi\rho_{psc}S_p}{B_p} \quad ; \quad \text{(A.7)}$$

where 'ϕ' is the porosity and 'S' is the fluid saturation.

Using these equations in Equation (A.5), the mass conservation becomes:

$$-\nabla\frac{\vec{v}_p}{B_p}-\frac{q_p}{\rho_{psc}}=\frac{\partial}{\partial t}\left(\frac{\phi S_p}{B_p}\right) \quad . \quad \text{(A.8)}$$

The Darcy fluid velocity is defined as:

$$v_{ip} = -K_i \lambda_p \frac{\partial}{\partial x}\left(P_p - \frac{\rho_p g z}{144 \rho_c} \right) \ ; \tag{A.9}$$

where 'λ_p' is the phase mobility and defined as $\lambda_p = \frac{k_{rp}}{\mu_p}$ where 'k_{rp}' is relative phase permeability and 'μ_p' is phase viscosity.

Substituting the velocity equation (A.9) into the mass conservation equation (A.8) and writing it in vector form:

$$\nabla \frac{\vec{K}\lambda_p}{B_p} \nabla P_p - \nabla \frac{\vec{K}\lambda_p}{B_p} \nabla\left(\frac{\rho_p z}{144} \right) - \frac{q_p}{\rho_{psc}} = \frac{\partial}{\partial t}\left(\frac{\phi S_p}{B_p} \right) \ . \tag{A.10}$$

Introducing the concept of capillary pressure, the water phase pressure can be written in terms of oil pressure:

$$P_w = P_o - P_{COW} \ ; \tag{A.11}$$

$$P_g = P_{CGO} + P_o \ . \tag{A.12}$$

So now the mass conservation equations for each phase can be written in terms of oil phase pressure as:

OIL: $$\nabla \frac{\vec{K}\lambda_o}{B_o} \nabla P_o - \nabla \frac{\vec{K}\lambda_o}{B_o} \nabla\left(\frac{\rho_o z}{144} \right) - \frac{q_o}{\rho_{osc}} = \frac{\partial}{\partial t}\left(\frac{\phi S_o}{B_o} \right) \ ; \tag{A.13}$$

WATER: $$\nabla \frac{\vec{K}\lambda_w}{B_w}\nabla P_o - \nabla \frac{\vec{K}\lambda_w}{B_w}\nabla\left(\frac{\rho_w z}{144} + P_{COW}\right) - \frac{q_w}{\rho_{wsc}} = \frac{\partial}{\partial t}\left(\frac{\phi S_w}{B_w}\right) \quad ; \qquad \text{(A.14)}$$

GAS: $$\nabla\left[\vec{K}\left(\frac{\lambda_g}{B_g} + \frac{R_{so}\lambda_o}{B_o} + \frac{R_{sw}\lambda_w}{B_w}\right)\right]\nabla P_o -$$

$$\nabla\left\{\vec{K}\left[\frac{\lambda_g}{B_g}\nabla\left(P_{CGO} - \frac{\rho_g z}{144}\right) - \frac{R_{so}\lambda_o}{B_o}\nabla\frac{\rho_o z}{144} - \frac{R_{sw}\lambda_w}{B_w}\nabla\left(P_{COW} - \frac{\rho_w z}{144}\right)\right]\right\} - \frac{q_g}{\rho_{gsc}}$$

$$= \frac{\partial}{\partial t}\left[\phi\left(\frac{S_g}{B_g} + \frac{R_{so}S_o}{B_o} + \frac{R_{sw}S_w}{B_w}\right)\right] \quad . \qquad \text{(A.15)}$$

Constructing Pressure Equations:

Applying the chain rule to the right hand side of the flow equations, we can write the RHS in terms of the pressure derivative:

$$L_o = \frac{\partial}{\partial t}\left(\frac{\phi S_o}{B_o}\right) = \frac{\phi}{B_o}\frac{\partial S_o}{\partial t} + \left[\frac{S_o}{B_o}\frac{\partial \phi}{\partial P_o} - \frac{S_o \phi}{B_o^{\,2}}\frac{\partial B_o}{\partial P_o}\right]\frac{\partial P_o}{\partial t} \quad ; \qquad \text{(A.16)}$$

$$L_w = \frac{\partial}{\partial t}\left(\frac{\phi S_w}{B_w}\right) = \frac{\phi}{B_w}\frac{\partial S_w}{\partial t} + \left[\frac{S_w}{B_w}\frac{\partial \phi}{\partial P_o} - \frac{S_w \phi}{B_w^{\,2}}\frac{\partial B_w}{\partial P_o}\right]\frac{\partial P_o}{\partial t} \quad ; \qquad \text{(A.17)}$$

$$L_g = \frac{\partial}{\partial t}\left[\phi\left(\frac{S_g}{B_g} + \frac{R_{so}S_o}{B_o} + \frac{R_{sw}S_w}{B_w}\right)\right]$$

$$= \frac{\phi}{B_g}\frac{\partial S_g}{\partial t} + \left[\frac{S_g}{B_g}\frac{\partial \phi}{\partial P_o} - \frac{S_g}{B_g^{\,2}}\frac{\partial B_g}{\partial P_o}\right]\frac{\partial P_o}{\partial t} + \frac{\phi R_{so}}{B_o^{\,2}}\frac{\partial S_o}{\partial t} + \left[\frac{R_{so}S_o}{B_o}\frac{\partial \phi}{\partial P_o} - \frac{\phi S_o}{B_o}\frac{\partial R_{so}}{\partial P_o} - \frac{R_{so}\phi S_o}{B_o^{\,2}}\frac{\partial B_o}{\partial P_o}\right]\frac{\partial P_o}{\partial t}$$

$$+ \frac{\phi R_{sw}}{B_w}\frac{\partial S_w}{\partial t} + \left[\frac{R_{sw}S_w}{B_w}\frac{\partial \phi}{\partial P_o} - \frac{\phi S_w}{B_w}\frac{\partial R_{sw}}{\partial P_o} - \frac{R_{sw}\phi S_w}{B_w^{\,2}}\frac{\partial B_w}{\partial P_o}\right]\frac{\partial P_o}{\partial t} \quad ; \qquad \text{(A.18)}$$

knowing that $S_o+S_w+S_g=1$, then:

$$\frac{\partial S_g}{\partial t} = -\frac{\partial S_o}{\partial t} - \frac{\partial S_w}{\partial t} \quad . \tag{A.19}$$

Substituting Equation (A.19) into L_g (A.18):

$$L_g = \left(\frac{R_{so}\phi}{B_o} - \frac{\phi}{B_g}\right)\frac{\partial S_o}{\partial t} + \left(\frac{\phi R_{sw}}{B_w} - \frac{\phi}{B_g}\right)\frac{\partial S_w}{\partial t} +$$
$$\left(\frac{S_g}{B_g}\frac{\partial \phi}{\partial P_o} - \frac{S_g\phi}{B_g^{\,2}}\frac{\partial B_g}{\partial P_o} + \frac{R_{so}S_o}{B_o}\frac{\partial \phi}{\partial P_o} + \frac{\phi S_o}{B_o}\frac{\partial R_{so}}{\partial P_o} - \frac{R_{so}\phi S_o}{B_o^{\,2}}\frac{\partial B_o}{\partial P_o} + \frac{R_{sw}S_w}{B_w}\frac{\partial \phi}{\partial P_o} + \frac{\phi S_w}{B_w}\frac{\partial R_{sw}}{\partial P_o} - \frac{R_{sw}\phi S_w}{B_w^{\,2}}\frac{\partial B_w}{\partial P_o}\right)\frac{\partial P_o}{\partial t} .$$

(A.20)

Now, we have three equations and three unknowns (P_o, S_o, S_w). Multiplying the oil equation (A.16) by (B_o-$R_{so}B_g$), the water equation (A.17) by (B_w-$R_{sw}B_g$) and the gas equation (A.20) by B_g and adding the results together gives:

$$\left(B_o - R_{so}B_g\right)L_o + \left(B_w - R_{sw}B_g\right)L_w + B_gL_g = \left(B_o - R_{so}B_g\right)\frac{\phi}{B_o}\frac{\partial S_o}{\partial t} + \left(B_w - R_{sw}B_g\right)\frac{\phi}{B_w}\frac{\partial S_w}{\partial t} + B_g\left(\frac{R_{so}\phi}{B_o} - \frac{\phi}{B_g}\right)\frac{\partial S_o}{\partial t}$$
$$+ B_g\left(\frac{\phi R_{sw}}{B_w} - \frac{\phi}{B_g}\right)\frac{\partial S_w}{\partial t} + \left(B_o - R_{so}B_g\right)\left[\frac{S_o}{B_o}\frac{\partial \phi}{\partial P_o} - \frac{S_o}{B_o^{\,2}}\frac{\partial B_o}{\partial P_o}\right]\frac{\partial P_o}{\partial t} + \left(B_w - R_{sw}B_g\right)\left[\frac{S_w}{B_w}\frac{\partial \phi}{\partial P_o} - \frac{S_w}{B_w^{\,2}}\frac{\partial B_w}{\partial P_o}\right]\frac{\partial P_o}{\partial t}$$
$$+ \left\{S_g\frac{\partial \phi}{\partial P_o} - \frac{S_g\phi}{B_g}\frac{\partial B_g}{\partial P_o} + \frac{B_gS_oR_{so}}{B_o}\frac{\partial \phi}{\partial P_o} + \frac{B_g\phi S_o}{B_o}\frac{\partial R_{so}}{\partial P_o} - \frac{B_g\phi S_oR_{so}}{B_o^{\,2}}\frac{\partial B_o}{\partial P_o} + \frac{B_gS_wR_{sw}}{B_w}\frac{\partial \phi}{\partial P_o} + \frac{B_g\phi S_w}{B_w}\frac{\partial R_{sw}}{\partial P_o} - \frac{B_gS_wR_{sw}}{B_w^{\,2}}\frac{\partial B_w}{\partial P_o}\right\}\frac{\partial P_o}{\partial t} .$$

(A.21)

This equation can be greatly simplified by combining terms resulting in:

$$\left(B_o - R_{so}B_g\right)L_o + \left(B_w - R_{sw}B_g\right)L_w + B_gL_g = \left(S_o + S_w + S_g\right)\frac{\partial \phi}{\partial P_o} - \frac{\phi S_g}{B_g}\frac{\partial B_g}{\partial P_o} + \phi S_o\left(\frac{B_g}{B_o}\frac{\partial R_{so}}{\partial P_o} - \frac{1}{B_o}\frac{\partial B_o}{\partial P_o}\right)$$
$$+ \phi S_w\left(\frac{B_g}{B_w}\frac{\partial R_{sw}}{\partial P_o} - \frac{1}{B_w}\frac{\partial B_w}{\partial P_o}\right)\frac{\partial P_o}{\partial t} \quad ;$$

(A.22)

where …

$$\phi c_r = \frac{\partial \phi}{\partial P_o} \quad ; \tag{A.23}$$

$$c_g = \frac{1}{B_g}\frac{\partial B_g}{\partial P_o} \quad ; \tag{A.24}$$

$$c_o = \frac{B_g}{B_o}\frac{\partial R_{so}}{\partial P_o} - \frac{1}{B_o}\frac{\partial B_o}{\partial P_o} \quad ; \tag{A.25}$$

$$c_w = \frac{B_g}{B_w}\frac{\partial R_{sw}}{\partial P_o} - \frac{1}{B_w}\frac{\partial B_w}{\partial P_o} \quad ; \tag{A.26}$$

and

$$\phi c_t = c_r + c_o S_o + c_w S_w + c_g S_g \quad . \tag{A.27}$$

Employing these definitions, Equations (A.16), (A.17) and (A.20) in (A.22) gives:

$$\begin{aligned} &\left(B_o - R_{so}B_g\right)\left[\nabla\frac{\vec{K}\lambda_o}{B_o}\nabla P_o + CG_o - \frac{q_o}{\rho_{osc}}\right] + \left(B_w - R_{sw}B_g\right)\left[\nabla\frac{\vec{K}\lambda_w}{B_w}\nabla P_o + CG_w - \frac{q_w}{\rho_{wsc}}\right] + \\ &B_g\nabla\left[\vec{K}\left(\frac{\lambda_g}{B_g} + \frac{R_{so}\lambda_o}{B_o} + \frac{R_{sw}\lambda_w}{B_w}\right)\right]\nabla P_o + CG_g - \frac{q_g}{\rho_{gsc}} = \phi c_t\frac{\partial P_o}{\partial t} \end{aligned} \quad ; \tag{A.28}$$

where:

$$CG_o = -\nabla\frac{\vec{K}\lambda_o}{B_o}\nabla\left(\frac{\rho_o z}{144}\right) \quad ; \tag{A.29}$$

$$CG_w = -\nabla\frac{\vec{K}\lambda_w}{B_w}\nabla\left(\frac{\rho_w z}{144} + P_{COW}\right) \quad ; \tag{A.30}$$

$$CG_g = -\nabla\left\{\vec{K}\left[\frac{\lambda_g}{B_g}\nabla\left(P_{CGO} - \frac{\rho_g z}{144}\right) - \frac{R_{so}\lambda_o}{B_o}\nabla\frac{\rho_o z}{144} - \frac{R_{sw}\lambda_w}{B_w}\nabla\left(P_{COW} - \frac{\rho_w z}{144}\right)\right]\right\}. \tag{A.31}$$

Equation (A.28) is called the pressure equation because no explicit time derivatives of saturations are present. BOAST numerically solves the flow equations for P_o then, it finds S_o, S_w and S_g from flow equations given in (A.13), (A.14), (A.15) and from $S_o+S_w+S_g=1$.

The partial differential flow equations presented earlier are approximated by algebraic equations known as finite difference equations. The finite difference equations are obtained by replacing derivatives with approximations derived from truncated Taylor series expansions. Converting partial differential equations to finite difference form is explained in Basic Applied Reservoir Simulation[56] and BOAST manual[53]. The finite difference pressure equation can be presented in a relatively simple form by making the following definitions:

$$QOWG=\left(B_o{}^n-R_{so}{}^nB_g{}^n\right)\left[\frac{q_oV_B}{\rho_{osc}}-GOWT\right]+\left(B_w{}^n-R_{sw}{}^nB_g{}^n\right)\left[\frac{q_wV_B}{\rho_{wsc}}-GWWT\right]+\left(B_g{}^n\right)\left[\frac{q_gV_B}{\rho_{gsc}}-GGWT\right];$$

(A.32)

$$AE_i=\left(B_o+\frac{1}{2}B_g\left(R_{so,i+1}-R_{so,i}\right)\right)A_{o,i+1/2}+\left(B_w+\frac{1}{2}B_g\left(R_{sw,i+1}-R_{sw,i}\right)\right)A_{w,i+1/2}+B_gA_{g,i+1/2};$$

(A.33)

$$AW_i=\left(B_o+\frac{1}{2}B_g\left(R_{so,i-1}-R_{so,i}\right)\right)A_{o,i-1/2}+\left(B_w+\frac{1}{2}B_g\left(R_{sw,i-1}-R_{sw,i}\right)\right)A_{w,i-1/2}+B_gA_{g,i-1/2};$$

(A.34)

$$AN_j=\left(B_o+\frac{1}{2}B_g\left(R_{so,j+1}-R_{so,j}\right)\right)A_{o,j+1/2}+\left(B_w+\frac{1}{2}B_g\left(R_{sw,j+1}-R_{sw,j}\right)\right)A_{w,i+1/2}+B_gA_{g,j+1/2};$$

(A.35)

$$AS_j=\left(B_o+\frac{1}{2}B_g\left(R_{so,j-1}-R_{so,j}\right)\right)A_{o,j-1/2}+\left(B_w+\frac{1}{2}B_g\left(R_{sw,j-1}-R_{sw,j}\right)\right)A_{w,j-1/2}+B_gA_{g,j-1/2};$$

(A.36)

$$AB_k=\left(B_o+\frac{1}{2}B_g\left(R_{so,k+1}-R_{so,k}\right)\right)A_{o,k+1/2}+\left(B_w+\frac{1}{2}B_g\left(R_{sw,k+1}-R_{sw,k}\right)\right)A_{w,k+1/2}+B_gA_{g,k+1/2};$$

(A.37)

$$AT_k = \left(B_o + \frac{1}{2} B_g \left(R_{so,k-1} - R_{so,k} \right) \right) A_{o,k-1/2} + \left(B_w + \frac{1}{2} B_g \left(R_{sw,k-1} - R_{sw,k} \right) \right) A_{w,k-1/2} + B_g A_{g,k-1/2} \cdot$$

(A.38)

All the parameters in Equations (A.32) through (A.38) are evaluated at the present time level (n). The pressure equation (A.28) then becomes:

$$\begin{aligned} &AT_k P_{k-1}{}^{n+1} + AS_j P_{j-1}{}^{n+1} + AW_i P_{i-1}{}^{n+1} \\ &+ AB_k P_{k+1}{}^{n+1} + AN_j P_{j+1}{}^{n+1} + AE_i P_{i+1}{}^{n+1} + EP^{n+1} = B \end{aligned} \quad ; \tag{A.39}$$

$$E = -\left[AT_k + AS_j + AW_i + AB_k + AN_j + AE_i + \frac{V_p{}^n c_t{}^n}{\Delta t} \right] \; ; \tag{A.40}$$

$$B = -\left[-QOWG + \frac{V_p{}^n c_t{}^n P^n}{\Delta t} \right] \; . \tag{A.41}$$

APPENDIX B – VERIFICATION OF PPT CODE WITH BP EXPERIMENT

BP petroleum company performed laboratory experiments at their Sunbury facilities attempting to evaluate the applicability of pressure pulse technology to the enhanced recovery of oil. [71] The results of these tests offer another example for validation of the PPT numerical simulation. While these experiments were unsuccessful in stimulating increased oil production, simulations using the PPT model indicate that the failure was likely due to the method in which the experimental apparatus was constructed. Additionally, the results of these simulations lead to recommendations for constructing future successful tests.

In these experiments, the porous medium was created from sandstone core plugs covered by a PVC membrane. This membrane covered medium was then placed in a cylindrical steel cell and subjected to a 2000 psi uniaxial stress. A brief schematic is given in Figure B-1.

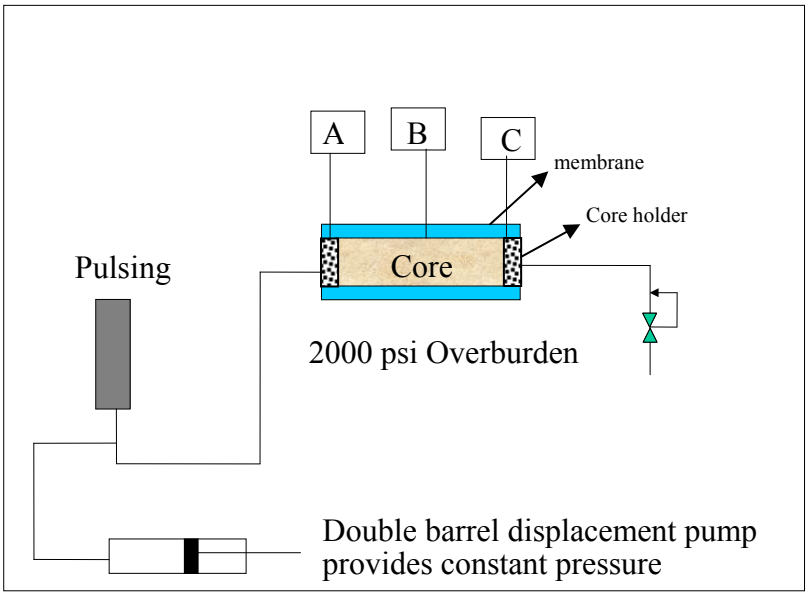

Figure B-1: Schematic of the pressure pulse experiment performed by BP

The sample used in these tests had a porosity of 20% and permeability of 30 mD. The sand was oil wet and was saturated with water as the mobile phase. Initially, a constant

head was created across the cell and flow was allowed to come to a steady-state rate. After a steady-state period, the sand pack was excited by pressure pulsing near the inlet port at varying pulse heights and frequencies. Pulsing was stopped for some interval and then started again and a number of cycles were carried out.

The measured pulsed flow results are given in Figure B-2 for a series of different pressure drops and are compared to the flowrates expected due to Darcy flow. The pulsed flow results are represented by an average of all the data points collected during the pulse and therefore do not represent the minimum or maximum flowrates generated by the pulse. These results show no clear benefit from pulsing over the frequencies and amplitudes tested for this system and led to the conclusion that pressure pulsing offered no benefits over steady-state flow.

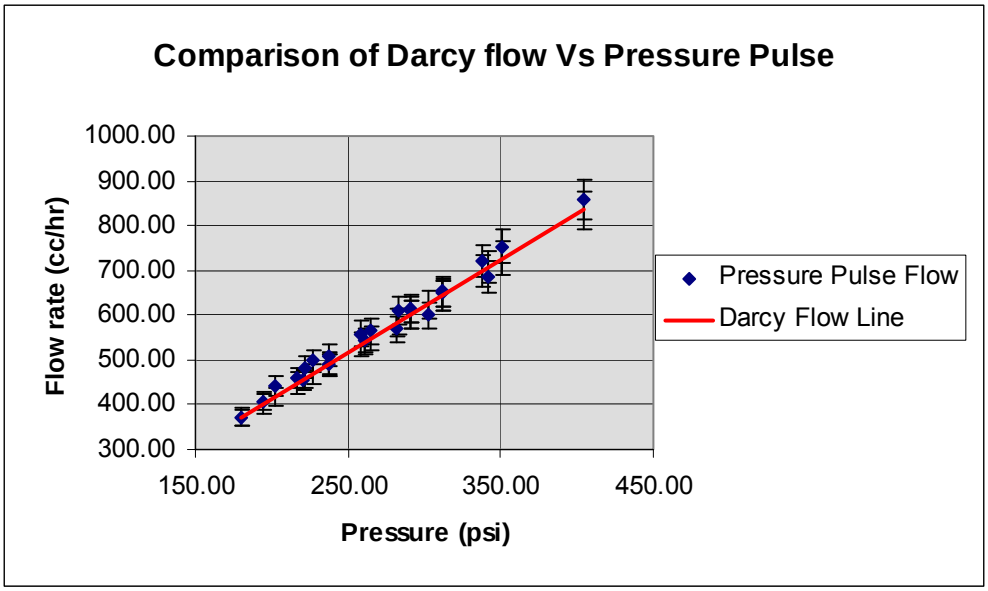

Figure B-2: Flowrate versus pressure resulting from the BP pressure pulse test

In order to understand why pressure pulsing did not lead to enhanced flow through the core, the experiment was simulated with the PPT-BOAST algorithm. In these simulations a 3D model was used consisting of seven layers with 17 gridblocks in the x–direction and 7 gridblocks in the y-direction. The first and seventh layers represented the membrane while the internal layers represented the porous medium. An x-z cross section

is shown in Figure B-3. The gridblocks representing the porous medium were given a permeability of 3 mD and a compressibility of $1x10^{-5}$ psi^{-1} while the space between the membrane and the porous media was modeled with a small permeability and large compressibility (0.3 mD and 0.1 psi^{-1}).

Figure B-3: Cross-section of the simulation model of the BP pressure pulse test

Two sets of simulated pressure transitions were examined: Figure B-4 shows the pressure transition in the porous medium and Figure B-5 shows the pressure transition in the membrane. In these figures, "A" represents the pressure near the injector, "B" represents the pressure at the mid-point in the sample, and "C" represents the pressure at the producer. As can be seen in the figures, there is a much larger pressure transition in the membrane than in the porous media. The membrane shows a pressure response due to the pulsing while there is virtually no reponse in the porous medium. This result shows that the pressure pulse did not propagate through the sample but instead propagated through the more compressible PVC membrane surrounding the porous medium. Therefore, a porosity wave was never generated in the porous medium.

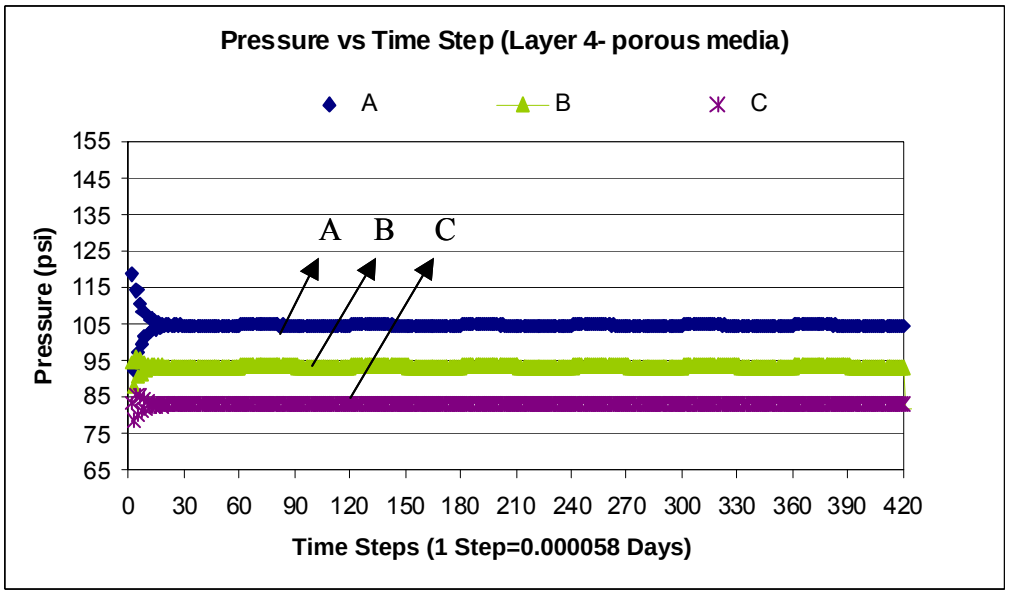

Figure B-4: Predicted pressure response at three locations within the porous medium

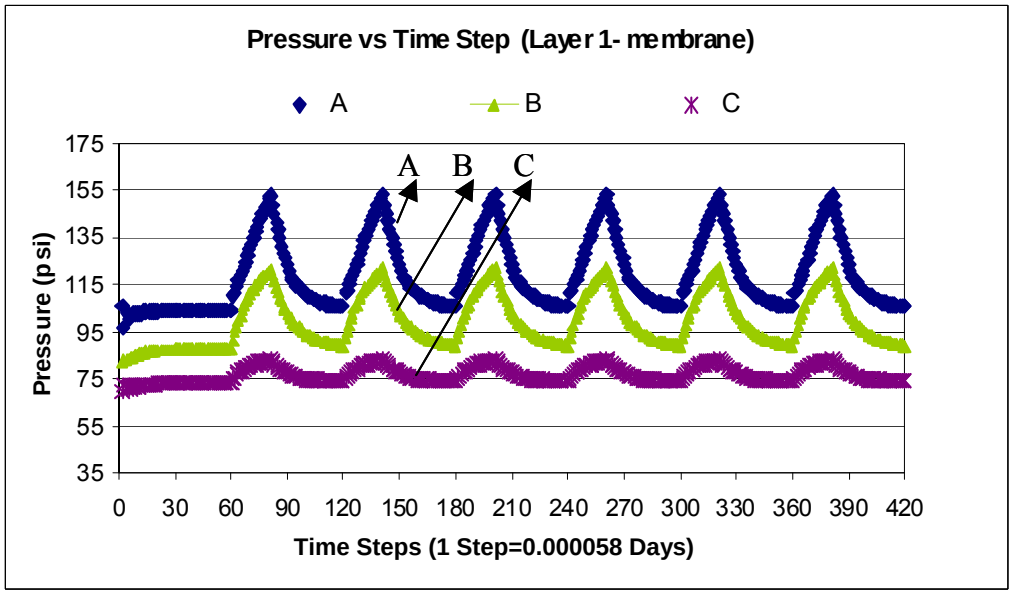

Figure B-5: Predicted pressure response at three locations within the membrane

The conclusion that can be drawn from these results is that highly compressible materials in contact with the porous medium (such as Neoprene, rubber, or like materials used as membranes to protect the specimen during testing) can dampen the impulse that is applied to the porous medium, adversely affecting the propagation of a porosity-pressure

wave and thereby resulting in no significant increase in fluid flow. This is due to the pulse wanting to follow the path of least resistance to deformation or, in other words, the path of highest compressibility. If this path is through a material external to the porous medium then a porosity wave will not be generated and pressure pulsing will have no effects. It is therefore recommended that for laboratory experiments attempting to examine the effects of pressure pulsing the core should be jacketed in a material that is much more rigid than the matrix itself. It should be noted that in the field, it is most likely that the path of least resistance to deformation would be through the fluid saturated reservoir rock.

REFERENCES

1. Pan, Y., "Reservoir analysis using intermediate frequency excitation," PhD dissertation, Stanford University, August 1999

2. de la Cruz, V., Sahay, P. N., Spanos, T. J. T., “Thermodynamics of Porous Media”, Proceedings of the Royal Society of London, 443(A):247-255, 1993.

3. Davidson B. C., Spanos, T. J. T., and Dusseault, M. B., Laboratory experiments on pressure pulse flow enhancement in porous media. In Proceedings of the 8th CIM Regina Petroleum Society Technical Meeting, Regina, Saskatchewan, October 1999.

4. Spanos, T. J. T., Davidson, B. C., Dusseault, M. B., Samaroo, M., “Pressure Pulsing at the Reservoir Scale: A New IOR Approach, 50th CIM Petroleum Society Annual Technical Meeting, Calgary, June 1999.

5. Geilikman, M. B., Spanos, T. J. T., Nyland, E., “Porosity Diffusion in Fluid-Saturated Media”, Tectonophysics, 217:111-115, 1993.

6. Hickey, C. J., Spanos, T. J. T., de la Cruz, V., “Deformation Parameters of Permeable Media”, Geophys. J. Int., 121:359-370, 1995.

7. de la Cruz, V., Spanos, T. J. T., Yang, D., “Macroscopic Capillary Pressure”, Letters in Mathematical Physics, 19:67-77, 1995.

8. Dusseault, M.B., Shand, D., Davidson, B. C., “Pressure Pulse Workovers in Heavy Oil”, SPE 79033, Calgary 2002.

9. de la Cruz, V., Spanos, T. J. T., "Thermomechanical Coupling During Seismic Wave Propagation in a Porous Medium", Journal of Geophysical Research, 94(B1): 637-642, January 10, 1989.

10. Belhaj, H. A., Agha, K. R., Butt, S. D., Islam, M. R., "Simulation of non-Darcy Flow in Porous Media Including Viscous, Inertial and Frictional Effects", SPE 84879, October 2003.

11. Li, D., Svec, R. K., Engler, T. W., Grigg, R. B., "Modeling and Simulation of the Wafer Non-Darcy Flow Experiments", SPE 68822, March 2001.

12. Biot, M. A., "Theory of Propagation of Elastic Waves in a Fluid-Saturated Porous Solid. I. Low Frequency Range" and "Theory of Propagation of Elastic Waves in a Fluid-Saturated Porous Solid. II. High Frequency Range", The Journal of Acoustical Society of America, 28(2): 168-191, March 1956.

13. Deresiewicz, H. and Rice, J. T., "The Effect of Boundaries on Wave Propagation in a Liquid Filled Porous Solid," *Bulletin of Seismology Society of America* (1962) Vol. 52, 595.

14. Birch, F., "Compressibility; Elastic Constants," Handbook of Physical Constants, (1966) 97, 97-174.

15. Stoll, R. D., and Bryan, G. M., "Wave Attenuation in Saturated Sediments," *Journal of Acoustical Society of America* (1970) 47(5), 1440.

16. Hamilton, M. F., "Fundamentals and Applications of Nonlinear Acoustics", *Nonlinear Wave Propagation in Mechanics –AMD-77*, America Society of Mechanical Engineering, New York. (1986).

17. Biot, M. A., “Mechanics of Deformation and Acoustic Propagation in Porous Media”, Journal of Applied Physics, 33(4): 1482-1498, April 1962.

18. Beresnev I. A., Johnson, P. A., “Elastic-Wave Stimulation of Oil Production: A Review of Methods and Results”, Geophysics, 59(6): 1000-1017, June 1994.

19. Foster, W. R., McMillen, J. M., Odeh, A. S., “The Equations of Motion of Fluids in Porous Media: I.Propagation Velocity of Pressure Pulses”, SPE 1967, December 1967.

20. Manga, M., Brodsky, E. E., Boone, M., Response of Streamflow to Multiple Earthquakes , Geophysical Research Letters, 2003, 30(5), 1214.

21. Spanos, T. J. T., Dusseault, M. B., Udey, N., Fundamental Thermodynamic Requirements for Porous Media Description, Chapter 75 from “Coupled Thermo-Hydro-Mechanical-Chemical Processes in Geo-Systems - Fundamentals, Modelling, Experiments and Applications”, Stephansson, Ove; Hudson, John A.; Jing, Lanru, Elsevier, 2004

22. Klinkenberg, L. J.: “The Permeability of Porous Solids to Liquids and Gases,” Drill. & Prod. Prac. (API 1941) 200.

23. Fatt, I.: “A Demonstration of the Effect of ‘Dead-End’ Volume on Pressure Transients in Porous Media,” Trans., AIME (1959) Vol. 216, 449-454.

24. Bruce, G. H., Peaceman, D. W., Rachford, H. H. and Rice, J. D.: "Calculation of Unsteady-State Gas Flow Through Porous Media," Journal of Petroleum Technology (March 1953) 79-92, Trans. AIME (1953), 198.

25. Oroveanu, T. and Pascal, K.: "On the Propagation of Pressure Waves in a Liquid Flowing Through a Porous Medium," *Revue de Mechanique Applique* (1959) 4, No. 3, 445.

26. Slattery, J. C.: "Flow of Viscoelastic Fluids Through Porous Media*" paper SPE 1684* (December 1966).

27. Foster, W. R., McMillen, J. M., and Wallick, G. C.: "The Equations of Motion of Fluids in Porous Media: II. Shape of Pressure Pulses," paper *SPE 2322* presented at the 1968 SPE Annual Meeting.

28. Odeh, A. S. and McMillen, J. M.: "Pulse Testing: Mathematical Analysis and Experimental Verification," *Society of Petroleum Engineers Journal* (October 1972) 403-409.

29. Haskett, S. E., Narahara, G. W. and Holditch, S. A.: "A Method for the Simultaneous Determination of Permeability and Porosity in Low-Permeability Cores," paper *SPE 15379* presented at the 1986 annual meeting, New Orleans.

30. Beresnev, I. A. and Johnson, P. A.: "Elastic-Wave Stimulation of Oil Production: A Review of Methods and Results," *Geophysics* (June 1994) 59, No. 6, 1000-1017.

31. Forchheimer, P. F.: "Wasserbewegung durch Boden," *Zeitschrift des Vereines deutscher Ingenieure* (1901) 45, No.5, 1781-1788.

32. Bonnet, G.: "Basic Singular Solution for a Poroelastic Medium in the Dynamic Range," *Journal of Acoustical Society of America* (November 1987) 82, No. 5, 1758-1762.

33. Zobnin, A. I., Kudryavtsev, B. A., and Parton, V. Z.: "Linearized Equations of Motion of a Viscous Fluid in a Porous Medium of Periodic Structure," *Fluid Dynamics* (March-April 1988) 23, No. 2, 260-266.

34. Depollier, C., Allard, J. F., and Lauriks, W.: "Biot Theory and Stress-Strain Equations in Porous Sound-Absorbing Materials" *Journal of Acoustical Society of America* (December 1988) 84, No. 6, 2277-2279.

35. Zinov'yeva, G. P., Nesterov, I. I., Zdhakhin Y. L., Artma E. E., and Gorbunov Y. V.: "Investigation of Rock Deformation Properties in Terms of the Nonlinear Acoustic Parameter," *Sov. Phys. Dokl., Science Section* (1989) 307, 337-341.

36. Hassanzadeh, S.: "Acoustic Modeling in Fluid Saturated Porous Media," *Geophysics* (1991) 56, 424-435.

37. Zhu, X. and McMechan, G. A.: "Finite-Difference Modeling of the Seismic Response of Fluid-Saturated, Porous, Elastic Media Using Biot Theory," *Geophysics* (1991) 56, 328-339.

38. Norris, A. N. and Grinfeld, M. A.: "Nonlinear Poroelasticity for a Layered Medium," *Journal of Acoustical Society of America* (August 1995) 98, No. 2, 1138-1146.

39. Johnson, P. A. and McCall, K. R.: "Observations and Implications of Nonlinear Elastic Wave Response in Rock," *Geophysics Research Letters* (1994) 21, 165-168.

40. Zimmerman, C. and Stern, M.: "Analytical Solutions for Harmonic Wave Propagation in Poroelastic Media," *Journal of Engineering Mechanics* (October 1994) 120, No. 10, 2154-2179.

41. Dai, N., Vafidis, A., and Kanasewich, E. R.: "Wave Propagation in Heterogeneous Porous Media: A Velocity-Stress, Finite-Difference Method," *Geophysics* (March-April 1995) 60, No. 2, 327-339.

42. Abousleiman, Y, Cheng A. H-D., Jiang , C., and Roegiers, J.-C.: "Poroviscoelastic Analysis of Borehole and Cylinder Problems," *Acta Mechanica* (1996) 119, No. 1-4, 199-219.

43. Johnson, P. A., Zinszner, B. and Rasolofosaon, P. N. J.: "Resonance and Elastic Phenomena in Rock," *Journal of Geophysical Research* (May 1996) Vol. 101, No. B5, 11553-11564.

44. Li, L. P., Cederbaum, G., and Schulgasser, K.: "Vibration of Poroelastic Beams with Axial Diffusion," *European Journal of Mechanics*, A: *Solids* (1996) 15, No. 6, 1077-1094.

45. Brown, R. J. S.: "Connection between Formation Factor of Electrical Resistivity and Fluid-Solid Coupling Factor in Biot's Equations for Acoustic Waves in Fluid-Filled Porous Media" Geophysics 45, 1269–1275 (1980)

46. Winkler, K. W., Nur, A.: "Seismic Attenuation: Effects of Pore Fluids and Frictional Sliding," *Geophysics* (January 1982) Vol. 47, 1-15.

47. Chang, S. K., Liu, H. L. and Johnson D. L.: "Low-Frequency Tube Waves in Permeable Rocks," *Geophysics* (April 1988) Vol. 53, No. 4, 519-527.

48. Auriault, J.-L.: "Heterogeneous Medium. Is an Equivalent Macroscopic Description Possible? " *International Journal of Engineering Sciences* (1991) 29, No. 7, 785-795.

49. Auriault J. L.: "Deformable Porous Media with Double Porosity. Quasi-Statics. I: Coupling Effects," *Transport in Porous Media* (1992) 7, 63-82.

50. Bernabe, Y.: "The Frequency Dependence of Harmonic Fluid Flow Through Networks of Cracks and Pores," *PAGEOPH* (1997) 147, No. 3, 489-506.

51. Winkler, .K. W., Liu, H. L. and Johnson D. L.: "Permeability and Borehole Stoneley Waves: Comparison Between Experiment and Theory," *Geophysics* (January 1989) Vol. 54, 66-75.

52. Pan, Y.: "*Reservoir Analysis Using Intermediate Frequency Excitation*," presented as a dissertation for the Degree of Doctor of Philosophy, Stanford University (August 1999).

53. BOAST Manual

54. Arastoopour, Hamid and Hariri, Hossein: "Analysis of Two-Phase Flow in a Tight Sand Gas Reservoir, Using BOAST", Society of Petroleum Engineers, 1986, 15837-MS

55. Schoeling, L.G and Mark, S: "Improved Reservoir Management/Characterization for Independent Operators in Mature Basins, A Case Study: South Slattery Field, Powder River Basin, Wyoming", Society of Petroleum Engineers, 2000, 59299-MS

56. Ertekin, Turgay et.al: "Basic Applied Reservoir Simulation", 2001, SPE Textbook Vol. 7.

57. Fatt, I. and Davis, D.H.: Reduction in Permeability with Overburden Pressure" Trans., AIME(1952) 195, 329

58. Gray, D.H., Fatt, I., and Bargamini, G.: "The Effect of Stress on Permeability of Sandstone Cores" SPEJ (June 1963) 95-100

59. Wilhelmi, B. and Somerton, W.H. : "Simultaneous Measurement of Pore and Elastic Properties of Rocks Under Triaxial Stress Conditions", SPEJ (September 1976) 283-94

60. Avasthi, J.M. *et. al.*: "In-Situ Stress Evaluation in the McElroy Field, West Texas", SPEFE(Sept. 1991) 301-9

61. Wright, C.A. *et. al.*: "Hydraulic Fracture Orientation and Production/Injection Induced Reservoir Stress Changes in Diatomite Waterfloods", paper SPE 29625 presented at the 1995 SPE Western Regional Meeting, Bakersfield, March 8-10.

62. Saltz, L.B.: "Relationship Between Fracture Propagation Pressure and Pore Pressure" paper SPE 6870 presented at the 1977 SPE Annual Technical Conference and Exhibition, Denver, Oct. 9-12.

63. Osorio, J.G.: "Numerical Simulation of the Impact of Flow Induced Geomechanical Response on the Productivity of Stress-Sensitive Reservoirs", paper SPE 51529 presented at the 1999 SPE Reservoir Simulation Symposium, Houston, Feb 14-17.

64. Chen, H.Y. *et. al.* : "Coupled Fluid Flow and Geomechanics in reservoir Study- I. Theory and Governing Equations", paper SPE 30752 presented at the 1995 SPE Annual Technical Conference and Exhibition, Dallas, Oct. 22-25.

65. J.R. Fanchi, Principles of Applied Reservoir Simulation, 3rd Edition, Butterworth-Heinemann, Boston (2006)

66. Ochs, D.E., Chen, H.Y. and Teufel, L.W.:"Relating In-Situ Stress and Transient Pressure Testing for a Fractured Well", Proceedings of The SPE Annual Technical Conference and Exhibition, October 1997, pt 1, 301-316

67. Williams, D. M., J. Zemanek, F.A. Angona, C.L. Denis and R.L. Caldwell 1984. The long space acoustic logging tool. Transactions of the SPWLA 25th Annual Logging Symposium, Paper T.

68. Osorio, J.G.: "Numerical Modeling of Coupled Fluid Flow/Geomechanical Behavior of Reservoirs with Stress Sensitive Permeability", Thesis Doctor of Philosophy, New Mexico, 1998

69. Nikolaevski, V.N., Lopukhov, G.P., Liao, Y. and Economides, M.J., 1996, Residual Oil Reservoir Recovery with Seismic Vibrations, SPE Production and Facilities, May, 89.

70. www.energy.gov.ab.ca/OilSands/pdfs/RPT_Chops_chptr13.pdf

71. Dusseault, M.B. "Pressure Pulse Technology at Wytch Farm", Prism Production Technologies Internal Report